COLLEGE DOCTORAL BRETAGNE
MATHS, TELECOMS
INFORMATIQUE, SIGNAL
SYSTEMES, ELECTRONIQUE

INSA INSTITUT NATIONAL DES SCIENCES APPLIQUÉES RENNES

THÈSE DE DOCTORAT DE

L'INSTITUT NATIONAL DES SCIENCES APPLIQUÉES DE RENNES

ÉCOLE DOCTORALE N° 601
Mathématiques, Télécommunications, Informatique, Signal, Systèmes, Électronique
Spécialité : *Électronique*

Par
Valentin MORIN

Contributions to Antenna Characterization from Non-Conventional Cartesian Near-Field Measurements: Application of Novel Near-Field to Far-Field Transform Methods on Non-Planar and Irregular Sampling Grids for Directive Antennas with Wide-Angle Beam Scanning.

Thèse présentée et soutenue à Rennes, le 27/11/2025
Unité de recherche : IETR
Thèse N° : 25ISAR 27 / D25 - 27

Rapporteur·trice·s avant soutenance :

Amélie LITMAN — Professeur, Institut Fresnel, Marseille, France
François GALLÉE — Professeur, Lab-STICC, Brest, France

Composition du Jury :

Président :	Manuel SIERRA CASTAÑER	Professeur, Université Polytechnique de Madrid, Madrid, Espagne
Examinateur·trice·s :	Amélie LITMAN	Professeur, Institut Fresnel, Marseille, France
	François GALLÉE	Professeur, Lab-STICC, Brest, France
	Claire MIGLIACCIO	Professeur, LEAT, Biot, France
	Nicolas MÉZIÈRES	Ingénieur de recherche, CNES, Toulouse, France
Co-encadrants :	Samuel CORRE	Ingénieur de recherche, IETR-UR, Rennes, France
	Éric ESTEBE	Ingénieur de recherche, Thales DMS, Élancourt, France
Dir. de thèse :	Renaud LOISON	Professeur, IETR-INSA, Rennes, France

Invité :

Co-encadrant : Laurent LE COQ — Ingénieur de recherche, IETR-UR, Rennes, France

Acknowledgement

Firstly, I would like to thank my entire supervisory team for the quality of our interactions, discussions and advice over the past three years. Their professionalism, kindness and trust enabled me to transition to a new field of activity under the best possible circumstances. Nicolas, in particular, guided me through a period of radical change and provided me with all the tools I needed to succeed, continuing to mentor me with his invaluable advice even after he left the laboratory. I am extremely grateful for this. Similarly, Samuel has been a constant source of support, always listening and offering increasingly interesting insights. Laurent was not only an unrivalled authority on scientific matters, but also always there for me in times of doubt. Renaud's organization and precision in monitoring the thesis made many things easier for me, teaching me how to work methodically in the process. Finally, I am extremely grateful to Eric, who helped me integrate seamlessly into the department and continues to involve me in Thales' development projects.

Finally, I would like to thank the people I had the pleasure of meeting for the many discussions I had with them and the moments of sharing. In the IETR laboratory: Julien, Thomas, Corinne, Fred, Marius, Stéphane, Jacky, ... And at my company Thales: Emilien, Pierrick, Alexandre, Valentin, Augustin and Clément. In particular, I'd like to extend my warmest thanks to my former Breton office colleagues Xavier, Laurent and Christophe, with whom we had a lot of fun and who created an excellent working atmosphere.

Finally, I have a special thought for my family, who was unfailingly supportive as usual. My parents Laurence and Patrice, my grandparents Annie and François, my grandmother Jeannine, my aunt Sylvie and my great-grandmother Paulette.

Table of Contents

Acronyms 5

Technical acronyms 6

Institutions 8

Nomenclature 9

Résumé 11

Introduction générale . . . 11
Objectifs et contributions . . . 12
Contenu du manuscrit . . . 13
Conclusion et perspectives . . . 16

Introduction 19

Global context . . . 19
Objectives and contributions . . . 21
Content of the manuscript . . . 23

I Antenna characterization 25

I.1 Introduction . . . 25
I.2 Antenna measurement . . . 27
I.2.a Antenna radiation . . . 27
I.2.b Characterization parameters . . . 30
I.2.c Measurement techniques . . . 35
I.2.d Metrics . . . 42
I.3 Planar near-field measurements . . . 46
I.3.a Plane wave expansion . . . 46
I.3.b Duration of the acquisition . . . 49
I.3.c Truncation effects . . . 51
I.4 Conclusion . . . 53

II Antenna characterization employing the equivalence principle 55
II.1 Introduction . . . 55
II.1.a Motivations . . . 55
II.1.b State of the art . . . 56
II.1.c Contributions . . . 58
II.2 Equivalent principle construction . . . 59
II.2.a Huygens principle . . . 59
II.2.b Equivalent model of infinitesimal dipoles . . . 60
II.2.c Discretization of the radiation operator . . . 62
II.2.d Construction of the radiation matrix . . . 65
II.2.e Validations . . . 67
II.3 Inverse problem . . . 70
II.3.a Implementation in the context of characterization . . . 70
II.3.b Determination of the equivalent currents . . . 73
II.3.c Validations: equivalent current determination . . . 76
II.3.d Application . . . 80
II.4 Parametric study of the model . . . 85
II.4.a Methodology . . . 85
II.4.b Planar equivalent surface Σ . . . 87
II.4.c Box-shaped equivalent surface Σ . . . 90
II.4.d Conclusion on the observations . . . 92
II.5 Near-field measurement surface S and truncation effects . . . 93
II.5.a Computed far-field zones . . . 94
II.5.b Methodology . . . 95
II.5.c Analysis of a non-steered main beam . . . 96
II.5.d Analysis of a steered main beam . . . 103
II.5.e Summary of observations . . . 110
II.6 Conclusion . . . 110

III Antenna characterization using a reduced-order model 113
III.1 Introduction . . . 113
III.1.a Motivations . . . 113
III.1.b State of the art . . . 114
III.1.c Contributions . . . 115
III.2 Construction of the reduced-order model . . . 116
III.2.a Singular value decomposition . . . 116
III.2.b Regularization . . . 119

III.2.c On the choice of the truncation index . . . 122
III.2.d Decomposition of the measured near-field . . . 123
III.3 Reduction of the number of samples . . . 124
III.3.a From the singular values to the number of samples . . . 124
III.3.b Sampling strategies . . . 125
III.3.c Characterization from an interpolated near field . . . 128
III.3.d Application . . . 132
III.4 Construction of the direct near-field to far-field transform . . . 140
III.4.a A new reading of the characterization problem . . . 140
III.4.b Validation . . . 142
III.5 Conclusion . . . 146

IV Application of characterization methods on experimental cases 149
IV.1 Introduction . . . 149
IV.1.a Motivations . . . 149
IV.1.b State of the art . . . 150
IV.1.c Contributions . . . 151
IV.2 Probe compensation . . . 152
IV.2.a Probe compensation in near-field measurements . . . 153
IV.2.b Determination of probe radiation characteristics . . . 154
IV.2.c Model integration of probe compensation . . . 163
IV.2.d Validations . . . 166
IV.3 Characterization of a W-band horn . . . 174
IV.3.a Characterization setup . . . 174
IV.3.b Classical errors for planar near-field measurements . . . 177
IV.3.c Characterization results and error analysis . . . 179
IV.4 Characterization of an X-band Luneburg lens . . . 191
IV.4.a Characterization setup . . . 192
IV.4.b Discussion on the measurement errors . . . 193
IV.4.c Characterization results and analysis . . . 199
IV.5 Conclusion . . . 208

Conclusion 211
Summary and outcomes . . . 211
Perspectives . . . 212

Appendices **215**

A Simulated CST X-band patch 215

B IETR measurement facilities for experimental validations 222

C Measured X-band Luneburg lens 232

Publication list **239**

Bibliography **241**

Technical acronyms

Notation	Description
M^2ARS	Manufacturing Measurement Analysis of Radiating Systems
AESA	Active Electronically Scanned Array
AUT	Antenna Under Test
BPDN	Basis Pursuit Denoising
BZ	Black Zone
CACENDRA	*CAractérisation en bande CENtimétrique de Dispositifs RAyonnants*, characterization of radiating devices in centimetric band
CAMILL	*Caractérisation d'Antennes en bande MILL et subMILLimétrique*, antennas characterization for mill and submillimetric bands
CATR	Compact Antenna Test Range
DFT	Discrete Fourier Transform
ENL	Equivalent Noise Level
FEM	Finite Element Method
FF	Far Field
FPGA	Field-Programmable Gate Array
FT	Fourier Transform
GZ	Gray Zone
HPBW	Half-Power Beam Width

Notation	Description
IDEM	*Imagerie et Diagnostic ElectroMagnétique*, imagery and electromagnetic diagnostic
IP	Inverse Problem
MoM	Method of Moments
NF	Near Field
NFFFT	Near-Field to Far-Field Transform
OEWG	Open-Ended Waveguide
PDE	Partial Differential Equation
PWE	Plane Wave Expansion
PWS	Plane Wave Spectrum
RA	Return on Aperture
ROM	Reduced-Order Model
SVD	Singular Value Decomposition
SWE	Spherical Wave Expansion
TSVD	Truncated Singular Value Decomposition
VNA	Vector Network Analyzer
WZ	White Zone

INSTITUTIONS

Notation	Description
ANRT	*Association Nationale de la Recherche et de la Technologie*, national association for research and technology
CIFRE	*Convention Industrielle de Formation par la REcherche*, industrial agreement on training through research
DMS	Defense Mission Systems
IETR	*Institut d'Électronique et des Technologies du numéRique*, institute of electronics and digital technologies
UNIVREN	*UNIVersité de RENnes*, university of Rennes

List of Symbols

The next list describes several symbols that will be later used within the body of the document. National Institute of Standards and Technology was referenced to provide the values of physical constants, and their corresponding units.

Physics Constants

ε_0	Vacuum electric permittivity	$8.854\,187\,818\,8 \times 10^{-12}\,\mathrm{F\,m^{-1}}$
μ_0	Vacuum magnetic permeability	$1.256\,637\,061\,27 \times 10^{-6}\,\mathrm{N/A^2}$
c	Speed of light in vacuum	$299\,792\,458\,\mathrm{m\,s^{-1}}$
η	Characteristic impedance of vacuum	$376.730\,313\,412\,\Omega$

Fundamental relations

$c = \frac{1}{\varepsilon_0 \mu_0}$	Relation between c, ε_0 and μ_0
$\eta = \sqrt{\frac{\mu_0}{\varepsilon_0}}$	Relation between η, ε_0 and μ_0
$\lambda = \frac{c}{f}$	Relation between the wavelength in vacuum λ, c and the frequency f
$k_0 = \frac{2\pi}{\lambda}$	Relation between the wavenumber k_0 and λ

Résumé

Introduction générale

Les antennes sont des dispositifs incontournables dans le paysage technologique actuel. Elles assurent la conversion entre ondes guidées et ondes électromagnétiques propagées dans l'espace libre, rendant possible la communication sans fil, la détection radar, la navigation satellitaire et de nombreuses autres applications. Leur rôle est d'autant plus critique que la société moderne repose sur un réseau dense et diversifié de systèmes connectés, allant des terminaux de téléphonie mobile aux radars embarqués pour l'aviation.

Depuis les années 1950, les innovations dans le domaine des antennes a accompagné les progrès spectaculaires des télécommunications. Les antennes sont devenues plus complexes, capables de fonctionner sur des bandes plus larges, à des fréquences plus élevées, avec des gains accrus et des capacités de formation de faisceaux agiles. Cette complexité accrue rend leur caractérisation essentielle, mais aussi de plus en plus difficile. La caractérisation consiste à mesurer ou estimer leurs performances électromagnétiques, et notamment leur diagramme de rayonnement en champ lointain (*Far Field*, FF).

Traditionnellement, la méthode la plus directe consiste à mesurer le champ en zone de Fraunhofer, c'est-à-dire à une distance suffisante pour que l'onde rayonnée puisse être assimilée à une onde plane. Or, cette approche est souvent coûteuse et contraignante, car les distances requises croissent avec la taille électrique de l'antenne (relative à sa fréquence de fonctionnement.). Pour les systèmes modernes de type AESA (*Active Electronically Scanned Arrays*, Réseaux électroniques à balayage actif), qui combinent grande dimension, fort gain et capacité de balayage angulaire important, les mesures directes en FF deviennent souvent irréalisables en pratique.

C'est pourquoi les techniques de mesure en champ proche (*Near Field*, NF) se sont développées depuis plusieurs décennies. Elles consistent à acquérir le champ électromagnétique à proximité de l'antenne, sur une surface plane, cylindrique ou sphérique, puis à appliquer une transformation champ proche-champ lointain (*Near-Field to Far-Field Transform*, NFFFT) pour reconstituer le rayonnement. Parmi ces techniques, la géométrie plane est particulièrement adaptée aux antennes lourdes et encombrantes, typiquement

les réseaux AESA, qui ne peuvent être aisément déplacés ou tournés pendant la mesure.

La méthode plane classique repose sur la transformée de Fourier pour effectuer une expansion en ondes planes (*Plane Wave Expansion*, PWE). Elle est robuste, mais impose des conditions d'échantillonnage strictes et se montre sensible aux effets de troncature liés à la taille finie de la surface mesurée. Ces limitations entraînent des temps de mesure très longs (plusieurs heures pour des réseaux de grande taille) et des pertes de précision pour les antennes dont le faisceau est incliné ou à large balayage.

Dans ce contexte, cette thèse vise à dépasser les limites de l'approche classique concernant des mesures NF planaires pour des AESAs.

Objectifs et contributions

L'objectif principal de cette recherche est de concevoir des méthodes de caractérisation adaptées aux antennes à réseau de type AESA, permettant de réduire le temps de mesure et d'améliorer la précision des NFFFTs liées à des mesures NF planaires, notamment à travers l'atténuation des effets de troncature. Pour cela, la démarche s'écarte volontairement du cadre strict d'une approche fondée sur la transformée de Fourier, afin d'introduire des modèles physiques plus flexibles, capables de s'adapter à des grilles d'échantillonnage non conventionnelles, voire irrégulières, et de tenir compte de surfaces de mesure à géométrie non plane.

Les contributions se déclinent en plusieurs volets complémentaires. Tout d'abord, le manuscrit présente le développement d'une méthode basée sur le principe d'équivalence, qui permet de modéliser l'antenne sous test (*Antenna Under Test*, AUT) par une distribution de courants équivalents construite sur une surface définie numériquement. Dans notre cas, ce concept est appliqué en utilisant une distribution de dipôles infinitésimaux électriques et magnétiques pour représenter l'AUT. Cette approche permet la construction d'une matrice de rayonnement entre les positions des dipôles et une surface définie dans l'espace de rayonnement. Dans notre contexte de caractérisation deux matrices sont définies pour la surface NF de mesure et pour la surface d'observation FF. Cela ouvre la voie à une formulation matricielle reliant directement les courants équivalents au champ mesuré, et permet de traiter la caractérisation comme un problème inverse (*Inverse Problem*, IP). Le calcul du FF est alors basé sur la détermination des courants équivalents de l'AUT. Par ailleurs, la matrice de rayonnement NF se repose sur une construction purement géométrique permettant de s'affranchir des contraintes liées à la répartition des

points de mesure. Ainsi, le modèle développé offre la possibilité d'envisager des échantillonnages non conventionnels, ayant pour conséquence de réduire les effets de troncature qui seraient induits par l'utilisation d'une grille planaire classique dans le cas d'une PWE.

Ensuite, un modèle d'ordre réduit (*Reduced-Order Model*, ROM) est introduit, basé sur la décomposition en valeurs singulières (*Singular Value Decomposition*, SVD) de la matrice de rayonnement. Ce modèle fournit d'une part un critère *a priori* sur le nombre minimal d'échantillons nécessaires pour atteindre une précision donnée, ce qui constitue un outil puissant pour optimiser les stratégies de mesure offertes par notre approche. Cela répond directement à la contrainte industrielle de réduire le temps de caractérisation, souvent critique dans la production en série d'antennes. Puis, le ROM permet également d'isoler une base réduite de décomposition du NF mesuré servant de moyen d'interpolation de données dans l'espace champ rayonné. Cette dernière propriété débloque le développement de nouvelles méthodes de caractérisation profitant de la régularisation amenée par la réduction du modèle.

Enfin, ces travaux proposent une nouvelle NFFFT directe basée sur la construction d'un ROM pour le problème de caractérisation en liant à la fois les espaces NF et FF aux dipôles modélisant l'AUT dans une seule matrice de rayonnement. La transformée repose sur le calcul d'une base réduite d'espace champ rayonné qui intègre à la fois la géométrie de mesure et les effets de la sonde et tire parti des propriétés énoncées pour le ROM. Cette matrice est pré-calculable pour une configuration de caractérisation donnée (notamment la fréquence de fonctionnement, les surfaces de mesure NF et d'observation FF, la sonde de mesure, le mode opérationnel de l'acrshortaut). Après ce calcul, cette transformation se réduit à une simple inversion de matrice suivie d'une multiplication matricielle, offrant une solution rapide, précise et facile à implémenter dans des environnements industriels.

Ces contributions sont validées à la fois par des simulations numériques et par des mesures expérimentales réalisées sur des cas concrets : un cornet en bande W et une lentille de Luneburg en bande X.

Contenu du manuscrit

Chapitre I : Fondements de la caractérisation d'antennes

Le premier chapitre de la thèse rappelle les bases théoriques de la caractérisation d'antennes. Une antenne est un système rayonnant dont les performances sont décrites

par divers paramètres : diagramme de rayonnement, directivité, gain, polarisation, largeur de lobe, etc. Ces paramètres sont définis dans la zone de Fraunhofer (FF), où le champ peut être considéré comme transverse et indépendant de la distance.

Différentes techniques de mesure existent pour retrouver le FF d'antennes. D'abord, les mesures directes en FF, réalisées soit en extérieur, soit dans des chambres anéchoïques, éventuellement à l'aide de systèmes CATR (*Compact Antenna Test Range*, banc d'essai compact pour antennes) pour reproduire un champ quasi-plan. Ces méthodes sont précises mais coûteuses et souvent longues. Ensuite, les mesures en NF, qui consistent à échantillonner le champ rayonné dans la zone de Fresnel. Elles nécessitent une NFFFT pour calculer le FF. Selon la géométrie de mesure, cette transformation peut reposer sur des expansions sphériques, cylindriques ou planes.

Le cas des mesures planes est étudié en détail. La méthode classique PWE repose sur la décomposition du champ mesuré en une superposition d'ondes planes. Elle est bien maîtrisée, mais impose des règles d'échantillonnage strictes dictées par le théorème de Nyquist afin d'éviter les effets d'aliasing. Cela conduit à des acquisitions longues et coûteuses pour des antennes de grande taille. De plus, les effets de troncature liés à la surface de mesure finie dégradent fortement la précision pour les faisceaux inclinés, ce qui constitue une limite importante pour les réseaux AESA.

Ces constats motivent la recherche de nouvelles approches, capables de s'affranchir des contraintes de Fourier et d'exploiter des échantillonnages plus souples.

Chapitre II : Approche par principe d'équivalence et problème inverse

Le second chapitre développe le cadre théorique des méthodes proposées. Il s'appuie sur le principe d'équivalence de Huygens, qui stipule que le rayonnement d'une antenne peut être remplacé par une distribution de courants équivalents sur une surface fermée englobant la source.

Dans cette thèse, la surface équivalente est discrétisée en un ensemble de dipôles infinitésimaux. Cette discrétisation permet de construire une matrice de rayonnement reliant directement les positions des dipôles à n'importe quelle surface dans l'espace de rayonnement. Dans notre contexte, cela se résume à la construction de deux matrices de rayonnement : l'une liée à la surface de mesure NF et une seconde associée à une surface d'intérêt en FF. Notamment, la modélisation de l'antenne par les dipôles permet

de débloquer des stratégies d'échantillonnage non conventionnels sur la surface de mesure et de s'affranchir de la grille régulière et dense imposée par la PWE, permettant de limiter les effets de troncature.

Le problème de caractérisation est alors reformulé comme un IP : à partir des mesures en NF, il s'agit de déterminer la distribution des courants équivalents qui reproduit le mieux le comportement physique de l'AUT. Une fois cette distribution obtenue, il est possible de propager analytiquement le champ vers toute surface d'observation, et en particulier vers la zone de Fraunhofer.

L'approche est validée par des études paramétriques et des simulations numériques. Elle montre une bonne précision, y compris dans des cas où la méthode classique PWE est pénalisée par les effets de troncature.

Chapitre III : Modèle d'ordre réduit et nouvelle transformation champ proche-champ lointain

Le troisième chapitre introduit un ROM destiné à réduire la complexité du problème de caractérisation. La matrice de rayonnement construite à partir du modèle équivalent et liée à la surface de mesure NF est soumise à une SVD. Cette opération permet d'identifier les modes dominants du problème et de négliger les composantes de moindre importance.

Deux principales conséquences découlent de cette étape. Premièrement, la réduction d'ordre du modèle fournit un critère *a priori* pour estimer le nombre minimal d'échantillons nécessaires et qui a été défini expérimentalement pour des mesures sphériques. La vérification de ce critère dans le cadre de mesures planaires a été effectuée. L'intérêt est de pouvoir réduire le temps de mesure et garantir une précision suffisante. Deuxièmement, la construction d'un ROM pour le problème permet l'identification d'une base réduite dans l'espace champ rayonné, ce qui débloque de nouvelles techniques de caractérisation.

Sur ces propriétés apportées par le ROM, la thèse propose également une nouvelle NFFFT directe. Contrairement à la PWE, qui nécessite des calculs systématiques adaptés à chaque cas de caractérisation pour des échantillonnages réguliers, cette transformation s'appuie sur la base réduite identifiée par la SVD, associée aux surfaces de mesure et d'observation et qui est précalculée pour des problèmes génériques. Cette matrice intègre la géométrie de la surface de mesure et les caractéristiques de la sonde. Ainsi, des sous-échantillonnages de la surface de mesure NF peuvent être directement appliqués pour réduire le nombre de points de mesure selon le critère *a priori*. De plus si cette surface est

non-conventionnelle, les effets de troncature sont également atténués. Le calcul final du FF se réduit à des simples opérations matricielle appliquées aux données NF mesurées, ce qui rend la procédure rapide, précise et facile à industrialiser.

L'application de ces nouvelles méthodes de caractérisation débloquées par le ROM ont montré l'intérêt de l'approche dans des cas de simulations critiques semblables aux caractéristiques d'antennes d'intérêt pour cette thèse.

Chapitre IV : Applications expérimentales

Le quatrième chapitre est consacré aux validations expérimentales.

En pratique, la sonde utilisée pour mesurer le NF n'est jamais parfaitement isotrope et impacte les données acquises avec ses propres caractéristiques de rayonnement. Une compensation de ces effets induits par la sonde doit être réalisée pour garantir une précision de caractérisation convenable. Ces travaux proposent d'intégrer ces effets directement dans la matrice de rayonnement, ce qui permet d'apporter une correction embarquée directement dans le modèle. Des simulations montrent que cette intégration améliore la précision des résultats.

Deux cas expérimentaux représentatifs sont ensuite étudiés.

Le premier est celui d'un cornet fonctionnant en bande W (longueurs d'onde millimétriques). Ce cas met en évidence la capacité des méthodes proposées à réduire l'impact des erreurs de mesure et à restituer avec précision le diagramme de rayonnement dans un contexte de forte contrainte fréquentielle.

Le second est celui d'une lentille de Luneburg fonctionnant en bande X. Cette antenne présente des faisceaux directifs et inclinés, caractéristiques proches de celles des AESAs. Les résultats expérimentaux montrent que la méthode basée sur le modèle réduit permet de réduire significativement le nombre d'échantillons nécessaires, tout en maintenant une précision comparable à celle obtenue avec des mesures sur une grille régulière classique. De plus, la nouvelle NFFFT directe se montre robuste face aux effets de troncature pour des très fortes contraintes de dépointage, confirmant ainsi son intérêt pratique.

Conclusion et perspectives

Cette thèse apporte une contribution significative au domaine de la métrologie des antennes. Elle démontre qu'il est possible de dépasser les limitations de la méthode classique

basée sur la transformée de Fourier (PWE) pour des mesures réalisées en NF planaire, en adoptant une approche fondée sur le principe d'équivalence et sur des outils de réduction d'ordre.

Les résultats expérimentaux montrent que les méthodes développées permettent à la fois de réduire le nombre d'échantillons nécessaires et de minimiser les effets de troncature. La NFFFT directe proposée dans ce manuscrit constitue une avancée majeure, en offrant une solution rapide, précise et facilement transposable à des applications industrielles.

Les perspectives de recherche sont nombreuses. On peut envisager d'étendre ces approches à des surfaces de mesure exotiques ou hybrides, d'intégrer ces outils dans des plateformes de mesure industrielles, ou encore de les appliquer à des bandes de fréquences plus élevées, jusqu'au domaine sub-térahertz. Ces perspectives sont particulièrement prometteuses dans le contexte du développement des communications 6G, des radars à haute résolution et des applications spatiales.

En définitive, cette thèse propose un ensemble cohérent de méthodes qui répondent efficacement aux contraintes actuelles de la caractérisation d'antennes complexes. Elle ouvre la voie à des pratiques de mesure plus rapides, plus flexibles et plus précises, adaptées aux besoins croissants de l'industrie et de la recherche.

INTRODUCTION

Global context

Nowadays, electronic systems are omnipresent in our daily lives, a trend that has accelerated over the last decades with the rise of embedded wireless technologies such as GPS, Wi-Fi, and Bluetooth. In this ultra-connected world, ensuring reliable communication between devices without transmission lines requires a key component: the antenna. Beyond telecommunications and navigation, antennas also play a central role in remote sensing, Earth observation, radar detection, and space exploration. They enable electromagnetic transmission, i. e., the exchange of information between transmitting and receiving systems in free space, or the collection of signals from natural or artificial sources. Consequently, verifying that antennas meet stringent performance requirements has become a central step in the modern production process for wireless electronic systems as well as in the development of advanced sensing applications.

Over the past 70 years, the rapid development of antenna technologies has propelled telecommunications forward. At the same time, the growing complexity of radiating systems has introduced new challenges for accurate characterization. Modern antennas often operate over broader frequency bands, at higher frequencies, and with increasingly high directivities and beam scanning capabilities, while frequently being embedded within devices. These factors significantly increase the difficulty of precisely evaluating their performance. Furthermore, accounting for interactions with their environment, combined with the higher accuracy requirements linked to electrically larger structures, makes purely numerical simulations both computationally expensive and, in many cases, impractical. As a result, measurement facilities often remain the most reliable option to ensure accurate and comprehensive antenna characterization. An example of such a measurement facility present in the *Institut d'Électronique et des Technologies du numéRique* (IETR) laboratory [1] is shown in Fig. 1.

The standard approach to evaluate antenna performance consists in measuring the Far Field (FF) radiated by the Antenna Under Test (AUT), typically at large distances (Fraunhofer zone) or using high-cost reflective systems.

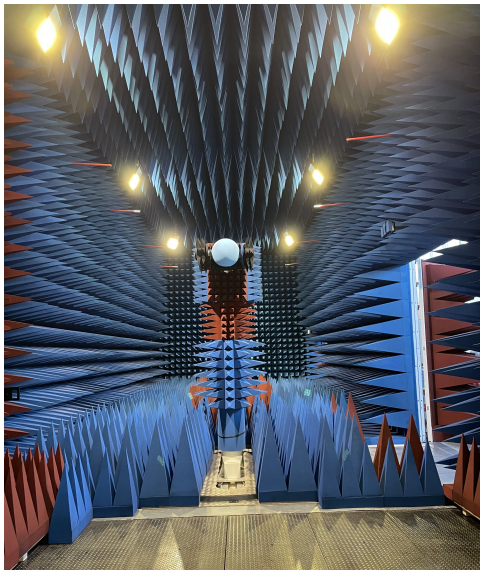

Figure 1 – Luneburg lens mounted on a positioner for direct far-field measurement in an anechoic chamber at the IETR laboratory.

With the emergence of Active Electronically Scanned Arrays (AESAs), which are electrically large antennas with multiple beam patterns, significant beam tilts, and various operating modes, characterization has become increasingly difficult, expensive, and time-consuming. An example of such an AESA system for airborne radar is given in Fig. 2.



Figure 2 – Illustration of the *Radar à Balayage Electronique 2* (RBE2) AESA radar mounted on a Rafale aircraft.

Recently, new antenna measurement techniques based on smaller antenna test range facilities have been developed to speed up procedures and are now commonly employed to characterize these challenging AESA. These techniques rely on measuring this time the Near Field (NF) radiated by the AUT to retrieve its radiation properties by perform-

ing a Near-Field to Far-Field Transform (NFFFT). For AESAs, planar NF measurement systems remain the most practical approach for characterizing this type of antenna. This is because, given the antenna dimensions, weight, and the wiring required for control, planar systems are more suitable than spherical or cylindrical facilities. The planar NF measurement surface geometry implies that the NFFFT that can be used to retrieve the radiated FF refers to the application of a Fourier Transform (FT). In this case, specific constraints on the NF data distribution in the space must be respected. Thus, the number and location of the NF samples are highly limiting to achieve a fast and accurate acquisition of the radiated field for large scan areas and dense sampling. Indeed, the greater the number of samples, the greater the acquisition time and therefore the cost of characterization. As an illustrative example, a step-by-step measurement in an anechoic chamber of the NF radiated by an antenna array with maximum dimensions of 8 wavelengths can take approximately 3 h for a scanning area of 20 wavelengths $\times$ 20 wavelengths. One main challenge is then to develop sampling strategies and characterization processes to overcome this limit by reducing the total acquisition duration. In addition to the constraints induced by the classical FT, the truncation of the information inherent to measuring on a planar surface is a well-known issue which directly impacts the accuracy when dealing with AUT allowing wide angular range beam steering such as AESAs.

Objectives and contributions

In this context, the main objective of this work is to develop new characterization methods for AESA-like antennas, focusing on optimizing both accuracy and measurement time. Notably, optimizations in the distribution and the size of the measurement samplings are detailed. Several approaches are therefore introduced to overcome the limitations of conventional post-processing techniques based on planar NF measurements, particularly when determining the FF radiation pattern of such complex antennas.

This PhD thesis has been carried out in France at the *UNIVersité de RENnes* (UNIVREN) in the IETR laboratory and at Thales Defense Mission Systems (DMS). The work presented in this manuscript have been achieved within the framework of an *Association Nationale de la Recherche et de la Technologie* (ANRT) funding relative to a *Convention Industrielle de Formation par la REcherche* (CIFRE) contract in partnership with Thales DMS.

The central theme of this research is to move beyond classical characterization tech-

nique based on the FT. All the proposed characterization methods, described in detail throughout this manuscript, are based on the physical concept of modeling the AUT using an arbitrary equivalent surface supporting its equivalent currents [2]. These currents are discretized through infinitesimal dipoles distributed over the equivalent surface, forming an equivalent model of the antenna. This model enables the construction of a radiation matrix that links the equivalent currents to the radiated field on any observation surface.

The first developed characterization method formulates the problem as an Inverse Problem (IP), in which the radiation matrix associated with the equivalent model and the planar NF measurement surface is used to retrieve an equivalent current distribution of the AUT at a fixed frequency. The field produced by these currents is propagated to compute the antenna radiation pattern in the FF region. To ensure that the technique remains applicable to practical measurement scenarios, the influence of the measurement probe is integrated into the model. This integration is validated through numerical simulations and subsequently confirmed on experimental datasets.

A second objective of this work is to mitigate truncation effects, which arise when relying solely on planar NF measurements and can significantly degrade FF computation accuracy. The flexibility offered by the equivalent model allows for non-conventional sampling strategies, providing freedom in the placement of measurement points and enabling the use of non-planar measurement surfaces. These alternative distributions are explored throughout the various characterization applications presented in this work.

Another major goal is to accelerate the NF measurement process by reducing the number of required samples while maintaining high accuracy. To achieve this, a Reduced-Order Model (ROM) is constructed from the radiation matrix associated with the NF measurement surface. This ROM first provides an *a priori* criterion to estimate of the number of samples necessary to achieve a specified accuracy level, offering a powerful pre-processing tool for optimizing sampling strategies. An experimental criterion previously established for spherical measurements has been successfully verified for planar NF measurements. Then, the construction of a ROM also enables the extraction of a reduced decomposition basis of the measured NF, which is useful to interpolate data in the radiated field space. This property paves the way for the development of new characterization methods that benefit from the regularization introduced by the reduction of the model order.

The final contribution of this work is a direct and simplified characterization technique that combines the advantages of the ROM properties while remaining easy to implement. This approach integrates geometrical information from both NF and FF domains relative

to the AUT model in a single radiation matrix. The transform relies on the computation of a reduced basis in the radiated field space, which inherently incorporates both the measurement geometry and probe effects, while leveraging the properties of the ROM. This matrix can be precomputed for a generic characterization configuration (including frequency, NF measurement surfaces, FF observation points, measurement probe, and AUT operational mode). Once this step is completed, the transformation reduces to a simple matrix inversion followed by a matrix multiplication, providing a fast, accurate, and easily implementable solution suitable for industrial environments. Consequently, the characterization procedure consists of a post-processing step represented by a straightforward matrix multiplication with the measured NF data to obtain the radiation pattern of the AUT. This new NFFFT constitutes a major contribution of this thesis. Its effectiveness has been validated through extensive experimental measurements on complex antenna systems exhibiting key properties of AESAs, including large dimensions, high directivity, and significant beam steering angles.

Content of the manuscript

The manuscript is organized into four main chapters.

Chapter I introduces the key parameters and measurement techniques required for antenna characterization. The primary focus is on computing the FF radiation pattern of AUTs from NF measurements using NFFFT. Metrics are defined to evaluate the accuracy of the computed FF. The classical approach based on the FT applied to planar NF measurements is presented, along with a discussion of its main limitations in terms of acquisition time and accuracy degradation due to truncation effects.

Chapter II develops the theoretical background of the equivalence principle, which underpins all the proposed characterization methods. The chapter describes the procedure for constructing an equivalent model of the AUT using infinitesimal dipoles. This discretization enables the construction of a radiation matrix directly linking the dipole positions to any surface in the radiation space. In our context, two radiation matrices are defined: one associated with the NF measurement surface and another linked to a FF surface of interest. Hence, from the measured NF data, the determination of the equivalent currents of the AUT by solving an IP can be achieved and then used to compute the radiation pattern. Notably, modeling the antenna using dipoles enables the implementation of non-conventional sampling strategies on the measurement surface and to overcome the

constraints of the regular, dense grid imposed by the PWE, thereby helping to mitigate truncation effects. Analytical and numerical validations are presented as key steps toward achieving a reliable IP-based method. Parametric studies are conducted to investigate how the model behaves and how the computed FF accuracy converges. The analysis also explores the influence of the NF measurement surface geometry.

Chapter III introduces the construction of a ROM for the characterization problem. A Singular Value Decomposition (SVD) of the radiation matrix associated with the NF measurement surface is employed to obtain a reduced representation of the problem. This decomposition provides a criterion to estimate the minimum number of NF samples required for accurate characterization. The criterion, initially derived in the context of spherical measurements, is validated on numerical test cases. Building upon these results, a unified NFFFT method is proposed, combining the advantages of previous approaches into a single pre-computed and straightforward transition matrix for direct characterization. This method supports non-conventional sampling strategies, enabling both reduced acquisition time and minimized truncation effects. Its performance is assessed through challenging numerical examples.

Chapter IV first focuses on the integration of probe effects into the developed methods. The correction of the radiation matrix to account for probe characteristics is explained and validated on simulated scenarios. Once validated, the approach is applied to experimental cases, including a W-band horn antenna and an X-band Luneburg lens, both representative of some properties of AESA-like systems. These antenna measurements have been performed by the Manufacturing Measurement Analysis of Radiating Systems (M^2ARS) platform [1], which gathers diverse measurement facilities for the research needs of the IETR laboratory located at the UNIVREN.

Finally, the manuscript concludes with a synthesis of the main findings and outlines perspectives for future research.

Chapter I

Antenna characterization

I.1 Introduction

Electronic communication systems and radars contain transmit (Tx) and receive (Rx) subsystems which use antennas. The main role of these elements is to enhance the exchange of information between the communicating devices as they enable the transition between guided and propagated electromagnetic waves. Thus, antenna characterization is a crucial step to ensure a correct transmission between wireless systems by verifying that their radiation characteristics meet the requirements.

The antenna to be characterized is usually called the AUT. The theoretical background leading to antenna radiation is quickly recalled in this chapter. This allows to contextualize the physical quantities and conventions we are supposed to follow in a characterization process. As explained further in this manuscript, field regions can be defined by the distance between the AUT and the probe antenna that is employed to acquire the data of interest. These regions are dependent on the electrical size of the AUT. The available distance between the AUT and the measurement probe dictates the type of measurement that is conducted, either NF or FF.

To efficiently determine the real radiation performances of the AUT only, the measurement is often isolated from external electromagnetic contributions in an anechoic chamber. An illustration of one of the measurement facility for the NF range present in the IETR laboratory, and used in the framework of this work, is shown in Fig. I.1.

The measurement results allow determining parameters that bring information on the FF radiation performances of the antenna. This characterization can be achieved by directly measuring the FF or through a post-processing step in the case of NF measurement. All these aspects of the measurement process are detailed.

In order to certify that the characterization process leads to an accurate evaluation of the real radiation behavior of the AUT, some metrics are proposed to compare the measured radiated FF with a reference one.

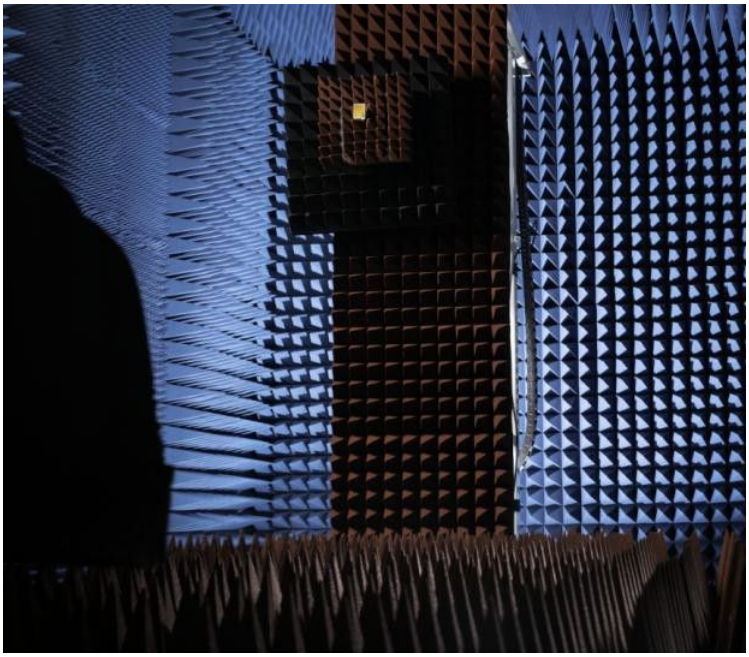

Figure I.1 – Illustration of a measurement facility for planar acquisitions available at IETR laboratory.

This thesis falls within the framework of planar NF measurements for AESA antennas [3]. These arrays are very challenging to characterize using planar NF measurements because of multiple aspects:

1. their size is often significant and thus leads to high directivity;
2. the beam scan can be very important and reaches grazing angles;
3. the beam agility leads to various operating modes that must be characterized independently.

A focus on the classical NFFFT used for planar NF measurements is presented. Then, two well-known limitations associated with solving this characterization problem for AUT under consideration such as AESA systems using classical transform are detailed. These limitations are:

1. the sampling distribution imposed by the classical NFFFT resulting in a long acquisition time for the NF;
2. the truncation effects induced by the restricted scanning area of the measurement surface for wide angular range beam steering AUT which impact the computed FF accuracy.

These limitations motivate the exploration of alternative characterization methods that overcome the rules required by the classical NFFFT, particularly in the case of AESA-like antennas.

I.2 Antenna measurement

I.2.a Antenna radiation

Before defining all the aspects of antenna measurements, some important physical concepts associated to the radiating systems under consideration must be introduced. Namely, definitions and conventions linked to the radiation of an antenna are discussed.

Global definitions and conventions

An antenna is a system that transforms incoming electromagnetic radio waves from a guided device to the free space in transmit (Tx) mode and conversely receive (Rx) mode. An electromagnetic wave is composed of an electric field $\mathbf{E}$ and a magnetic $\mathbf{H}$ field, both defined on spacetime $\mathbb{R}^3 \times \mathbb{R}$. In this manuscript, boldface $\mathbf{E}$ will be used to distinguish vectors from scalars. The behavior of electromagnetic waves depends on the operating frequency of the antenna, and studying these waves directly in the space-time domain can be complicated. In order to simplify the analysis, electromagnetic waves are often considered monochromatic or harmonic, with a sinusoidal waveform. Thus, for the electric field:

$$\mathbf{E}(\mathbf{r}, t) = \mathrm{Re}\{\mathbf{E}(\mathbf{r}) \exp(j\omega t)\} \tag{I.1}$$

where $\mathbf{r}$ represents the spatial coordinate of the wave, t the temporal coordinate and $\omega = 2\pi f$ the angular frequency in $\mathrm{rad\,sec}^{-1}$ which depends on the fixed frequency f. The time convention can either be positive or negative, denoting the sign of the exponent, here it is positive, i. e. $\exp(j\omega t)$.

Therefore, at a fixed angular frequency ω, the electric field $\mathbf{E}(\mathbf{r})$ radiated by an antenna is a complex-valued function in $\mathbb{C}^3$.

Coordinate system

The radiation of an antenna is expressed naturally in a spherical coordinate system. Figure I.2, represents the spatial coordinates (r, θ, ϕ) and the associated unitary vectors $(\hat{\boldsymbol{r}}, \hat{\boldsymbol{\theta}}, \hat{\boldsymbol{\phi}})$ used in this system.

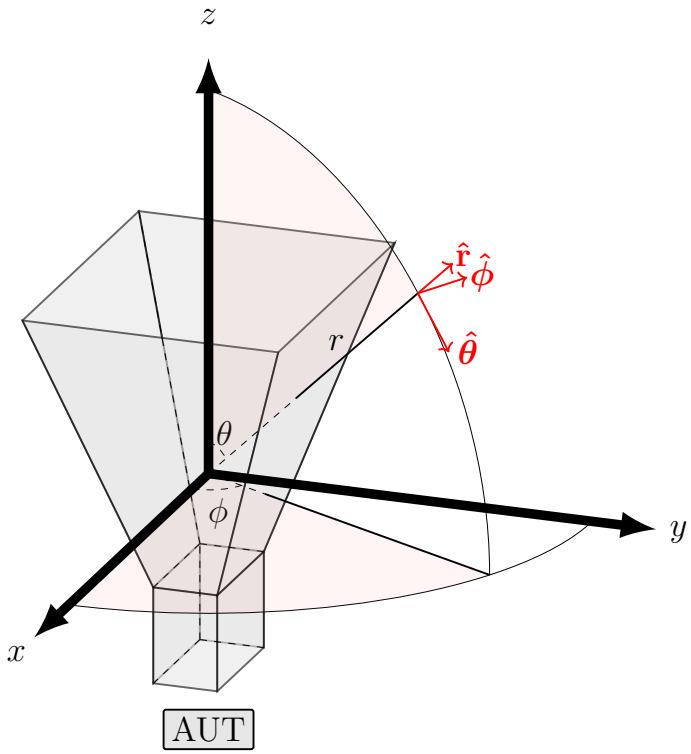

Figure I.2 – Representation of the spherical coordinate system regarding the antenna position.

To observe the electromagnetic wave in all the directions of the space both θ and ϕ must vary on well-defined intervals according conventions:

- $\theta \in [-\pi, \pi]$ and $\phi \in [0, \pi[$
- $\theta \in [0, \pi]$ and $\phi \in [0, 2\pi[$

Here, the unitary vectors of the spherical system can be expressed in the Cartesian one defined by the triplet $(\hat{\boldsymbol{x}}, \hat{\boldsymbol{y}}, \hat{\boldsymbol{z}})$:

$$\begin{aligned} \hat{\boldsymbol{r}} &= \sin(\theta)\cos(\phi)\hat{\boldsymbol{x}} + \sin(\theta)\sin(\phi)\hat{\boldsymbol{y}} + \cos(\theta)\hat{\boldsymbol{z}} \\ \hat{\boldsymbol{\theta}} &= \cos(\theta)\cos(\phi)\hat{\boldsymbol{x}} + \cos(\theta)\sin(\phi)\hat{\boldsymbol{y}} - \sin(\theta)\hat{\boldsymbol{z}} \\ \hat{\boldsymbol{\phi}} &= -\sin(\phi)\hat{\boldsymbol{x}} + \cos(\phi)\hat{\boldsymbol{y}} \end{aligned} \tag{I.2}$$

As analyses in the spherical system can sometimes be cumbersome, another widely used representation is the 2D UV system. This system maps the hemisphere $z \geq 0$ onto coordinates (u, v) in the Cartesian basis $(\hat{\boldsymbol{x}}, \hat{\boldsymbol{y}})$:

$$\begin{aligned} u &= \sin(\theta)\cos(\phi) \\ v &= \sin(\theta)\sin(\phi) \end{aligned} \tag{I.3}$$

This coordinate system is particularly convenient for visualizing the angular distribution of the fields over the XOY plane.

Finally, the last system used in this work is the Horizontal-Vertical (HV) system $(\hat{\boldsymbol{r}}, \hat{\boldsymbol{h}}, \hat{\boldsymbol{v}})$ which is defined as a rotation of the spherical one around the z-axis by an angle ϕ, in accordance with the Ludwig-III formalism [4]:

$$\begin{aligned} \hat{\boldsymbol{h}} &= \cos(\phi)\hat{\boldsymbol{\theta}} - \sin(\phi)\hat{\boldsymbol{\phi}} \\ \hat{\boldsymbol{v}} &= \sin(\phi)\hat{\boldsymbol{\theta}} + \cos(\phi)\hat{\boldsymbol{\phi}} \end{aligned} \tag{I.4}$$

This HV system has the convenient property of given a fixed value of the field for the pole $z = 1$.

Field regions

The properties of the electromagnetic field radiated by an antenna vary according to the distance defined between the observation point and the AUT location. Figure I.3 shows the different field regions that define radiation as a function of distance r.

At very short distance from the antenna, the NF is mainly reactive which means that the electromagnetic waves emitted by the surface currents of the AUT contain evanescent waves which do not propagate.

In the Fresnel zone (Fig. I.3), the radiating field becomes dominant, and the wavefronts can be locally approximated as spherical. The angular distribution of the field depends on the observation distance.

At the FF range, the radiated waves are considered to be plane waves which implies that the angular distribution of the field is no more dependent on the distance r, the emitting source is seen as punctual. The radial component of the field is now negligible, and the electromagnetic waves are transverse and propagate towards the radial direction away from the antenna.

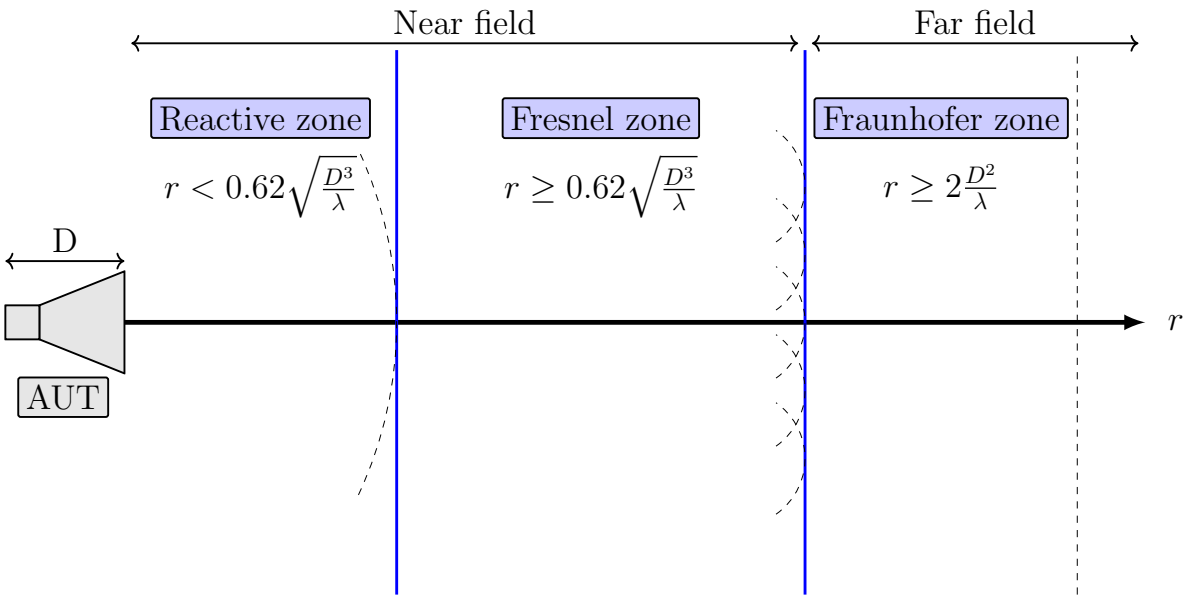

Figure I.3 – Different regions of the radiated field defined from the AUT maximum size D and the radial observation distance r [5].

In the Fraunhofer region, the radiated field still exhibits a phase variation with the observation distance, but this variation is uniform across the entire radiation pattern. As a result, the wavefront can be considered locally planar in any plane perpendicular to the propagation direction. Consequently, the antenna radiation characteristics are defined in this region. Thus, to assess the radiation performances of an AUT in a long distance scenario, its radiated FF must be determined.

I.2.b Characterization parameters

Antenna measurement is a general term that refers to the measurement of the various parameters describing the radiation of the antenna at FF range. A list of these parameters is established with a brief description to understand which physical quantity is measured when talking about characterization. To precisely introduce the parameters presented in this section, the quoted texts directly refer to the IEEE standards definitions [6].

Radiation pattern

The radiation pattern of an antenna is "the spatial distribution of a quantity that characterizes the electromagnetic field generated by an antenna". The quantities of interest considered in this manuscript are the magnitude and/or phase of the electric field com-

ponents, the total field magnitude and the directivity or the gain. The radiation pattern describes one of these radiation parameters as a function of space coordinates defined in a system associated to the antenna positioning in the measurement facility. The radiation pattern is always determined in FF region on spherical observation surface with a constant observation distance r. Indeed, all the parameters refer to the electric field $\mathbf{E}(\theta, \phi)$ with no dependence to the distance of observation r as defined in the following expression:

$$\mathbf{E}(\theta, \phi) = E_r(\theta, \phi)\hat{\boldsymbol{r}} \; + \; E_\theta(\theta, \phi)\hat{\boldsymbol{\theta}} \; + \; E_\phi(\theta, \phi)\hat{\boldsymbol{\phi}} \tag{I.5}$$

The field components E_r, E_θ and E_ϕ being complex-valued functions defined on $\mathbb{R}^3$. Where E_r is close to zero because of r distance is at FF range.

In this manuscript, the magnitude of a complex number z will be denoted $|z|$ and its phase $\angle z$. Furthermore, the magnitude of the field $\mathbf{E}(\theta, \phi)$ or of its components is expressed in the SI unit of Vm^{-1} [7] while the phase of the components is given in degree (°).

The most widely used representation of the magnitude patterns is in dB compared to in linear. A radiation pattern in dB allows emphasizing behaviors of the field for low magnitude levels comparatively to the linear one. The conversion from a linear scale to a logarithmic one is performed on a quantity Y that is homogeneous to the square root of power, such as the magnitude of the field or of its components:

$$Y_{\mathrm{dB}} = 20 \log_{10}(Y) \tag{I.6}$$

In this manuscript, the patterns are typically normalized to their maximum value in linear before being converted to dB. Hence, the value of the main beam radiated by the antenna is equal to 0 dB and is easily recognizable. Different illustrations of a radiation pattern are shown in 3D in Fig. I.4, 2D in Fig. I.5 and 1D in Fig. I.6.

Finally, depending on the radiation pattern of the antenna, three different types of antenna can be clearly identified:

1. a directive antenna which radiates electromagnetic field more efficiently in few directions of the space (as shown in the example in Fig. I.4, I.5 and I.6);
2. an omnidirectional antenna which has no radiation focusing capability or is directive in one plane and non-directive in the orthogonal one;
3. an isotropic antenna is a theoretical concept where no losses are considered such that the antenna radiates equally in all the directions of the space.

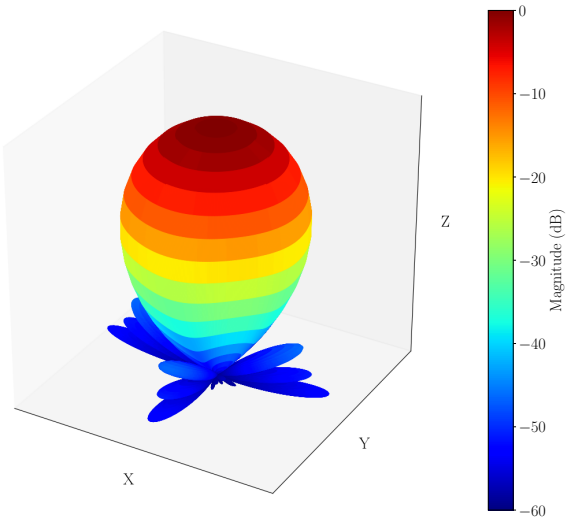

Figure I.4 – 3D representation of a radiation pattern.

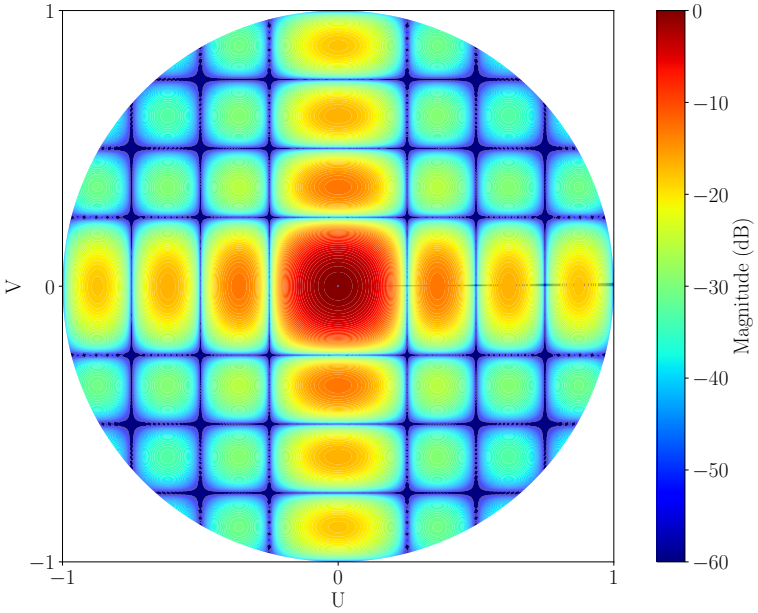

Figure I.5 – 2D representation of a radiation pattern on a UV grid.

Directivity and gain

To describe how the radiated power of an antenna is distributed in space, the concept of directivity is introduced. The directivity is defined as "the ratio of the radiation intensity in a given direction from the antenna to the radiation intensity averaged over all directions". The radiation intensity being "in a given direction, the power radiated from an antenna per unit solid angle" and mathematically defined as:

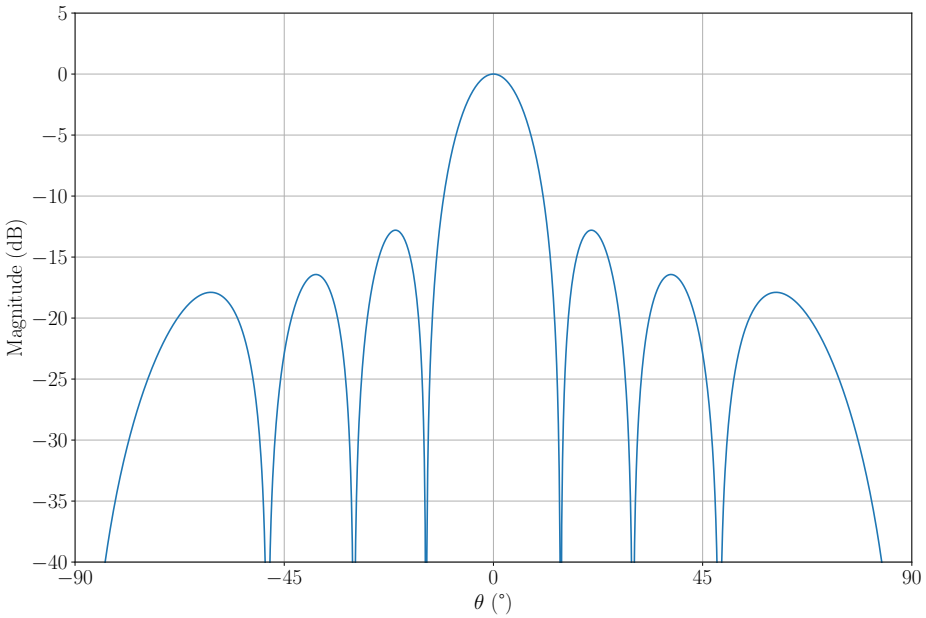

Figure I.6 – 1D representation of a radiation pattern.

$$U(\theta,\phi) = \frac{1}{2\eta}(|E_\theta(\theta,\phi)|^2 + |E_\phi(\theta,\phi)|^2) \tag{I.7}$$

More simply, the radiation intensity U radiated by the antenna in one direction is compared relatively to the radiation intensity U_0 radiated by a theoretical isotropic source which radiates the same total power. This isotropic radiation intensity corresponds to the power radiated by the antenna P_{rad} divided by the area of the unit sphere, 4π. Thus, the formula for the directivity is:

$$D(\theta,\phi) = \frac{U(\theta,\phi)}{U_0} = \frac{4\pi U(\theta,\phi)}{P_{\text{rad}}} \tag{I.8}$$

From the definition of the directivity the gain is also introduced. The gain is "the ratio of the radiation intensity in a given direction to the radiation intensity that would be produced if the power accepted by the antenna were isotropically radiated". This statement takes into account the radiation efficiency e_{cd} of the antenna, which depends on the conduction and dielectric efficiencies [5]. The following relation is given for the gain:

$$G(\theta,\phi) = e_{\text{cd}} D(\theta,\phi) \tag{I.9}$$

Now, both directivity and gain can be expressed in dBi, decibels relative to an isotropic source. Let Y represents the directivity or the gain which are quantities expressed as a function of power:

$$Y_{\text{dB}} = 10 \log_{10}(Y) \tag{I.10}$$

Polarization

Another important parameter is the polarization which is "in a given direction from the antenna, the polarization of the wave transmitted by the antenna". The polarization of the electromagnetic wave can be seen as the curve defined by the electric field vector through the time along the propagation direction. Fundamentally, the polarization of an electromagnetic wave is elliptical. A representation of this elliptical polarization is given in Fig. I.7.

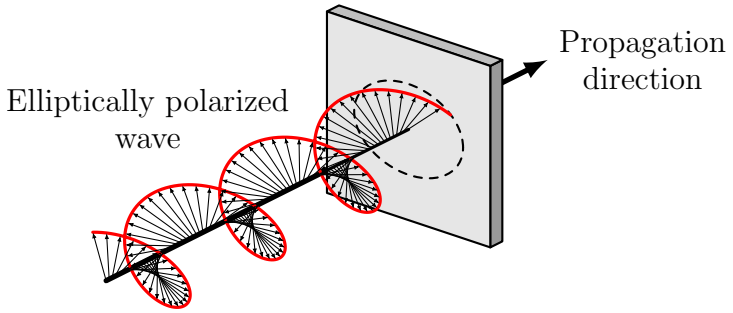

Figure I.7 – Elliptical polarization of a wave.

In addition to the amplitude and phase of the radiated field, the polarization provides essential information about the orientation of the electric field vector in space and time. The main objective in controlling the antenna polarization is to maximize the transmitted or received power in the intended polarization direction while minimizing undesired components. This is formally described by the concepts of co-polarization and cross-polarization defined by Ludwig [8] as "what one measures when antenna patterns are taken in the usual manner". This idea is a key to understand antenna measurements. Thus, it is of use to define from the design step which polarization is expected to fully transmit or receive information also known as the co-polarization. Therefore, antenna designers seek to maximize the co-polarization. Inversely, the cross-polarization refers to the direction of polarization which is not expected and is usually minimized during the conception phase.

In practice, antenna engineers generally focus on two particular cases of elliptical polarization: linear polarization and circular polarization.

First, the linear polarization is defined such that the electric field vector through the time belongs to the same plane parallel to the direction of propagation. Then, in a fixed direction (θ, ϕ), the field components are in phase or in opposition with:

$$\angle E_\theta(\theta, \phi) = \angle E_\phi(\theta, \phi) + k\pi \tag{I.11}$$

where $k \in \mathbb{Z}$.

For this type of polarization, the field component which is carried by the unitary vector of the reference polarization is the co-polarization while the orthogonal component is the cross. Commonly, the plane in which the co-polarization oscillates is called the E-plane and the orthogonal one the H-plane.

Then, the circular polarization is introduced. This time in a direction (θ, ϕ), the relation between the magnitude and phase of the field components is:

$$\begin{aligned} |E_\theta(\theta, \phi)| &= |E_\phi(\theta, \phi)| \\ \angle E_\theta(\theta, \phi) &= \angle E_\phi(\theta, \phi) + k\pi + \frac{\pi}{2} \end{aligned} \tag{I.12}$$

where $k \in \mathbb{Z}$.

The curve described by the field vector through the time is a circle. Besides, a circular polarization defines a direction of rotation through the time. The polarization can be either a right-handed or left-handed polarization according to the direction of propagation.

A clarification is needed regarding the importance of using the HV system previously defined. In the particular case of an antenna linearly polarized along x- or y-axis, the analysis of the radiation pattern in the spherical basis becomes very hard to achieve as each component E_θ and E_ϕ depends at the same time on both co- and cross-polarization. Here is the interest of using HV system which is defined as a rotation of the spherical system around z-axis by ϕ coordinate to match as much as possible the orientations $(\hat{\boldsymbol{h}}, \hat{\boldsymbol{v}})$ with $(\hat{\boldsymbol{x}}, \hat{\boldsymbol{y}})$, respectively. This allows analyzing the behaviors of the radiated field polarizations in relation to the physical polarization of the AUT.

I.2.c Measurement techniques

Once the antenna parameters have been identified and clearly defined, they must be measured using appropriate experimental techniques. The choice of measurement method

depends on the AUT properties (dimensions, weight, frequency band, radiation characteristics) and the intended application.

Measurement process of the antenna parameters

In a typical antenna measurement process, the AUT is placed within a controlled measurement environment, and its radiated field is sampled over a set of spatial points covering the directions of interest. The main objective is to acquire accurate complex field data (magnitude and phase) or polarization variation, enabling the assessment of the antenna radiation characteristics [9].

A complete measurement setup generally includes:

- the AUT, mounted on a mechanical positioner. For spherical measurement systems, this positioner must allow rotation along at least two orthogonal axes to enable full spatial coverage of the radiated field;
- one or more measurement probes to measure the electromagnetic radiated field. Modern facilities often employ multi-probe systems to reduce acquisition time by simultaneously sampling multiple spatial positions [10]. These probes can themselves be mounted on positioners such as planar NF systems, cylindrical NF systems, gantry arms, or even robotic arms, depending on the measurement facility;
- a measurement instrument, typically a Vector Network Analyzer (VNA) or equivalent receiver, to record the amplitude and phase response over the frequency range of interest;
- a controlled measurement environment designed to minimize reflections and external electromagnetic interference [11].

A clarification is needed when multiple polarizations of the radiated field are acquired: a linearly polarized probe can simply be rotated to align with the polarization direction of interest. Hence, for each point among N measurement positions, k polarizations are measured, with $k \in \{1, 2\}$ corresponding to the number of electric field components acquired at that point. In the spherical basis, these typically correspond to the θ and ϕ components. These measurements are referred to as samples, and consequently a total of kN samples are acquired.

The measurement sequence involves positioning the AUT and probe(s) according to a predefined sampling grid, recording the field values at each position, and subsequently

processing the data to extract the desired antenna parameters. An illustration of a generic antenna measurement configuration is given in Fig. I.8.

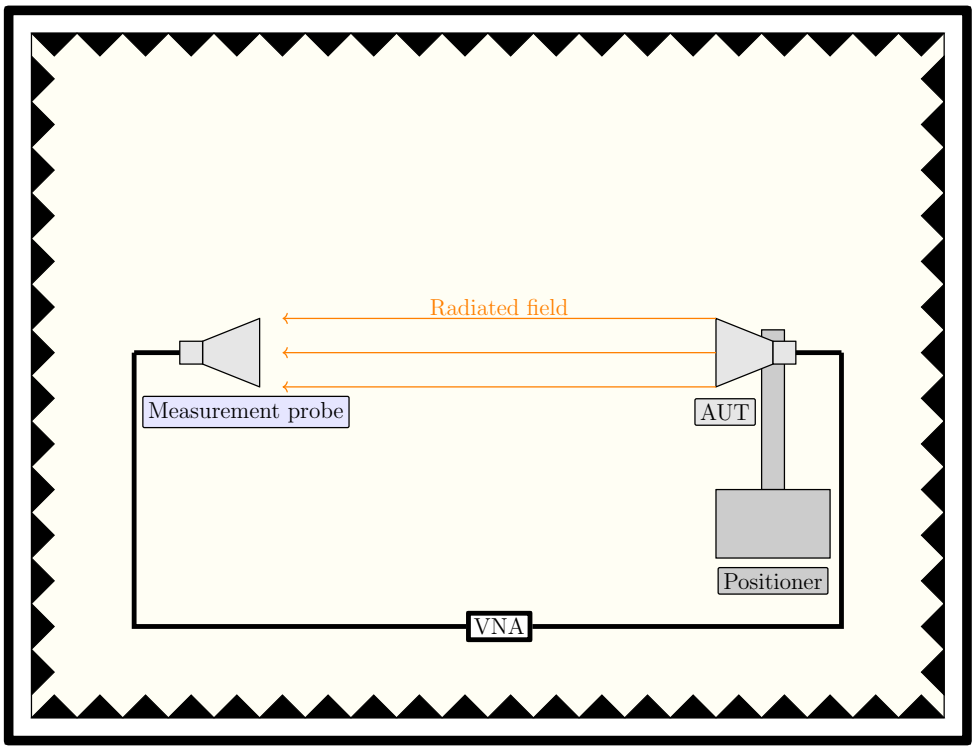

Figure I.8 – Simplified illustration of the generic configuration of an antenna measurement.

Depending on the measurement strategy and instrumentation, automation and calibration steps are integrated to ensure accuracy and repeatability.

Far-field techniques

FF measurements consist of directly sampling the radiated field in the Fraunhofer region, where the wavefront is locally planar. This is possible only if the measurement distance between the AUT and the probe (usually a single probe for FF measurements) satisfies the quasi-plane-wave illumination criterion i. e. the spherical wavefronts can be locally approximated as planar.

Depending on the AUT dimensions and operating frequency, FF measurements can be performed either:

- outdoors, allowing the characterization of very large antennas but exposing the setup to environmental interference;

- indoors, in an anechoic chamber that isolates the AUT from external perturbations and suppresses internal reflections via radio-frequency absorbers.

When the required FF distance is impractically large, Compact Antenna Test Range (CATR) systems are used. These employ reflectors or lenses to collimate the probe radiated field, creating a quiet zone in which the AUT receives a quasi-plane wave (Fig. I.9).

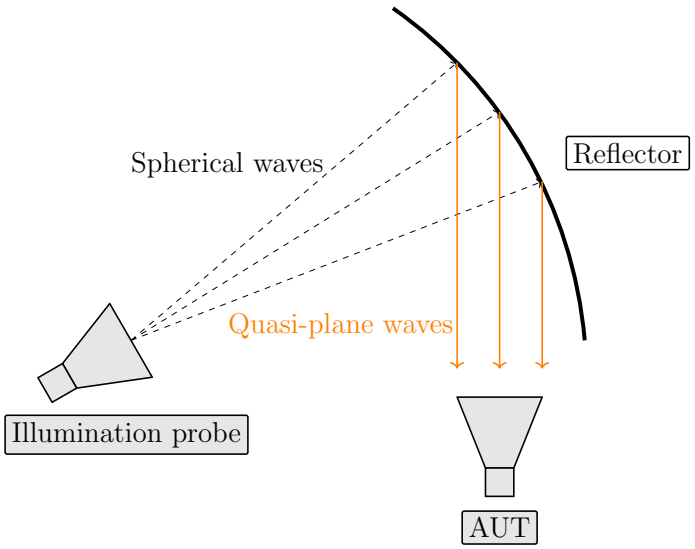

Figure I.9 – Illustration of the principle of a CATR.

CATR systems allow FF conditions to be replicated indoors in an anechoic chamber, although they require precise alignment and are costly to implement.

The AUT is typically rotated along at least two orthogonal axes to enable sampling of the radiated field over a complete solid angle. This is essential for full radiation pattern characterization and is a major factor in determining total acquisition time, especially for electrically large antennas (with high physical dimensions in terms of wavelength).

The main limitations of FF techniques are:

- the significant measurement distance required, which becomes prohibitive for electrically large antennas;
- difficulty in positioning large or heavy AUTs with sufficient accuracy, especially at high frequencies;
- high infrastructure costs, particularly for large chambers or CATR systems.

Interpolation techniques exist to reduce the total acquisition time. For example, the use of sparse spherical harmonic expansion as an interpolation tool has been investigated and shown to reduce FF measurement time [12, 13].

To further reduce facility size, simplify characterization, and limit costs, direct FF measurements are sometimes replaced by indirect characterization from NF measurements.

Near-field techniques

NF measurements have been developed to overcome the constraints of FF setups. By measuring the field in the Fresnel region, the required distance between the AUT and probe(s) is drastically reduced, allowing for more compact systems and shorter acquisition times. The main idea is to sample the field on a closed or open measurement surface in the NF region, then transform this data into the FF pattern using a NFFFT. This transformation is generally based on a modal expansion in a basis suited to the measurement geometry. Three main geometries are commonly used:

- spherical, where the AUT is enclosed in a virtual sphere and the probes move over its surface (Fig. I.10);
- cylindrical, suitable for antennas with omnidirectional patterns (Fig. I.11);
- planar, where the field is sampled over a flat aperture, often used for large and heavy antennas that cannot be rotated such as AESAs (Fig. I.12).

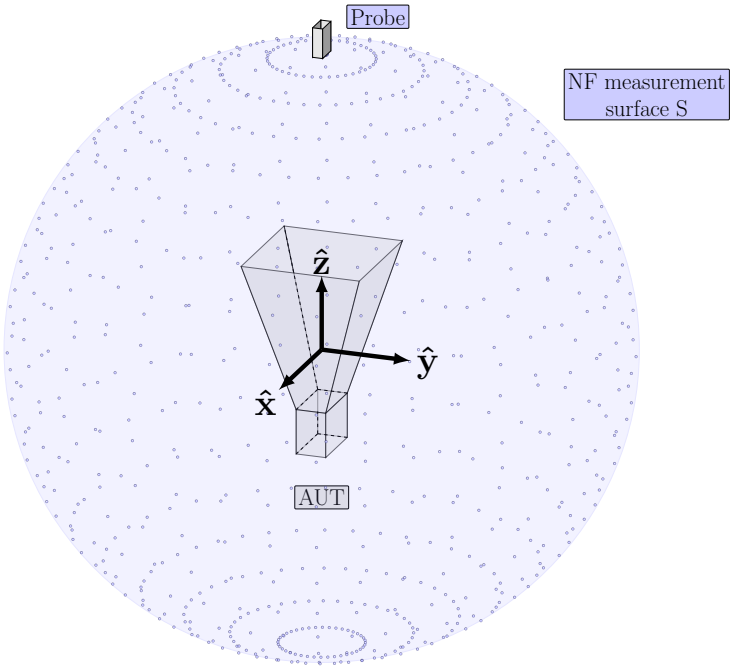

Figure I.10 – Spherical NF measurement configuration of the AUT.

Each configuration has advantages and drawbacks in terms of measurement time, mechanical complexity, and achievable accuracy.

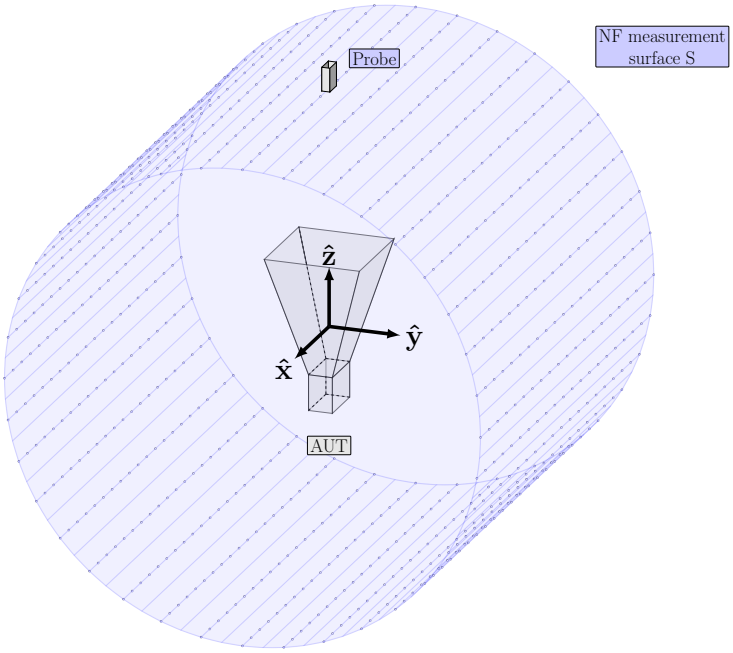

Figure I.11 – Cylindrical NF measurement configuration of the AUT.

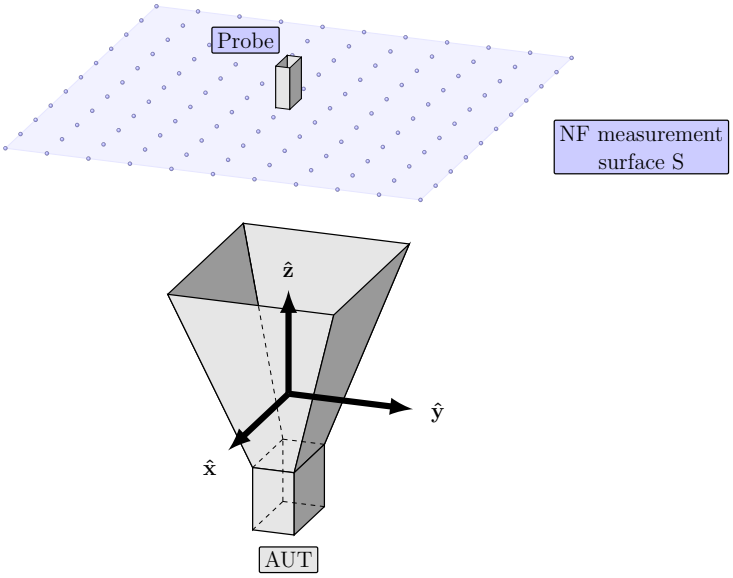

Figure I.12 – Planar NF measurement configuration of the AUT.

The choice of measurement probe depends on the configuration; single probes on mechanical scanners, multi-probe arrays, or arch-based scanning systems are common. An example of an arch-based system from MVG is shown in Fig. I.13.

In all cases, the probe characteristics must be de-embedded from the measurements during the NFFFT to compute the true radiation pattern of the AUT, without probe

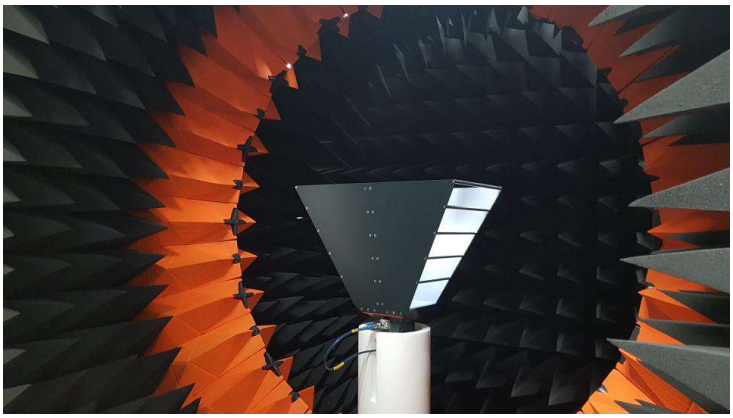

Figure I.13 – Representation of the Microwave Vision Group StarLab system installed in the IETR laboratory.

effects. In this manuscript, we consider only the case of a single probe measurement system.

To determine the FF from the NF data, a NFFFT post-processing step must be employed. Each geometry has an associated classical FT. These transforms are mature and well-documented but may have limitations regarding sampling requirements and sensitivity to mechanical inaccuracies.

Spherical systems are classically based on the well-known Spherical Wave Expansion (SWE) defined by Hansen [14]. This standard method is widely used because of its high characterization accuracy [15], but it requires constant angular steps, leading to long acquisition times in some cases. Although these sampling constraints are particularly relevant for NFFFTs, the underlying sampling principles remain valid and useful for FF measurements as well.

Cylindrical measurement techniques are very similar to spherical ones and are often used for specific cases, such as the characterization of omnidirectional antennas that radiate equally in all directions perpendicular to an axis [16].

However, for heavy and cumbersome AUTs, using a spherical or cylindrical system is sometimes impractical since it requires rotating the AUT. Planar NF measurements are often the only viable option for such antennas. The classical planar NF measurement technique, as defined by Wang [17] and later by Gregson [11], is based on a modal expansion of the NF measured on a plane within a limited scanning area. This technique, called the Plane Wave Expansion (PWE), employs a FT with strict requirements on sampling distribution. Section I.3 provides a description of this transform and its related challenges.

While NF techniques reduce physical constraints compared to FF measurements, they introduce computational complexity and require precise knowledge of probe characteristics. Furthermore, measurement time remains significant for high-accuracy characterization, as full angular coverage is still needed. This defines the context and challenges in which the work of this thesis is positioned.

I.2.d Metrics

Once the measurement of the NF or FF has been performed, the radiation pattern obtained by NFFFT or by direct measurement must be compared to a reference using well-defined metrics in order to evaluate the characterization procedure. Two types of metrics can be employed to assess the accuracy of the obtained radiation pattern: local metrics and global metrics. These metrics are defined by norms calculated on the considered field and can be expressed on different scales. Local metrics compare two quantities point by point, without taking into account the overall field distribution considered in global metrics. Thus, applying a local metric to calculate the error between two radiation patterns results in an error curve. Global metrics, on the other hand, provide an averaged accuracy expressed by a single value. Both types of metrics are employed throughout this work to enable precise comparisons between characterization methods.

For simplicity, new notations are introduced in this section. $\tilde{\mathbf{a}}$ denotes the electric field in a general sense (as the metrics are applied to both NF and FF in this manuscript), while $\mathbf{a}$ represents the reference field. Both are defined at each point i among the N points on an observation surface.

Norms

As a reminder, the electric field can be regarded as a complex vector field defined in the finite-dimensional Euclidean space $\mathbb{R}^3$. When the field is discretized via spatial sampling, any finite-dimensional ℓ-norm can be employed to measure or analyze local field properties. The ℓ_p-norms are useful analysis tools to characterize vectors in different ways. For $p \in \mathbb{R}$ with $p \geq 1$, the ℓ_p-norm of a vector $\mathbf{a}_i \in \mathbb{C}^3$ with components $a_{i,k}$ ($k \in \{1, 2, 3\}$) is defined as [18, 19]:

$$\|\mathbf{a}_i\|_p = \left(\sum_{k=1}^{3} |a_{i,k}|^p \right)^{\frac{1}{p}} \tag{I.13}$$

From this definition, the three most important norms are derived: the ℓ_1-norm, the ℓ_2-norm, and the ℓ_∞-norm. The latter corresponds to the limit of the ℓ_p-norms for $p \to \infty$:

$$\|\mathbf{a}_i\|_\infty = \max_{k \leq 3} |a_{i,k}| \tag{I.14}$$

The vector analysis strongly depends on the chosen ℓ_p-norm, as illustrated in Fig. I.14. Selecting the appropriate norm to emphasize the behavior of interest is thus a key step in the analysis.

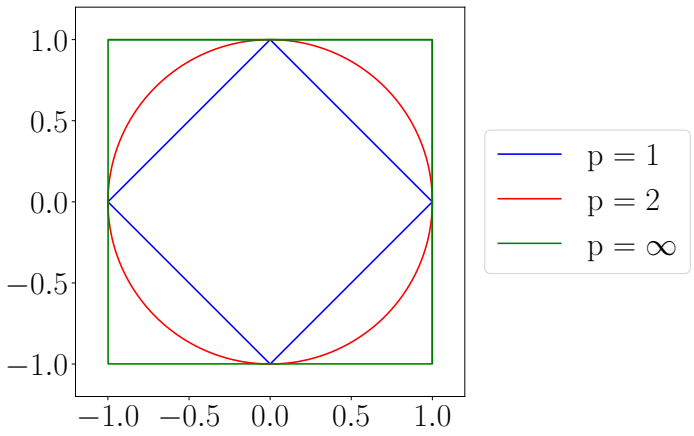

Figure I.14 – Lamé curves (or superellipses) representing the ℓ_1-, ℓ_2-, and ℓ_∞-norms defined on $\mathbb{R}^2$. The norms are calculated on the unit vectors of the vector space.

Furthermore, the ℓ_2-norm, also called the Euclidean norm, corresponds in physics to the vector magnitude. In a spherical basis, the magnitude of the electric field observed at (θ, ϕ) is given by:

$$\|\mathbf{E}(\theta,\phi)\|_2 = \sqrt{|E_r(\theta,\phi)|^2 + |E_\theta(\theta,\phi)|^2 + |E_\phi(\theta,\phi)|^2} \tag{I.15}$$

Local metrics

To locally assess the accuracy of the field computation (for example obtained from the characterization process), the error between the computed field $\|\tilde{\mathbf{a}}_i\|_2$ and the reference $\|\mathbf{a}_i\|_2$, both normalized with respect to the maximum of the reference, is defined as:

$$Err_i = 20\log_{10}\frac{\left|\left\|\tilde{\mathbf{a}}_i\right\|_2 - \left\|\mathbf{a}_i\right\|_2\right|}{\max\limits_{i\leq N}\left\|\mathbf{a}_i\right\|_2} \tag{I.16}$$

To compare the polarization component $\tilde{a}_{i,k}$, a metric accounting simultaneously for the magnitude and the phase of the field components is used:

$$Err_{i,k} = 20\log_{10}\frac{\left|\tilde{a}_{i,k} - a_{i,k}\right|}{\max\limits_{i\leq N}\left\|\mathbf{a}_i\right\|_2} \tag{I.17}$$

For example in the spherical basis, the error associated with the θ- and ϕ-component is denoted $Err_{i,\theta}$ and $Err_{i,\phi}$, respectively.

The same calculation restricted to the magnitude of the components is denoted by $Err_{\mathrm{mag},i,k}$:

$$Err_{\mathrm{mag},i,k} = 20\log_{10}\frac{\left|\left|\tilde{a}_{i,k}\right| - \left|a_{i,k}\right|\right|}{\max\limits_{i\leq N}\left\|\mathbf{a}_i\right\|_2} \tag{I.18}$$

Global metrics

While point-to-point errors provide a detailed assessment of the computation accuracy, a weighted average based on the number of observation points offers a global evaluation, facilitating easier comparisons between different methods for obtaining the FF, for example. However, when strong dynamic ranges are present i. e., significant differences between the lowest and highest field magnitudes, an averaged error may obscure discrepancies at low field levels. In such cases, reporting the standard deviation alongside the mean error provides a more representative picture of the overall accuracy and highlights regions where the field is weak. To address this, most of the results in this manuscript are presented on a logarithmic scale.

The chosen global metric in this work is the Equivalent Noise Level (ENL), also referred to as the equivalent error signal. For the entire field distribution across the N observation points, the ENL is defined as:

$$ENL = 20\log_{10}\sum_{i=1}^{N}\frac{\sqrt{\left|\tilde{a}_{i,\theta} - a_{i,\theta}\right|^2 + \left|\tilde{a}_{i,\phi} - a_{i,\phi}\right|^2}}{N\max\limits_{i\leq N}\left\|\mathbf{a}_i\right\|_2} \tag{I.19}$$

It is important to note the impact of both the distribution and the number of points on the observation surface, as well as the dynamic range, on a global metric such as the

ENL. Since this metric represents an average, if most observation points are located in regions of high field magnitude, the resulting ENL value is expected to be larger than in regions of lower field magnitude. Furthermore, when the metric is computed from only a limited number of points, the outcome must be interpreted with caution, as the field dynamics are only partially captured. In such cases, the result may differ significantly from that obtained with a finer discretization of the observation surface.

Normalization and analyzed quantity

All the metrics introduced above rely on reference normalization. However, in some cases, the distance of the reference field is unknown. In such situations, normalization cannot be computed using the maximum of the reference, since the field magnitude decays inversely with distance. Instead, self-normalization must be applied. For example, Eq. (I.16) becomes:

$$Err_i = 20\log_{10}\left|\frac{\|\tilde{\mathbf{a}}_i\|_2}{\max\limits_{i\leq N}\|\tilde{\mathbf{a}}_i\|_2} - \frac{\|\mathbf{a}_i\|_2}{\max\limits_{i\leq N}\|\mathbf{a}_i\|_2}\right| \tag{I.20}$$

When normalization is performed with respect to a reference, the metrics evaluate both the computed power and the angular distribution of the field. Conversely, if the reference distance is unknown, the computed power relative to the reference is lost, and the metrics only assess the angular distribution of the power.

In addition to amplitude normalization, the phase of the computed fields must also be aligned before error evaluation. For reference-based normalization, the global phase is fixed relative to the reference field by multiplying all values by the complex conjugate of the reference phase at the main beam direction. This ensures that both the computed and reference fields are compared with a common phase origin. Conversely, in self-normalization, no such phase alignment with the reference is possible, and the computed phases are therefore considered directly.

Since both normalization approaches are employed in this work, the applied method will be specified in each case.

I.3 Planar near-field measurements

In this thesis, we focus on the characterization of AESAs. Since these antennas are electrically large, these antennas are typically characterized using NF measurements. However, due to their cumbersome and heavy mechanical design, the use of spherical or cylindrical measurement systems becomes complex.

Therefore, the framework of this manuscript is based on the characterization of the radiation pattern using a NFFFT from NF samples obtained with planar measurement systems. The classical field expansion employed for this type of characterization is presented. The current limitations of this method, in terms of acquisition time and the effects induced by the restricted scanning area of the measurement surface, are also discussed.

I.3.a Plane wave expansion

The usual NFFFT associated with a planar measurement geometry is the PWE, which relies on analytical solutions of Maxwell's equations. Since the 1970s, many works [20, 21, 22] have investigated planar NF measurements and developed a complete method to recover the FF through the decomposition of the field into plane waves, while also accounting for probe compensation [23, 24].

Definition of PWE from Maxwell's equations

The electromagnetic wave composed of the fields $\mathbf{E}$ and $\mathbf{H}$, propagating in a linear, homogeneous, and isotropic medium with a harmonic time dependency $e^{j\omega t}$, is a solution of Maxwell's equations [25, 26, 27]:

$$\begin{aligned} \nabla \cdot \mathbf{E} &= \frac{\rho}{\epsilon} \\ \nabla \cdot \mathbf{H} &= 0 \\ \nabla \times \mathbf{E} &= -j\omega\mu\mathbf{H} \\ \nabla \times \mathbf{H} &= \mathbf{J} + j\omega\epsilon\mathbf{E} \end{aligned} \tag{I.21}$$

where ρ is the electric charge density in $\mathrm{C/m^3}$, ϵ the permittivity in $\mathrm{F\,m^{-1}}$, and μ the permeability of the medium in $\mathrm{H\,m^{-1}}$.

Commonly, antenna measurements are performed in a source free region where $\rho = 0$ and $\mathbf{J} = \mathbf{0}$ just like in vacuum medium. From there, the vector Helmholtz or wave equation is derived of Maxwell's equations [11]:

$$\nabla^2 \mathbf{E} + k_0^2 \mathbf{E} = 0 \tag{I.22}$$

To facilitate the solution of this Partial Differential Equation (PDE), an integral transform, such as the FT, can be applied to each scalar equation associated with the components of $\mathbf{E}$. A component of the field $\mathbf{E}$ is denoted u for the following explanation. Hence, the resulting scalar wave equation is:

$$\nabla^2 u + k_0^2 u = 0 \tag{I.23}$$

Expansion of the near field

The FT $\mathcal{F}$ is an integral transform that decomposes complex-valued functions f defined on $\mathbb{R}^n$ and belonging to the Lebesgue space $L^1(\mathbb{R}^n)$ into a continuous superposition of complex exponentials. These exponentials serve as the basis functions of the frequency domain, also referred to as the transform domain. The general formula of the two-dimensional FT of a function f is given by:

$$\mathcal{F}\{f(x,y)\} = \int_{-\infty}^{\infty} \int_{-\infty}^{\infty} f(x,y) e^{j(k_x x + k_y y)}\, dx\, dy \tag{I.24}$$

where k_x and k_y are the spatial-frequency variables associated to x and y, respectively.

In antenna planar measurements, $u(x,y,z)$ denotes one of the field components E_x, E_y, or E_z of the electric NF measured on a planar surface at $z = 0$ relative to the AUT, such that $f(x,y) = u(x,y,0)$. The practical measurement of one NF component $u(x,y,z=0)$ over a finite plane ($x \in [x_1, x_2], y \in [y_1, y_2]$) is then represented by the function $f(x,y)$. The corresponding solution of the scalar Helmholtz equation in Eq. (I.23), expressed in the Fourier domain, is [11]:

$$F(k_x, k_y) = \mathcal{F}\{f(x,y)\} = \int_{y_1}^{y_2} \int_{x_1}^{x_2} f(x,y) e^{j(k_x x + k_y y)}\, dx\, dy \tag{I.25}$$

Here, k_x and k_y are the transverse components of the wave vector $\mathbf{k}$ associated with a fixed frequency and the points on the FF observation surface. The term $e^{j(k_x x + k_y y)}$ represents the complex exponential basis functions used in the angular spectrum decomposition. This operation maps the contributions of spatial positions in the NF to the various plane-wave components, thereby transforming the field from the spatial domain

(NF) into the angular spectrum domain (FF), i. e., from one vector space to another.

The measured component f is thus decomposed into a basis of plane waves $e^{j(k_x x+k_y y)}$. The resulting spectrum $F(k_x, k_y)$ is referred to as the Plane Wave Spectrum (PWS), since it quantifies the contribution of each plane wave to the composition of the measured field.

The corresponding solution in the spatial (Cartesian) coordinate system is obtained via the inverse transform:

$$u(x,y,z) = \mathcal{F}^{-1}\{F(k_x,k_y)\} = \frac{1}{4\pi^2}\int_{k_{x1}}^{k_{x2}}\int_{k_{y_1}}^{k_{y_2}} F(k_x,k_y)e^{j(k_x x+k_y y+k_z z)}\,dk_x\,dk_y \tag{I.26}$$

Thus, $u(x, y, z)$ can be interpreted as a superposition of plane waves with different propagation directions $\mathbf{k}$.

From Eq. (I.26) and recalling that $\nabla \cdot \mathbf{F} = 0$, the solution of the vector wave equation in free space, Eq. (I.22), can be deduced to yield the full field computation by means of the PWE:

$$\begin{aligned}\mathbf{E}(x,y,z) = \frac{1}{4\pi^2}\int_{k_{x1}}^{k_{x2}}\int_{k_{y_1}}^{k_{y_2}}\Bigg[&F_x(k_x,k_y)\hat{\boldsymbol{x}} + F_y(k_x,k_y)\hat{\boldsymbol{y}} \\ &+ \frac{k_x F_x(k_x,k_y)\hat{\boldsymbol{x}} + k_y F_y(k_x,k_y)\hat{\boldsymbol{y}}}{k_z}\hat{\boldsymbol{z}}\Bigg] e^{j(k_x x+k_y y+k_z z)}\,dk_x\,dk_y\end{aligned} \tag{I.27}$$

An approximation then enables direct evaluation of the FF radiation pattern from the PWS $\mathbf{F}(k_x, k_y)$, computed for a fixed direction along the z-axis at any observation position (r, θ, ϕ):

$$\mathbf{E}(r,\theta,\phi) \approx j\frac{e^{-jk_0 r}}{\lambda r}\cos(\theta)\mathbf{F}(k_x,k_y) \tag{I.28}$$

In practice, the measurement surface is finite, and the field is sampled at discrete points. Consequently, the continuous transform in Eq. (I.25) is replaced by a Discrete Fourier Transform (DFT) [11]. To reduce computation time, the fast FT algorithm is often employed, providing an efficient means of computing the spectral coefficients and enabling a direct transition from sampled NF data to its spectral representation. In this manuscript, however, the classical DFT is employed when applying the PWE characterization method.

The main challenge in the PWE method lies in accurately determining the plane-wave spectrum of the measured NF $\mathbf{F}(k_x, k_y)$ to achieve a reliable computation of the FF. Since the PWE is based on analytical solutions of Maxwell's equations, the accuracy of the Fourier coefficients depends critically on the accuracy of the measured tangential components of the NF.

Although this NFFFT is widely used for planar NF measurements [28, 29, 30], some intrinsic limitations discussed in the following sections pose significant challenges in certain applications, such as the characterization of AESA antennas considered in this thesis.

I.3.b Duration of the acquisition

To ensure the accuracy of the characterization procedure using a FT, appropriate sampling rules must be respected. Indeed, a direct relationship exists between the spacing on the NF measurement surface and the discretization of the FF observation surface. Thus, to ensure an accurate computation of the FF in the observation angular directions, a sufficiently dense sampling of the NF measurement surface is required.

However, the finite dimensions of the NF measurement plane impose a spatial filtering effect, which restricts the angular spectrum available for the PWE. This intrinsic property of the considered transform implies that the decomposition basis is bandwidth-limited. Indeed, in Eq. (I.27) the field is computed from a limited domain $k_{x1} \leq k_x \leq k_{x2}$ and $k_{y_1} \leq k_y \leq k_{y_2}$. Hence, all the conditions are fulfilled to apply the Nyquist-Shannon theorem [31]. To correctly identify a signal with a limited bandwidth, the sampling frequency defined by the theorem must be at least twice the maximum frequency of the band to avoid aliasing effects, as illustrated in Fig. I.15.

The corollary to the case of PWE yields the definition of a safe sampling criterion [32] as follows:

$$\Delta_x = \Delta_y = \frac{\lambda}{2\sin(\theta_{\max})} \tag{I.29}$$

where $\theta_{\max}$ is the maximum angle covered by the plane measurement with respect to the AUT positioning, i. e. the validity angle up to which the FF computation is achieved with maximum information provided by the measurement surface. An illustration of the definition of this angle for a square NF measurement surface is given in Fig. I.16.

Consequently, the sampling distribution is constrained to a grid with regularly spaced points. This requirement can be highly constraining when dealing with AESA-like an-

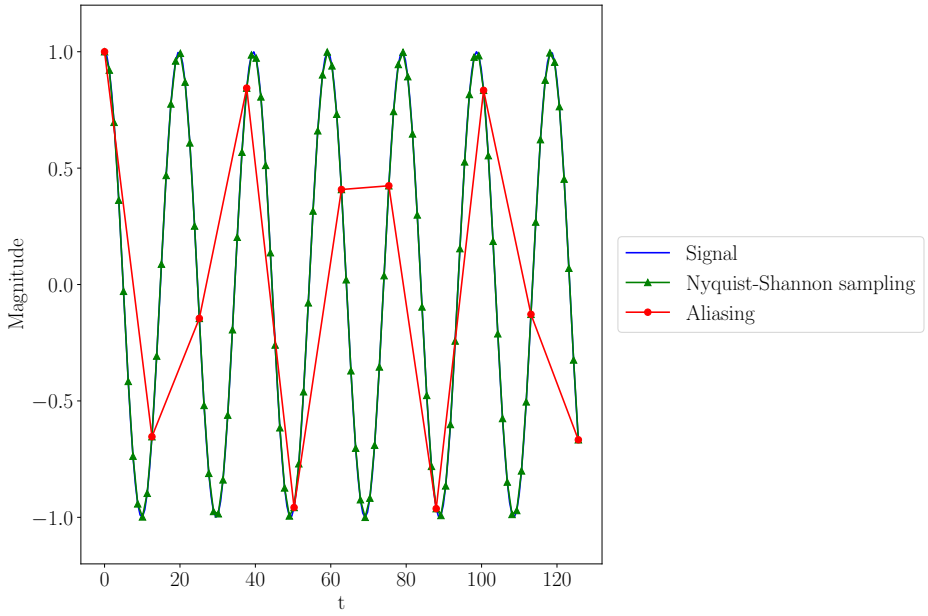

Figure I.15 – Representation of the Nyquist-Shannon theorem. A signal (blue) is sampled in two ways: first, by respecting the sampling theorem (green) and then without respecting it, creating aliasing (red).

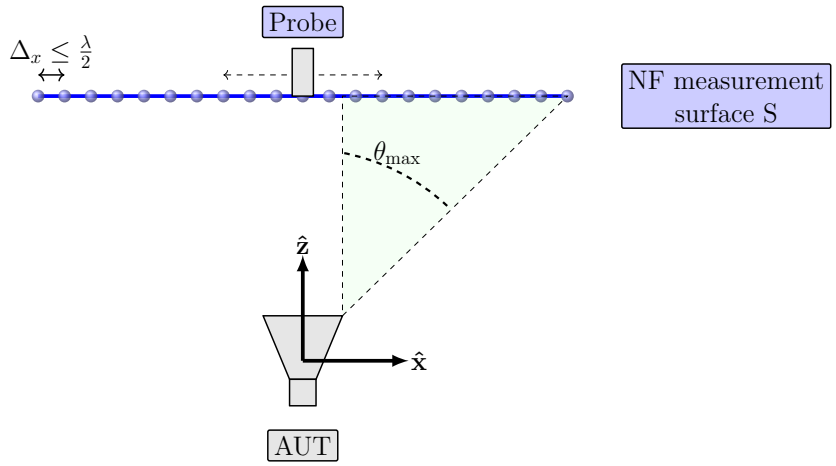

Figure I.16 – Definition of the validity angle $\theta_{\max}$ in a simplified measurement configuration of a square and regular grid, for which only the sampling step Δ_x on the x-axis is represented.

tennas because of the number of samples involved. Indeed, electrically large AUT with strong beam tilts and wide operating frequency ranges are particularly challenging to characterize using planar NF measurement techniques. The larger the plane dimensions are, the greater the number of samples required by the PWE sampling rule. In practice, the greater the number of samples, the longer the measurement time and therefore the higher the cost of characterization. As an illustrative example, at Thales the measurement

time in an anechoic chamber for the radiation pattern of an antenna array with maximal dimensions of about 20 wavelengths lasts approximately one hour.

Over the last decades, many works have investigated ways to circumvent these limitations and relax the sampling distribution. For example, Bucci *et al.* [33] proposed to exploit non-redundant measurements performed on a plane polar NF sampling grid to interpolate the field onto a regular grid before applying the classical PWE. This technique reduces the number of samples and accelerates the characterization procedure without degrading the FF computation. Recently, Gregson *et al.* [34] refined this approach, showing its potential to significantly lower the acquisition time of complex antennas. Similarly, other methods of NF interpolation from reduced sampling sets [35, 36] have been developed, again enabling substantial reductions in measurement time. Qureshi *et al.* [37] introduced an adaptive sampling strategy that extrapolates the field in low-variation zones, allowing measurements only at key positions with maximum useful information. Another adaptive method, based on progressive calculations of sample-by-sample errors, was also investigated [38].

Furthermore, in 1998 Bucci *et al.* [39] proposed constructing an equivalent model of the considered AUT. This major breakthrough enabled the exploitation of available *a priori* information on the AUT to build a numerical model of the antenna and combine it with the above techniques [40, 41]. The resulting gain in characterization accuracy and reduction in measurement time comes at the cost of increased computation associated with the AUT model. This trade-off is intrinsic to the use of numerical methods.

Although all the above-mentioned works present clear improvements, the proposed procedures remain strongly dependent on regular sampling distributed over a finite measurement plane. Consequently, the number of samples necessary to accurately characterize the AUT remains significant, and so does the measurement time. Therefore, to overcome the inherent limitations imposed by the PWE method on sampling distribution, this manuscript will investigate new characterization techniques dissociated from FTs.

I.3.c Truncation effects

To compute the PWS, boundary conditions must be defined on a NF measurement surface of finite dimensions. This induces a spatial filtering of the resulting spectrum, which is directly linked to the chosen NF scan area. At the same time, the challenge of reducing the acquisition time while satisfying the sampling distribution imposed by the Nyquist-Shannon criterion often leads to limiting the size of the measurement surface.

Consequently, truncation effects arising from the finite dimensions of the scanning area are reinforced by the properties of FT. These effects stem from the lack of information provided by the NF measurement surface in the angular zones of field pattern computation.

To delimit the characterization validity zone, an angle $\theta_{\max}$ is defined for the considered measurement setup (Fig. I.16). If the computation of the radiated FF is performed on observation points with $\theta > \theta_{\max}$, errors will appear due to truncation [42]. Although research efforts, such as those by Cutshall *et al.* [43], have proposed a new definition of the valid zone to minimize errors near the edges of the measurement plane, residual errors remain significant at high angles for the FF computation.

In the case of AESAs, the radiated beam often reaches extreme elevation angles $\theta_{\text{beam}} > \theta_{\max}$, sometimes approaching grazing with respect to the AUT aperture plane, as illustrated in Fig. I.17.

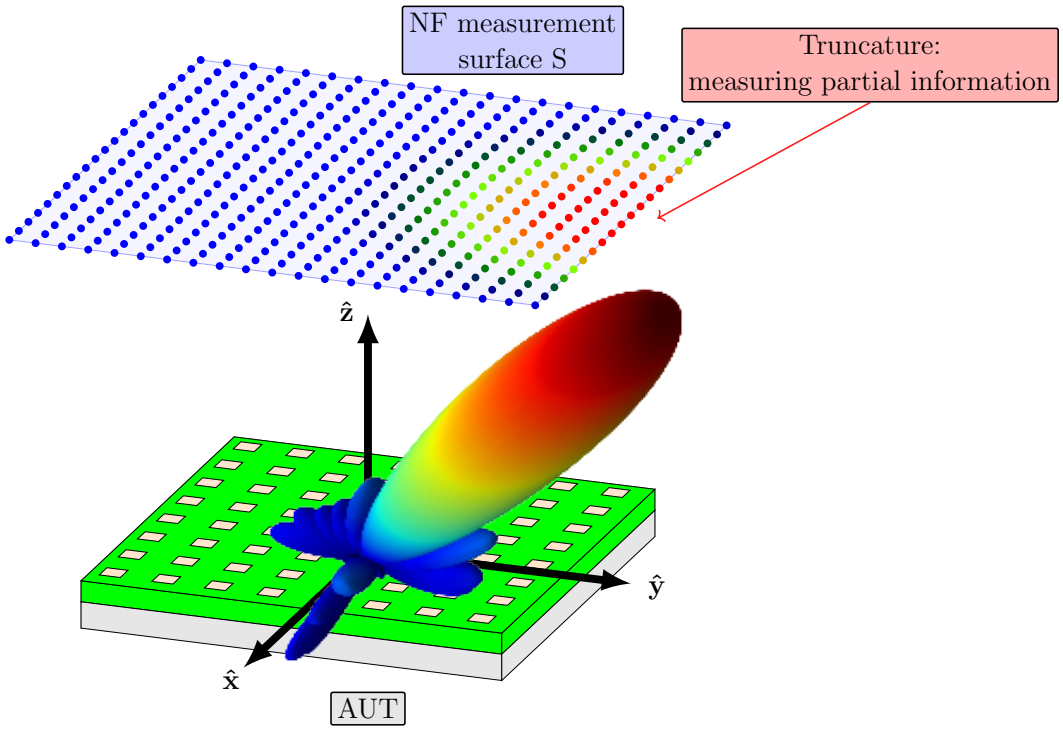

Figure I.17 – Representation of truncation effects induced by a planar measuring surface for an AUT radiating in a high-angle direction.

Therefore, when applying the PWE method to characterize this type of antenna, a compromise must be found between enlarging the measurement surface to cover the dif-

ferent possible angular regions of beam directions and minimizing the number of samples to reduce acquisition time.

To address this issue, Bucci *et al.* [44] investigated interpolation techniques to improve the FF computation in angular regions beyond $\theta_{\max}$. More recently, iterative approaches proposed by Martini *et al.* [45] and Cano-Fácila *et al.* [46] have enabled effective extrapolation of the field in invalid zones, resulting in improved characterization accuracy compared to the classical PWE method.

I.4 Conclusion

In this first chapter, the fundamental aspects of antenna characterization have been established. Starting from the theoretical principles of antenna radiation, the main parameters describing antenna performance such as gain, directivity, and polarization have been recalled and linked to their physical interpretation. A review of measurement techniques then highlighted the complementarity of FF and NF approaches, while underlining the importance of controlled environments and suitable probe configurations to ensure accuracy.

A particular emphasis has been placed on planar NF measurements, which are central to this work. While classical PWE provides a reliable framework for retrieving FF information, its practical use is constrained by strict sampling requirements and sensitivity to truncation. These limitations are especially critical for large, directive, and beam-steering antennas such as AESAs.

The issues identified in this chapter justify the need for more flexible and efficient characterization methods. They set the stage for the following chapters, which will introduce alternative characterization methods based on the equivalence principle.

Chapter II

Antenna characterization employing the equivalence principle

II.1 Introduction

II.1.a Motivations

The characterization of antennas from NF measurements requires using a NFFFT which is directly related to the geometry of the measurement surface. As this work focuses on techniques to assess the radiation performance of AESAs, we are mainly interested in planar NF measurement systems. For this planar geometry, the PWE [11] is based on analytical orthogonal basis formed by plane waves which are well-known solutions of the Maxwell's equations in the Cartesian coordinate system. The use of this basis to decompose the measured NF relies on compliance with specific rules concerning the sampling distribution. These rules simultaneously affect the required number of samples and give rise to significant truncation effects, which reduce the accuracy of the characterization, as detailed in Section I.3. To overcome these limitations imposed by the PWE, recent methods based on the construction of an equivalent numerical model of the AUT based on the equivalence principle have proved useful as they allow non-conventional sampling distributions. This property could lead to a significant reduction in acquisition time by reducing the number of samples required for NF measurements and the truncation effects induced.

II.1.b State of the art

In the framework of the NFFFT process, several equivalent numerical models have been proposed as alternatives to classical field transformation techniques. To provide a clear perspective, we first review the main families of these approaches, tracing their historical development and highlighting their relevance for antenna characterization.

The emergence of computational electromagnetics in the 20th century laid the groundwork for developing numerical methods to solve PDEs governing physical phenomena such as Maxwell's equations. In the 1960s, the boundary element method, more commonly known in electromagnetics as the Method of Moments (MoM) [47], was introduced. This approach solves integral equations by enforcing boundary conditions over the surface of the domain, discretized using meshing elements. Figure II.1 shows an example of triangular surface meshing applied to an Open-Ended Waveguide (OEWG) using CST Studio Suite [48].

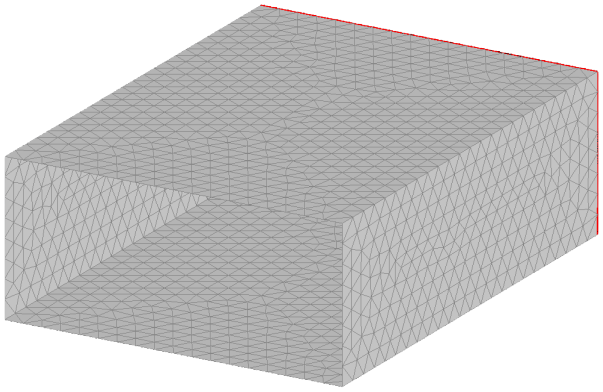

Figure II.1 – Illustration of the created surface mesh while applying MoM to an OEWG on CST.

In contrast to the more widely known Finite Element Method (FEM) which discretizes the entire volume of the computational domain to reduce the problem into local subproblems [49], MoM inherently accounts for the full mutual interactions between all surface elements. Thanks to this ability to model surface currents and radiation phenomena with high accuracy, MoM has become a standard method in many commercial full-wave electromagnetic solvers, such as FEKO [50] and CST, while other solvers, like HFSS [51], primarily rely on FEM.

A notable advantage of surface-based modeling is the ability to reduce the number of required samples while also mitigating truncation effects during NFFFT [52, 53, 54]. However, the use of MoM still requires accurate meshing of the actual antenna geome-

try, which may become computationally expensive or impractical for electrically large or geometrically complex structures.

A major breakthrough came with the work of Bucci *et al.* [2], who introduced the concept of using an equivalent surface Σ enclosing the AUT to represent its radiation properties. This surface, independent of the physical geometry, allows one to define a simplified radiating model capable of reproducing the external fields. The principle, illustrated in Fig. II.2, opened the door to equivalent modeling techniques, where the field computation problem is decoupled from the antenna structural complexity.

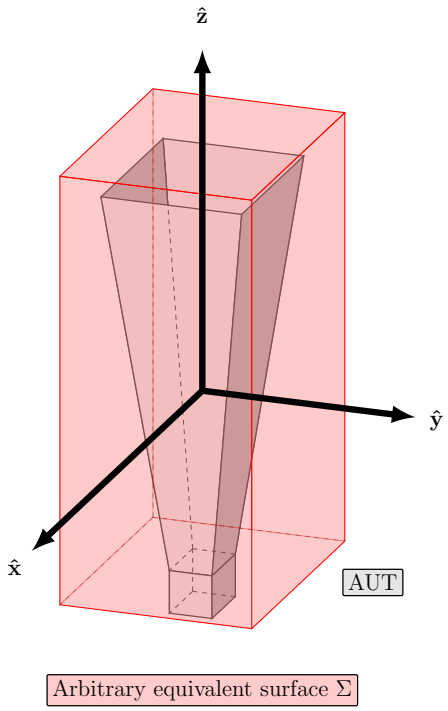

Figure II.2 – Representation of a horn antenna and in red its arbitrary equivalent surface Σ based on the principle stated by Bucci [2].

This paradigm shift allowed for the use of strong *a priori* knowledge either from full-wave simulations [55] or mechanical constraints [41] to inform reduced or overcomplete expansion bases. As a result, the complexity of the radiation problem can be drastically reduced without compromising the characterization accuracy.

More recent advances have explored new discretization strategies of the equivalent surface Σ to enhance the flexibility and efficiency of equivalent models. Among these, two main approaches have emerged:

1. MoM-based meshing techniques, which still rely on traditional discretizations of equivalent surface Σ, such as triangular meshes with Rao-Wilton-Glisson (RWG)

basis functions [56]. These techniques rigorously enforce the continuity of surface currents and provide high accuracy in full-wave formulations. However, their computational burden increases with the complexity of the surface and the number of unknowns, which can limit their practical use for large or irregular equivalent surfaces Σ;

2. dipole-based discretization, which represents the field radiated by the AUT using distributions of infinitesimal electric or magnetic dipoles. Unlike RWG basis functions, dipole elements do not require current continuity, enabling them to approximate a wider variety of field distributions with fewer elements and simplified positioning rules [57, 58, 59, 60, 61]. Nevertheless, in the context of antenna characterization, dipole-based equivalent models remain subject to sampling constraints, as is generally the case for auxiliary or fictitious source methods: an insufficient dipole density may lead to an inaccurate representation of the physical currents of the AUT. This formulation grants high modeling flexibility and supports irregular or sparse sampling schemes. Castañer *et al.* [62] give a global view of the interest of using this type of source modeling.

Finally, the use of equivalent models has demonstrated strong potential for simultaneously increasing characterization accuracy and reducing the number of required NF samples, particularly in FF computation contexts based on inverse source techniques. In the case of spherical measurements, Mézières *et al.* [13] employed such models to achieve accurate computed FF from undersampled data. In planar configurations, Fuchs *et al.* [63] shown that dipole-based models could reduce acquisition time by up to 60% compared to the dense sampling required by classical PWE method.

II.1.c Contributions

This work is a continuation of the development proposed in [63] as it is based on the use of an equivalent model constructed with infinitesimal dipoles to characterize complex antennas from planar NF measurements. In this framework, a complete characterization procedure with a fully integrated probe compensation is developed. All the details on the creation of an equivalent model for the antenna and the construction of the associated radiation matrix that links the currents on the arbitrary equivalent surface Σ surrounding the AUT with the positions of the radiated field are described. The correct determination of these currents are validated on several characterization cases. In addition, the global

validation of the model ensures that the characterization methods developed in the following sections are built upon a robust and reliable foundation. Then, the results of a non-exhaustive parametric study conducted to understand the behavior of the model are discussed in this chapter. Finally, definitions on new validity zones and solutions based on non-conventional samplings enabled by our method to limit the truncation effects are given. The investigations made on the reduction of the number of samples are extended in the next chapter.

II.2 Equivalent principle construction

The characterization methods detailed in this manuscript are based on the use of the equivalence principle. In this section all the elementary bricks allowing to create an equivalent model for the AUT are addressed up to the construction of the radiation matrix that maps the resulting model to the field radiated by the antenna. Some validations are achieved to verify the correct behavior of the developed numerical scheme.

II.2.a Huygens principle

The whole numerical methods developed in this work are based on the creation of a model for the AUT made possible by the application of the Huygens principle or equivalence principle. This fundamental concept in electromagnetics allows representing a radiating system by equivalent currents flowing on an arbitrary equivalent surface Σ which completely encloses the system [64]. In a more mathematical formulation, the electric and magnetic fields ($\mathbf{E}$, $\mathbf{H}$) are radiated by the internal electric and magnetic sources ($\mathbf{J}$, $\mathbf{M}$) of a system surrounded by a closed equivalent surface Σ defining a volume V. In the equivalent problem, the fictitious equivalent currents ($\mathbf{J}_{\text{eq}}$, $\mathbf{M}_{\text{eq}}$) flowing tangentially to this equivalent surface Σ radiate the same fields ($\mathbf{E}$, $\mathbf{H}$) as the initial system outside Σ, while the fields inside Σ ($\mathbf{E}_V$, $\mathbf{H}_V$) can be constrained arbitrarily depending on the applied boundary conditions, as illustrated in Fig. II.3. The relationship between the fields radiated in the various regions and the equivalent surface currents on Σ can be deduced from the boundary conditions at the interface of two linear, homogeneous and isotropic media.

This theoretical support is often used to simplify complex electromagnetic problems that are otherwise difficult to solve using full-wave integral equation formulations. By

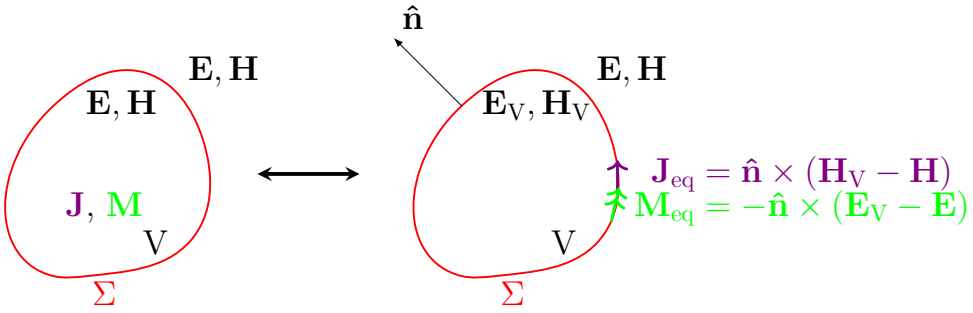

Figure II.3 – Representation of the Huygens principle: the initial problem (left) addressed and the equivalent one (right).

enabling the decomposition of fields into basis related to equivalent sources on the equivalent surface Σ, this principle provides access to powerful numerical methods that facilitate solving the original problem. For example, such simplifications are employed in the MoM, where typically only one type of equivalent current either electric $\mathbf{J}_{\text{eq}}$ or magnetic $\mathbf{M}_{\text{eq}}$ is used. This is possible when only the electric or magnetic field is known, assuming that the volume V can be treated as a perfect electric or magnetic conductor, thereby canceling the unused current. In contrast, the present work utilizes both types of equivalent currents to construct the model, since no assumptions are made regarding the electromagnetic properties of the AUT.

II.2.b Equivalent model of infinitesimal dipoles

The application of the equivalence principle implies to create an arbitrary equivalent surface Σ that can be discretized by a distribution of synthetic radiating elements. The choice of those elements is very important because it defines the equivalent model of the AUT, and therefore it impacts the properties of the numerical basis used to expand the field radiated by the antenna.

A well-known discretization technique is the triangle cells and the corresponding RWG functions [56] that ensure a continuity between the different triangles that are distributed over Σ. More recently, research works decided to use infinitesimal dipoles (with a length $l \ll \lambda$) to discretize the equivalent surface Σ [63, 65]. A distribution of electrically small dipoles allows breaking the continuity between the different nodes of the mesh created over the equivalent surface Σ. The freedom in the localization and the orientation of the dipoles with respect to the AUT geometry enables an adaptive model to be produced. Indeed, the dipoles are placed all over the arbitrary equivalent surface Σ and their orientations can be chosen freely in the tangent plane to Σ, as represented in Fig. II.4.

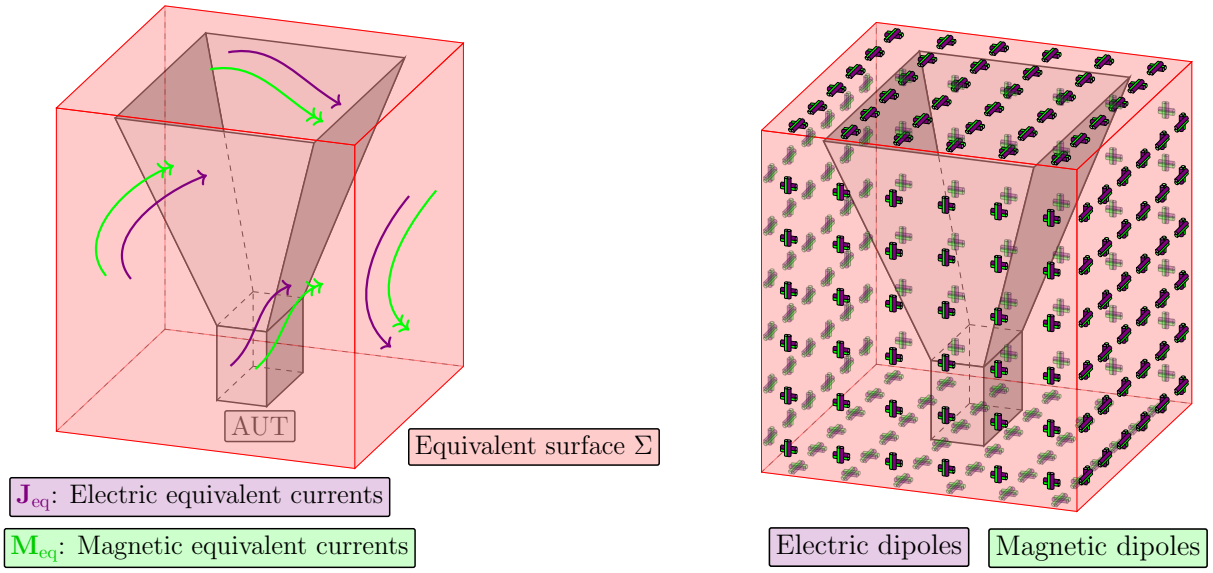

(a) Definition of Σ (b) Discretization of Σ

Figure II.4 – Illustration of a box-shaped equivalent model constructed for a horn antenna: the application of the Huygens principle (a) and the discretization of the equivalent surface Σ with couples of electric and magnetic infinitesimal dipoles oriented orthogonally with each other (b).

Thus, these dipoles are used as elementary bricks to represent a scalable and flexible basis for decomposing the equivalent currents. The infinitesimal dipoles are therefore the radiating elements used in this manuscript to construct an equivalent model of the AUT. All the equivalent surfaces Σ processed will be Euclidean, with the dipoles placed at the center of cells defined by a regular mesh.

Furthermore, the classical formulation of Huygens' principle requires an equivalent surface Σ that completely encloses the AUT. Nevertheless, in practice, when the radiating behavior of the system is predominantly determined by a specific component such as the aperture in the case of a horn antenna, open or partially closed equivalent surfaces Σ can often provide a sufficiently accurate representation of the antenna physical currents. This approximation relies on the physical insight that, depending on the geometry and radiation characteristics of the AUT, the radiated field may be predominantly determined by currents over specific regions. In such scenarios, the boundary conditions imposed on the equivalent surface Σ are adjusted accordingly. When Σ is open, the standard assumption of a perfectly closed boundary no longer strictly holds. Instead, radiation conditions at infinity such as the Sommerfeld radiation condition, which states that the radiated field must behave as an outward-propagating spherical wave that decays with distance,

may be implicitly assumed. This ensures that, despite the equivalent surface Σ being open, the field behaves as if it has been enclosed by a perfectly closed boundary. This relaxation reduces computational cost and complexity while still capturing the dominant electromagnetic behavior. In this work, this hypothesis is exploited in certain cases by carefully selecting an open geometry for the equivalent surface Σ that balances numerical efficiency with physical accuracy, without requiring detailed assumptions about the material properties of the AUT.

Since both types of currents on the equivalent surface Σ are considered in our application of the Huygens principle, namely, electric and magnetic surface currents, the equivalent model used throughout this manuscript consists of a regular distribution of dipole pairs. Each point on the equivalent surface Σ hosts two pairs of crossed dipoles for each type of current (electric and magnetic) oriented tangentially to Σ. This configuration with a local quadrupole structure allows for the accurate representation of both electric and magnetic surface current components in the orthogonal basis formed by the electromagnetic pairs while maintaining tangential conformity to the equivalent surface Σ.

Now, it is necessary to formally introduce the radiation operator, which establishes the link between the equivalent currents defined on the equivalent surface Σ and the radiated electric field, either in the NF or FF. This operator plays a dual role: on the one hand, it enables the computation of the radiated field from the equivalent model of the AUT, and on the other hand, it allows the determination of these equivalent currents directly from the measured NF data. In this sense, the radiation operator provides the mathematical framework required to connect the equivalent surface Σ with both NF measurement and FF computation processes. Finally, its discretization constitutes a key step in practical implementations and forms a fundamental element of the characterization methods developed in this thesis.

II.2.c Discretization of the radiation operator

From the Maxwell's equations in Eq. (I.21), the potential functions $\mathbf{F}_{\mathrm{J}}$ and $\mathbf{F}_{\mathrm{M}}$ generated in a source-free region at a given observation point located at a distance r from the equivalent currents on Σ by $\mathbf{J}_{\mathrm{eq}}$ and $\mathbf{M}_{\mathrm{eq}}$, respectively, can be introduced [5]:

$$\begin{aligned}\mathbf{F}_{\mathrm{J}}(r) &= \frac{\mu_0}{4\pi}\iint_{\Sigma}\mathbf{J}_{\mathrm{eq}}\frac{e^{-jk_0r}}{r}\,d\sigma \\ \mathbf{F}_{\mathrm{M}}(r) &= \frac{\epsilon_0}{4\pi}\iint_{\Sigma}\mathbf{M}_{\mathrm{eq}}\frac{e^{-jk_0r}}{r}\,d\sigma\end{aligned} \tag{II.1}$$

The electric field $\mathbf{E}$ radiated outside Σ by the equivalent currents $(\mathbf{J}_{\mathrm{eq}}, \mathbf{M}_{\mathrm{eq}})$ with a harmonic time dependency is expressed through the expression of the following local radiation operator:

$$\mathbf{E} = -j\omega\mathbf{F}_{\mathrm{J}} - j\frac{1}{\omega\mu_0\epsilon_0}\nabla(\nabla\cdot\mathbf{F}_{\mathrm{J}}) - \frac{1}{\epsilon_0}\nabla\times\mathbf{F}_{\mathrm{M}} \tag{II.2}$$

The decomposition of the equivalent currents into a basis associated to the distribution of dipoles proposed on Σ yields to the discretization of the radiation operator which is called a radiation matrix.

In the case of an infinitesimal electric dipole defined in the Cartesian coordinate system and oriented along the z-axis, as represented in Fig. II.5, the equivalent currents $\mathbf{J}_{\mathrm{eq}}$ can be expressed locally to the position of the ith dipole of the distribution by the current $X_{\mathrm{J},i}$ flowing inside it [11].

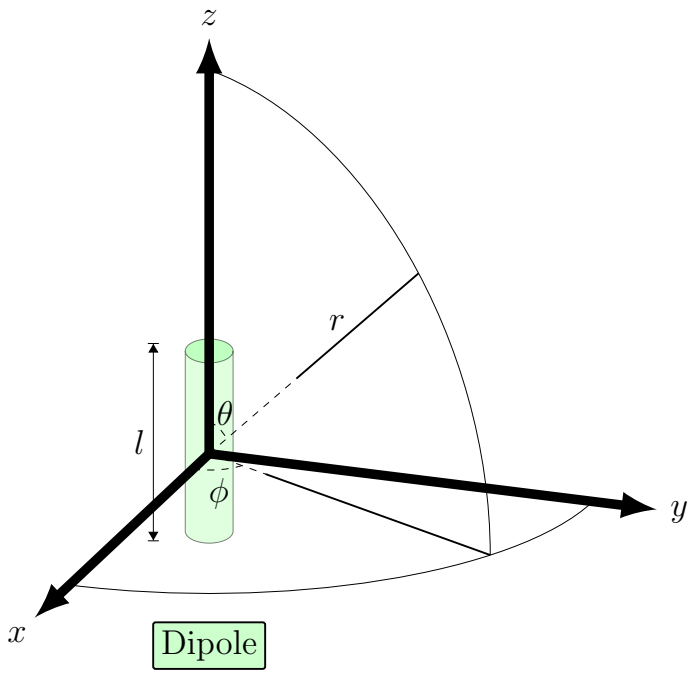

Figure II.5 – Representation of an infinitesimal dipole in the Cartesian coordinate system.

The potential vector $\mathbf{F}_{\mathrm{J},i}$ on the contour C defined by the length of the dipole becomes:

$$\mathbf{F}_{\mathrm{J},i}(x,y,z) = \frac{\mu_0}{4\pi}\int_C X_{\mathrm{J},i}\frac{e^{-jk_0r}}{r}\,dl'\hat{\mathbf{z}} = \frac{\mu_0 X_{\mathrm{J},i}}{4\pi r}e^{-jk_0r}\int_{-\frac{l}{2}}^{\frac{l}{2}} dz'\hat{\mathbf{z}} = \frac{\mu_0 X_{\mathrm{J},i}\,l}{4\pi r}e^{-jk_0r}\hat{\mathbf{z}} \tag{II.3}$$

Then, the resulting radiated field can be deduced in the spherical system:

$$\begin{aligned}
E_{r,i}(r,\theta,\phi) &= \eta\frac{X_{\mathrm{J},i}\,l\cos\theta}{2\pi r^2}\left[1+\frac{1}{jk_0r}\right]e^{-jk_0r}\\
E_{\theta,i}(r,\theta,\phi) &= j\eta\frac{k_0 X_{\mathrm{J},i}\,l\sin\theta}{4\pi r}\left[1+\frac{1}{jk_0r}-\frac{1}{(k_0r)^2}\right]e^{-jk_0r}\\
E_{\phi,i}(r,\theta,\phi) &= 0
\end{aligned} \tag{II.4}$$

The corresponding radiation pattern of an electric infinitesimal dipole is given in Fig. II.6.

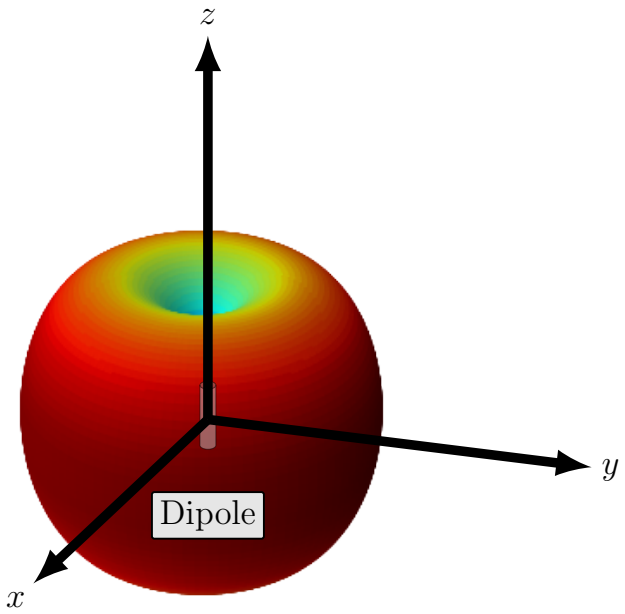

Figure II.6 – Radiation pattern of an infinitesimal dipole.

In the same way, the expression of $\mathbf{F}_{\mathrm{M},k}$ associated to the radiation of the kth magnetic infinitesimal dipole of the distribution with a current $X_{\mathrm{M},k}$ yields to the formulas for the electric field:

$$
\begin{aligned}
E_{r,k}(r,\theta,\phi) &= 0 \\
E_{\theta,k}(r,\theta,\phi) &= 0 \\
E_{\phi,k}(r,\theta,\phi) &= j\frac{k_0 X_{\mathrm{M},k} l \sin\theta}{4\pi r}\left[1+\frac{1}{jk_0 r}\right]e^{-jk_0 r}
\end{aligned}
\tag{II.5}
$$

To accurately retrieve the field radiated by the distribution of infinitesimal dipoles, it is necessary to determine the associated vectors $\mathbf{X}_{\mathrm{J}}$ and $\mathbf{X}_{\mathrm{M}}$, which contain the complex decomposition coefficients $X_{\mathrm{J},i}$ and $X_{\mathrm{M},k}$ corresponding to the electric and magnetic equivalent currents, respectively. To ensure a proper balance between the contributions of these two types of dipoles, a scaling factor η (the characteristic impedance of vacuum, approximately $376.7\,\Omega$) must be applied to the magnetic dipole coefficients X_{M}. This compensates for the difference in their radiative behavior relative to the electric dipoles.

II.2.d Construction of the radiation matrix

In practice, the infinitesimal dipoles distributed over Σ are located at different positions and oriented tangentially to the equivalent surface. However, only the formulas linked to a dipole centered and oriented along the z-axis are necessary [5]. In this configuration, translation, rotation, and coordinate system transformations are taken into account in the construction of the radiation matrix for an arbitrary dipole distribution on Σ and for arbitrary observation points.

For the sake of comprehension, a simple case is proposed to detail all the construction steps for the radiation matrix in the Cartesian system, as shown in Fig. II.7. Thus, an infinitesimal electric dipole is placed at the coordinates (-1, 0, 0). This dipole is oriented along the y-axis. The field radiated by this unique dipole is observed at a single point (1, 0, 0).

First, the translation of the observation point relative to the dipole location is performed to consider the dipole at the center of a local coordinate system. The observation position is now (2, 0, 0) in the new reference. Now, the dipole has to be oriented along the z-axis in the local system to use the field expressions given by Balanis [5]. To achieve this, Rodrigue's formulas [66] are used to manage the rotations of a vector $\mathbf{v}$ in $\mathbb{R}^3$ around a unitary axis $\mathbf{u}$ by a given angle α which results in a vector $\mathbf{v}_{\mathrm{rot}}$:

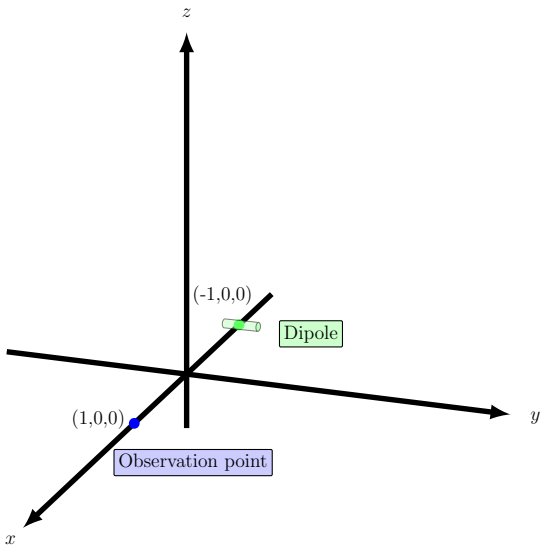

(a) Initial configuration

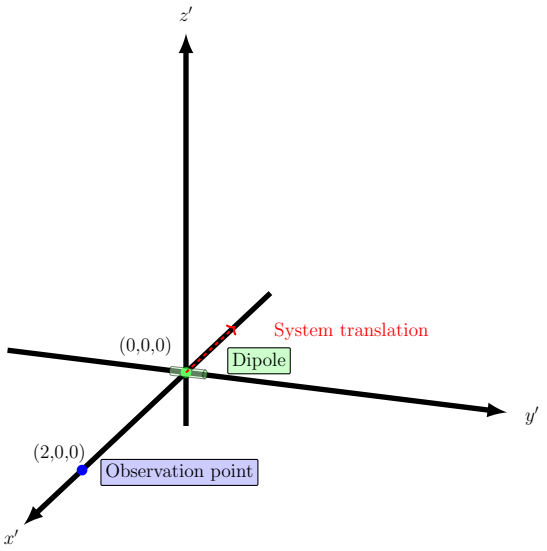

(b) Translation of the initial system to a local system referred to the dipole location

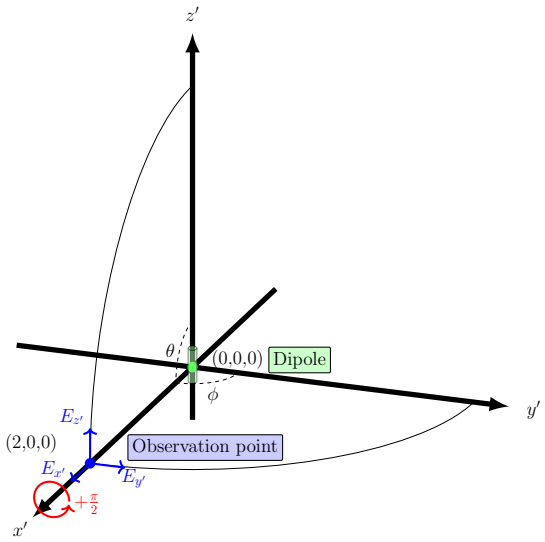

(c) Rotation of the observation point in the local system

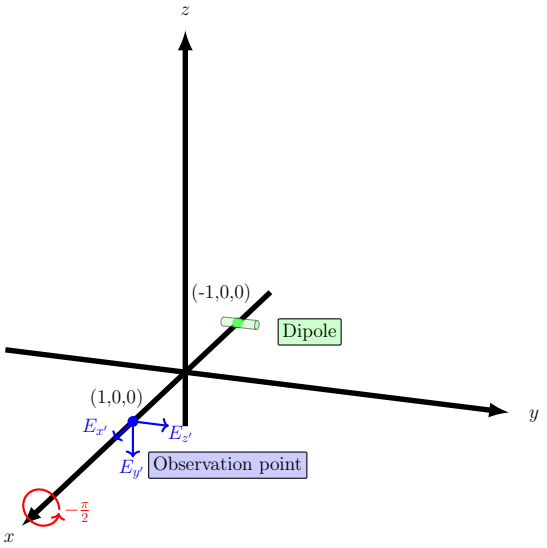

(d) Rotation of the field to come back in the initial system

Figure II.7 – Illustration of an example with all the procedure to construct a radiation matrix associated to an electric infinitesimal dipole oriented along the y-axis and shifted from the origin and an observation point placed on the x-axis in the Cartesian coordinate system. The geometric operations applied are colored in red.

$$\mathbf{v}_{\text{rot}} = \mathbf{v}\cos\alpha + (\mathbf{u}\times\mathbf{v})\sin\alpha + \mathbf{u}(\mathbf{u}\cdot\mathbf{v})(1-\cos\alpha) \tag{II.6}$$

Here, $\mathbf{u}$ is (1, 0, 0) and α is equal to $\frac{\pi}{2}$. The electric field radiated by the dipole can be

computed at the point (2, 0, 0). To come back in the initial system, the vector associated to the electric field is rotated by -α around $\mathbf{u}$. Once returned to the initial coordinate system, the last step consists in associating the field values to the observation point in this system (1, 0, 0).

This procedure allows constructing a radiation matrix linking the dipole position to the observation point. It and can be extended to K any dipoles on Σ and N any observation points. Since, quadrupoles are used to discretize the equivalent surface Σ with the same number of electric and magnetic dipoles, if M_p is the number of positions on Σ, $K = 4M_p$. Thus, the resulting radiation matrix $\mathbf{A}$ is of dimensions $(3N \times K)$ related to the electric field $\mathbf{E}$ (of dimensions 3, hence $3N$) radiated by the distribution of dipoles yields to the linear system in the spherical system:

$$\mathbf{E} = \mathbf{AX} \iff \begin{bmatrix} E_r \\ E_\theta \\ E_\phi \end{bmatrix} = \begin{bmatrix} A_{\mathrm{J}r} & \eta A_{\mathrm{M}r} \\ A_{\mathrm{J}\theta} & \eta A_{\mathrm{M}\theta} \\ A_{\mathrm{J}\phi} & \eta A_{\mathrm{M}\phi} \end{bmatrix} \begin{bmatrix} X_{\mathrm{J}} \\ X_{\mathrm{M}} \end{bmatrix} \tag{II.7}$$

where E_r, E_θ and E_ϕ are the field components. $A_{\mathrm{J}r}$ is the r-component of the field radiated by the electric infinitesimal dipoles of the distribution while $A_{\mathrm{M}r}$ is the same for the magnetic dipoles. Finally, X_{J} and X_{M} gather all the weighting excitations of the electric and magnetic dipoles to be determined from the measured NF. These equivalent currents are required to compute the FF. To resume, the radiation matrix is assembled column-by-column with the field radiated by each dipole from the equivalent surface Σ at the different positions on an observation surface.

II.2.e Validations

The discretization of the radiation operator using a distribution of infinitesimal electric dipoles to represent the equivalent currents of the AUT leads to the construction of a radiation matrix. The accurate formulation of this matrix is essential to ensure that the equivalent surface Σ radiates coherently with the real antenna. To validate the correctness of its construction, several benchmark tests are performed based on well-established analytical results.

These validation tests primarily aim to verify the integrity of all geometric operations involved in building the radiation matrix, including translations, rotations, and coordinate transformations. Furthermore, the correct association between the different dipoles in the distribution and their ability to form steered beams are also evaluated.

For each validation scenario, the objective is to reproduce the reference analytical FF data reported by Balanis [5] for a theoretical antenna using its equivalent model, and to compare the obtained results with the analytical solution. As the considered theoretical antennas are composed by only electric infinitesimal dipoles, the equivalent model considered is the antenna itself. The main goal being to verify the radiation of our model built with these dipoles.

The working frequency is fixed at 10 GHz, and radiation patterns are computed on a hemispherical observation surface S' located in the FF region with an equiangular distribution of $\Delta_\theta = \Delta_\phi = 1°$. This hemisphere will be the FF observation surface S' for all the validations presented here after. Results are presented for the two principal cut-planes at $\phi = 0°$ and $\phi = 90°$. The error metrics are computed using a reference-based normalization.

Linear array of electric infinitesimal dipoles

Consider a linear array of length 5λ, with dipoles oriented and distributed along the z-axis, spaced at $\frac{\lambda}{4}$. The field radiated by the equivalent surface Σ is numerically computed and compared with the field obtained from linear array analytical formulas. The results are presented in Fig. II.8.

The computed electric FF shows great agreement with the analytical solution, with a low error level defined in Eq. (I.19) quantified as $ENL = -122.1$ dB. This result confirms the correctness of the translation operations used in constructing the radiation matrix. The behavior of a linear array of dipoles is well reproduced by the model, as expected.

Planar array of electric infinitesimal dipoles

Next, a two-dimensional planar array is considered, with dimensions $5\lambda \times 5\lambda$ and a spacing of $\frac{\lambda}{4}$ in both directions. The dipoles are oriented along the x-axis and distributed over the XOY plane. Here, in addition to verifying the translation operations along two directions, the implementation of rotation in the model through dipole orientations different from z-axis is also investigated. Thus, the field radiated by the associated equivalent surface Σ is compared to the field obtained from planar array analytical formulas. The resulting FF comparison is shown in Fig. II.9.

Again, the FF computation error is extremely low, with $ENL = -125.9$ dB. These results confirm the proper implementation of element arraying and validate the rotation operations applied in the radiation matrix construction.

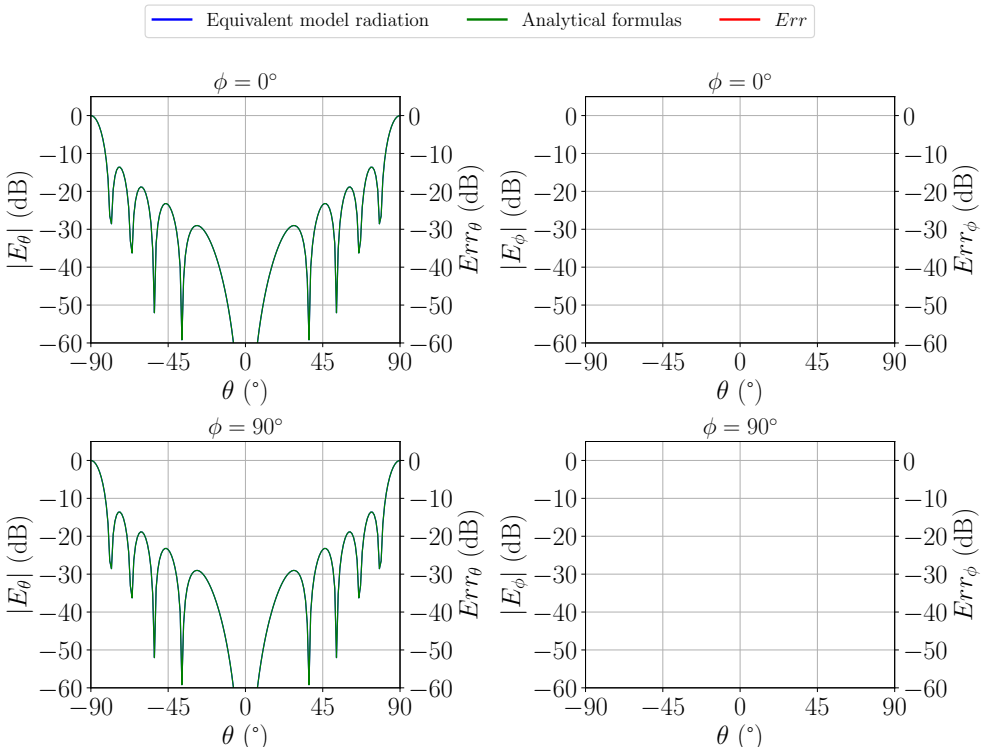

Figure II.8 – Linear array of dipoles: comparison between the FF radiated by the equivalent surface Σ and the reference FF data from analytical formulas. The ϕ-component of the field is at the numerical noise level.

Planar array of electric infinitesimal dipoles with phase shifting

In the final test case, the same planar array geometry and spacing are used, but the dipoles are now oriented along the y-axis. A phase excitation law is applied to steer the main beam toward the direction defined by $(\theta_{\text{beam}} = 50°, \phi_{\text{beam}} = 90°)$. To incorporate this beam steering into the equivalent model, an individual phase shift is applied to each dipole when constructing the radiation matrix from the relative phase difference computed regarding the dipole position. As reminder, this relative phase difference for a linear array of dipoles distributed along z-axis is:

$$\psi = k_0 d \cos(\theta_{\text{beam}}) \tag{II.8}$$

with θ_{beam} the angle of direction of the main beam relative to the z-axis.

The comparison of the computed FF using the equivalent model and the planar array analytical formulas with a phase law is shown in Fig. II.10.

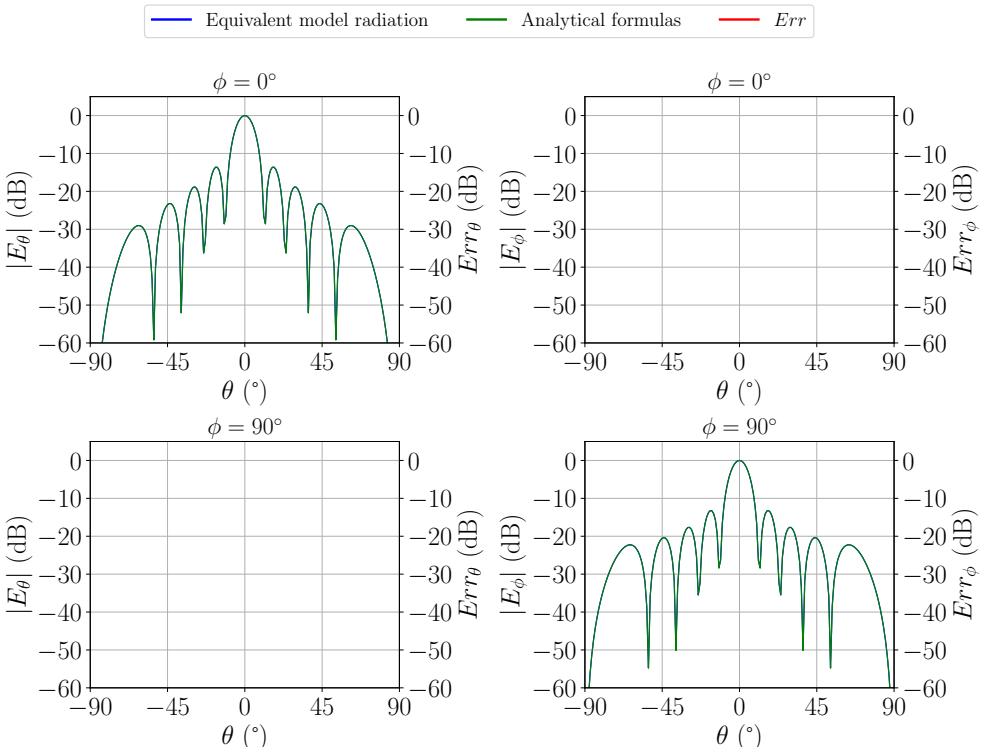

Figure II.9 – Planar array of dipoles: comparison between the FF radiated by the equivalent surface Σ and the reference FF data from analytical formulas. The crossed component of the field is at the numerical noise level.

The FF computation remains highly accurate, with an error level of $ENL = -128.9\,\text{dB}$. This final validation confirms the capability of the radiation matrix to correctly handle all necessary geometric transformations, including rotations, translations, and phase control.

These results confirm that the dipole distribution accurately reproduces the intended field patterns, serving as a necessary validation step for the equivalent modeling approach adopted in this work. Consequently, the developed dipole-based representation is well-suited for use in the antenna characterization methods addressed in the following sections.

II.3 Inverse problem

II.3.a Implementation in the context of characterization

The main objective of this thesis is to investigate novel characterization methods for AESA-like antennas using planar NF measurements. A correct characterization implies

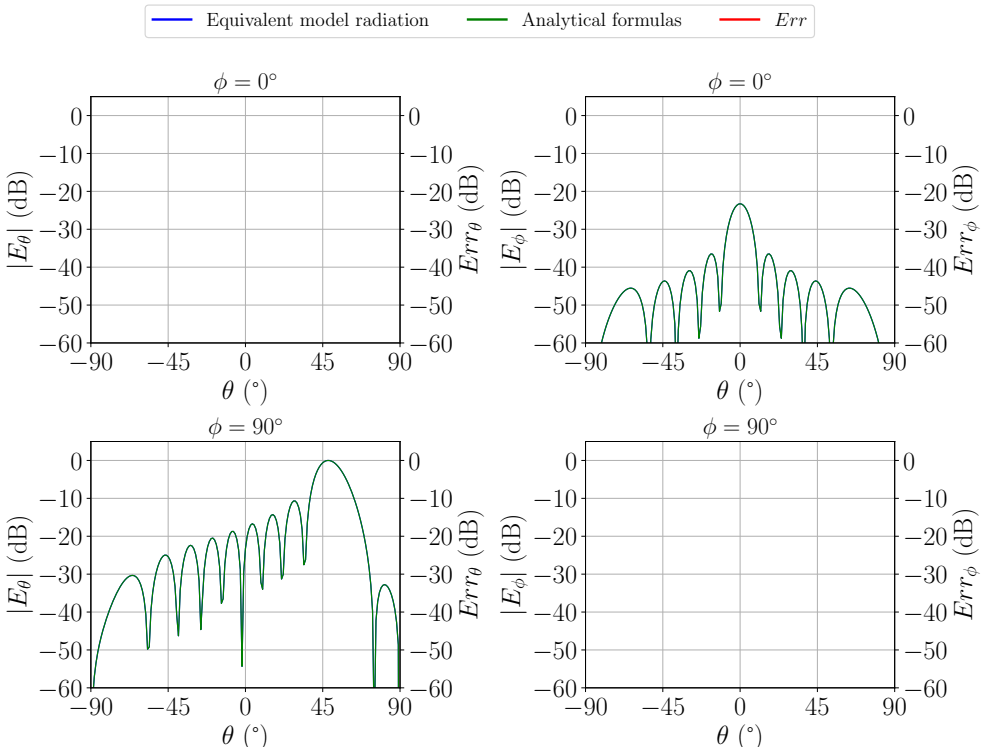

Figure II.10 – Planar array of dipoles with phase shift: comparison between the FF radiated by the equivalent surface Σ and the reference FF data from analytical formulas. The crossed component of the field is at the numerical noise level.

accurately computing the radiation pattern of the AUT in the FF region from the acquired NF data. Hence, to characterize the AUT, the equivalent currents first must be determined by solving the linear system in Eq. (II.7) and then be used to achieve the FF computation. In this manuscript, the NF measurement surface is denoted by S, while S' refers to the observation surface located at a FF distance.

As described in the previous section, the proposed methods rely on the use of an equivalent model of the AUT, constructed from a distribution of infinitesimal dipoles. These dipoles are connected to observation positions through a radiation matrix. Depending on the formulation of the characterization problem, these positions may correspond either to NF samples $\mathbf{E}$ measured on surface S, or to FF samples $\tilde{\mathbf{E}}'$ computed on observation surface S'. The notation $\tilde{Q}$ is used throughout this manuscript to denote any quantity Q determined using the proposed approach. Accordingly, the radiation matrices are denoted by $\mathbf{A}$ for the NF measurement surface S and $\mathbf{A}'$ for the FF surface, as illustrated in Fig. II.11.

Thus, the equivalent currents of the AUT are associated to the radiated NF $\mathbf{E}$ through

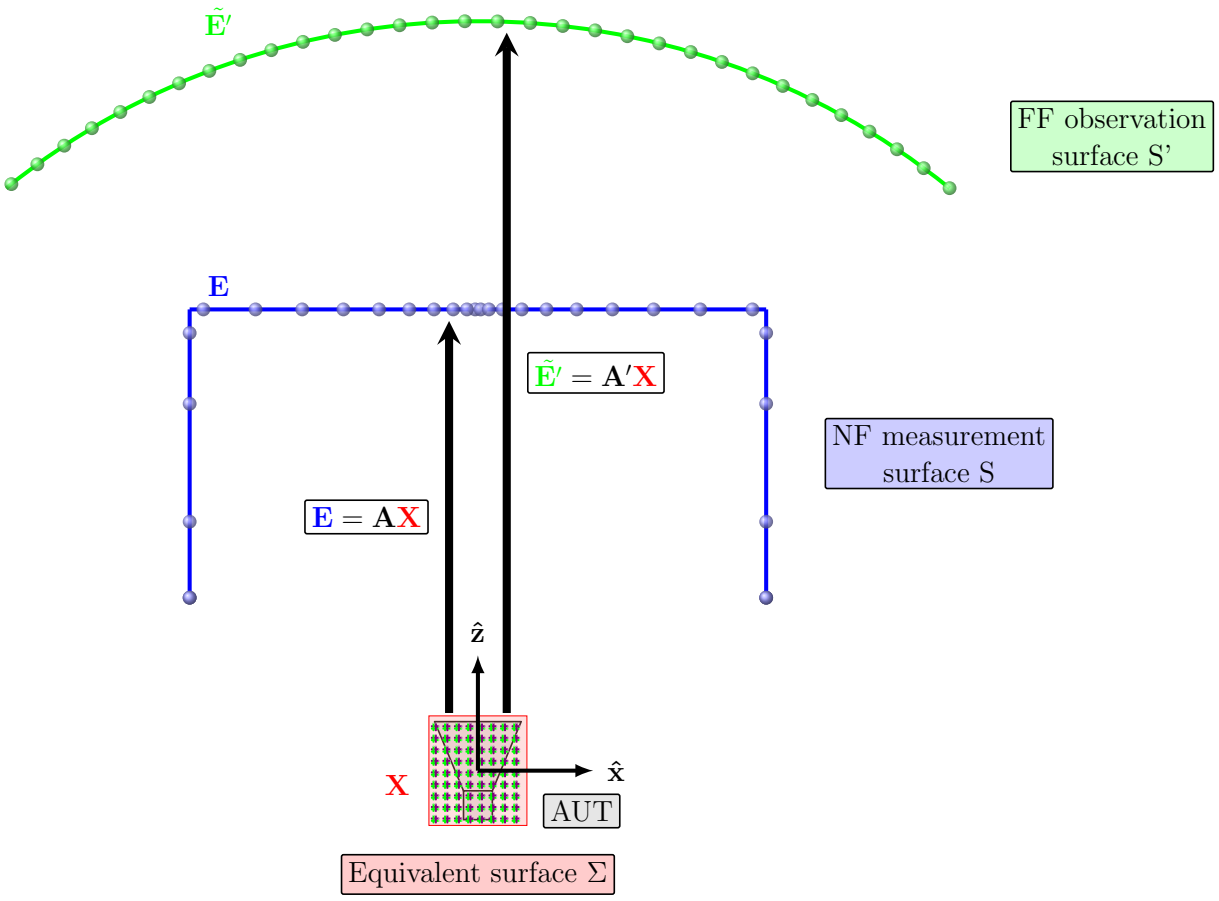

Figure II.11 – Matrices $\mathbf{A}$ and $\mathbf{A}'$ linking the equivalent surface Σ to the samples on the NF measurement surface S and to the observation positions on the FF observation surface S'.

$\mathbf{A}$, as exposed in Eq. (II.7). Then, the field $\tilde{\mathbf{E}}'$ radiated by those currents is derived on S' with $\mathbf{A}'$ from:

$$\tilde{\mathbf{E}}' = \mathbf{A}'\mathbf{X} \tag{II.9}$$

In classical PWE, regardless of the geometry of the NF measurement surface S, the core challenge lies in identifying an appropriate expansion basis for the NF data to enable a decomposition-based FF computation. In contrast, one of the methods applied in this work uses a procedure that first determines the equivalent currents on the equivalent surface Σ of the AUT. These currents are then employed to compute the FF.

II.3.b Determination of the equivalent currents

The characterization problem treated in this thesis involves using the measured NF data to retrieve the equivalent sources of the AUT responsible for generating the observed field. This process inverts the physical causality, in which sources produce fields. By invoking the principle of electromagnetic reciprocity, which allows sources and observation points to be interchanged, this inverse approach is justified. It forms the basis of the characterization methods developed in this thesis, referred to as the IP approach.

A representation of this IP method is given in Fig. II.12.

An accurate computed FF of the radiated field $\tilde{\mathbf{E}}'$ using the IP method relies on the precise estimate of the approximated equivalent currents $\mathbf{X}$ on the AUT, obtained by solving the linear system in Eq. (II.7). However, this IP is typically ill-posed in the sense defined by Hadamard [67], where a problem is considered well-posed only if its solution exists, is unique, and is stable with respect to small perturbations in the data.

In practice, the radiation matrix $\mathbf{A}$ is usually non-square, which leads to the system being either underdetermined or overdetermined, depending on the relative number of NF samples and infinitesimal dipoles. These two parameters corresponding to the amount of available data and the number of unknowns significantly influence the stability and solvability of the system.

Additionally, the discretization of the NF measurement surface S and the equivalent surface Σ, imposed by the finite acquisition zone and practical implementation constraints, introduces further challenges. This approximation can result in an ill-conditioned system, where small perturbations in the measured data can cause large deviations in the computed solution. Moreover, the spatial distributions of sampling points on the NF measurement surface S and of infinitesimal dipoles on the equivalent surface Σ can lead to high degrees of linear dependence among the columns of $\mathbf{A}$. As a result, the matrix may exhibit poor orthogonality properties, necessitating the use of regularization techniques to stabilize the inversion process and ensure a meaningful solution.

One widely used approach to address this issue is the least-squares method, which seeks to minimize the residual norm $\|\mathbf{AX} - \mathbf{E}\|_2$. This can be efficiently implemented using a Truncated Singular Value Decomposition (TSVD), where small singular values that contribute disproportionately to noise amplification are discarded. An exhaustive definition of a SVD will be discussed in the next chapter, but for now, the singular values can be defined as scalar quantities that indicate the strength or significance of each mode in the system. In computational environments such as MATLAB [68] or Python [69], this

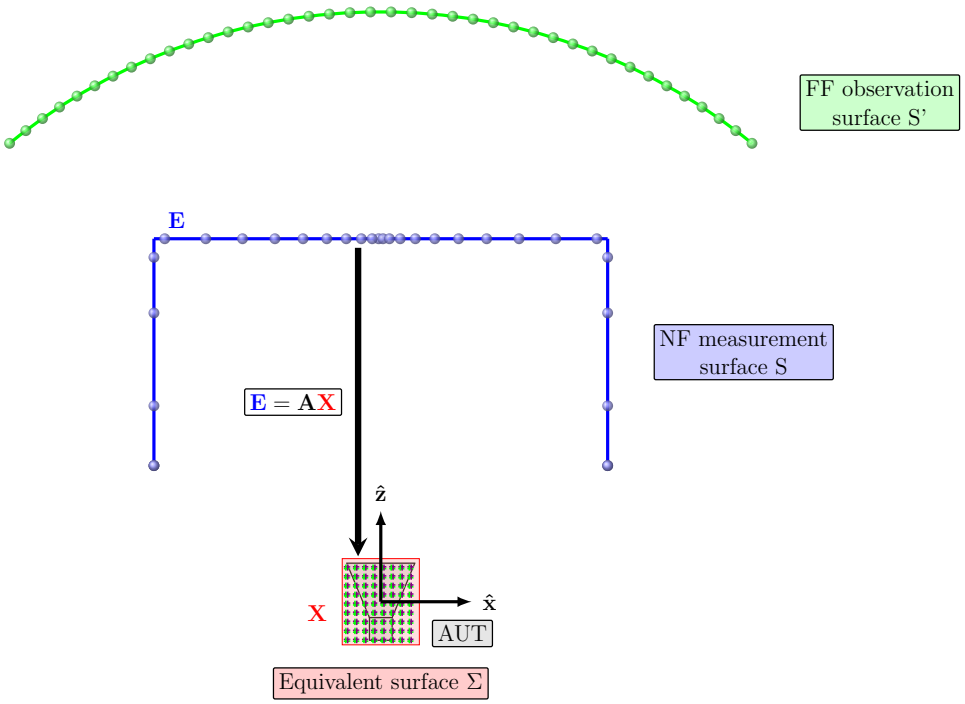

(a) Determination of the equivalent currents

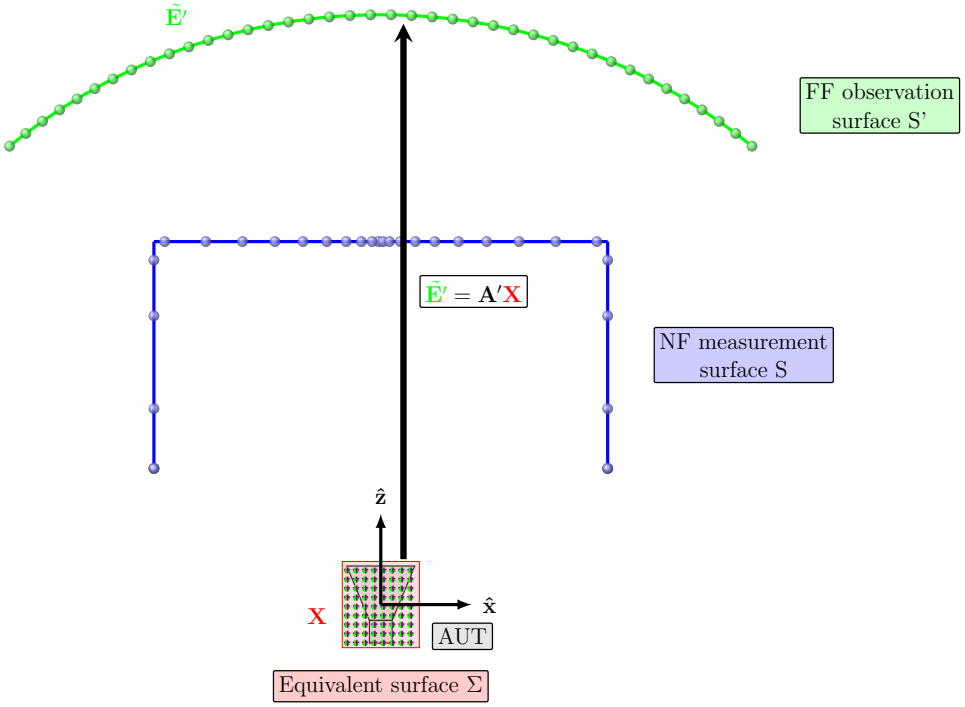

(b) FF computation

Figure II.12 – Steps of the IP resolution: the calculation of the equivalent currents (a) and the FF computation (b).

is achieved using a threshold parameter typically referred to as *rcond*. It is directly related to the conditioning of the problem, a concept implicitly connected to the notion of ill-posedness which can be quantified by the ratio between the largest and smallest singular values. Singular values smaller than *rcond* are considered numerically insignificant and are ignored in the inversion process. This acts as a regularization mechanism, effectively reducing the condition number of the problem and improving the stability of the solution at the cost of a slight loss in estimation fidelity.

The choice of *rcond* is a critical trade-off. If *rcond* is set too high, significant singular values may be discarded, leading to a loss of information and underfitting of the system, which reduces the accuracy of the computed fields. Conversely, if *rcond* is set too low, nearly all singular values including those dominated by noise are retained, which can result in unstable solutions and excessive amplification of measurement or computational errors, particularly in non-regularized problems. Therefore, *rcond* must be carefully selected to balance numerical robustness and solution accuracy. In practice, it is often tuned empirically or based on prior knowledge of the noise level in the data, ensuring that the estimated solution remains both stable and faithful to the underlying physical system.

To summarize before introducing validation cases, the IP method can be synthesized in a simple diagram represented in Fig. II.13.

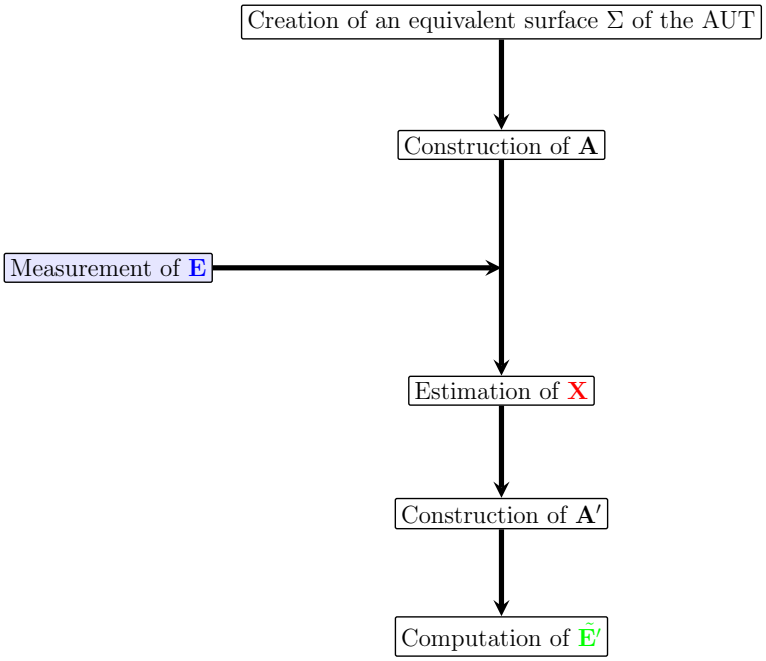

Figure II.13 – Schematic view of the different steps of the IP method.

II.3.c Validations: equivalent current determination

Before testing the IP method on characterization cases, it is necessary to validate the crucial step of determining the equivalent currents. First, this verification is performed using FF data to retrieve the currents flowing at the aperture of the antenna, a method known as Return on Aperture (RA). For highly regular cases, where the measurement data and system matrix are well-conditioned, the *rcond* parameter can be set relatively low, for example $rcond = 10^{-4}$, in order to retain as much information as possible from the problem. This ensures that all significant singular values are included in the inversion, maximizing estimation fidelity while still avoiding numerical instabilities associated with extremely small singular values. In a second step, the field radiated by the resulting currents is computed and compared to the FF reference data, as done in Section II.2.e. This time, both electric and magnetic dipoles are considered. These dipoles are tangentially oriented to the AUT aperture along the x- and y-axes, resulting in the formation of quadrupoles evenly distributed across the equivalent surface Σ. The presented error metrics have been computed using a reference-based normalization.

Theoretical uniform distribution aperture in free space

The first test is conducted on an analytical case involving a rectangular aperture supporting a uniform distribution in free space and operating at a frequency of 10 GHz. The equivalent surface Σ used is a plane of dimensions $5\lambda \times 4\lambda$ with a dipole spacing set to $\frac{\lambda}{4}$. Σ is located over the rectangular aperture of length $a = 3\lambda$ and width $b = 2\lambda$, as illustrated in Fig. II.14.

The theoretical formulas for the equivalent currents at the aperture are given in [5]:

$$\left.\begin{aligned} \mathbf{E}_a &= E_0\hat{\boldsymbol{y}} \\ \mathbf{H}_a &= -\frac{E_0}{\eta}\hat{\boldsymbol{x}} \end{aligned}\right\} \quad \begin{aligned} -\frac{a}{2} \leq x \leq \frac{a}{2} \\ -\frac{b}{2} \leq y \leq \frac{b}{2} \end{aligned}$$
$$\left.\begin{aligned} \mathbf{M} &= -\hat{\boldsymbol{n}} \times \mathbf{E}_a \\ \mathbf{J} &= \hat{\boldsymbol{n}} \times \mathbf{H}_a \\ \mathbf{M} &= \mathbf{J} = 0 \end{aligned}\right\} \quad \begin{aligned} -\frac{a}{2} \leq x \leq \frac{a}{2} \\ -\frac{b}{2} \leq y \leq \frac{b}{2} \\ \text{elsewhere} \end{aligned} \tag{II.10}$$

where $\hat{\boldsymbol{n}}$ is the unit vector normal to the aperture, i. e., $\hat{\boldsymbol{n}} = \hat{\boldsymbol{z}}$. The theoretical FF radiated by this aperture, which serves as the reference analytical FF data, is also defined:

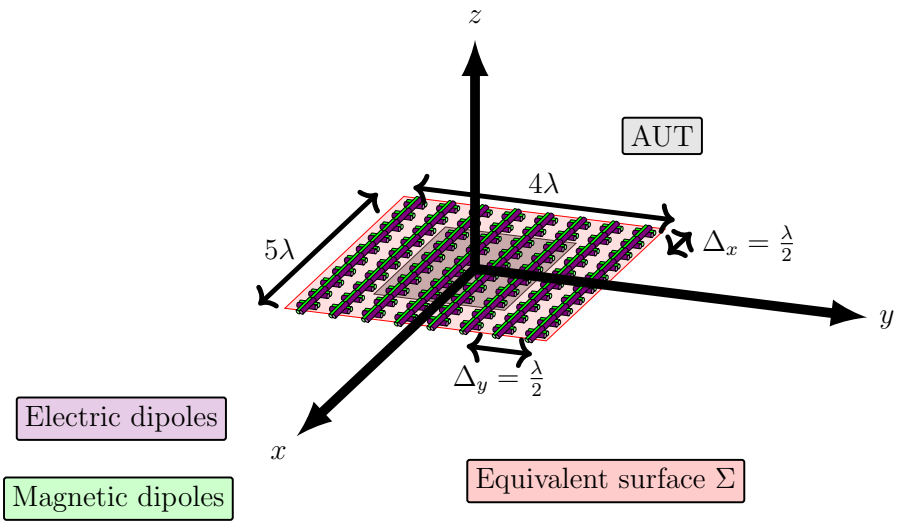

Figure II.14 – Uniform distribution aperture: illustration of the aperture in free space with the associated equivalent surface Σ.

$$
\begin{aligned}
W &= \frac{k_0 a}{2}\sin(\theta)\cos(\phi) \\
Y &= \frac{k_0 b}{2}\sin(\theta)\sin(\phi) \\
C &= j\frac{abk_0 E_0 \exp(-jk_0 r)}{2\pi r} \\
E_r &= 0 \\
E_\theta &= \frac{C}{2}\sin(\phi)(1+\cos(\theta))\frac{\sin(W)}{W}\frac{\sin(Y)}{Y} \\
E_\phi &= \frac{C}{2}\cos(\phi)(1+\cos(\theta))\frac{\sin(W)}{W}\frac{\sin(Y)}{Y}
\end{aligned}
\tag{II.11}
$$

$\mathbf{A}'$ matrix associated to the RA method is of dimensions 65520×1280. The number of dipoles is 1280 and the number of observation points is 32760. The retrieved equivalent currents are shown in Fig. II.15.

The results match the analytical behavior well: the solution yields dominant electric currents along the y-axis and magnetic currents along the x-axis. Furthermore, the expected uniform distribution only inside the aperture is correctly captured.

Radiation patterns for the two principal cut-planes, $\phi = 0°$ and $\phi = 90°$, are shown in Fig. II.16.

With an $ENL = -115.7\,\text{dB}$, the accuracy of the computed FF is sufficient to validate the current determination process before propagating the solution to the FF observation surface S'. In this case the computed FF errors can be attributed to two main factors. First,

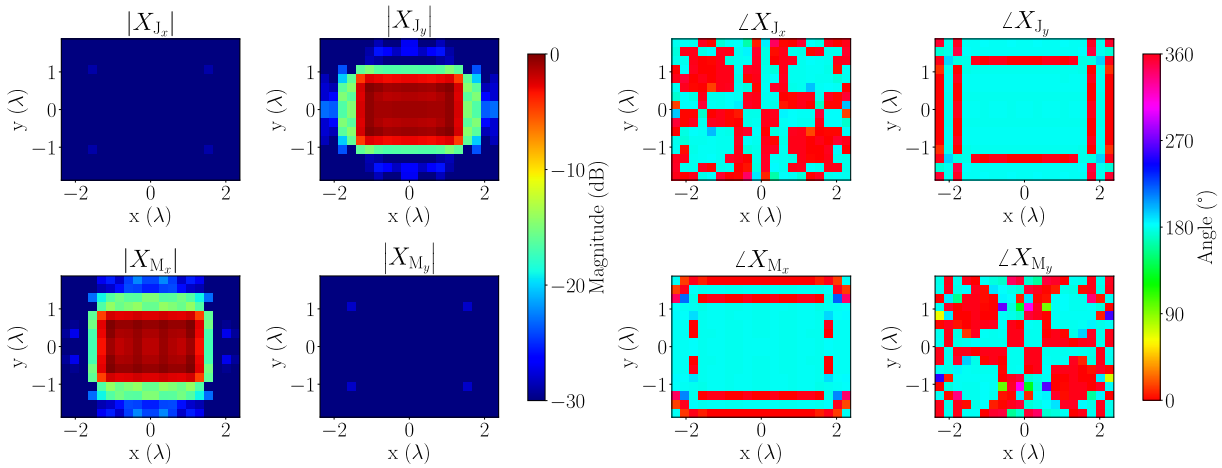

(a) Magnitude (b) Phase

Figure II.15 – Uniform distribution aperture: the magnitude (a) and the phase (b) of the estimated equivalent currents.

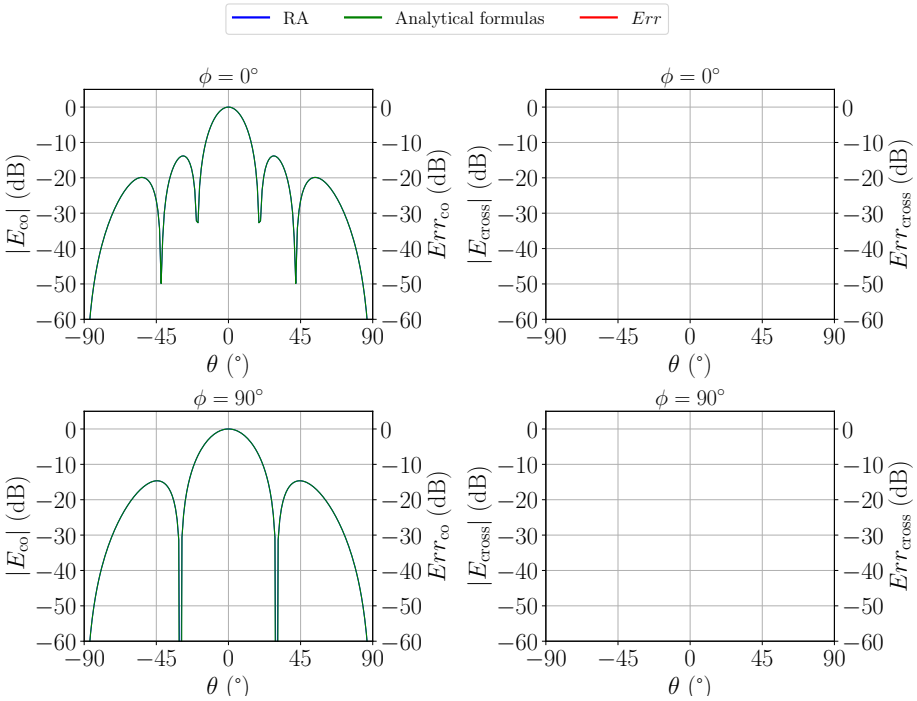

Figure II.16 – Uniform distribution aperture: comparison between the FF radiated by the equivalent currents obtained by RA method and the reference FF data from analytical formulas.

the least-squares method used to solve the system yields one possible solution among an infinite set, rather than a unique or exact one. This solution is particularly sensitive to the choice of the *rcond* parameter. Second, the computed equivalent currents are inherently

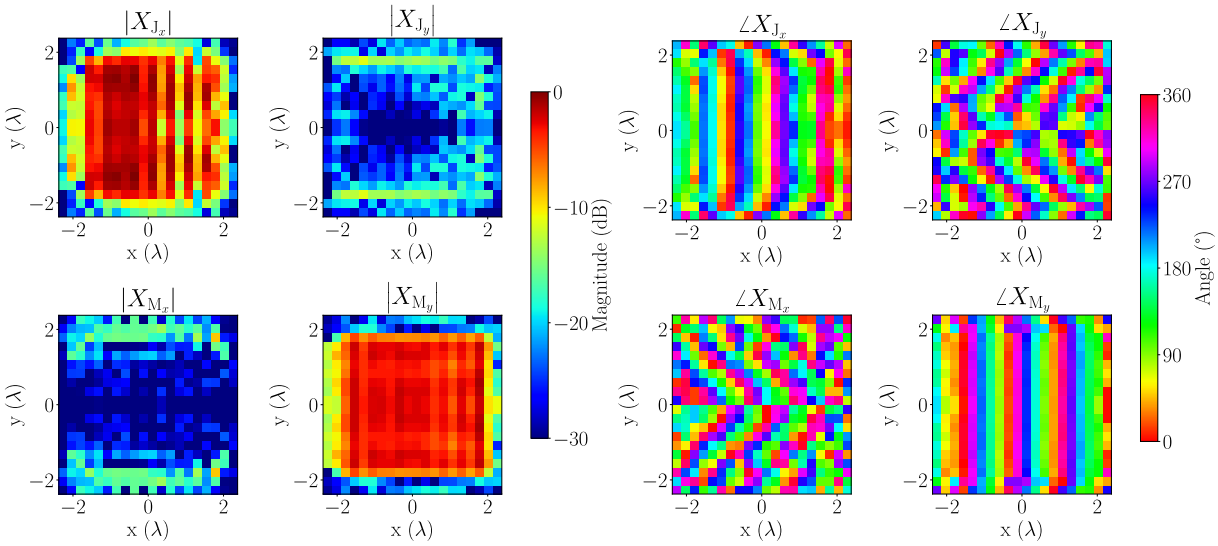

(a) Magnitude (b) Phase

Figure II.17 – Patch array 8×8: the magnitude (a) and the phase (b) of the estimated equivalent currents.

dependent on the discretization of the equivalent surface Σ, which significantly affects the accuracy and resolution of the computed FF.

Simulated 8×8 array of X-band patch antennas

Next, the same procedure is applied to an X-band 64-element patch array (detailed in Appendix A) operating at 9.7 GHz, simulated in CST. This new application case enables testing our model on a numerical benchmark, allowing for a direct comparison between the characterization results obtained using our approach and those produced by a commercial full-wave simulation tool. The array dimensions are $3.9\lambda \times 3.9\lambda \times 0.1\lambda$, with $\frac{\lambda}{2}$ spacing between the patches. The equivalent surface Σ is a plane of dimensions $5\lambda \times 5\lambda$ positioned at the antenna aperture, sampled with a regular step of $\frac{\lambda}{4}$. A phase law is applied to steer the beam towards $(\theta_{\text{beam}} = 50°, \phi_{\text{beam}} = 0°)$; the E-plane corresponds to the XOZ plane.

The equivalent currents retrieved with the matrix $\mathbf{A}'$ of dimensions 65520×1600 (1600 dipoles and 32760 observation points) are presented in Fig. II.17.

The estimated currents exhibit the expected behavior, with predominant electric currents along the x-axis and magnetic currents along the y-axis. It is worth noting that these equivalent currents differ from those obtained in the aperture case, making them less directly representative of the physical currents on the AUT. In particular, magnetic equivalent currents exhibit non-zero contributions for the patch array, despite the array

being nominally polarized along the x-axis, highlighting inherent differences in the IPs regarding regularity and dynamic range.

The resulting FF computation is shown in Fig. II.18 for $\phi = 0°$ and $\phi = 90°$.

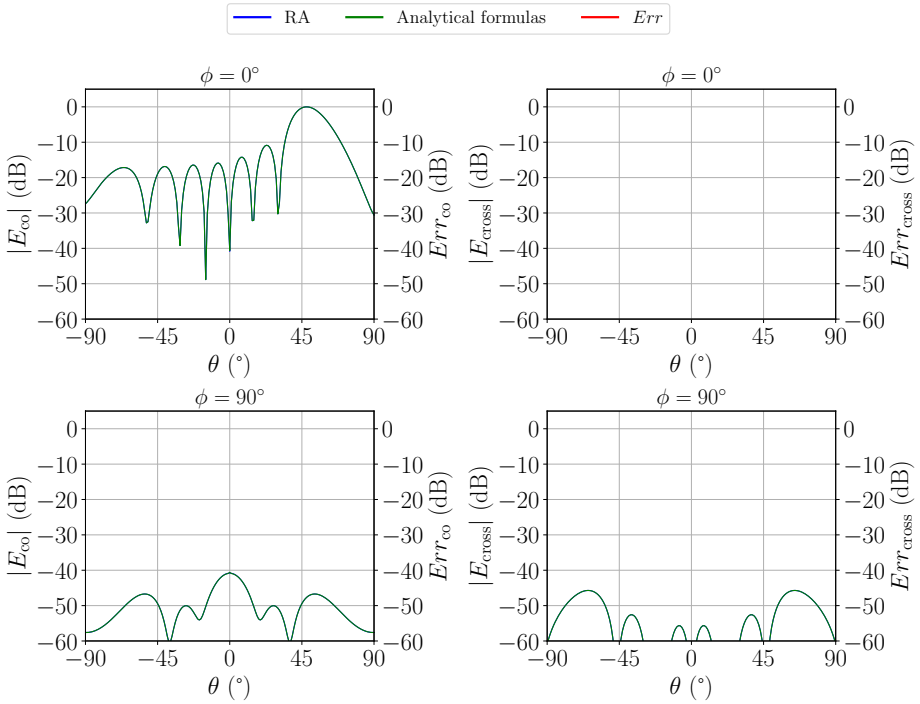

Figure II.18 – Patch array 8×8: comparison between the FF radiated by the equivalent currents obtained by RA method and the reference FF data from analytical formulas.

Once again, the quality of the FF computation with $ENL = -93.8\,\text{dB}$ validates the entire method chain before applying it to characterization scenarios.

II.3.d Application

Following the previous validations, it has been demonstrated that the construction of an equivalent model of the AUT using dipoles, the radiation from this model, and the retrieval of currents from FF data all operate correctly. Therefore, the IP characterization method can now be applied to a simulation example designed in CST. The following case reflects the AUT of interest: a highly directive planar array with strong beam steering and electrically large dimensions.

The selected antenna is a 60×1 patch array (Appendix A) operating in the X-band at 9.7 GHz. The array dimensions are $29.1\lambda \times 1.0\lambda \times 0.1\lambda$, with an inter-element spacing of $\frac{\lambda}{2}$. The equivalent model is a box-shaped equivalent surface Σ with dimensions $30\lambda \times 1\lambda \times 1\lambda$,

centered at the origin of the coordinate system, which corresponds to the antenna geometric center. Σ is discretized uniformly in all directions with a step size of $\frac{\lambda}{3}$, resulting in a total of 4392 dipoles. The regularization parameter is set to $rcond = 10^{-2}$. Both electric and magnetic dipoles are used with tangential orientations to the equivalent surface Σ. The main beam direction is set to $(\theta_{\text{beam}} = 0°, \phi_{\text{beam}} = 0°)$. Moreover, this AUT has a Half-Power Beam Width (HPBW) i. e. the width of the radiated FF beam at $-3\,\text{dB}$ of 1.5°. Therefore, the step of FF observation surface S' is set to $\Delta_\theta = \Delta_\phi = 0.5°$ to provide sufficient accuracy on the main lobe for the representations.

NF data are simulated on a $40\lambda \times 40\lambda$ planar surface S located at a distance of 8λ above the antenna, sampled with a step of $\frac{\lambda}{2}$. The corresponding number of measurement points is 6561. A visualization of the characterization configuration is shown in Fig. II.19, and the simulated NF data are presented in Fig. II.20.

The determination of the equivalent currents is achieved using the matrix $\mathbf{A}$ of dimensions 13122×4392. The resulting computed FF is displayed in the principal planes $\phi = 0°$ and $\phi = 90°$ in Fig. II.21. The error metrics refers to a normalization based on the reference simulated CST FF data.

The error metric $ENL = -54.4\,\text{dB}$ confirms the accuracy of the computed FF and validates the entire method functions before applying it to further characterization cases. However, this value remains higher than in previous validation cases, primarily due to the non-smooth nature of the radiated field, truncation effects introduced by the planar NF measurement surface S, and non-optimized resolution parameters.

The next step is to evaluate the regularization performance of the IP method compared with PWE in the presence of noise. Figure II.22 first presents the characterization achieved by PWE using noiseless NF data.

The ENL between the FF obtained using the PWE method and the reference simulated FF data from CST is computed as $-42.1\,\text{dB}$.

Subsequently, Gaussian white noise at a level of $-30\,\text{dB}$ is added to the NF data, and the resulting performance of both methods is compared. To observe the effects of the Gaussian noise on the accuracy, the parameters of the surfaces Σ, S and S' remain the same, and the regularization parameter is adjusted to $rcond = 10^{-1}$. A comparison of the FF computation using the proposed IP method and the classical PWE technique is shown in Fig. II.23 for the two main cut planes.

The error level of the IP method, with $ENL = -47.7\,\text{dB}$, is significantly lower than that of the PWE technique ($ENL = -36.8\,\text{dB}$). This highlights the robustness of the

regularized IP approach when dealing with noisy measurement data.

The benchmark of the proposed IP characterization method yields satisfactory results compared to the classical PWE for the simulation case considered. However, to fully understand the behavior and robustness of the method across various characterization

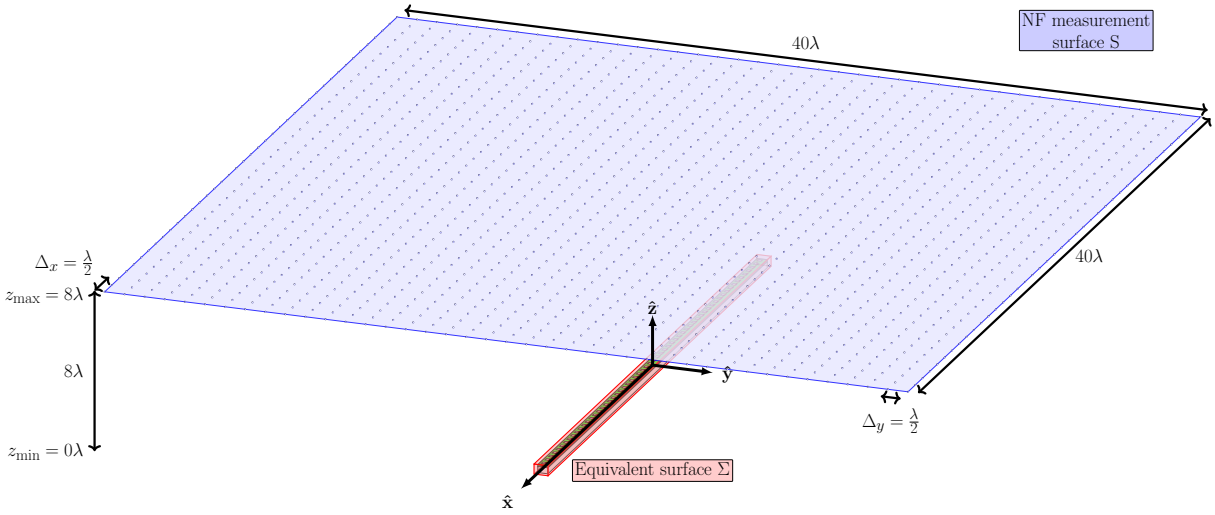

(a) 3D representation

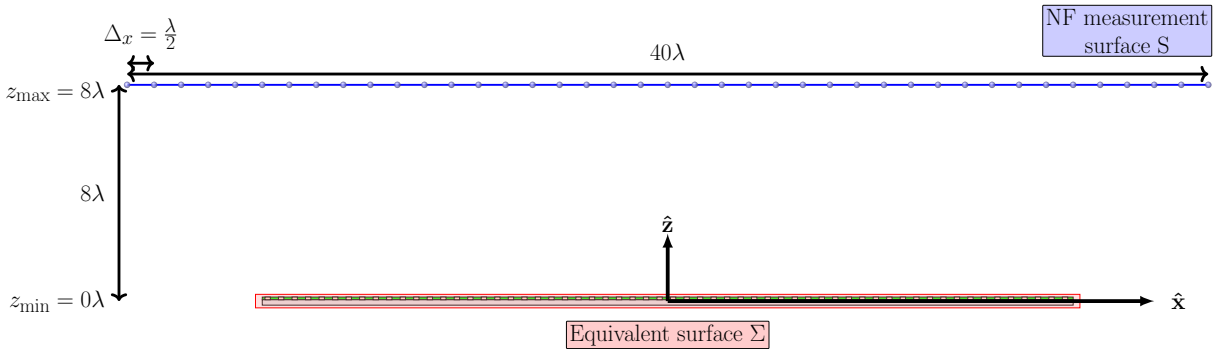

(b) 2D representation: XOZ plane

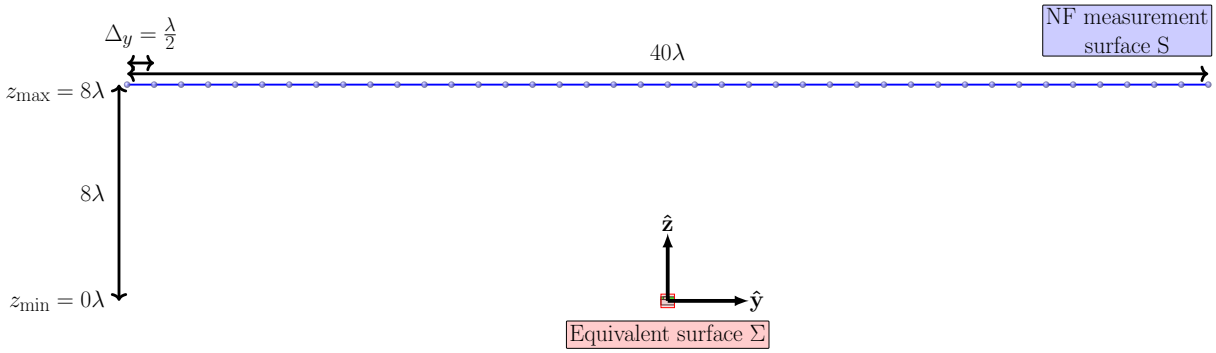

(c) 2D representation: YOZ plane

Figure II.19 – Patch array 60×1: characterization configuration.

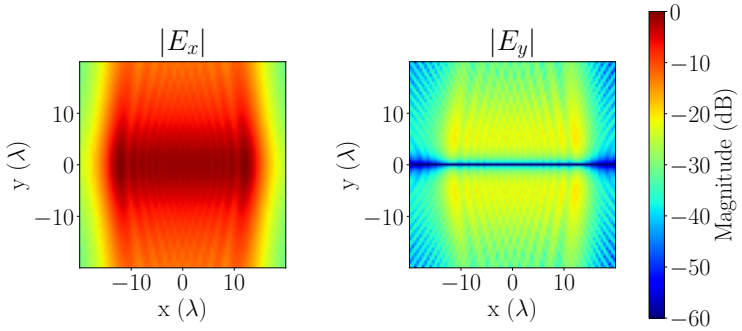

(a) Magnitude

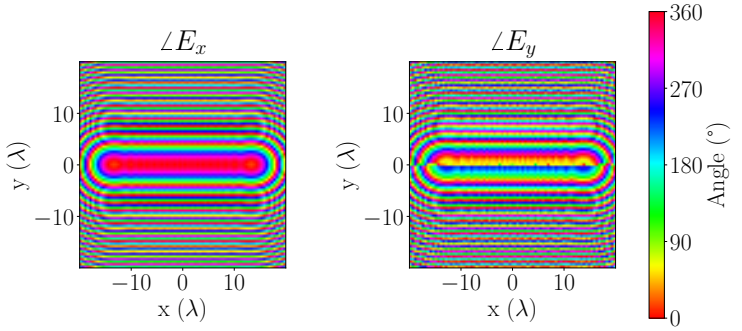

(b) Phase

Figure II.20 – Patch array 60×1: CST simulated NF data.

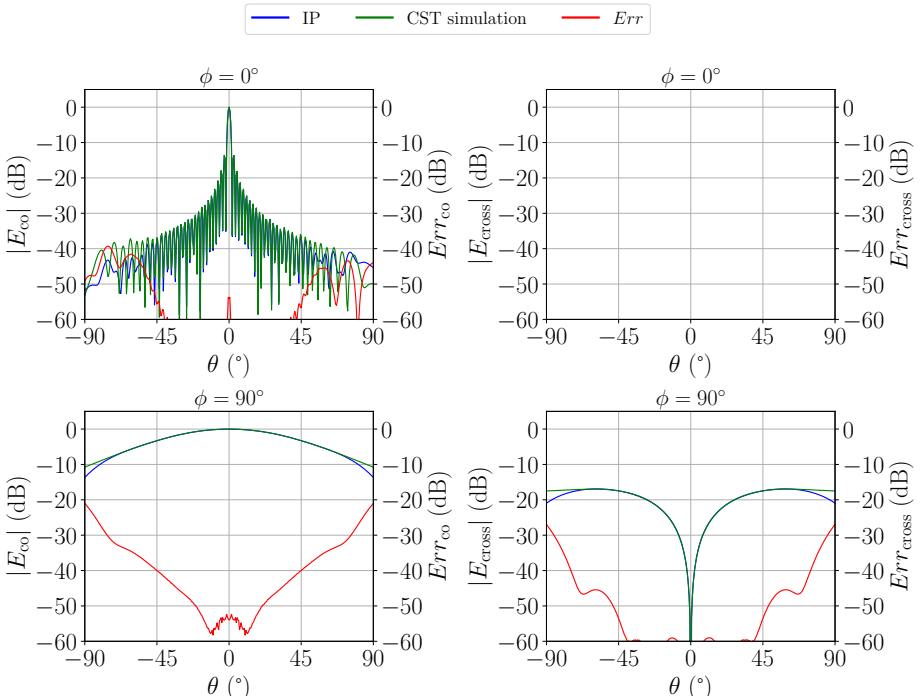

Figure II.21 – Patch array 60×1: comparison between the FF radiated by the equivalent surface Σ and the reference simulated FF data from CST.

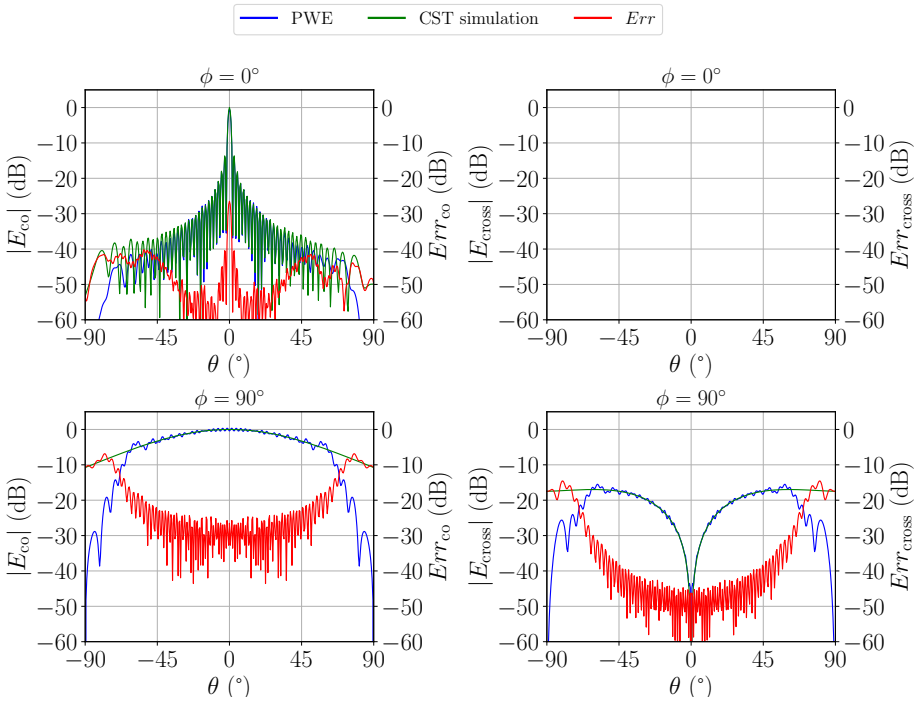

Figure II.22 – Patch array 60 × 1: comparison between the FF computed by PWE and the reference simulated FF data from CST.

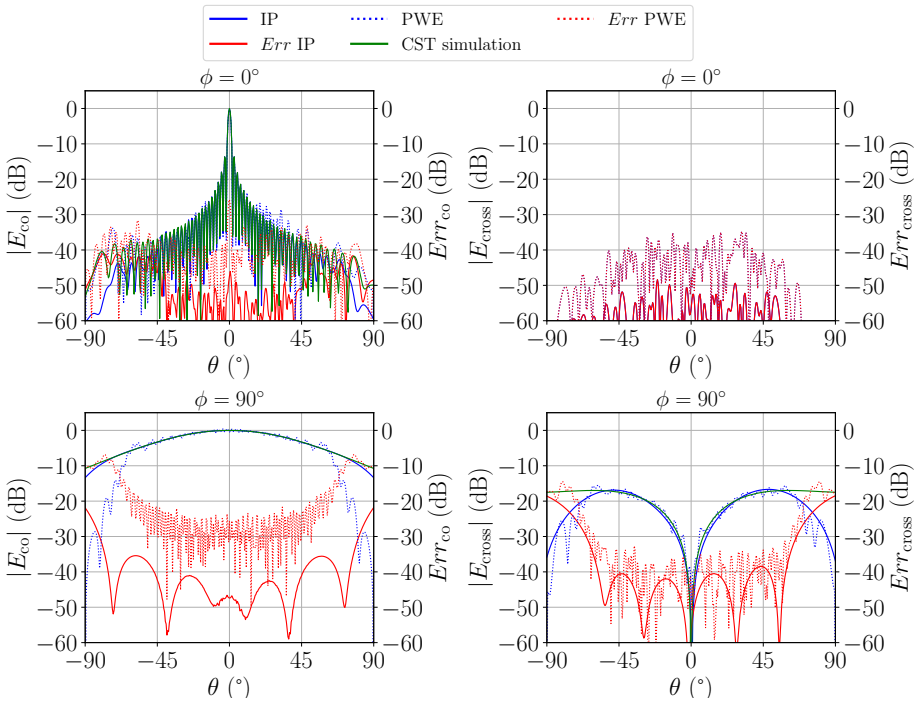

Figure II.23 – Patch array 60 × 1: comparison of computed FF using IP method and classical PWE in noisy conditions with the reference simulated FF data from CST.

scenarios, a sensitivity analysis must be conducted on the multiple influencing parameters before transitioning to experimental cases.

II.4 Parametric study of the model

To analyze the influence of various parameters on the computed FF accuracy, a parametric study is performed on the developed equivalent model. Given the complexity introduced by the high dimensionality of the parameter space, a partial factor analysis approach is adopted. The definition parameters of the dipole distribution on the equivalent surface Σ are varied independently, while the parameters of the NF measurement surface S are held fixed. This allows for the identification of general trends in model behavior without exhaustive analysis of the entire parameter space. The specific case presented below serves to highlight key guidelines for the effective use of the model. While this example is illustrative, it reflects trends that have been consistently observed across a wide range of scenarios and antenna types. Finally, a more detailed investigation of the influence of the NF measurement surface S and associated truncation effects is deferred to the next section.

II.4.a Methodology

The AUT used throughout this study is the X-band 8×8 patch array (Appendix A) introduced previously in Section II.3.d. To recall, the array has physical dimensions of $3.9\lambda \times 3.9\lambda \times 0.1\lambda$ and its main beam is directed toward $(\theta_{\text{beam}} = 0°, \phi_{\text{beam}} = 0°)$. For this analysis, the resolution of the FF observation surface S' is relaxed to $\Delta_\theta = \Delta_\phi = 1.5°$ in order to reduce the size of the radiation matrices and lower overall computational burden. Indeed, for a step of 1.5° the number of rows for the matrix $\mathbf{A}'$ is lowered down to 29280 compared to the 65520 rows for a discretization of 1°. The NF measurement surfaces S are defined with a sufficiently high resolution, as detailed in the following section, to ensure that they do not introduce any bias into the results. This allows the analysis to focus exclusively on the influence of the dipole distribution parameters on the equivalent surface Σ. The objective is not to identify an optimal parameter set but to reveal robust trends that inform parameter selection in more general settings. The metric used to assess of the accuracy of the computed radiation pattern is the ENL metric normalized relative to the FF reference from CST.

In all test cases, the three Cartesian field components are obtained through simulation and then fed into the IP. Furthermore, the *rcond* regularization parameter of the least-squares method is set to 10^{-2}, justified by the well-conditioned nature of the radiation matrices in these scenarios.

Equivalent dipole distribution parameters

The parametric study evaluates the impact of the following variables, depending on the geometry used for the equivalent surface Σ.

1. Planar equivalent surface Σ:
   - dipole orientations: tangential to the planar surface, or all three ($\hat{\boldsymbol{x}}$, $\hat{\boldsymbol{y}}$, $\hat{\boldsymbol{z}}$);
   - dimensions: $3\lambda \times 3\lambda$, $5\lambda \times 5\lambda$, or $10\lambda \times 10\lambda$;
   - discretization step: λ or $\frac{\lambda}{2}$ or $\frac{\lambda}{3}$ or $\frac{\lambda}{4}$ or $\frac{\lambda}{5}$;
   - position along z-axis: shift of 0λ or $\frac{\lambda}{2}$ from the AUT aperture.
2. Box-shaped equivalent surface Σ:
   - dipole orientations: tangential to the box surface, or all three directions $\hat{\boldsymbol{x}}$, $\hat{\boldsymbol{y}}$, $\hat{\boldsymbol{z}}$;
   - dimensions: $3\lambda \times 3\lambda \times 1\lambda$, $5\lambda \times 5\lambda \times 1\lambda$, or $10\lambda \times 10\lambda \times 2\lambda$;
   - discretization step: λ or $\frac{\lambda}{2}$ or $\frac{\lambda}{3}$ or $\frac{\lambda}{4}$ or $\frac{\lambda}{5}$.

Near-field measurement surfaces S

Two NF measurement surfaces S are used, both designed to avoid introducing bias in the parametric study by ensuring complete coverage and sufficient sampling.

1. Spherical NF measurement surface S:

   this surface follows the SWE Nyquist criterion, which determines the minimum number of required points for accurate field computation [70, 14]:

$$\begin{aligned} P &= \lfloor k_0 a \rfloor + n_0 \\ N_{\mathrm{SWE}} &= 2(2P+1)(P+1) \end{aligned} \tag{II.12}$$

   where a is the radius of the smallest sphere enclosing the AUT, and n_0 is a safety margin (typically 10) used to mitigate truncation errors. $\lfloor \cdot \rfloor$ is an operator to round a number down to the nearest integer. For the array under test, this yields $N_{\mathrm{SWE}} =$

4050 as the minimum number of required points. Thus, an equiangular grid with a step of 4° is adopted.

2. Box NF measurement surface S:

   a box of dimensions $20\lambda \times 20\lambda \times 20\lambda$ is used, with a uniform sampling step of $\frac{\lambda}{4}$. The minimal distance from the AUT center to the box is 20λ. A quick trigonometric check yields a maximum angular increment of $\theta = \arctan\left(\frac{0.25\lambda}{10\lambda}\right) \approx 1.4°$, which is smaller than the resolution (1.5°) of the FF observation surface S', confirming that the discretization is sufficiently fine.

II.4.b Planar equivalent surface Σ

Spherical measurement surface S

For this part, the NF measurement surface S is a sphere. The results for this configuration are presented in Figs. II.24 and II.25, for tangential dipole orientations on Σ or aligned along the three directions $\hat{\boldsymbol{x}}$, $\hat{\boldsymbol{y}}$ and $\hat{\boldsymbol{z}}$, respectively.

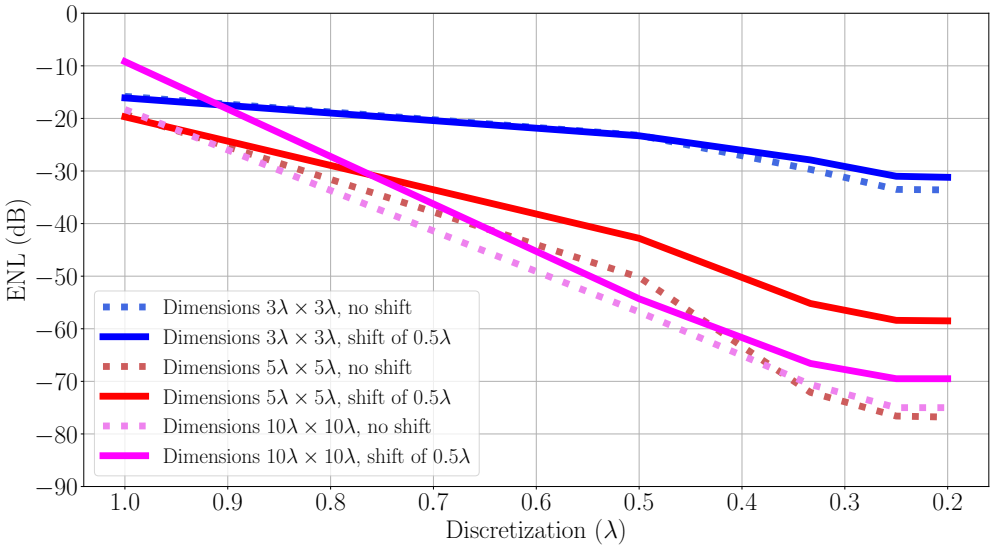

Figure II.24 – Planar Σ with dipole orientations tangent and a spherical S: computed FF accuracy through three different dimensions of Σ and two shifts along the z-axis from the AUT aperture.

A discretization step of $\frac{\lambda}{4}$ consistently yields the most accurate FF computations across all configurations. Using three orthogonal dipole orientations gives slightly better results than purely tangential dipoles, although the difference is minor. Correct FF computation is achieved when the equivalent surface Σ is positioned directly at the antenna aperture

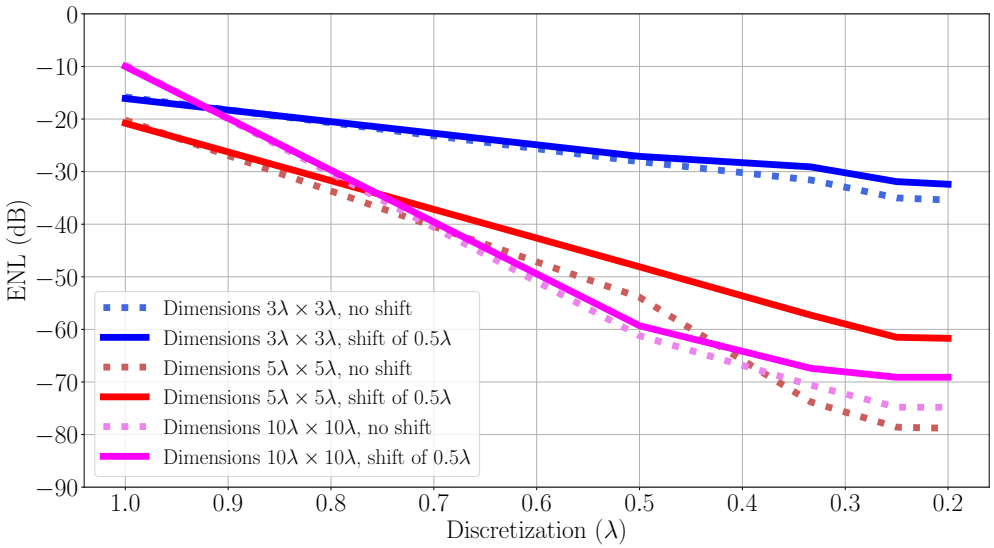

Figure II.25 – Planar Σ with dipole orientations $\hat{\boldsymbol{x}}$, $\hat{\boldsymbol{y}}$, $\hat{\boldsymbol{z}}$ and a spherical S: computed FF accuracy through three different dimensions of Σ and two shifts along the z-axis from the AUT aperture.

along the z-axis, and when its dimensions slightly exceed the physical size of the AUT. An oversized Σ offers additional improvements in precision, but this must be balanced against the increased number of dipoles and, consequently, the higher problem complexity. For example, with a step of $\frac{\lambda}{4}$, a $5\lambda \times 5\lambda$ surface requires 1600 dipoles, compared to 6400 dipoles for a $10\lambda \times 10\lambda$ surface, representing a factor of 4.

Box-shaped measurement surface S

In this configuration, the NF measurement surface S is now also box-shaped. The results for this setup are presented in Figs. II.26 and II.27, depending on whether the dipole orientations on the equivalent surface are tangential to Σ or aligned with the three directions $\hat{\boldsymbol{x}}$, $\hat{\boldsymbol{y}}$ and $\hat{\boldsymbol{z}}$, respectively.

This study confirms some, but not all, of the trends observed for the spherical case. Again, the best accuracy is reached with a dipole spacing of $\frac{\lambda}{4}$. Positioning Σ at the aperture along the z-axis remains optimal. However, in this case, dipole orientations tangential to Σ are sufficient for accurate FF computation, adding the normal components does not significantly improve results. Moreover, choosing dimensions of Σ larger than the aperture is a good criterion for achieving accurate characterization, and here again, using a very large Σ brings more accurate results. However, the gain in precision must be analyzed with respect to the increase in numerical complexity.

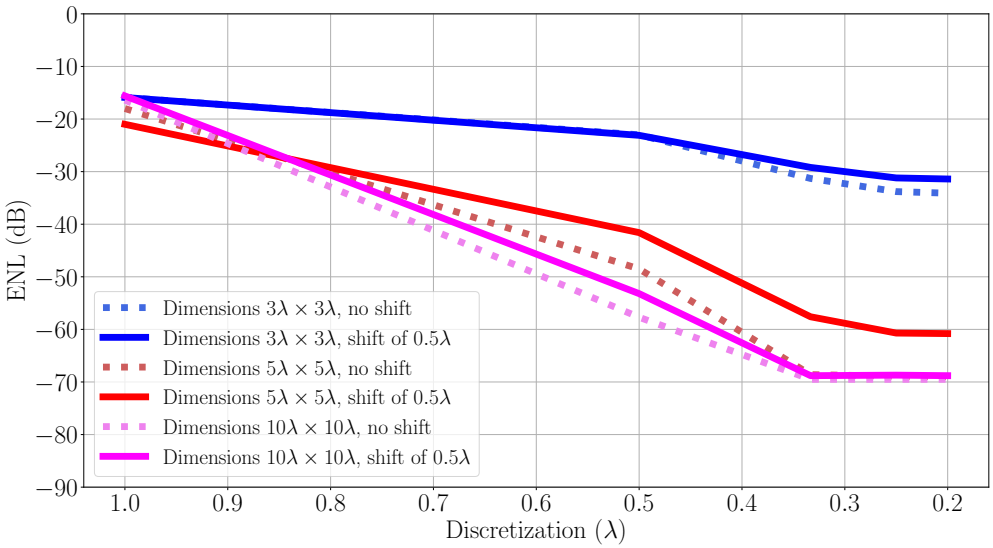

Figure II.26 – Planar Σ with dipole orientations tangent and a box-shaped NF measurement surface S: computed FF accuracy through three different dimensions of Σ and two shifts along the z-axis from the AUT aperture.

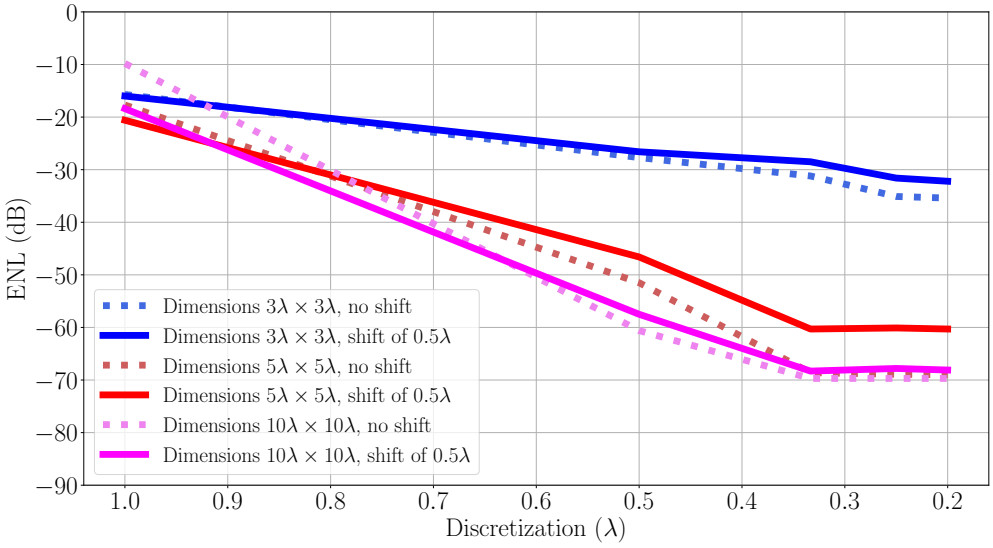

Figure II.27 – Planar Σ with dipole orientations $\hat{\boldsymbol{x}}$, $\hat{\boldsymbol{y}}$, $\hat{\boldsymbol{z}}$ and a box-shaped NF measurement surface S: computed FF accuracy through three different dimensions of Σ and two shifts along the z-axis from the AUT aperture.

Summary

For both spherical and box-shaped NF measurement surfaces S, a dipole spacing of $\frac{\lambda}{4}$ provides a robust trade-off between accuracy and computational cost. Positioning the equivalent surface Σ directly at the antenna aperture along the z-axis appears to improve

precision, but this must be qualified, as it is clearly evident only for the $5\lambda \times 5\lambda$ surface. This observation should also be considered in relation to the choice of the *rcond* value, which can affect numerical stability and degrade ENL values for a shifted $5\lambda \times 5\lambda$ surface along the z-axis. However, in all tested cases, it is essential that the equivalent surface Σ exceed the physical dimensions of the AUT.

While using three orthogonal dipole orientations yields marginally better accuracy in the spherical case, tangential orientations alone are generally sufficient. For example, with a $5\lambda \times 5\lambda$ Σ, the error difference between both configurations is of 2 dB for an already very low ENL (≤ -75 dB), making the impact negligible. This difference may result from numerical artifacts, confirming that tangential dipoles are sufficient for building a reliable equivalent model.

II.4.c Box-shaped equivalent surface Σ

Spherical measurement surface S

The study now focuses on a box-shaped equivalent surface Σ, while the NF measurement surface S remains spherical. Results are presented in Fig. II.28, for the two cases where the dipoles are oriented either tangentially to the surface Σ or along the three directions $\hat{\boldsymbol{x}}$, $\hat{\boldsymbol{y}}$ and $\hat{\boldsymbol{z}}$, respectively.

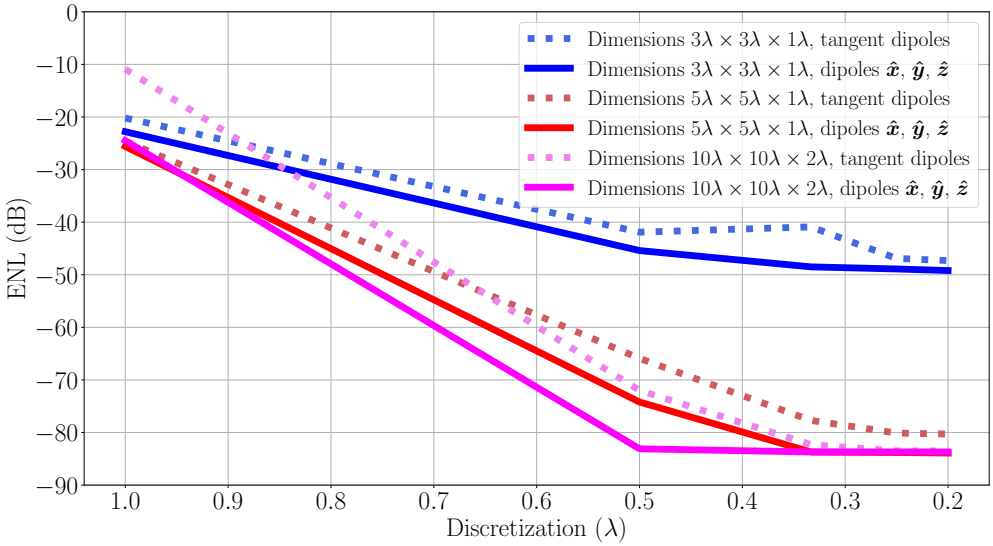

Figure II.28 – Box-shaped Σ and a spherical S: computed FF accuracy through three different dimensions of Σ and two dipole orientations.

As with the planar case, a discretization of $\frac{\lambda}{4}$ leads to the best accuracy. Cartesian orientations ($\hat{\boldsymbol{x}}$, $\hat{\boldsymbol{y}}$, $\hat{\boldsymbol{z}}$) offer slightly better precision than tangential orientations. Additionally, Σ must fully enclose the AUT. Then, a deeper analysis of the figure shows that tangential dipoles appear more sensitive to the dimensions of Σ than the Cartesian orientations. Here again, this conclusion may be influenced by numerical behavior related to the problem regularization.

Box-shaped measurement surface S

In this configuration, both the equivalent surface Σ and the NF measurement surface S are box-shaped. Results are again shown in Fig. II.29, distinguishing the cases of tangential dipole orientations and full Cartesian orientations on Σ.

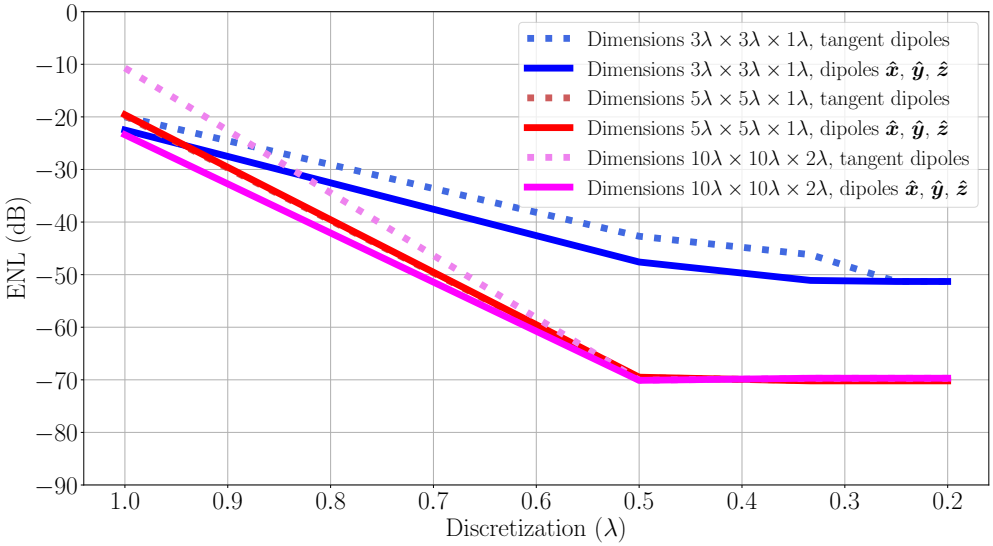

Figure II.29 – Box-shaped Σ and a box-shaped NF measurement surface S: computed FF accuracy through three different dimensions of Σ and two dipole orientations.

Several key guidelines emerge from the analysis of the box-shaped equivalent surface Σ with a box-shaped S. First, dipoles oriented tangentially to Σ are sufficient to obtain accurate computed FF, making the use of full Cartesian orientations optional. Then, the equivalent surface Σ must enclose the AUT to capture the radiated field correctly. However, the best results are obtained when Σ is tightly fitted around the AUT physical dimensions. Finally, a discretization step of $\frac{\lambda}{3}$ offers a good trade-off between computed FF accuracy and computational cost.

Summary

When a box-shaped equivalent surface Σ is used, the following key points can be established. Accurate characterization is achieved when Σ closely conforms to the AUT geometry and the dipole spacing is set to $\frac{\lambda}{3}$. Indeed, again in the case of a spherical S, the difference between the errors for a spacing of $\frac{\lambda}{3}$ and $\frac{\lambda}{4}$ can be considered negligible. Besides, dipoles oriented tangentially to the equivalent surface Σ are sufficient and including normal components provides only marginal improvements.

II.4.d Conclusion on the observations

From the parametric analysis of the equivalent surface Σ applied to the characterization of a 8×8 X-band patch array (Appendix A), several global trends can be highlighted.

1. Planar equivalent surface Σ:
    - incorporating the dipole component normal to Σ does not significantly affect the computed FF accuracy;
    - accurate results are obtained when: the dimensions exceed the AUT aperture, dipole spacing is set to $\frac{\lambda}{4}$;
    - however, for the tested positions of the equivalent surface Σ with respect to the AUT aperture, no clear conclusion can be drawn.
2. Box-shaped equivalent surface Σ:
    - similar conclusions apply regarding dipole orientation and the dimensions of Σ;
    - a discretization of $\frac{\lambda}{3}$ is sufficient to capture the equivalent currents while keeping the number of unknowns manageable;
    - the global accuracy is slightly better than for the planar Σ.

These results provide practical guidelines for selecting configurations and discretization strategies for the equivalent surface Σ when applying the developed method to more complex or real-world antenna systems. However, although the characterization precision is presented for this specific application case, the trends have been verified during the thesis on various antennas types. For instance, a box-shaped equivalent surface Σ, which strictly satisfies the Huygens principle, will be used to achieve the most accurate characterization possible. In contrast, a planar Σ can be employed to reduce the complexity of the problem, making it suitable for studying the convergence behavior of the method.

Finally, it is important to note that this study applies to antennas with dimensions larger than λ. For smaller antennas, the discretization margins evaluated here are no longer effective and must be adjusted accordingly.

II.5 Near-field measurement surface S and truncation effects

This section analyzes the impact of the geometry of the NF measurement surface S on the accuracy of the FF computation. The study is conducted using the X-band 60×1 patch array (Appendix A) introduced in Section II.3.d. Two beam directions are considered: a boresight configuration with ($\theta_{\text{beam}} = 0°, \phi_{\text{beam}} = 0°$), and a steered beam at ($\theta_{\text{beam}} = 80°, \phi_{\text{beam}} = 0°$). This antenna has been chosen over the 8×8 array due to its higher directivity and narrower HPBW, making it a more challenging and insightful test case for evaluating truncation effects. Indeed, due to the beam steering capability of the considered patch array, the truncation induced by a classical planar measurement surface S implies that only a portion of the total radiated NF is captured. Consequently, the computation of the FF radiation pattern can be negatively affected.

As with the previous analysis on the behavior of the equivalent model, it is important to emphasize that this parametric study serves as an illustrative case. The objective here is to identify general trends, which have been consistently observed across all antenna characterization setups evaluated throughout the thesis.

To manage computational cost, the resolution of the FF observation surface S' is set to $\Delta_\theta = \Delta_\phi = 1°$, except for radiation pattern plots, which use $\Delta_\theta = \Delta_\phi = 0.5°$. The equivalent model employs a planar distribution of tangential dipoles over a $30\lambda \times 1\lambda$ area with $\frac{\lambda}{4}$ spacing. The inversion regularization parameter is set to $rcond = 10^{-2}$. The computed FF accuracy is assessed using the ENL metric, normalized relative to the CST FF reference.

Additionally, to better evaluate the computed FF accuracy in relation to the extent and geometry for the NF measurement surface S, we define new computed FF zones independently of the AUT aperture. This enables us to observe the effects of non-conventional sampling on truncation phenomena which are inherent to the equivalent surface Σ.

II.5.a Computed far-field zones

To correctly analyze how the geometry of the NF measurement surface S affects the FF computation, specific computed FF zones must be defined with respect to the spatial distribution of dipoles on the equivalent surface Σ. Unlike the PWE approach, which defines validity zones solely from the AUT aperture and the measurement plane S dimensions, our model radiates FF from the equivalent surface Σ through a radiation matrix. This shifts the reference for defining the maximal validity angles from the external dimensions of the AUT to those of its equivalent surface Σ, thereby redefining the conditions under which accurate FF computations can be ensured.

In a traditional planar setup, a validity zone is defined as the angular region within which the AUT radiation is accurately computed. This region is determined by the dimensions of both the AUT and the NF measurement surface S, and their separation distance. Outside this region, truncation effects dominate, and reliable characterization becomes impossible.

In contrast, our model allows computed FF zones to be defined directly from the geometry of Σ, the NF measurement surface S, and the FF observation surface S', as illustrated in Fig. II.30.

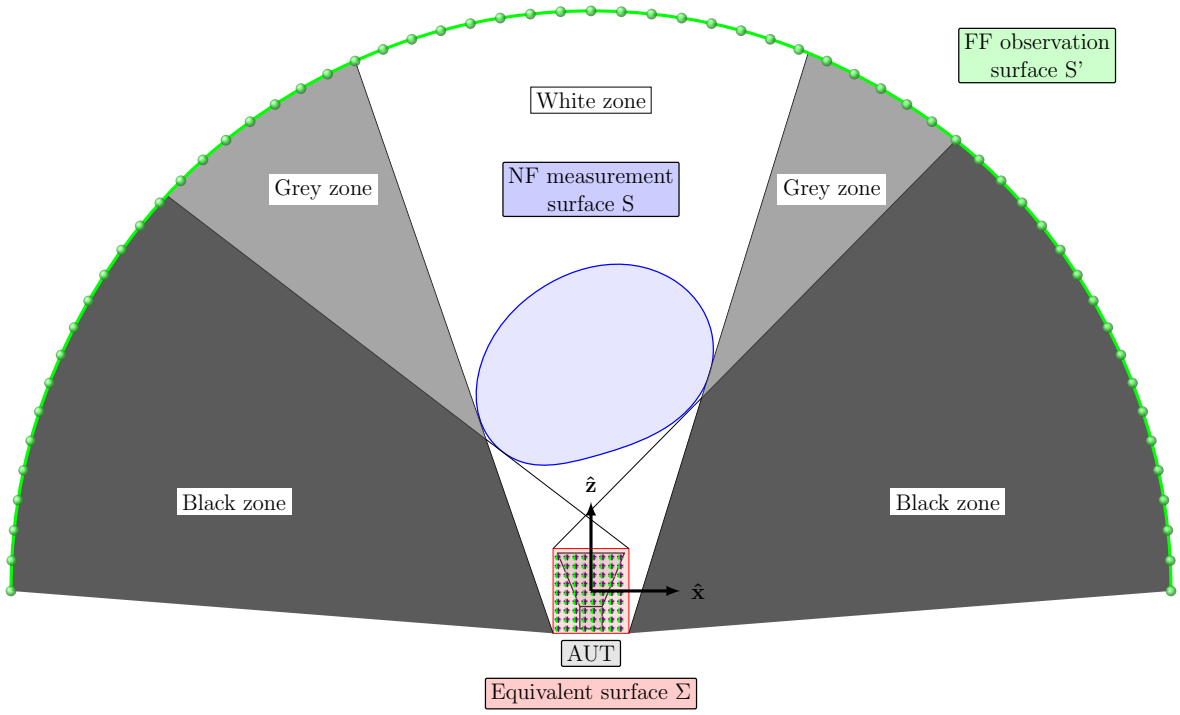

Figure II.30 – Definition of computed FF zones associated with the equivalent surface Σ and any NF measurement surface S.

We define three angular regions:

- White Zone (WZ): region within the angular span jointly defined by the boundaries of Σ and S. Computed FF in this zone is expected to be accurate;
- Gray Zone (GZ): partially informed region where only partial NF data contributes to the FF computation;
- Black Zone (BZ): region with no NF contribution from S, hence highly prone to truncation errors.

To quantify computed FF accuracy in each region, the ENL metric is computed separately as ENL_{WZ}, ENL_{GZ}, and ENL_{BZ}, respectively. Each ENL is defined as the mean error over its respective zone, normalized by the peak amplitude over the entire FF observation surface S' (reference or computed). Thus, for example, the formula for the ENL computed in the WZ is defined as:

$$ENL_{\mathrm{WZ}} = 20\log_{10}\sum_{i=1}^{N}\frac{\sqrt{|\tilde{a}_{i,\theta,\mathrm{WZ}} - a_{i,\theta,\mathrm{WZ}}|^2 + |\tilde{a}_{i,\phi,\mathrm{WZ}} - a_{i,\phi,\mathrm{WZ}}|^2}}{N\max\limits_{i\leq N}\|\mathbf{a}_i\|_2} \tag{II.13}$$

$\tilde{\mathbf{a}}$ and $\mathbf{a}$ denote, respectively, the computed and the reference FF, both defined on each point i among the N points distributed on the observation surface S'. $a_{i,\theta,\mathrm{WZ}}$ and $a_{i,\phi,\mathrm{WZ}}$ are the vector of the θ- and ϕ-component of the reference field given in the WZ, respectively.

II.5.b Methodology

To evaluate how the geometry and parameters of the NF measurement surface S influence the accuracy of the computed FF, several configurations are tested. Two types of NF measurement surfaces S are considered.

1. Planar NF measurement surface S:
    - measured components: E_x, E_y (components tangential to S), or all components E_x, E_y, and E_z (full Cartesian);
    - dimensions: $40\lambda \times 40\lambda$ or $50\lambda \times 50\lambda$;
    - discretization: λ or $\frac{\lambda}{2}$ or $\frac{\lambda}{4}$;
    - distance from AUT (along z-axis): 5λ or 8λ.
2. Half-box-shaped NF measurement surface S:

- measured components: E_x, E_y; tangential to S; or full Cartesian components E_x, E_y, E_z;
- dimensions: $40\lambda \times 40\lambda \times 5\lambda$ or $50\lambda \times 50\lambda \times 5\lambda$;
- discretization: λ or $\frac{\lambda}{2}$ or $\frac{\lambda}{4}$;
- upper plane distance from AUT (along z-axis): 5λ or 8λ.

The distance from AUT to the planar NF measurement surfaces S is selected in accordance with IEEE standards [32], ensuring that the NF measurements are performed within the Fresnel zone. Furthermore, the chosen values for dimensions and sampling steps are based on the demonstrative analysis presented in this section, which relies on a series of representative and illustrative test cases.

The half-box NF measurement surface S is systematically compared to a planar S positioned at the same distance from the AUT and sharing identical top-plane dimensions. This setup ensures that the observed differences in computed FF accuracy are directly attributable to the geometry of the NF measurement surface S. Such a comparison is especially relevant in scenarios involving beam steering, where truncation effects become more severe and their influence on the different computed FF zones defined with respect to the planar NF measurement surface S becomes more evident.

From an IP perspective, extending the measurement surface to include lateral faces provides additional independent field information that improves the conditioning of the radiation operator linking the equivalent currents on Σ to the measured NF [71, 72, 73]. As a result, the IP becomes better constrained, reducing ambiguities in the reconstruction of the equivalent currents and mitigating truncation-induced artifacts.

To better understand how the power radiated by the AUT is distributed over the FF observation surface S' regarding the different computed FF zones, plots of the reference simulated CST FF data are provided. These visualizations highlight the zone boundaries corresponding to each parameter set used in the analysis.

II.5.c Analysis of a non-steered main beam

In this case, the AUT radiates a boresight beam ($\theta_{\text{beam}} = 0°, \phi_{\text{beam}} = 0°$) with no applied phase law. Reference simulated FF data from CST are presented in Fig. II.31. The corresponding FF zones, computed for a planar NF measurement surface S located at a distance of 5λ from the AUT, are superimposed to illustrate how varying the dimensions of S influences the distribution of observation points across these zones.

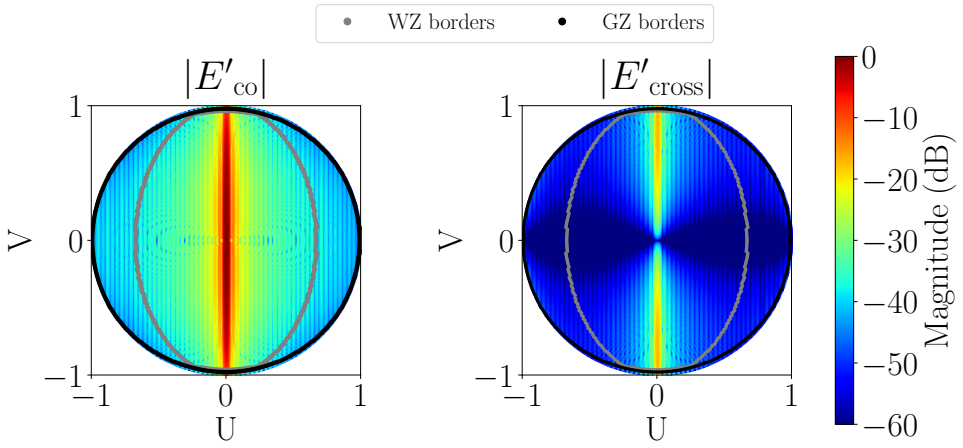

(a) $40\lambda \times 40\lambda$

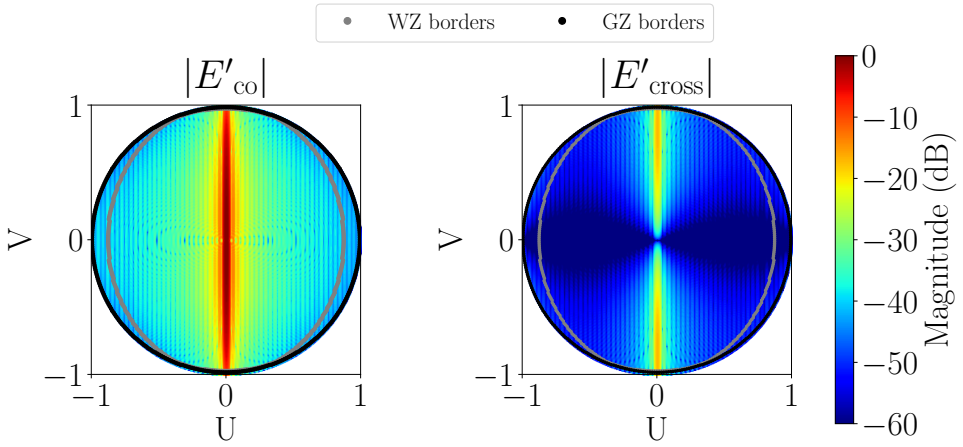

(b) $50\lambda \times 50\lambda$

Figure II.31 – Beam direction to ($\theta_{\text{beam}} = 0°, \phi_{\text{beam}} = 0°$): co- and cross-polarizations of the reference simulated CST FF data on the E-plane. The FF zones corresponding to a planar NF measurement surface S at a distance from AUT of 5λ for two different dimensions of S are represented.

The visual comparison of the WZ and GZ boundaries in the UV plots emphasizes the benefit of increasing the size of the NF measurement surface S for a fixed distance from AUT. In particular, the $50\lambda \times 50\lambda$ S results in a significantly larger WZ than the $40\lambda \times 40\lambda$ configuration, thereby improving angular coverage mainly on the E-plane. As a consequence, the computed FF accuracy is expected to improve with larger dimensions of the NF measurement surface S. However, due to the limited field dynamic within the angular region added by the WZ in this boresight configuration, the gain in accuracy will remain minimal. Nonetheless, such a setup proves advantageous for further analyses involving beam tilts and higher radiated power in the critical GZ and BZ regions.

Figure II.32 presents the same reference simulated CST FF data. Now with S positioned at a distance of 8λ from the AUT center. The FF zones, computed for this distance of 8λ from the AUT, are represented to study see how the dimensions of S and the distance from the AUT influence the distribution of observation points across these zones.

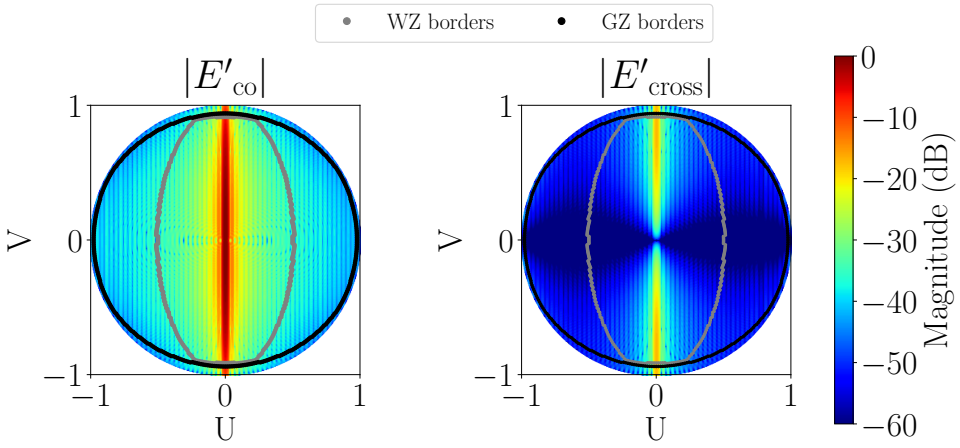

(a) $40\lambda \times 40\lambda$

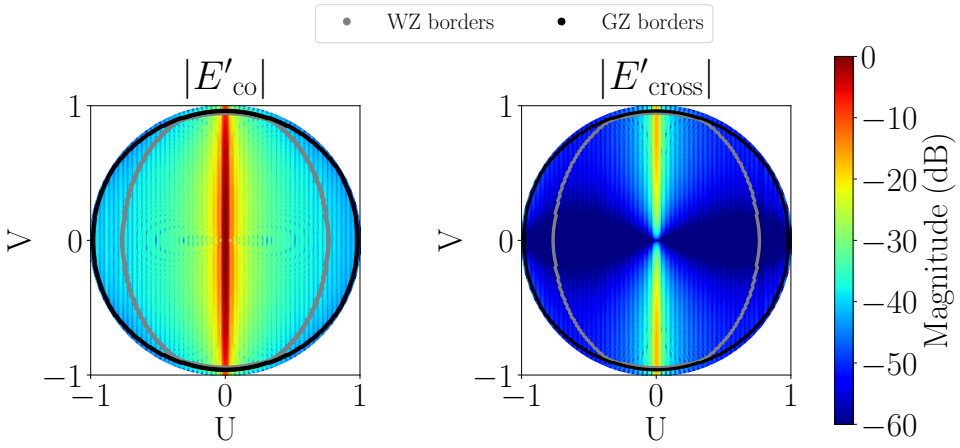

(b) $50\lambda \times 50\lambda$

Figure II.32 – Beam direction to ($\theta_{\text{beam}} = 0°, \phi_{\text{beam}} = 0°$): co- and cross-polarizations of the reference simulated CST FF data on the E-plane. The FF zones corresponding to a planar NF measurement surface S at a distance from AUT of 8λ for two different dimensions of S are represented.

As in the previous case, the increase in size of the NF measurement surface S from $40\lambda \times 40\lambda$ to $50\lambda \times 50\lambda$ leads to an expanded WZ, thus suggesting improved accuracy of the computed FF. However, due to the increased distance between the AUT aperture and the measurement surface S (8λ), the WZ is inherently narrower for both configurations compared to the 5λ case. Therefore, for a given dimension, a degradation in computed

FF accuracy is expected as the measurement distance from AUT increases. Once again, the difference in accuracy between the two dimensions of the NF measurement surface S will remain minimal in this boresight configuration, due to the limited field dynamic in the angular region delimited by the difference between both WZ. Nonetheless, this configuration is more practical for analyzing cases with tilted beams. Moreover, the S-plane positioned at a distance of 8λ from AUT enables the definition of larger GZ and BZ regions, which is particularly useful for assessing the benefits of a half-box geometry. In such cases, the presence of lateral faces helps extend WZ coverage over a larger portion of FF observation surface S' compared to the 5λ configuration.

Planar measurement surface S

Tables II.1 and II.2 report the FF computation metrics for tangential and full Cartesian measurements, respectively.

Discretization	Distance z	ENL (dB)	ENL_{WZ} (dB)	ENL_{GZ} (dB)	ENL_{BZ} (dB)
0.25λ	5λ	-60.2	-64.4	-57.8	-52.1
0.25λ	8λ	-56.5	-63.2	-53.6	-51.1
0.5λ	5λ	-60.2	-64.4	-57.9	-52.0
0.5λ	8λ	-56.5	-63.3	-53.6	-51.1
λ	5λ	-59.8	-62.4	-58.7	-52.9
λ	8λ	-56.4	-62.9	-53.5	-51.1

(a) $40\lambda \times 40\lambda$

Discretization	Distance z	ENL (dB)	ENL_{WZ} (dB)	ENL_{GZ} (dB)	ENL_{BZ} (dB)
0.25λ	5λ	-62.1	-64.3	-60.0	-53.7
0.25λ	8λ	-59.9	-63.5	-58.8	-52.3
0.5λ	5λ	-62.1	-64.3	-60.1	-53.8
0.5λ	8λ	-60.0	-63.5	-58.9	-52.3
λ	5λ	-60.7	-62.8	-58.8	-52.4
λ	8λ	-59.5	-62.8	-58.9	-52.0

(b) $50\lambda \times 50\lambda$

Table II.1 – Planar NF measurement surface S with measured x and y tangential field components, beam direction to $(\theta_{\text{beam}} = 0°, \phi_{\text{beam}} = 0°)$: computed FF accuracy through two different dimensions of S.

From the results presented in the tables, several trends can be identified. First, measuring only the tangential x- and y-components of the NF is sufficient to achieve accurate FF computation, indicating that full vector sampling is not strictly necessary. Second,

Discretization	Distance z	ENL (dB)	ENL_{WZ} (dB)	ENL_{GZ} (dB)	ENL_{BZ} (dB)
0.25λ	5λ	-60.7	-64.8	-58.2	-52.9
0.25λ	8λ	-57.7	-63.0	-56.3	-51.6
0.5λ	5λ	-60.9	-64.8	-58.7	-53.2
0.5λ	8λ	-57.7	-63.0	-56.2	-51.6
λ	5λ	-61.4	-64.8	-59.7	-53.7
λ	8λ	-57.7	-63.0	-56.2	-51.6

(a) $40\lambda \times 40\lambda$

Discretization	Distance z	ENL (dB)	ENL_{WZ} (dB)	ENL_{GZ} (dB)	ENL_{BZ} (dB)
0.25λ	5λ	-63.0	-64.6	-62.9	-54.9
0.25λ	8λ	-59.7	-63.8	-58.5	-51.5
0.5λ	5λ	-63.0	-64.6	-63.0	-54.9
0.5λ	8λ	-59.7	-63.8	-58.5	-51.4
λ	5λ	-62.9	-64.5	-63.2	-54.9
λ	8λ	-59.7	-63.8	-58.7	-51.4

(b) $50\lambda \times 50\lambda$

Table II.2 – Planar NF measurement surface S with full measured field components, beam direction to $(\theta_{\mathrm{beam}} = 0°, \phi_{\mathrm{beam}} = 0°)$: computed FF accuracy through two different dimensions of S.

the computed FF accuracy assessed by the global ENL tends to improve when the NF measurement surface S is both larger and positioned closer to the AUT. This conclusion has been anticipated based on the analysis of the zone distribution over the FF observation surface S' (larger WZ for larger dimensions of S). Finally, while a sampling step of $\leq \frac{\lambda}{2}$ remains a reliable criterion for ensuring high-fidelity characterization, a coarser discretization up to λ still yields acceptable results in this specific configuration.

Half-box-shaped measurement surface S

Results for E_x and E_y components, tangential fields, and full 3D measurements are given in Tables II.3, II.4, and II.5.

This study, conducted on a half-box-shaped NF measurement surface S, complements the analysis of how the NF measurement surface S influences computed FF accuracy. As in previous case, measuring only the x- and y-components of the NF is sufficient to achieve accurate results. Moreover, a NF measurement surface S positioned closer to the

Discretization	Distance z (upper plane)	ENL (dB)	ENL_{WZ} (dB)	ENL_{GZ} (dB)	ENL_{BZ} (dB)
0.25λ	5λ	-63.5	-64.3	-66.9	-56.6
0.25λ	8λ	-62.2	-62.7	-67.3	-56.4
0.5λ	5λ	-63.5	-64.3	-66.8	-56.5
0.5λ	8λ	-62.2	-62.7	-67.5	-56.5
λ	5λ	-62.9	-63.5	-66.5	-56.3
λ	8λ	-61.7	-62.1	-66.2	-56.4

(a) $40\lambda \times 40\lambda$

Discretization	Distance z (upper plane)	ENL (dB)	ENL_{WZ} (dB)	ENL_{GZ} (dB)	ENL_{BZ} (dB)
0.25λ	5λ	-62.8	-64.2	-63.7	-55.3
0.25λ	8λ	-61.7	-63.2	-65.2	-55.0
0.5λ	5λ	-62.8	-64.2	-63.7	-55.3
0.5λ	8λ	-61.7	-63.2	-65.2	-55.1
λ	5λ	-62.0	-63.1	-63.3	-54.8
λ	8λ	-61.6	-62.9	-65.2	-55.2

(b) $50\lambda \times 50\lambda$

Table II.3 – Half-box-shaped NF measurement surface S with measured x and y field components, beam direction to $(\theta_{\mathrm{beam}} = 0°, \phi_{\mathrm{beam}} = 0°)$: computed FF accuracy through two different dimensions of S.

Discretization	Distance z (upper plane)	ENL (dB)	ENL_{WZ} (dB)	ENL_{GZ} (dB)	ENL_{BZ} (dB)
0.25λ	5λ	-64.7	-64.6	-68.3	-59.8
0.25λ	8λ	-62.3	-63.0	-66.9	-56.5
0.5λ	5λ	-64.7	-64.6	-68.3	-59.9
0.5λ	8λ	-62.4	-63.0	-66.9	-56.7
λ	5λ	-63.8	-63.4	-68.0	-59.9
λ	8λ	-62.2	-62.5	-66.7	-56.9

(a) $40\lambda \times 40\lambda$

Discretization	Distance z (upper plane)	ENL (dB)	ENL_{WZ} (dB)	ENL_{GZ} (dB)	ENL_{BZ} (dB)
0.25λ	5λ	-63.8	-64.5	-65.8	-58.0
0.25λ	8λ	-62.3	-63.5	-65.5	-56.3
0.5λ	5λ	-63.8	-64.5	-65.9	-58.1
0.5λ	8λ	-62.4	-63.5	-65.6	-56.4
λ	5λ	-63.3	-63.7	-65.6	-58.2
λ	8λ	-62.2	-63.1	-65.6	-56.8

(b) $50\lambda \times 50\lambda$

Table II.4 – Half-box-shaped NF measurement surface S with tangential measured field components, beam direction to $(\theta_{\mathrm{beam}} = 0°, \phi_{\mathrm{beam}} = 0°)$: computed FF accuracy through two different dimensions of S.

AUT and having minimal dimensions is already sufficient to ensure the convergence of the ENL metrics. Thus, enclosing the upper half of the radiation space to recover most of the FF observation surface S' through the WZ appears to offer a safe margin for achieving

Discretization	Distance z (upper plane)	ENL (dB)	ENL_{WZ} (dB)	ENL_{GZ} (dB)	ENL_{BZ} (dB)
0.25λ	5λ	-64.7	-64.7	-68.5	-59.7
0.25λ	8λ	-62.3	-63.0	-66.9	-56.4
0.5λ	5λ	-64.7	-64.7	-68.5	-59.7
0.5λ	8λ	-62.6	-62.9	-67.5	-57.0
λ	5λ	-64.6	-64.5	-68.5	-59.9
λ	8λ	-62.6	-62.8	-67.5	-57.1

(a) $40\lambda \times 40\lambda$

Discretization	Distance z (upper plane)	ENL (dB)	ENL_{WZ} (dB)	ENL_{GZ} (dB)	ENL_{BZ} (dB)
0.25λ	5λ	-63.9	-64.6	-66.2	-57.8
0.25λ	8λ	-62.3	-63.6	-65.6	-56.2
0.5λ	5λ	-63.9	-64.6	-66.2	-57.9
0.5λ	8λ	-62.4	-63.6	-65.7	-56.3
λ	5λ	-63.9	-64.5	-66.2	-58.0
λ	8λ	-62.4	-63.5	-65.8	-56.5

(b) $50\lambda \times 50\lambda$

Table II.5 – Half-box-shaped NF measurement surface S with full measured field components, beam direction to ($\theta_{\mathrm{beam}} = 0°, \phi_{\mathrm{beam}} = 0°$): computed FF accuracy through two different dimensions of S.

good performance. A sampling step of $\frac{\lambda}{2}$ provides a good compromise between the number of samples and characterization accuracy. For example, let consider a NF measurement surface S of dimensions $40\lambda \times 40\lambda \times 5\lambda$, sampled with a step of $\frac{\lambda}{2}$ and where only the x- and y-components of the NF are measured. Indeed, for a sampling step of $\frac{\lambda}{2}$ the number of samples is lowered down to 13122 compared to the 51842 samples for a spacing of $\frac{\lambda}{4}$.

Since the computed FF zones are defined with respect to the planar NF measurement surface S, which corresponds to the upper face of the half-box geometry, a direct comparison between both configurations is possible. To highlight the benefits of employing non-conventional geometries for accurate characterization, the same configuration used previously to compare sampling density is considered here. The characterization results obtained using the half-box NF measurement surface S are compared against to those based solely on the upper planar surface. The resulting computed FF accuracy is summarized in Table II.6.

Significant improvements are mainly observed in the GZ and BZ, where the added lateral faces of the half-box configuration reduce truncation effects and enhance FF computation fidelity. These trends will be further investigated in the beam-steered scenario.

Geometry	ENL (dB)	ENL_{WZ} (dB)	ENL_{GZ} (dB)	ENL_{BZ} (dB)
Plane	-60.2	-64.4	-57.9	-52.0
Half-box	-63.5	-64.3	-66.8	-56.5

Table II.6 – Comparison of the computed FF accuracy for planar and half-box-shaped NF measurement surfaces S and a beam direction to ($\theta_{\mathrm{beam}} = 0°, \phi_{\mathrm{beam}} = 0°$). Crucial comparison values are highlighted in blue.

II.5.d Analysis of a steered main beam

In this case, a phase law is applied to steer the beam to ($\theta_{\mathrm{beam}} = 80°, \phi_{\mathrm{beam}} = 0°$). Reference FF data simulated on CST are shown in Fig. II.33. The associated FF zones, computed for a planar NF measurement surface S located at a distance of 5λ from the AUT, are added to visualize how varying the dimensions of S impact the distribution of observation points across these zones.

In the case of a tilted main beam, the relevance of testing different configurations of NF measurement surface S at a fixed distance from AUT becomes evident. Since the radiated power is now distributed across both the GZ and BZ, expanding the WZ becomes a critical factor for accurate characterization. This is clearly illustrated in the UV plots, where the $50\lambda \times 50\lambda$ NF measurement surface S yields a significantly larger WZ compared to the $40\lambda \times 40\lambda$ configuration. Moreover, due to the inclination of the main beam, the region of maximum power on S shifts toward the edges of the scanning area. From a radiated field perspective, as the main lobe is steered toward grazing angles, the contribution of the z-component becomes increasingly significant. Consequently, measuring this component is likely to provide essential information for solving the IP. Therefore, in this scenario, the use of a larger NF measurement surface S is expected to yield noticeably improved FF computation performance.

The same reference FF data simulated on CST are illustrated in Fig. II.34. This time, S is positioned at a distance from AUT of 8λ. The FF zones defined by this planar measurement surface S are computed to understand the variation of these zones through the dimensions of S and the distance from the AUT.

At this distance from AUT, the benefits of using the half-box-shaped NF measurement surface S over the planar configuration become more apparent, as the GZ occupies a significantly larger portion of the angular space compared to the 5λ case. Additionally, the

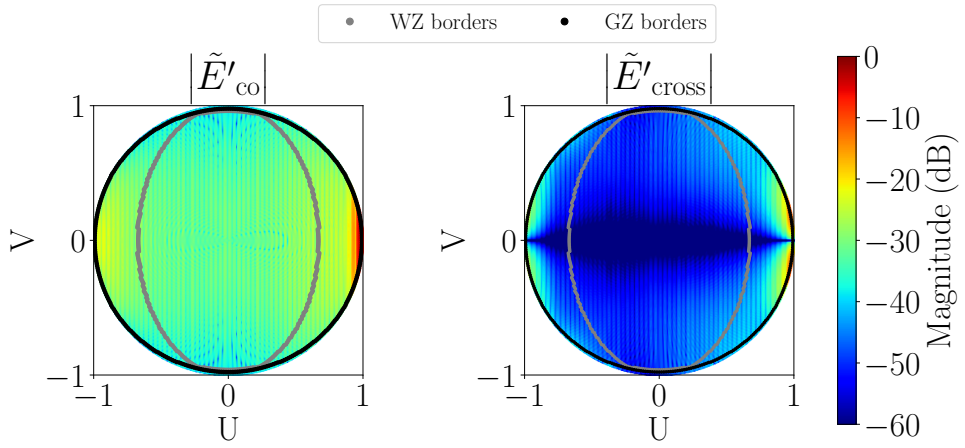

(a) $40\lambda \times 40\lambda$

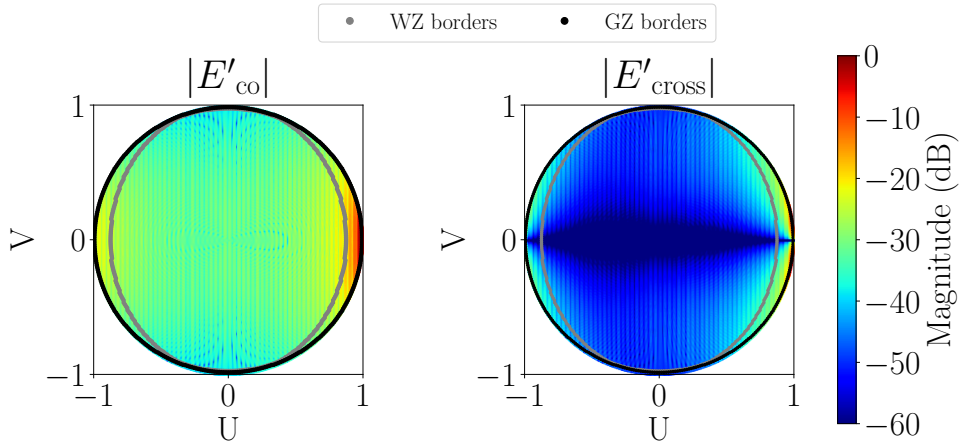

(b) $50\lambda \times 50\lambda$

Figure II.33 – Beam direction to $(\theta_{\text{beam}} = 80°, \phi_{\text{beam}} = 0°)$: co- and cross-polarizations of the reference simulated CST FF data on the E-plane. The FF zones corresponding to a planar NF measurement surface S at a distance from AUT of 5λ for two different dimensions of S are represented.

dimensions of the NF measurement surface S influence the computed FF accuracy: a larger planar S is expected to capture more relevant NF information due to the expansion of the WZ, thereby mitigating truncation effects and enabling more accurate FF computation than a smaller NF measurement surface S.

Planar measurement surface S

The variation of the computed FF accuracy using a planar NF measurement surface S for a steered main beam are studied. Results are summarized in Tables II.7 and II.8.

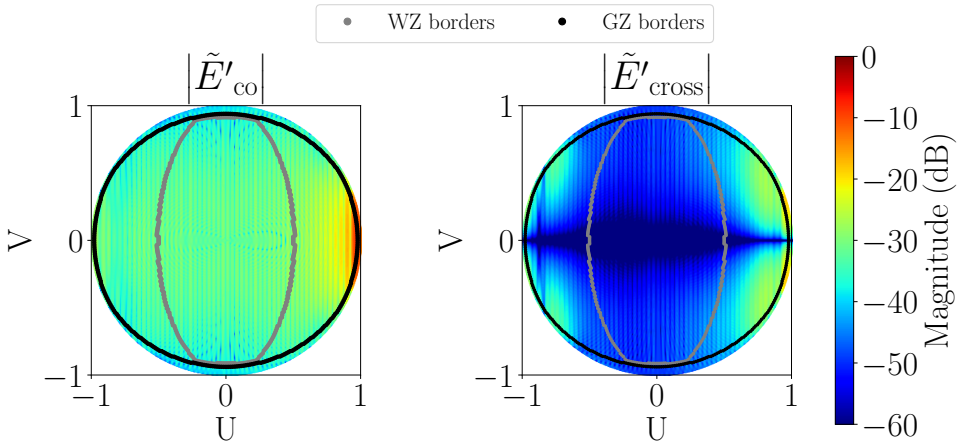

(a) $40\lambda \times 40\lambda$

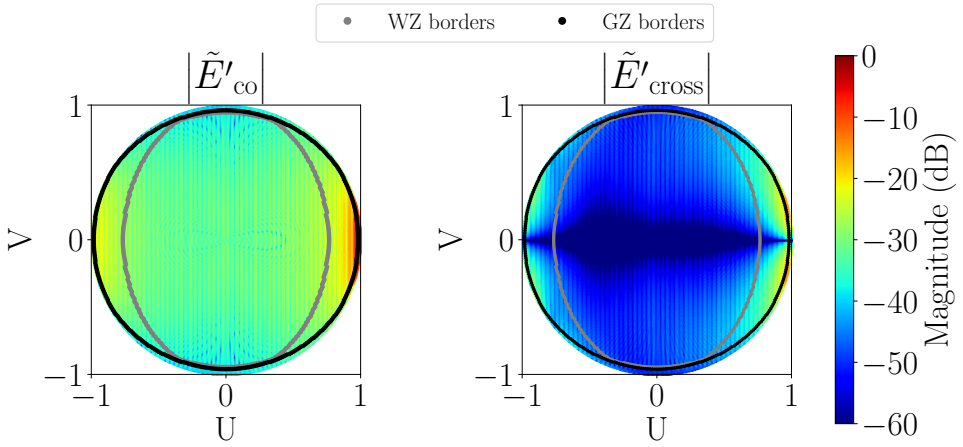

(b) $50\lambda \times 50\lambda$

Figure II.34 – Beam direction to ($\theta_{\text{beam}} = 80°, \phi_{\text{beam}} = 0°$): co- and cross-polarizations of the reference simulated CST FF data on the E-plane. The FF zones corresponding to a planar NF measurement surface S at a distance from AUT of 8λ for two different dimensions of S are represented.

The analysis of the results provides valuable insight into the reliability of the equivalent model when characterizing antennas with strong beam tilts. Contrary to initial expectations, including the z-component of the NF has only a limited impact on the computed FF accuracy. The information carried by the x and y-components alone is sufficient to achieve accurate results especially when the sampling step is finer than $\frac{\lambda}{2}$ and the measurement distance from AUT is 5λ. This is a key finding, as it confirms that reliable characterization can be obtained by measuring only two components of the field, despite the presence of notable truncation effects, which explain the relatively high ENL levels (around $-35\,\text{dB}$).

Regarding sampling, the results indicate that a step of $\frac{\lambda}{2}$ provides a good trade-off,

Discretization	Distance z	ENL (dB)	ENL_{WZ} (dB)	ENL_{GZ} (dB)	ENL_{BZ} (dB)
0.25λ	5λ	-36.3	-55.0	-29.2	-25.8
0.25λ	8λ	-31.2	-47.5	-27.0	-23.6
0.5λ	5λ	-36.2	-53.7	-29.3	-25.7
0.5λ	8λ	-31.2	-47.2	-27.1	-23.6
λ	5λ	-34.7	-45.7	-28.6	-25.7
λ	8λ	-31.5	-46.6	-27.7	-23.7

(a) $40\lambda \times 40\lambda$

Discretization	Distance z	ENL (dB)	ENL_{WZ} (dB)	ENL_{GZ} (dB)	ENL_{BZ} (dB)
0.25λ	5λ	-42.4	-49.7	-35.9	-29.5
0.25λ	8λ	-34.3	-50.9	-24.6	-24.2
0.5λ	5λ	-42.5	-49.9	-36.1	-29.6
0.5λ	8λ	-34.4	-51.1	-26.5	-24.2
λ	5λ	-40.7	-45.4	-36.5	-29.5
λ	8λ	-34.0	-47.6	-26.5	-24.2

(b) $50\lambda \times 50\lambda$

Table II.7 – Planar NF measurement surface S with measured x and y field components, beam direction to $(\theta_{\mathrm{beam}} = 80°, \phi_{\mathrm{beam}} = 0°)$: computed FF accuracy through two different dimensions of S.

Discretization	Distance z	ENL (dB)	ENL_{WZ} (dB)	ENL_{GZ} (dB)	ENL_{BZ} (dB)
0.25λ	5λ	-35.6	-48.5	-29.7	-25.2
0.25λ	8λ	-32.5	-51.8	-28.5	-24.3
0.5λ	5λ	-35.7	-48.4	-29.8	-25.2
0.5λ	8λ	-32.5	-51.6	-28.6	-24.3
λ	5λ	-35.8	-48.0	-30.2	-25.3
λ	8λ	-32.6	-51.1	-28.8	-24.3

(a) $40\lambda \times 40\lambda$

Discretization	Distance z	ENL (dB)	ENL_{WZ} (dB)	ENL_{GZ} (dB)	ENL_{BZ} (dB)
0.25λ	5λ	-41.6	-47.8	-35.2	-29.8
0.25λ	8λ	-36.5	55.1	-29.5	-25.4
0.5λ	5λ	-41.7	-47.8	-35.3	-29.8
0.5λ	8λ	-36.6	-54.8	-29.6	-25.4
λ	5λ	-41.8	-47.8	-35.7	-30.0
λ	8λ	-36.7	-54.4	-29.9	-25.4

(b) $50\lambda \times 50\lambda$

Table II.8 – Planar NF measurement surface S with full measured field components, beam direction to $(\theta_{\mathrm{beam}} = 80°, \phi_{\mathrm{beam}} = 0°)$: computed FF accuracy through two different dimensions of S.

although slightly coarser discretization may still yield acceptable FF computation performance. Finally, increasing the size from $40\lambda \times 40\lambda$ to a larger planar NF measurement surface S enhances the accuracy in the main beam region by expanding the WZ and thereby reducing truncation-induced errors.

Half-box-shaped measurement surface S

Now, computed FF metrics for a half-box-shaped NF measurement surface S are provided in Tables II.9, II.10, and II.11.

Discretization	Distance z (upper plane)	ENL (dB)	ENL_{WZ} (dB)	ENL_{GZ} (dB)	ENL_{BZ} (dB)
0.25λ	5λ	-48.7	-59.1	-48.3	-35.0
0.25λ	8λ	-43.9	-52.9	-45.9	-33.6
0.5λ	5λ	-48.6	-58.8	-48.2	-34.9
0.5λ	8λ	-45.1	-54.1	-47.5	-34.7
λ	5λ	-44.8	-47.6	-47.7	-34.8
λ	8λ	-44.5	-52.2	-46.2	-34.7

(a) $40\lambda \times 40\lambda$

Discretization	Distance z (upper plane)	ENL (dB)	ENL_{WZ} (dB)	ENL_{GZ} (dB)	ENL_{BZ} (dB)
0.25λ	5λ	-47.9	-56.0	-43.2	-33.5
0.25λ	8λ	-46.7	-55.1	-47.4	-34.7
0.5λ	5λ	-47.9	-56.0	-43.1	-33.5
0.5λ	8λ	-46.9	-55.4	-47.7	-34.8
λ	5λ	-44.7	-48.3	-43.2	-33.5
λ	8λ	-46.5	-53.2	-48.0	-35.1

(b) $50\lambda \times 50\lambda$

Table II.9 – Half-box-shaped NF measurement surface S with measured x and y field components, beam direction to $(\theta_{\text{beam}} = 80°, \phi_{\text{beam}} = 0°)$: computed FF accuracy through two different dimensions of S.

The investigation of a non-planar geometry for the NF measurement surface S, specifically a half-box-shaped S, offers valuable insights into the actual benefits of using an equivalent model to mitigate truncation effects. First, regarding the measured NF components, the analysis confirms that capturing only the x and y-components is sufficient to achieve accurate FF computation, even under large beam-steering conditions. While the use of tangential or full Cartesian components does lead to improved precision, the difference remains relatively minor.

Furthermore, the marginal gain in accuracy achieved by including the tangential or full component set must be weighed against the increased number of unknowns and samples introduced in the model. This trade-off is clearly illustrated in Table II.13, which presents

Discretization	Distance z (upper plane)	ENL (dB)	ENL_{WZ} (dB)	ENL_{GZ} (dB)	ENL_{BZ} (dB)
0.25λ	5λ	-52.8	-57.2	-50.0	-45.0
0.25λ	8λ	-42.5	-50.8	-43.8	-33.0
0.5λ	5λ	-53.1	-57.1	-50.2	-45.7
0.5λ	8λ	-43.3	-51.4	-44.7	-33.7
λ	5λ	-45.3	-44.5	-48.2	-45.2
λ	8λ	-42.3	-48.0	-43.0	-34.0

(a) $40\lambda \times 40\lambda$

Discretization	Distance z (upper plane)	ENL (dB)	ENL_{WZ} (dB)	ENL_{GZ} (dB)	ENL_{BZ} (dB)
0.25λ	5λ	-51.5	-53.7	-47.6	-44.7
0.25λ	8λ	-46.9	-53.6	-46.6	-36.2
0.5λ	5λ	-51.5	-53.6	-47.7	-45.2
0.5λ	8λ	-47.1	-53.7	-46.8	-36.4
λ	5λ	-44.3	-43.7	-47.5	-47.1
λ	8λ	-44.7	-47.4	-46.9	-36.9

(b) $50\lambda \times 50\lambda$

Table II.10 – Half-box-shaped NF measurement surface S with tangential measured field components, beam direction to ($\theta_{\mathrm{beam}} = 80°, \phi_{\mathrm{beam}} = 0°$): computed FF accuracy through two different dimensions of S.

Discretization	Distance z (upper plane)	ENL (dB)	ENL_{WZ} (dB)	ENL_{GZ} (dB)	ENL_{BZ} (dB)
0.25λ	5λ	-54.2	-58.6	-51.9	-45.9
0.25λ	8λ	-43.9	-52.9	-45.5	-33.8
0.5λ	5λ	-54.3	-58.6	-51.9	-46.2
0.5λ	8λ	-44.0	-52.8	-45.5	-34.1
λ	5λ	-53.3	-56.2	-51.6	-46.6
λ	8λ	-43.9	-52.3	-45.2	-34.3

(a) $40\lambda \times 40\lambda$

Discretization	Distance z (upper plane)	ENL (dB)	ENL_{WZ} (dB)	ENL_{GZ} (dB)	ENL_{BZ} (dB)
0.25λ	5λ	-53.2	-56.1	-48.7	-45.1
0.25λ	8λ	-47.6	-54.6	-47.5	-36.6
0.5λ	5λ	-53.3	-56.1	-48.7	-45.4
0.5λ	8λ	-47.9	-54.7	-47.7	-36.9
λ	5λ	-52.8	-55.2	-48.6	-45.8
λ	8λ	-48.0	-54.3	-48.1	-37.4

(b) $50\lambda \times 50\lambda$

Table II.11 – Half-box-shaped NF measurement surface S with full measured field components, beam direction to ($\theta_{\mathrm{beam}} = 80°, \phi_{\mathrm{beam}} = 0°$): computed FF accuracy through two different dimensions of S.

the results obtained for a NF measurement surface S of dimensions $40\lambda \times 40\lambda \times 5\lambda$, discretized with a sampling step of $\frac{\lambda}{2}$.

Even though the best compromise appears to be the use of tangential components,

Field components	Number of samples	ENL (dB)	ENL_{WZ} (dB)	ENL_{GZ} (dB)	ENL_{BZ} (dB)
x and y	19522	-48.6	-58.8	-48.2	-34.9
tangent	19522	-53.1	-57.1	-50.2	-45.7
full	29283	-54.3	-58.6	-51.9	-46.2

Table II.12 – Comparison of the characterization accuracy for the measurement of different NF components on a half-box-shaped NF measurement surface S with a beam direction to ($\theta_{\mathrm{beam}} = 80°, \phi_{\mathrm{beam}} = 0°$).

another important aspect must be taken into account: the measurement technique. Specifically, acquiring the z-component of the NF typically requires the use of a rotative arm to orient the probe appropriately, as noted in [74]. However, such equipment is both costly and mechanically complex. By contrast, the measurement of only the x- and y-components is much more practical and compatible with conventional planar NF scanning systems. It merely requires a positioning system capable of translating along the z-axis, in addition to scanning in the XOY plane.

Moreover, as in the non-steered beam case, the optimal computed FF accuracy is achieved when S is placed closer to the AUT. This is particularly advantageous for the half-box configuration, as it eliminates the need to enlarge the area of the NF measurement surface S to compensate for truncation effects unlike with a single planar S. This trend becomes more pronounced in the presence of beam tilts, thereby confirming the effectiveness of employing non-conventional geometries for NF acquisition.

To reinforce this conclusion, a comparison is made between the half-box geometry and its upper planar face for a NF measurement surface S of dimensions $40\lambda \times 40\lambda \times 5\lambda$, discretized with a step of $\frac{\lambda}{2}$, and with only the x- and y-components of the NF measured. The corresponding FF computation accuracies are presented in Table II.13.

Geometry	ENL (dB)	ENL_{WZ} (dB)	ENL_{GZ} (dB)	ENL_{BZ} (dB)
Plane	-36.2	-53.7	-23.9	-25.7
Half-box	-48.6	-58.8	-48.2	-34.9

Table II.13 – Comparison of the characterization accuracy for planar and half-box-shaped NF measurement surfaces S and a beam direction to ($\theta_{\mathrm{beam}} = 80°, \phi_{\mathrm{beam}} = 0°$). Crucial comparison values are highlighted in blue.

The half-box geometry significantly reduces truncation effects. Lateral faces enhance accuracy in the GZ and BZ, lowering ENL_{GZ} and ENL_{BZ}.

Finally, the criterion of $\frac{\lambda}{2}$ for the sampling step is, once again, a good marker to ensure an accurate FF computation.

II.5.e Summary of observations

In conclusion, this study demonstrates that the geometry and positioning of the NF measurement surface S have a significant impact on the accuracy of FF computation for directive antennas. For standard configurations, a planar NF measurement surface S with appropriate dimensions and sampling density is generally sufficient. However, in more demanding scenarios involving beam steering or constrained scanning apertures, enclosing the radiating half-space with a half-box-shaped NF measurement surface S proves to be a robust and effective solution. This configuration substantially mitigates truncation effects and enables high-fidelity FF computation without requiring full 3D measurement setups.

Importantly, these findings underscore the potential of the proposed equivalent modeling approach to enable non-conventional sampling strategies in practical NF measurement environments. By decoupling the FF computation process from the classical dependence on a regular discretization of the planar NF measurement surface S, this methodology allows for more flexible and efficient measurement configurations. Ultimately, this paves the way for the next chapter in which sample reduction strategies are investigated to result in a highly competitive characterization method capable of overcoming the limitations of conventional PWE technique.

II.6 Conclusion

The construction of an equivalent model of the AUT using an infinitesimal dipole distribution has been introduced and detailed to propose a novel characterization method for radiation pattern computation from planar NF measurements. Each step leading to the development of the method has been reviewed through both analytical and simulation-based cases. Once the full process has been validated, the IP method has been presented and applied directly, including a comparison case that demonstrated the advantages of this approach over the PWE, particularly in terms of computed FF accuracy.

Furthermore, an extensive parametric study conducted on the model confirmed the robustness and reliability of the proposed solution. The influence of the NF measurement surface especially when using non-planar sampling distributions on the limitation of truncation effects has been also analyzed. These investigations revealed the intrinsic properties of the equivalent model-based NFFFT, highlighting its adaptability. In particularly through the use of half-box geometries and more permissive discretization, which enable it to handle significant beam tilts more effectively than traditional scanning schemes

In addition, the model ability to support irregular sampling distributions opens the door to reducing the number of required NF samples. This aspect is explored in the next chapter, where new characterization strategies are introduced.

Chapter III

Antenna characterization using a reduced-order model

III.1 Introduction

III.1.a Motivations

The developed NFFFT method based on the use of an equivalent model of the AUT enables the implementation of non-conventional NF sampling strategies. Unlike traditional approaches constrained by regular grids and the Nyquist criterion, this framework allows for flexible sampling schemes that can address some of the key limitations of the PWE technique namely, the mitigation of truncation effects and the reduction of the number of required measurement points. Provided that the equivalent currents are accurately determined, the FF radiation pattern of the AUT can be computed with high fidelity.

Nevertheless, solving the associated IP remains a critical step, as it is inherently ill-posed. In particular, the radiation matrix constructed from the NF data often exhibits poor conditioning, making the inversion process sensitive to noise and modeling inaccuracies. To overcome this, a regularization step is generally required.

This chapter introduces the use of a ROM. In general, a ROM is obtained by projecting a high-dimensional system onto a low-dimensional subspace spanned by its dominant modes, thereby preserving the essential physical behavior while significantly reducing computational cost and improving numerical robustness. Specifically, the ROM can be regarded as an advanced regularization technique based on a SVD. Its goal is to enhance the conditioning of the radiation matrix and to improve the efficiency of the AUT characterization, particularly through NF data interpolation and advanced analysis methods for estimating the minimal number of required measurement points. Then, the ROM contributes to a significant reduction in the sampling size, aligned with the use of the customized sampling distributions enabled by the proposed equivalent model to limit the

effects of truncation.

Ultimately, the construction of a ROM introduces a novel approach to the characterization problem, complementing the equivalent model-based method explored thus far. This leads to the development of a user-friendly direct NFFFT represented by a single transition matrix. Overall, this NFFFT incorporates all the key properties related to sampling distribution, as enabled by both the equivalent model and the ROM, in order to meet the defined objectives.

III.1.b State of the art

Various electromagnetic solvers benefit from leveraging *a priori* information on the spatial extent of radiating structures. This allows simplification of the governing integral equations using advanced numerical techniques. However, for electrically large or geometrically complex systems, the associated computational cost remains high. As a result, a balance must be struck between model fidelity and tractability. In this context, recent advances in scattering problems have proposed the use of ROM to retain only the most significant features of a system while discarding redundancies [75, 76, 77].

The concept of ROM shares conceptual foundations with Compressed Sensing (CS) as applied in the field of antenna measurements [12, 13, 78]. Both frameworks aim to exploit the sparsity of the physical or mathematical model to reduce its dimensionality and accelerate computation. In the antenna domain, this principle has recently been tested in the characterization of radiating structures via planar NF measurements. For instance, Parini *et al.* [79] applied ROM to detect thermal-induced pattern deviations across frequency with promising accuracy and reduced sampling requirements.

The application of ROM for accelerating antenna characterization procedures has gained momentum in the last few years. Fuchs *et al.* [63] proposed a framework in which an equivalent dipole model is used in conjunction with ROM to reduce the number of NF planar measurement points. The authors report a reduction of up to 60% in acquisition time compared to the classical $\frac{\lambda}{2}$-spaced grid. This approach was later adapted to spherical measurement setups by Mézières *et al.* [80], who employed a continuous triangular meshing of the equivalent surface Σ and observed similarly favorable sampling reductions.

Further developments have integrated ROM into classical modal expansion techniques. Varela *et al.* [81] demonstrated that the PWE method could benefit from ROM by isolating a subset of dominant plane-wave modes. This allowed characterization from a non-uniform sampling grid over a limited angular sector, thus reducing the overall acquisition time.

In addition to acquisition speed up, ROM techniques have also been investigated for their ability to interpolate or extrapolate FF data from sparse samplings. Mézières *et al.* [70] demonstrated that ROM can be used to accelerate FF acquisition by analyzing the radiation operator structure. Their results highlight a close relationship between the geometry of the equivalent surface Σ and the physical aperture of the AUT. This relationship was further explored by Corre *et al.* [82], who carried out a parametric analysis to better understand the impact of various ROM parameters on model performance and stability.

Finally, a recent trend merges ROM techniques with machine learning, aiming to automate the identification of the most informative data for solving IPs. Capozzoli *et al.* [83] proposed a learned-ROM framework to optimize the selection of sampling positions and enhance inversion accuracy, suggesting a promising direction for future hybrid methods.

III.1.c Contributions

The construction of a ROM is based on the analysis of the radiation matrix and leads to an estimate of the number of samples needed from the equivalent model defined. Moreover, the interpolation ability is a very important property as it allows developing new characterization methods without the step of determining the equivalent currents. Therefore, as introduced in [63] a ROM of the equivalent model created with a distribution of infinitesimal dipoles is constructed. Characterization methods developed from the interpolation of NF data with the obtained reduced basis are detailed. Then, the analysis of the radiation matrix linked to the NF samples is carried out to determine a minimum number of samples to measure to ensure a correct accuracy for the FF computation. Various non-conventional sampling strategies are presented to distribute the resulting number of samples over the NF measurement surface S leading to reduction of the sampling size. The application of those methods combined to non-usual geometries for the NF measurement surface S on an application case shows great agreement with the expected performances improvement compared to the PWE. The obtained results confirm the trends observed by Fuchs *et al.* [63] on the speed up of the acquisition. Furthermore, the verification of a criterion given by Mézières *et al.* [70] to establish a safety margin to estimate this reduction of number of samples for the characterization situation under investigation is described. All the developed methods, each offering distinct advantages, collectively enable the introduction of a new direct NFFFT in the final section of this chapter. This advanced characterization approach represents the cornerstone of the equivalent model-based tech-

niques proposed in this work. It integrates the strengths offered by the ROM construction into an easy-to-use operator, designed to streamline the characterization process while mitigating several limitations inherent to the other NFFFTs discussed throughout this thesis. Additionally, all the characterization strategies presented in this manuscript are validated using experimental cases in the following chapter.

III.2 Construction of the reduced-order model

III.2.a Singular value decomposition

As detailed in Section II.3.b, the IP method aims to solve an ill-posed system. Specifically, we seek to find a solution $\mathbf{X}$ that satisfies the linear problem minimization:

$$\min_{\mathbf{X}} \|\mathbf{E} - \mathbf{A}\mathbf{X}\|_2 \tag{III.1}$$

where $\mathbf{E}$ represents the measured NF data, $\mathbf{A}$ is the discretized radiation operator, and $\mathbf{X}$ contains the unknown equivalent currents on Σ. This formulation corresponds to the standard least-squares approach, which seeks a solution minimizing the residual energy in the ℓ_2 norm.

Nonetheless, this represents just one possible formulation. In recent years, alternative minimization strategies have emerged, particularly with the development of CS method, where sparsity of the solution is leveraged to improve robustness and reduce the number of required measurement points. One widely used approach is the Basis Pursuit Denoising (BPDN) problem:

$$\min_{\mathbf{X}} \|\mathbf{X}\|_1 \quad \text{subject to} \quad \|\mathbf{E} - \mathbf{A}\mathbf{X}\|_2 \leq \delta \tag{III.2}$$

where the ℓ_1 norm promotes sparsity in the solution, and the constraint allows for noise tolerance within a bound δ. BPDN and similar formulations have already shown promising results in electromagnetic IPs and antenna characterization [12, 13, 78, 79].

These formulations can offer better performance in scenarios where the underlying model, such as the equivalent current distribution, is known to be sparse or compressible, or when data is incomplete or noisy. Therefore, the choice between minimization strategies (e. g., ℓ_2 least-squares, ℓ_1 sparse recovery, or hybrid regularized formulations) depends on the assumptions made on the solution structure and the desired trade-off between FF computation fidelity and model complexity.

In our case, using least-squares approach, a regularized form of the problem enforces an error tolerance δ to be introduced:

$$\|\mathbf{E} - \mathbf{AX}\|_2 \leq \delta \tag{III.3}$$

The aim is to find the best possible estimate of $\mathbf{X}$ that minimizes the difference between the measured field $\mathbf{E}$ and the reconstructed field $\mathbf{AX}$, while controlling the error through the tolerance parameter δ [84].

In practice, the characterization problem involves a finite set of NF samples and unknown currents on Σ, which often results in an ill-conditioned system due to high redundancy in the matrix $\mathbf{A}$. This means that different current distributions on Σ can produce similar field patterns $\mathbf{E}$, reflecting strong linear dependencies among the columns of $\mathbf{A}$. This loss of orthogonality in the radiated modes motivates the need for a more stable basis in the solution space.

To analyze and regularize the problem, the SVD of the matrix $\mathbf{A} \in \mathbb{C}^{m\times n}$ is performed:

$$\mathbf{A} = \mathbf{USV}^{\mathrm{H}} \tag{III.4}$$

where:

- $\mathbf{U} \in \mathbb{C}^{m\times m}$ is a unitary matrix whose columns form an orthonormal basis for the radiated field space;
- $\mathbf{V} \in \mathbb{C}^{n\times n}$ is a unitary matrix representing an orthonormal basis for the current distribution domain on Σ. $\mathbf{V}^{\mathrm{H}}$ is denoted as the conjugate transpose of $\mathbf{V}$;
- $\mathbf{S} \in \mathbb{R}^{m\times n}$ is a diagonal matrix containing the singular values. By convention, it is usual to sort the singular values by decreasing order $\sigma_1 \geq \sigma_2 \geq \cdots \geq \sigma_n \geq 0$.

These singular values can be interpreted as coupling strengths between the current modes (from $\mathbf{V}$) and the corresponding radiated field modes (from $\mathbf{U}$). Therefore, the SVD of $\mathbf{A}$ allows expressing the initial matrix in two semi-unitary bases associated to two distinct domains.

To better illustrate the concept underlying the construction of a ROM, Fig. III.1 provides a schematic example for the case of a field measured on a spherical surface.

The detailed structure of the SVD components is represented:

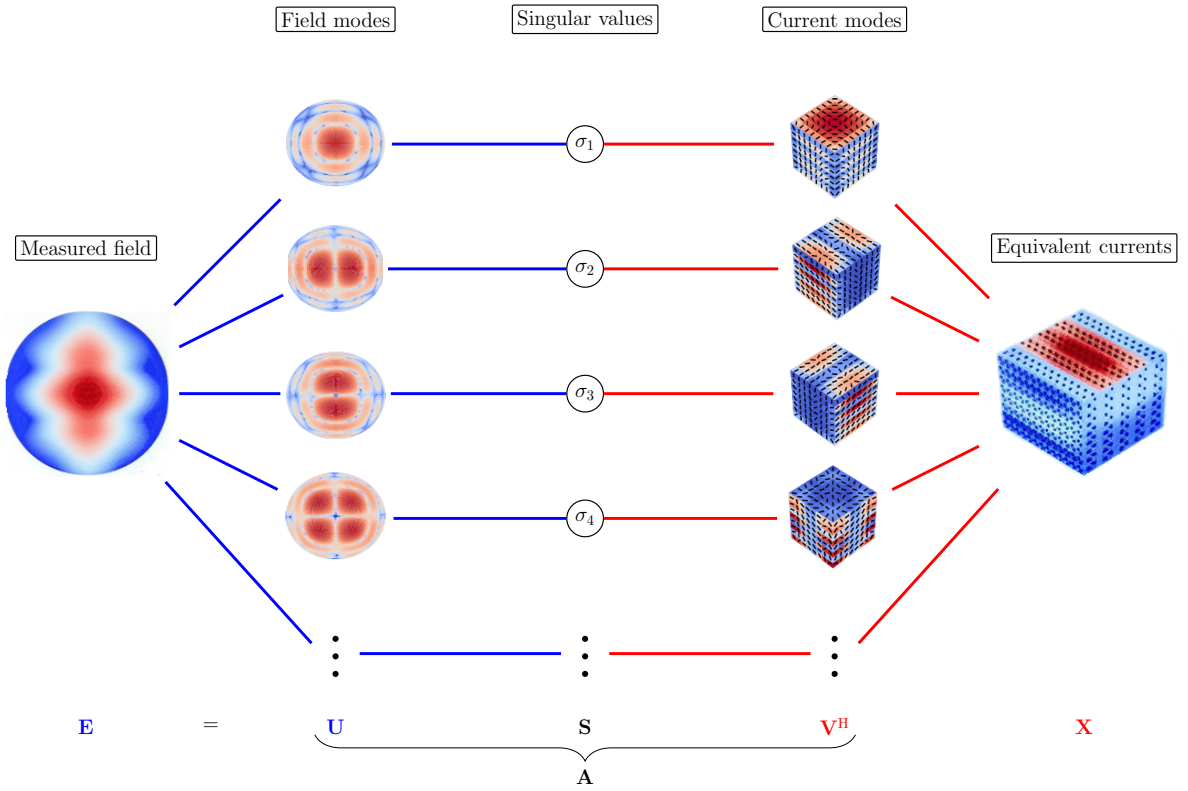

Figure III.1 – Illustration of the ROM concept, inspired by Fig. 2 in [82], in the case of a field measured on a spherical surface.

$$\mathbf{A} = \underbrace{\begin{bmatrix} a_{11} & a_{12} & \dots & a_{1n} \\ a_{21} & a_{22} & \dots & a_{2n} \\ \vdots & \vdots & \ddots & \vdots \\ a_{m1} & a_{m2} & \dots & a_{mn} \end{bmatrix}}_{m \times n} = \mathbf{U}\mathbf{S}\mathbf{V}^{\mathrm{H}}$$

$$= \underbrace{\begin{bmatrix} | & | & & | \\ \mathbf{u}_1 & \mathbf{u}_2 & \dots & \mathbf{u}_m \\ | & | & & | \end{bmatrix}}_{m \times m} \underbrace{\begin{bmatrix} \sigma_1 & 0 & \dots & 0 \\ 0 & \sigma_2 & \dots & 0 \\ \vdots & \vdots & \ddots & \vdots \\ 0 & 0 & \dots & \sigma_n \\ 0 & 0 & \vdots & 0 \end{bmatrix}}_{m \times n} \underbrace{\begin{bmatrix} — & \mathbf{v}_1^H & — \\ — & \mathbf{v}_2^H & — \\ & \vdots & \\ — & \mathbf{v}_n^H & — \end{bmatrix}}_{n \times n} \tag{III.5}$$

For the remainder of this work, the focus will be on the matrices $\mathbf{U}$ and $\mathbf{S}$, since $\mathbf{V}$ describes current modes on the equivalent surface Σ, which are not directly exploited in the characterization process. Classically, the singular values are computed and then normalized with respect to their maximum value.

III.2.b Regularization

The distribution of singular values inherently captures how the geometry, sampling distribution, and relative positioning (distance) of the considered surface influence its associated radiation matrix. NF measurement surfaces S that are overly large, positioned far from the AUT, or discretized too finely can introduce redundant degrees of freedom that do not bring new information to the radiated field. This redundancy manifests itself in a distribution of singular values that rapidly decrease toward zero. Hence, when dealing with an ill-conditioned matrix $\mathbf{A}$, a large portion of its singular values may be close to zero, indicating the presence of linear dependencies between the radiated and equivalent current modes, as captured by the bases $\mathbf{U}$ and $\mathbf{V}^{\mathrm{H}}$. Such dependencies arise due to oversampling, poor discretization, or intrinsic redundancy in the modeled system. Conversely, a well-chosen surface geometry and sampling scheme produce a more compact and stable set of dominant singular values, clearly showing that the essential radiated modes are well-resolved by the considered configuration. As such, the SVD not only provides a powerful tool for regularization but also serves as an insightful diagnostic to optimize surface design and sampling strategies.

To illustrate these effects, consider an X-band 8×8 patch array (Appendix A) with an equivalent surface Σ, modeled as a plane of dimensions $5\lambda \times 5\lambda$, discretized at $\frac{\lambda}{3}$. The FF observation surface S' is a spherical-like surface with a fine angular discretization of $\Delta_\theta = \Delta_\phi = 0.5°$.

The SVD of the associated radiation matrix $\mathbf{A}'$ for the spherical FF observation surface S' reveals a rapid decay in its singular values, as illustrated in Fig. III.2.

This rapid decay indicates that only a limited number of dominant modes significantly contribute to field propagation, while the remaining modes mainly represent numerical instabilities or redundant basis vectors. In particular, in the presence of measurement noise, some higher-order modes may overfit the noise during the system-solving process, producing inaccurate or physically meaningless solutions.

In this example, the equiangular sampling of the FF observation surface S', especially with fine angular steps, introduces many points that contribute little independent infor-

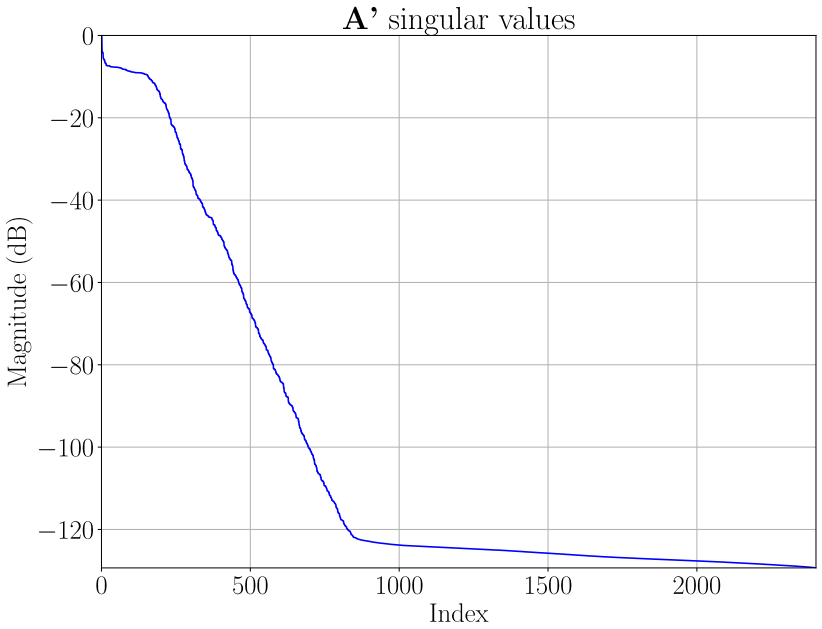

Figure III.2 – Example of singular value distribution illustrating the high redundancy in the radiation matrix $\mathbf{A}'$.

mation. Notably, the point density naturally increases near the poles, causing localized over-sampling, rapid singular value decay, and poor conditioning. In contrast, better conditioning characterized by a slower decay and a less abrupt drop could be achieved by reducing over-sampling and aligning the discretization more efficiently with the spatial bandwidth of the radiated fields.

To mitigate this issue and stabilize the solution, regularization is essential. Several well-known techniques such as Tikhonov method [85, 86], total variation [87], the LASSO scheme [88] and iterative methods [89] allow achieving this step. Another widely adopted approach is to apply a TSVD (also referred to as economy SVD), which reduces the rank of the matrix approximation to filter out the ill-conditioned components. This involves approximating the original matrix $\mathbf{A}$ as:

$$\mathbf{A} \approx \mathbf{A}_T = \mathbf{U}_T \mathbf{S}_T \mathbf{V}_T^{\mathrm{H}} \tag{III.6}$$

where the truncated matrix $\mathbf{S}_T$ retains only the T largest singular values, and $\mathbf{U}_T$, $\mathbf{V}_T^{\mathrm{H}}$ are the corresponding semi-unitary matrices. The truncation index T is determined based on a singular value threshold R, typically defined in decibels. All singular values smaller than R are discarded. The reduced-order representation of the matrix $\mathbf{A}$, obtained through

a TSVD that retains only the dominant singular values and their associated modes, is expressed as:

$$\mathbf{A} \approx \mathbf{U}_T \mathbf{S}_T \mathbf{V}^{\mathrm{H}}{}_T$$

$$= \overbrace{\begin{bmatrix} | & | & & | \\ \mathbf{u}_1 & \mathbf{u}_2 & \dots & \mathbf{u}_m \\ | & | & & | \end{bmatrix}}^{T} \overbrace{\begin{bmatrix} \sigma_1 & 0 & \dots & 0 \\ 0 & \sigma_2 & \dots & 0 \\ \vdots & \vdots & \ddots & \vdots \\ 0 & 0 & \dots & \sigma_n \\ 0 & 0 & \vdots & 0 \end{bmatrix}}^{T} \overbrace{\begin{bmatrix} — & \mathbf{v}_1^H & — \\ — & \mathbf{v}_2^H & — \\ & \vdots & \\ — & \mathbf{v}_n^H & — \end{bmatrix}}^{T} \tag{III.7}$$

This technique is implemented on Python environment through NumPy [90], SciPy [91] and Scikit-learn [92] libraries.

Without regularization, attempting to solve the IP directly using the Moore-Penrose pseudo-inverse $\mathbf{A}^{\dagger} = \mathbf{V}\mathbf{S}^{-1}\mathbf{U}^{\mathrm{H}}$ can yield numerically unstable or physically incorrect solutions. Small singular values amplify noise in the measured data $\mathbf{E}$, causing the least-squares solution $\mathbf{X}$ to diverge from any meaningful physical interpretation.

This problem is tightly linked to the convergence behavior of the solution toward the true physical currents of the AUT. In ill-posed problems, the least-squares solution may not converge to the true current distribution as the noise level decreases unless regularization is introduced. More formally, if no regularization is applied, the computed solution may minimize the residual norm $\|\mathbf{E} - \mathbf{A}\mathbf{X}\|_2$ but not necessarily approximate the true physical current distribution $\mathbf{X}$, especially in the presence of noise. Indeed, due to the principle of equivalence, there exists an infinite set of equivalent current distributions $\mathbf{X}$ that produce the same external field, making the inversion inherently non-unique in a physical sense.

Truncating the SVD ensures that only the modes with well-conditioned singular values contribute to the FF computation. This results in [93, 94, 95]:

- better numerical stability;
- improved robustness to noise;
- more physically consistent solutions;
- faster and more reliable convergence during iterative optimization procedures.

On the contrary, if the regularization is too strong, the retained modes may not be able to accurately capture more complex physical phenomena, leading to an oversimplified solution that cannot adequately describe more complex physical behaviors.

Hence, for each application case treated in this work, a cut-off threshold has been empirically found to yield a good trade-off between accuracy and robustness for most configurations considered.

III.2.c On the choice of the truncation index

The choice of the truncation index T is a critical step in the regularization of the radiation matrix $\mathbf{A}$, as it directly determines which singular vectors are retained in the ROM. Retaining too many modes may reintroduce ill-conditioning and noise sensitivity, while an overly excessive truncation may remove important content, degrading the quality of the solution.

Once a truncation is applied, the original minimization problem defined in Eq. (III.3) becomes a reduced-order approximation:

$$\|\mathbf{E} - \mathbf{A}_T\mathbf{X}\|_2 \leq \delta \tag{III.8}$$

where $\mathbf{A}_T$ is the radiation matrix issued from the TSVD step retaining only the first T dominant singular values.

To understand the behavior of this truncated system, we first consider an upper bound on the field norm. Given that $\mathbf{E}$ is the measurement vector over M sampling points, we have:

$$\|\mathbf{E}\|_2 \leq \sqrt{M}\|\mathbf{E}\|_\infty \leq \sigma_1\|\mathbf{X}\|_2 \tag{III.9}$$

where σ_1 is the largest singular value of $\mathbf{A}$, and the second inequality follows from the energy-preserving property of the SVD decomposition.

The impact of truncation on the approximation quality of the forward model can be characterized as:

$$\|\mathbf{AX} - \mathbf{A}_T\mathbf{X}\|_2 = \|(\mathbf{A} - \mathbf{A}_T)\mathbf{X}\|_2 \leq \|\mathbf{A} - \mathbf{A}_T\|_2\|\mathbf{X}\|_2 = \sigma_{T+1}\|\mathbf{X}\|_2 \tag{III.10}$$

where σ_{T+1} is the first discarded singular value. This expression highlights that the error

introduced by truncation depends directly on the norm of the excluded modes and the size of the current vector $\mathbf{X}$.

The truncation index T is determined via a threshold R (in decibels), which relates the smallest retained singular value σ_T to the largest σ_1 [70]:

$$\frac{\sigma_{T+1}}{\sigma_1} \leq 10^{R/20} \tag{III.11}$$

This choice of R should reflect the noise floor in the measured NF data $\mathbf{E}$. In practice, higher singular values often correspond to physically meaningful radiation modes, while lower ones are dominated by measurement noise or numerical artifacts [70]. Therefore, by setting an appropriate threshold, we suppress modes that only serve to overfit the noise in the IP.

From the previous bounds, the total error tolerance δ for the reduced problem can be explicitly expressed as:

$$\delta = \sqrt{M}\|\mathbf{E}\|_\infty 10^{R/20} \tag{III.12}$$

This expression offers an a priori estimate of the achievable computed FF error, depending on the chosen threshold R, the infinity norm of the data, and the number of measurement points M.

Furthermore, we can define a normalized error metric ENL that quantifies the relative fitting quality:

$$ENL = \frac{\|\mathbf{E} - \mathbf{A}_T\mathbf{X}\|_2}{\sqrt{M}\|\mathbf{E}\|_\infty} \leq 10^{R/20} \tag{III.13}$$

This shows that the singular value threshold R not only controls the truncation index T, but also imposes an upper bound on the achievable ENL level.

III.2.d Decomposition of the measured near-field

The choice of the singular value threshold R and by extension, the truncation index T is a crucial step in the regularization of the radiation matrix. It determines which radiative modes are preserved to construct the basis $\mathbf{U}_T$ in the radiation domain. This truncated matrix, derived from the full left-singular matrix $\mathbf{U}$, retains only the dominant T modes and thus forms a semi-unitary basis, satisfying $\mathbf{U}_T^{\mathrm{H}}\mathbf{U}_T = \mathbf{I}$ with $\mathbf{I}$ the identity matrix. The semi-unitary property ensures that $\mathbf{U}_T$ preserves orthogonality in its column space,

a critical feature for numerical stability and robustness in field decomposition.

This reduced basis provides a compact yet expressive representation of the radiated field $\mathbf{E}$. Indeed, the field can now be projected onto the dominant subspace spanned by $\mathbf{U}_T$ using the following decomposition:

$$\mathbf{E} \approx \mathbf{U}_T \mathbf{\Gamma} \tag{III.14}$$

where $\mathbf{\Gamma}$ is the vector of modal coefficients to be determined. This formulation enables an efficient reconstruction of the NF using only the essential radiation modes.

Moreover, this regularization step contributes to convergence stability: in the context of an ℓ_2-norm minimization, ill-conditioned or redundant basis vectors may lead to false minima, particularly when data is noisy or undersampled. Truncation eliminates these unstable modes, ensuring that the solution converges toward a physically meaningful minimum.

Importantly, with this construction of a ROM via the semi-unitary basis $\mathbf{U}_T$, the need to explicitly compute surface currents on equivalent surface Σ becomes optional. As will be demonstrated in the following section, alternative characterization techniques based directly on the field decomposition can be employed to describe the AUT, further simplifying the modeling procedure.

III.3 Reduction of the number of samples

The adverse effects of solving an ill-conditioned problem on the solution for the equivalent currents of the AUT can be avoided by regularizing the radiation matrix $\mathbf{A}$ associated with the NF measurement surface S. This regularization is performed using a TSVD that results in the construction of a ROM. By fixing a cut-off threshold R on the singular values to keep, a truncation index T defines the reduction of the model that has been operated. In this section, the direct relationship between the model order reduction and the required number of NF measurement points is demonstrated.

III.3.a From the singular values to the number of samples

The main consequence of lowering the model complexity through the selection of the T most fundamental radiation modes of $\mathbf{U}$ to express the NF is the reduction of the number of samples on S. Indeed, the index T can also be used to estimate a safe number of

samples needed to reach an accurate characterization result. This idea was first introduced by Bucci *et al.* [2]. Mézières *et al.* [70] then proposed to study this relationship between the number of measurement points N_{SVD} to keep and the order T of the reduced model in the context of using a ROM for spherical interpolation to speed up the FF measurements. An empirical criterion is established for several uniform sampling distributions on the spherical measurement surface:

$$N_{\text{SVD}} = \alpha T \tag{III.15}$$

where N_{SVD} is the estimated number of measurement points and α is an over-sampling factor set to 1.25 in the reference paper [70].

To sum up, the analysis of the singular values of $\mathbf{A}$ allows for estimating the minimum number of measurement points required within a dense sampling to retain sufficient information for solving the corresponding radiation problem. In our case, this corresponds to the number of NF measurement points necessary to achieve accurate FF computation.

Although this over-sampling factor is defined for spherical measurements and a specific application case of the ROM, one objective of this thesis is to adapt and verify this relation in our context.

III.3.b Sampling strategies

To reuse the relation defined by Mézières, the main challenge lies in employing the same uniform samplings defined on a spherical surface and applying them in our case of a planar NF measurement surface S, and furthermore on Euclidean non-conventional S enabled by our approach. Therefore, the positions of these N_{SVD} points must be determined using the well-known spherical uniform distributions used in the paper by Mézières.

1. The igloo sampling defined on a half-sphere by $\Delta\phi = \frac{\Delta\theta}{\sin\theta}$ [12], as illustrated in Fig. III.3.
2. The Fibonacci sampling or spiral sampling, constructed for each point k among the K points distributed on a half-sphere, is defined by $\phi_k = 2\pi\frac{1+\sqrt{5}}{2}(k-1)$ with $\theta_k = \arccos\left(1 - \frac{2(k-1)}{K}\right)$ [96, 97], as shown in Fig. III.4.

To preserve the angular distributions defined by these meshes on the Euclidean NF measurement surface S used in our model, a projection must be applied. Therefore, a perspective projection of these samplings from the mechanical reference system of the AUT onto the NF measurement surface S is performed, as detailed in Fig. III.5.

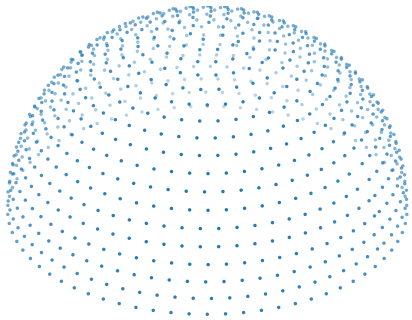

Figure III.3 – An igloo distribution of points over a half-sphere.

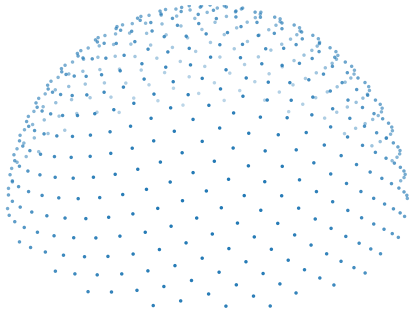

Figure III.4 – A Fibonacci distribution of points over a half-sphere.

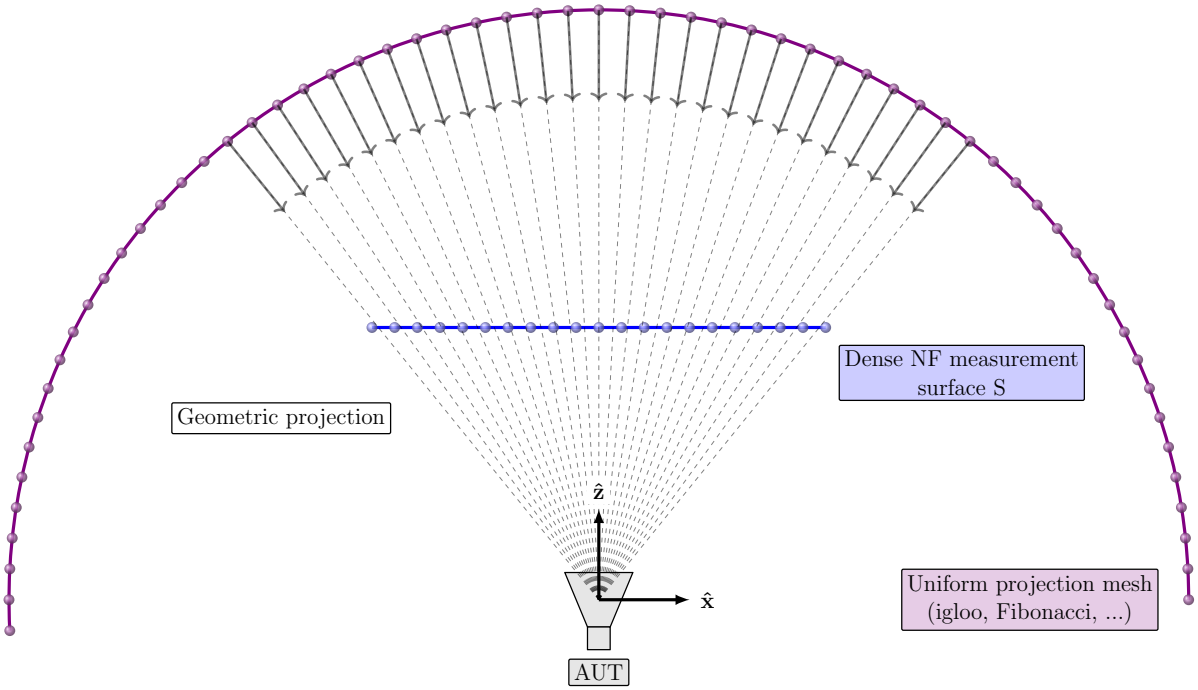

Figure III.5 – Illustration of the construction of non-conventional samplings for a planar NF measurement surface S using perspective projection of a spherical mesh.

By doing this, the resulting non-conventional sampling distributions on the NF measurement surface S have exactly the same angular distribution as the uniform meshes originally used to predetermine the number of measurement points to keep among the projected points. An example of an igloo and Fibonacci samplings defined over a regular grid on a planar measurement surface S are given in Fig. III.6 and Fig. III.7, respectively.

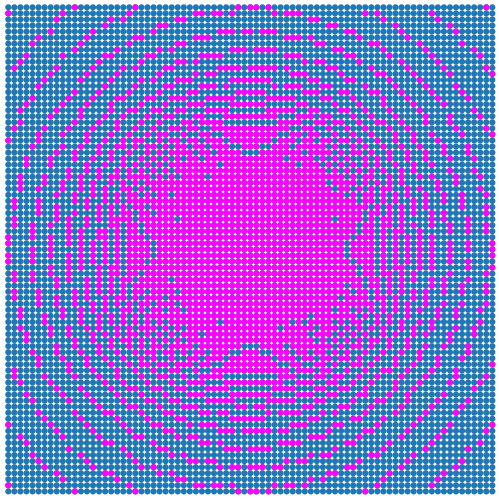

Figure III.6 – Example of a perspective projection of an igloo sampling (magenta) of 2571 points into a regular sampling over a planar NF measurement surface S (blue) of 6561 points.

In this manuscript, all these irregular distributions are constructed on dense and regular samplings on S. Thus, they can be defined as coarse sub-samplings of the NF measurement surface S. Therefore, their efficiency with respect to the probe path can be of interest. Finally, determining non-conventional samplings by this projection procedure yields a reduction in the number of NF samples, which enables us to verify the ROM property for estimating the number of measurement points.

It is also worth noting that the resulting sampling positions generally exhibit an aggregation of samples close to the boundaries of the measurement domain. This behavior is intrinsic to the projection-based construction and is consistent with observations reported in the literature on non-uniform and adaptive sampling strategies over planar surfaces. Several recent studies have addressed related issues, including the influence of boundary effects and sampling density distributions ([98], [99], [100]).

Moreover, these samplings can be directly applied to the NF measurement surface S

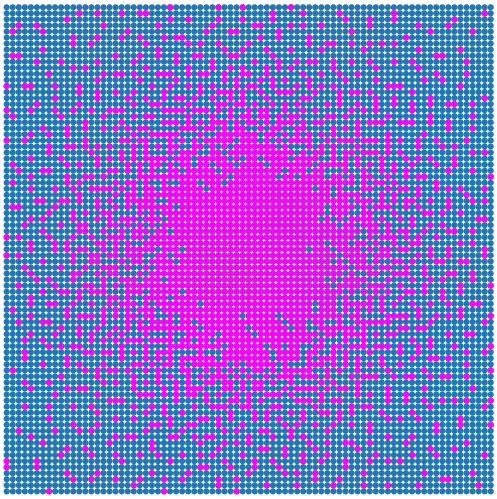

Figure III.7 – Example of a perspective projection of a Fibonacci sampling (magenta) of 2370 points into a regular sampling over a planar NF measurement surface S (blue) of 6561 points.

for a characterization method like IP without an additional analysis step.

III.3.c Characterization from an interpolated near field

Although the construction of a ROM enables the analysis of the number of samples required to achieve an accurate characterization, it also serves as a robust interpolation tool.

Methodology

The TSVD constructed on the radiation matrix $\mathbf{A}$ results in the determination of a decomposition basis for the radiated NF $\mathbf{U}_T$. From the estimate of the number of samples necessary to achieve correct characterization, the NF $\mathbf{E}_{\text{sub}}$ is then measured on the few points kept among the initial sampling related to the definition of $\mathbf{A}$. Moreover, the subsampling selection can be performed on the bases extracted from the ROM, namely on $\mathbf{U}_T$. This results in the following expression:

$$\mathbf{E}_{\text{sub}} = \mathbf{U}_{T,\text{sub}}\mathbf{\Gamma} \tag{III.16}$$

with $\mathbf{\Gamma}$ the decomposition coefficients to be determined.

By solving this linear system using the least-squares method, the coefficients $\mathbf{\Gamma}$ can be found. This solution then allows computing a NF on any measurement surface S by multiplying the coefficients by the corresponding basis containing the radiation modes, such as $\mathbf{U}_T$. In addition, since the radiation matrix $\mathbf{A}$ has been constructed on an initial sampling that is dense compared to the subsampling determined by the SVD analysis, interpolation of the NF on this initial sampling is possible:

$$\tilde{\mathbf{E}} = \mathbf{U}_T \mathbf{\Gamma} \tag{III.17}$$

Therefore, by decomposing a subsampled NF $\mathbf{E}_{\text{sub}}$ measured at selected points from the dense sampling used in the ROM construction, an interpolated NF $\tilde{\mathbf{E}}$ can be computed over the full dense sampling using the obtained weights $\mathbf{\Gamma}$. Furthermore, this interpolation is inherently regularized through the use of $\mathbf{U}_T$ in the computation.

Orthonormality and sampling size

Selecting only a limited subset of rows from the matrix $\mathbf{U}_T$ results in the loss of the orthonormality property inherent to the SVD. This degradation introduces errors in the interpolated NF data, which can become significant when the system is underdetermined due to excessive reduction in the sampling size.

To illustrate this effect, consider the usual X-band 8×8 patch antenna array, whose radiated NF is simulated on a planar NF measurement surface S of dimensions $10\lambda \times 10\lambda$ at a distance of 8λ above the array, with a spatial sampling interval of $\frac{\lambda}{2}$. The total number of measurement points is 441. The NF data components for this configuration are depicted in Fig. III.8.

A ROM is constructed by truncating singular values below a threshold of $-40\,\text{dB}$, corresponding to a truncation index $T = 146$. The estimated number of measurement points $N_{\text{SVD}} = 1.25T$ required to preserve the essential information is 182, corresponding to approximately 41.4% of the initial sampling.

First, a subsampling of the NF measurement surface S is generated using the igloo projection method, retaining 42% of the original measurement points (i. e., 187 points), as shown in Fig. III.9.

The asymmetry observed in the planar sampling distribution originates from the intrinsic discontinuities of the igloo sampling on the sphere. Since the spherical igloo partition is not perfectly uniform, its projection onto the planar NF surface leads to a non-symmetric

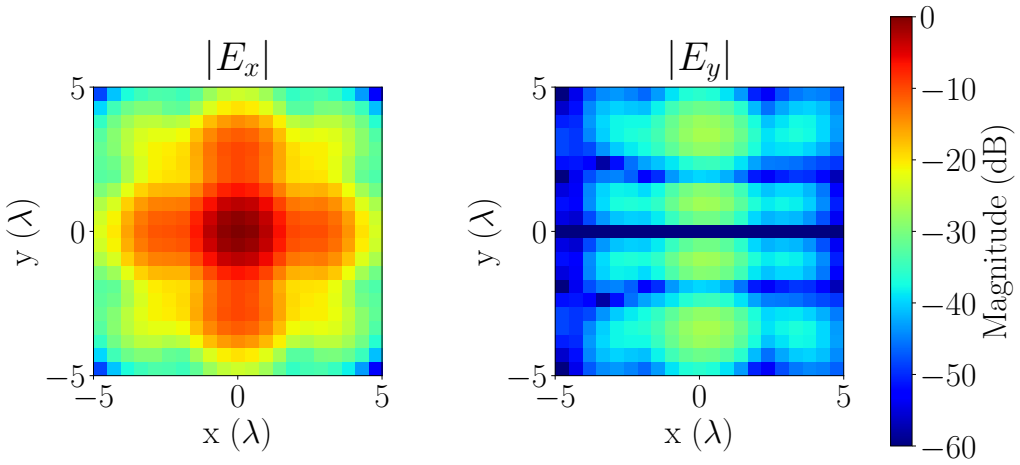

Figure III.8 – Representation of the measured polarizations of the NF data simulated using CST.

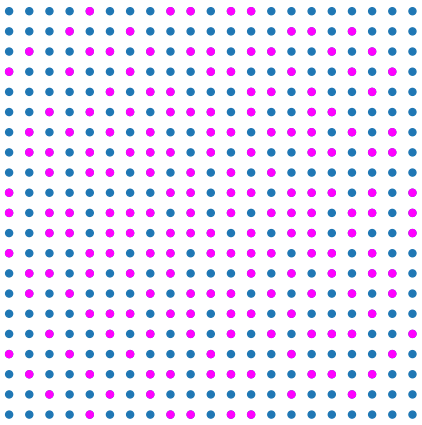

Figure III.9 – Subsampling selection via igloo projection (magenta), retaining 187 points from the regular planar NF measurement grid (blue) of 441 points.

spatial distribution of the retained sampling points.

The NF reconstructed using $\mathbf{U}_T$ at this subsampling level is given in Fig. III.10.

The interpolation error between the densely sampled NF data and the NF reconstructed using $\mathbf{U}_T$ is quantified by an ENL equals to -84.1 dB (reference-based normalization). This indicates that, when the number of measurement points is equal or higher than N_{SVD}, the NF $\tilde{\mathbf{E}}$ can be accurately interpolated despite the reduced sampling and the loss of orthonormality.

Next, a coarser subsampling is performed to exceed the criterion N_{SVD}, retaining only 40 measurement points (9.1% of the initial sampling), as illustrated again in Fig. III.11.

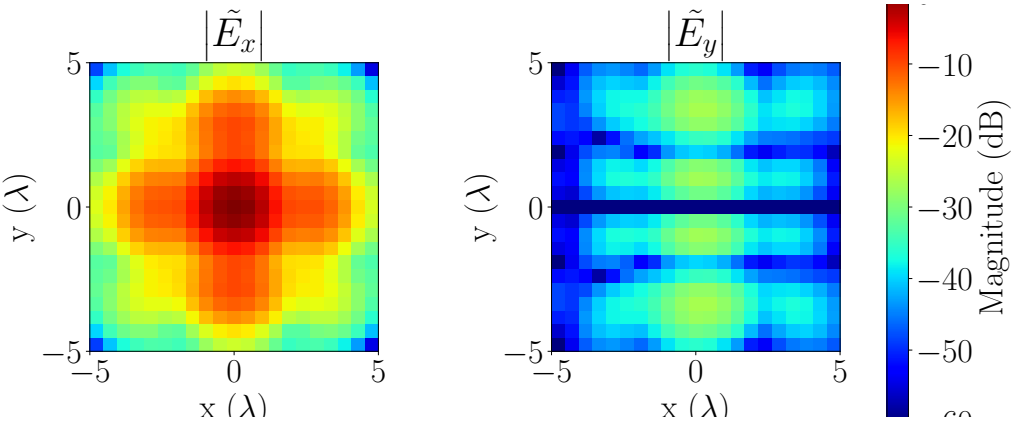

Figure III.10 – Representation of the reconstructed polarizations of the NF using $\mathbf{U}_T$.

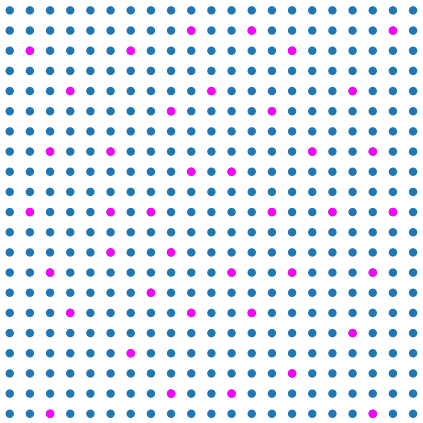

Figure III.11 – Subsampling selection via igloo projection (magenta), retaining 40 points from the planar NF measurement grid (blue) of 441 points.

The corresponding interpolation error, illustrated in Fig. III.12, shows a degradation with an ENL value of $-21.6\,\mathrm{dB}$. This increase in error occurs because the number of measurement points falls below the critical threshold N_{SVD}, leading to significant loss of orthonormality and inaccurate interpolation.

Therefore, adhering to the sampling criterion N_{SVD} is essential to ensure accurate NF interpolation.

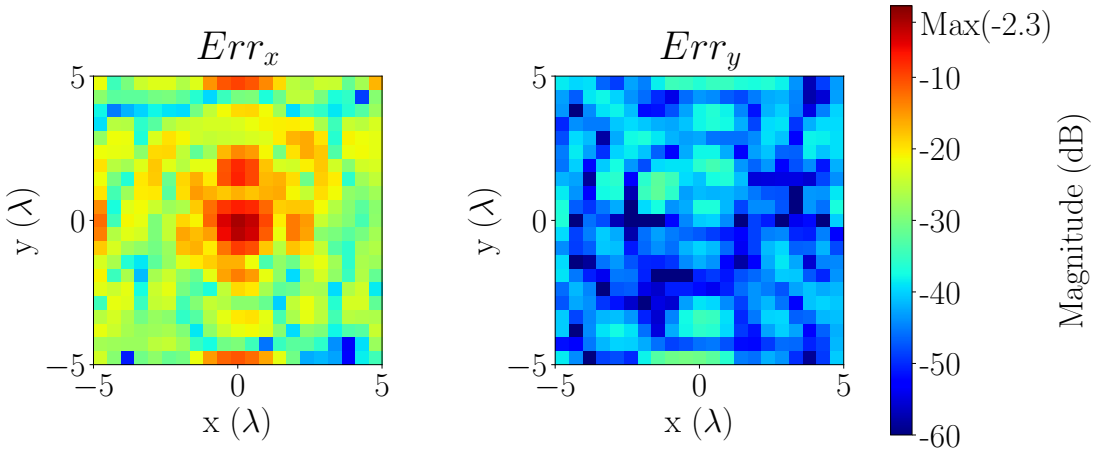

Figure III.12 – Interpolation error of the NF using ROM relative to the dense NF data.

Characterization methods based on an interpolation

Despite the error induced by the loss of orthonormality when applying a subsampling, these interpolated NF data can still be used for NFFFT to achieve the FF computation.

Indeed, if the initial sampling is chosen to be a regular dense sampling that respects the Nyquist criterion, the classical PWE method can be applied to the interpolated data, giving rise to a new characterization method named ROM-PWE. Alternatively, the IP method can also be employed, with the determination of the currents step coming from the interpolation, leading to a new ROM-IP method. This results in two new characterization methods: ROM-PWE and ROM-IP.

Finally, the characterization methods based on the construction of a ROM of the problem are summarized in the diagram shown in Fig. III.13.

III.3.d Application

The complete procedure for constructing a ROM must be validated on a practical application case to verify two main aspects:

1. that the over-sampling criterion of $\alpha = 1.25$ determined by Mézières for predicting the number of measurement points over a spherical surface required to achieve accurate characterization remains valid for NF acquisitions on Euclidean measurement surfaces S;
2. that interpolating NF data from a subsampling using both the ROM-PWE and ROM-IP methods yields accurate computed FF.

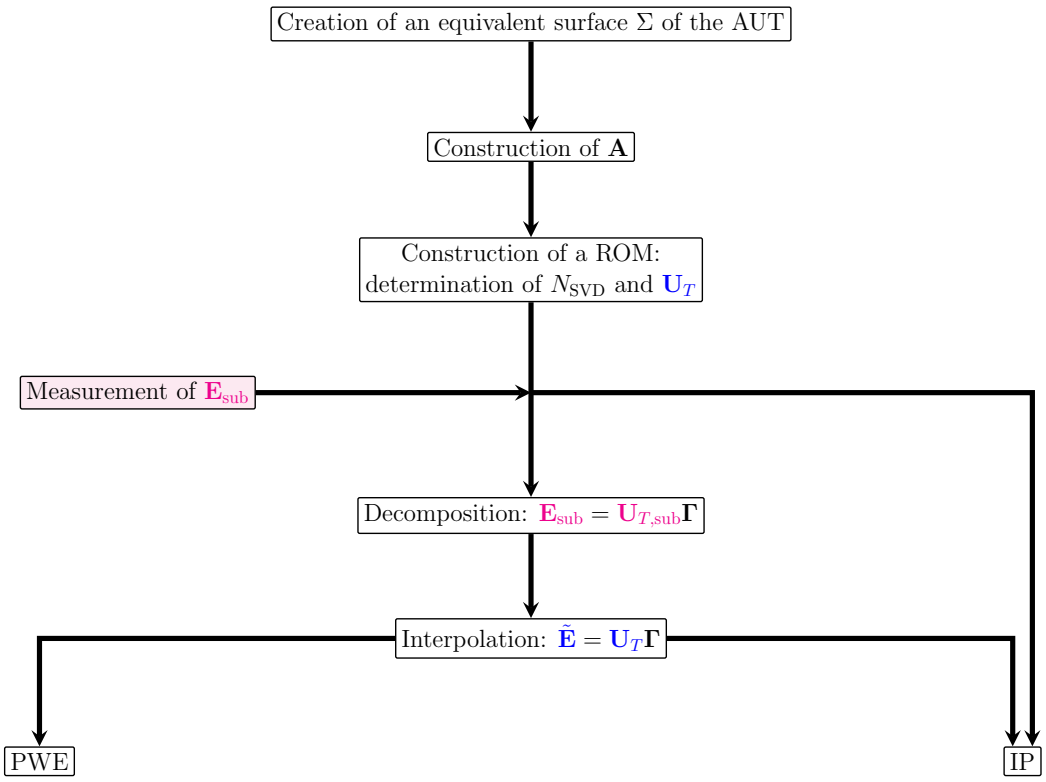

Figure III.13 – Schematic view of the various characterization methods offered by the construction of a ROM.

Additionally, since non-conventional NF measurement surfaces S are used to evaluate the ROM performance, the trends observed in the previous truncation effects study are compared to the results obtained for reduced sampling with and without an interpolation step.

This application is based on works that have been made during this thesis and that led to publications [101, 102, 103].

Methodology

The AUT used is the X-band 60×1 patch array (Appendix A) introduced in Section II.5. Two beam directions are considered: a boresight configuration at ($\theta_{\text{beam}} = 0°, \phi_{\text{beam}} = 0°$), and a steered beam at ($\theta_{\text{beam}} = 80°, \phi_{\text{beam}} = 0°$). The equivalent surface Σ is a box-shaped distribution of tangential dipoles with dimensions $30\lambda \times 1\lambda \times 1\lambda$ and a spacing of $\frac{\lambda}{3}$ (see Section II.4). The total number of dipoles is 4392. The E_x and E_y components are simulated for two geometries of the NF measurement surface S: a plane and a half-box. The planar S measures $40\lambda \times 40\lambda$ and is placed 8λ from the coordinate origin, with a

sampling step of $\frac{\lambda}{2}$. The corresponding number of measurement points is equal to 6561. The half-box has the same dimensions and sampling as the planar surface, but includes four lateral faces extending up to $z = 0$, enclosing the upper half-space and resulting in a total of 11681 points.

All characterization methods introduced previously (IP, ROM-IP, and ROM-PWE) are applied and systematically compared to the classical PWE. To reduce the number of samples on these NF measurement surfaces S, igloo and Fibonacci sampling projections are used. The number of measurement points selected by the subsampling is denoted N, and the reference sampling, defined on a regular grid satisfying the Nyquist criterion with $\frac{\lambda}{2}$ spacing, has N_{PWE} points.

The truncation level for singular values is set to $R = -40\,\text{dB}$. Both regularization parameters *rcond* for the decomposition of the subsampled NF and the equivalent current determination are set to 10^{-2}. The resolution of the FF observation surface S' is $\Delta_\theta = \Delta_\phi = 1°$, except for radiation pattern plots where $\Delta_\theta = \Delta_\phi = 0.5°$. The characterization accuracy is evaluated using the ENL metric, normalized with respect to the CST FF reference. Finally, the computed FF zones are defined by the extent of the planar NF measurement surface S to illustrate the benefits of using non-conventional geometries for S to mitigate truncation effects. A UV representation of the radiated pattern relative to these zones for both operating mode with and without beam tilt is given in Fig. III.14.

No beam steering

The first study considers the boresight direction ($\theta_{\text{beam}} = 0°, \phi_{\text{beam}} = 0°$) with a planar NF measurement surface S. From the over-sampling factor $\alpha = 1.25$ determined by Mézières *et al.* [70], the number of measurement points estimated by the singular value analysis is $N_{\text{SVD}}/N_{\text{PWE}} = 14.1\%$. The evolution of the ENL between the computed FF according to the number of sampling points (N/N_{PWE}) is given in Fig. III.15 for the methods IP, ROM-IP and ROM-PWE and for two types of projections (igloo and Fibonacci).

With classical sampling (N_{PWE} points), the PWE method reaches an ENL of $-42.1\,\text{dB}$. The ROM-based approaches allow a significant reduction in the number of samples while achieving even higher accuracy. The over-sampling criterion α reliably predicts the maximum possible reduction for planar NF measurements. Non-conventional sampling strategies such as igloo and Fibonacci exhibit similar trends and enable the ROM to reach its predicted limits. When the number of points is reduced significantly, concentrating

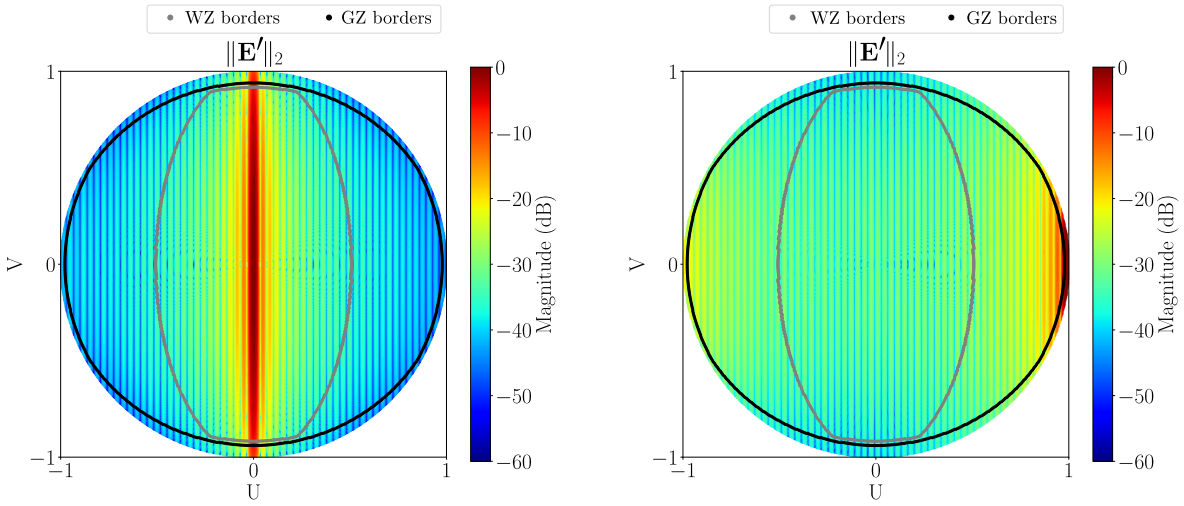

(a) No beam tilt

(b) Steered main beam

Figure III.14 – Amplitude of the simulated FF with borders of the computed FF zones defined by the planar NF measurement surface S for no beam tilt (a) and with an inclination of $\theta_{\text{beam}} = 80°$ (b). As reminder, the WZ refers to the zone where the computed FF is expected to be accurate, while GZ corresponds to partially informed region where only partial NF data contributes to the FF computation.

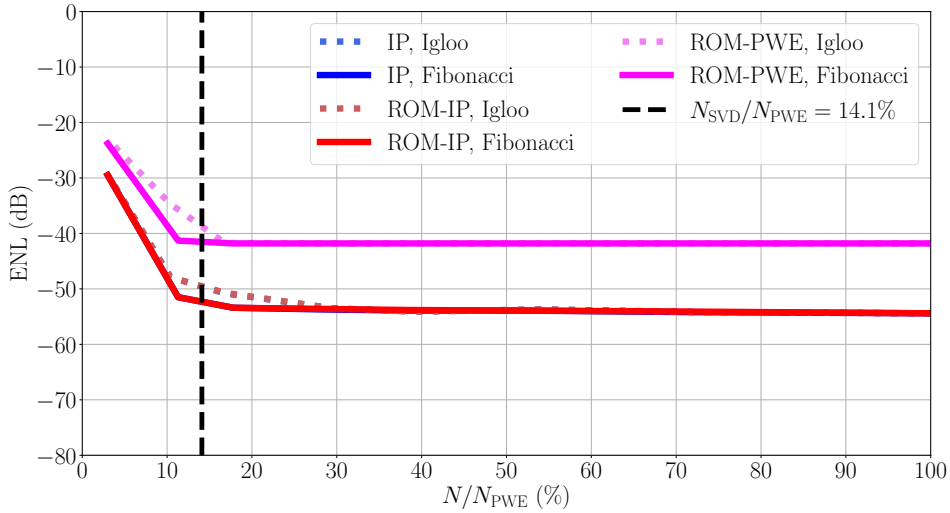

Figure III.15 – Beam at $\theta_{\text{beam}} = 0°$, planar NF measurement surface S: accuracy of the various methods as a function of the number of measurement points relative to classical PWE distribution of samples, for different sampling strategies. The curves corresponding to the Inverse Problem (IP) method are overlapped by that of the ROM-IP method, making them visually indistinguishable in the figure.

most of them in the center appears most appropriate with respect to characterization accuracy. Although the ROM-PWE results are slightly less accurate than directly determining equivalent currents, the FF computation quality remains robust against further sampling reduction thanks to interpolation. This confirms the effectiveness of the ROM for pre-determining the required number of measurement points. In this case, the IP and ROM-IP methods yield the best computed FF, maintaining better accuracy than classical PWE while using only about 12% of the original samples.

Inclination of the main beam

Next, the array main beam is steered to $(\theta_{\text{beam}} = 80°, \phi_{\text{beam}} = 0°)$. The same convergence study is performed for a half-box NF measurement surface S. Using the same over-sampling factor and truncation level than in the previous study, the ROM predicts $N_{\text{SVD}}/N_{\text{PWE}} = 18.2\%$. Figure III.16 shows the computed FF accuracy for IP and ROM-IP with igloo and Fibonacci projections on the half-box.

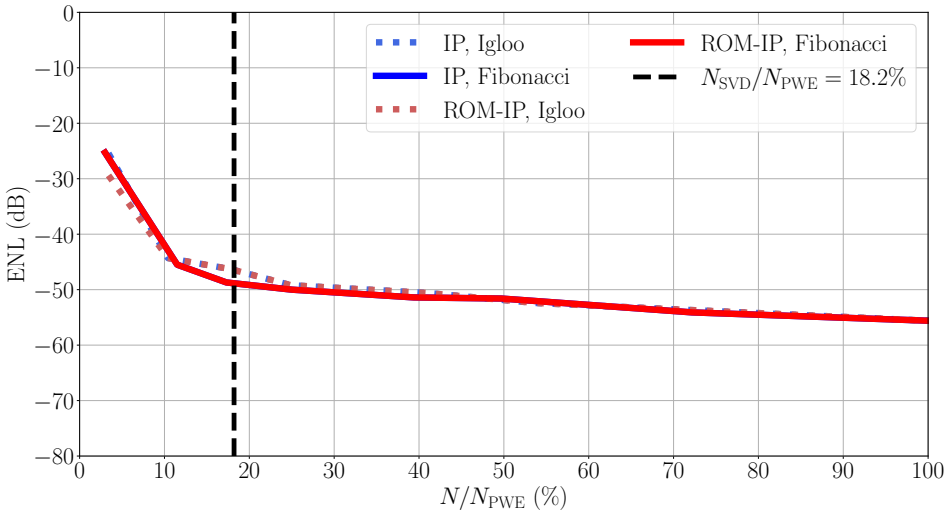

Figure III.16 – Beam at $\theta_{\text{beam}} = 80°$, half-box NF measurement surface S: accuracy of the methods as a function of the number of measurement points relative to classical PWE distribution of samples, for different sampling strategies. Here again, the curves corresponding to the IP method are overlapped by that of the ROM-IP method, making them visually indistinguishable in the figure.

Because the ROM-PWE approach combines the computation errors of both the ROM-based model and the classical Fourier-based PWE, the analyses in the remainder of this manuscript are limited to methods that rely solely on the equivalent model framework.

This restriction allows for a more direct and unbiased assessment of the interpolation performance and robustness of our approach under conditions of significant sampling reduction.

In the specific case of a half-box geometry with a beam direction of ($\theta_{\text{beam}} = 80°, \phi_{\text{beam}} = 0°$), the PWE is additionally computed for the planar measurement surface S, serving as a reference for comparison with the results obtained using our methods.

Again, a significant sampling reduction is achieved. Despite the high beam inclination, the over-sampling criterion α still provides a reliable estimate of the minimum required sampling. Approximately 20% of the classical samples are sufficient to ensure an $ENL \leq -50\,\text{dB}$, compared to $-28.1\,\text{dB}$ for the PWE method (100% of the points). Both igloo and Fibonacci projections yield similar trends, therefore only the Fibonacci projection is used in further tests. A remark can be made regarding the distribution of the sampling points: although the maximum radiated power is concentrated near the edges of the upper measurement plane of the half-box-shaped NF measurement surface S, the considered projections result in sampling patterns with a higher density of points near the center. Despite this mismatch between the sampling distribution and the location of the main beam, the characterization accuracy remains satisfactory.

To further analyze the behavior of the different characterization methods, a metric is introduced to quantify the difference in FF computation errors between the IP and ROM-IP approaches. This metric is defined as $|\Delta ENL|$ with $\Delta ENL = ENL_{\text{IP}} - ENL_{\text{ROM-IP}}$. The variations of $|\Delta ENL|$ for both igloo and Fibonacci sampling projections are shown in Fig. III.17.

The results show that, regardless of whether the IP or ROM-IP method is used, the computed FF accuracy remains nearly identical, except for very low sampling ratios in the case of the igloo projection. This behavior is due to the regularization applied during the least-squares solution for determining the equivalent currents. Since the same *rcond* parameter (10^{-2}) is used for both methods, the resulting FF computations exhibit similar errors relative to the reference. Furthermore, in the ROM-IP method, both the TSVD step and the subsampled NF decomposition benefit from regularization, ensuring stable results. These consistent performances underline the flexibility and robustness of the model, which maintains reliable accuracy even when the sampling size is significantly reduced.

To assess the impact of the geometry of the NF measurement surface S on truncation effects and the accuracy of the computed FF patterns, a comparison is carried out between planar and half-box-shaped surfaces S at $\theta_{\text{beam}} = 80°$ using the Fibonacci projection.

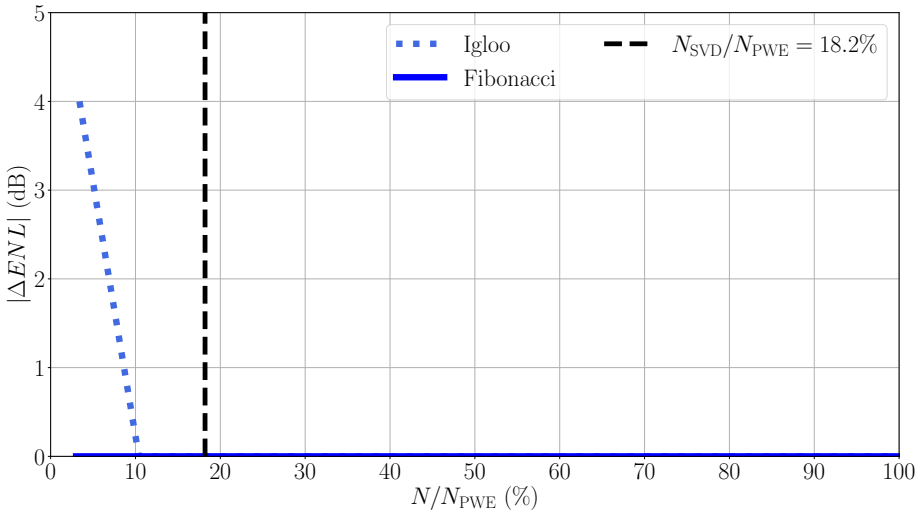

Figure III.17 – Beam at $\theta_{beam} = 80°$, half-box NF measurement surface S: evolution of the difference in computed FF accuracy between the IP and ROM-IP methods for the two sampling projections.

Subsequently, the computed FF zones obtained from the planar NF measurement surface S are used as a reference to evaluate the effect on the FF computation accuracy provided by the half-box geometry of S. Using a non-planar S clearly improves accuracy, with mean ENL values of -32.6 dB (planar) versus -51.8 dB (half-box) for a number of measurement points $N \geq N_{SVD}$. This is illustrated in Fig. III.18, which compares the co-polarization cut-plane at $\phi = 0°$ computed with IP for $\frac{N}{N_{PWE}} = 20\%$ (around 1310 measurement points relative to the classical measurement setup).

To better illustrate the distribution of the points corresponding to the selected sub-sampling on the half-box, Fig. III.19 is provided.

The benefits of the enhancement of the WZ through the use of a half-box-shaped NF measurement surface S is evident and is reflected by ENL values in the WZ, GZ, and BZ as presented in Table III.1.

Geometry	ENL (dB)	ENL_{WZ} (dB)	ENL_{GZ} (dB)	ENL_{BZ} (dB)
plane	-33.0	-53.2	-30.1	-23.7
half-box	-48.9	-57.6	-51.6	-38.3

Table III.1 – Beam at $\theta_{beam} = 80°$: comparison of the computed FF accuracy using the IP method between a planar NF measurement surface S and a half-box-shaped surface, while conserving 20% of the NF samples.

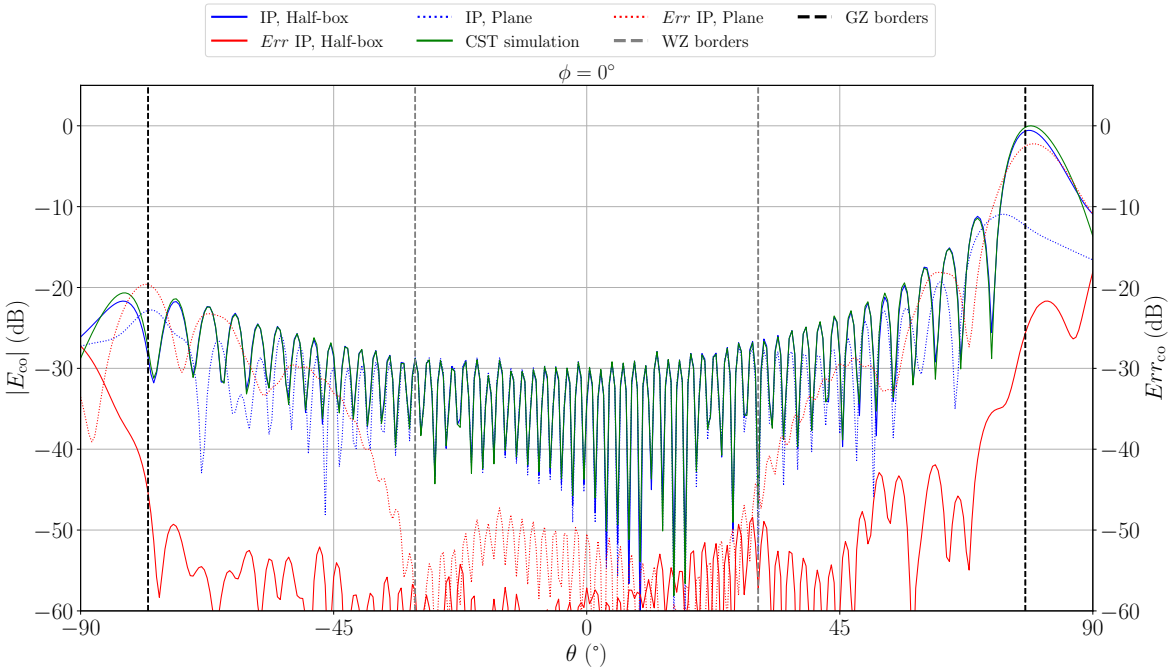

Figure III.18 – Beam at $\theta_{\text{beam}} = 80°$: comparison of computed co-polarization with IP using Fibonacci subsampling for planar and half-box NF measurement surfaces S. The computed FF zones are associated to the planar S.

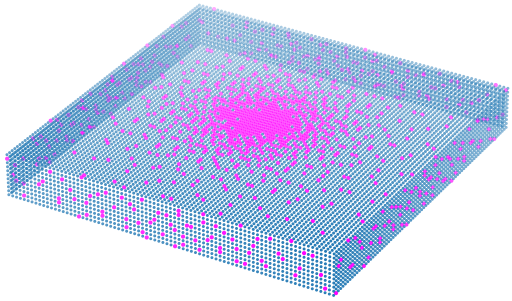

Figure III.19 – Representation of the selected 20% of points ($\frac{N}{N_{\text{PWE}}} = 20\%$) on the half-box-shaped NF measurement surface S.

In summary, applying the ROM to the tilted beam case confirms that the oversampling criterion α remains valid even for highly directive beams and non-planar measurement geometries. Using a half-box NF measurement surface S effectively mitigates truncation effects, improving computed FF accuracy across all zones while maintaining the excursion in the XOY plane. The stability of the IP and ROM-IP methods con-

firms the robustness of the proposed approach, achieving high accuracy with significant sampling reduction and practical subsampling projections.

Summary

Overall, this application study demonstrates that the ROM framework is a reliable and efficient tool for guiding NF sampling on Euclidean measurement surfaces S. It confirms the validity of the over-sampling criterion, allows a significant reduction in measurement effort, and guarantees accurate computed FF when combined with ROM-PWE or ROM-IP. Moreover, adapting the geometry of the NF measurement surface S to the AUT radiation characteristics clearly enhances FF prediction by limiting truncation effects. The proposed ROM-based approach therefore provides a robust strategy for optimizing NF measurement campaigns, balancing reduced acquisition time with high-fidelity results.

III.4 Construction of the direct near-field to far-field transform

The construction of an equivalent model of the AUT using dipoles unlocks characterization methods that overcome the limitations of the classical transform. Indeed, the IP, ROM-IP, and ROM-PWE have been presented in this chapter, and their advantages in the context of planar NF measurements have been highlighted on application cases. However, to simplify the use of both the equivalent model and the ROM to achieve the easiest characterization with the lowest number of samples and truncation effects, a new approach to the problem is needed.

III.4.a A new reading of the characterization problem

Until now, the problem treated in this manuscript has been summarized by the illustration given in Section II.3.a, specifically in Fig. II.11.

As a reminder, the radiation matrix $\mathbf{A}$ links the dipole distribution to the NF measurement surface S, while $\mathbf{A}'$ plays the same role for the FF observation surface S'. In this formulation, a radiation matrix is associated with each surface of the problem.

The idea is to exploit the core property of the radiation matrix, which establishes a link between two point clouds defined in distinct geometric spaces, independently of the

physical quantities observed at these points. Therefore, this new reading of the characterization problem leads to the introduction of a new, unique radiation matrix $\mathbf{A}_\mathrm{c}$ to bind both NF measurement surface S and FF observation surface S' to the equivalent surface Σ using only one mathematical object:

$$\mathbf{A}_\mathrm{c} = \begin{bmatrix} \mathbf{A} \\ \mathbf{A}' \end{bmatrix} \tag{III.18}$$

First, the TSVD of $\mathbf{A}_\mathrm{c}$ yields to the determination of three matrices $\mathbf{U}_T$, $\mathbf{S}_T$ and $\mathbf{V}_T^\mathrm{H}$ containing information on both surfaces S and S'. The determination of the decomposition basis $\mathbf{U}_T$ in this new formulation is crucial, as this matrix contains orthonormal field modes for the NF and FF surfaces simultaneously.

Thus, a direct path between the measured NF $\mathbf{E}$ and computed FF $\tilde{\mathbf{E}}'$ is now made possible through a transition matrix:

$$\tilde{\mathbf{E}}' = \mathbf{U}_{T,|\mathrm{S}'}\mathbf{U}_{T,|\mathrm{S}}^\dagger\mathbf{E} \tag{III.19}$$

where $\mathbf{U}_{T,|\mathrm{S}}$ and $\mathbf{U}_{T,|\mathrm{S}'}$ are the restrictions of $\mathbf{U}_T$ to the rows associated with surfaces S and S', respectively.

With this transition matrix, there is no need to compute the equivalent currents or to decompose the measured NF as in the IP, ROM-IP, and ROM-PWE methods. Indeed, we constructed a transition matrix using only $\mathbf{U}_T$. Thus, using a direct NFFFT avoids determining a regularization criterion for solving the linear system.

This new method, named ROM-NFFFT, fully exploits the advantages offered by the use of an equivalent model and ROM analysis while enabling a direct NFFFT with a single radiation matrix. Furthermore, this easy-to-use method allows the transition matrix to be computed for a generic characterization configuration, i. e., for fixed surfaces Σ, S, and S'.

Indeed, in a scenario where the AUT position and external dimensions are known, as well as the operating frequency, a box-shaped equivalent surface Σ can be defined around the AUT. Then, the positions of a sufficiently enclosing NF measurement surface S such as a half-box with a dense and regular sampling in accordance with the available NF measurement means as well as those of an observation surface S' at FF range, can be determined. The corresponding radiation matrix $\mathbf{A}_\mathrm{c}$ can be computed, the SVD analysis performed, and the transition matrix $\mathbf{U}_{T,|\mathrm{S}'}\mathbf{U}_{T,|\mathrm{S}}^\dagger$ constructed.

Thus, the configuration associated with this final matrix can be reused in a series

of characterization tests, fitting the dimensions of the pre-processed setup, for different sampling strategies included in the initial sampling on S as well as on S'. The ROM, which can be applied to any radiation matrix, could be combined with the ROM-NFFFT to compute the FF on a subsampled FF surface S', ultimately achieving the characterization on a dense sampling grid, as is common practice, for example, in the article by Corre *et al.* [82].

In summary, the steps of the developed direct NFFFT based on the construction of a ROM of the problem are shown in Fig. III.20.

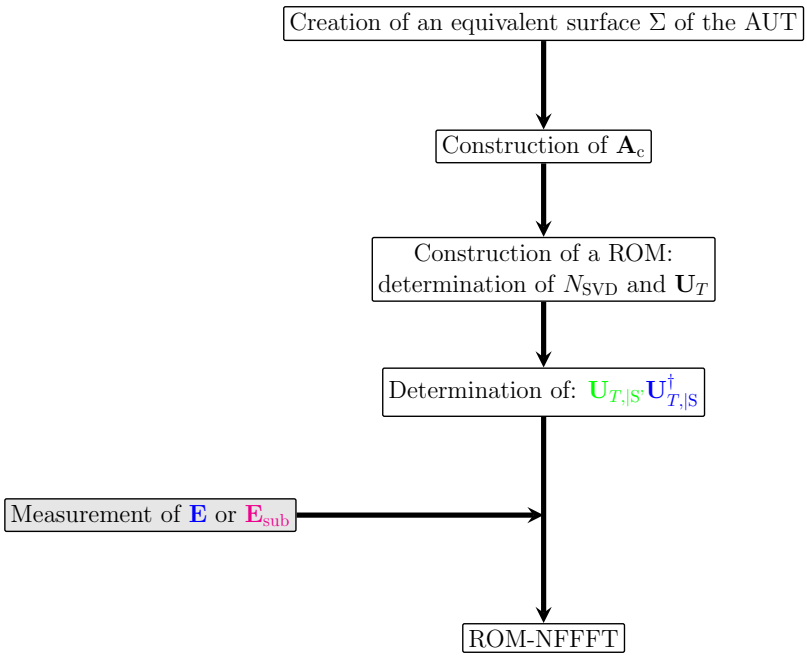

Figure III.20 – Schematic view of the direct NFFFT based on the construction of a ROM.

III.4.b Validation

To validate this new characterization method, ROM-NFFFT, on a concrete application case for which the results of the other methods are known, the same example introduced in Section III.3.d is used. As a reminder, this numerical case considers an X-band patch array with 60 elements, radiating along two main beam directions: ($\theta_{\text{beam}} = 0°, \phi_{\text{beam}} = 0°$) and ($\theta_{\text{beam}} = 80°, \phi_{\text{beam}} = 0°$).

The ROM-NFFFT is applied to the most challenging characterization scenario studied so far, with a main beam steered to ($\theta_{\text{beam}} = 80°, \phi_{\text{beam}} = 0°$). Here again, the computed FF zones are computed with respect to the planar NF measurement surface S.

As explained previously, the distribution of the singular values $\mathbf{S}$ reflects how the geometry, the sampling strategy, and the positioning of the surface associated with the radiation matrix affect the conditioning. In this new formulation, where NF and FF surfaces are linked within a single matrix, the SVD of $\mathbf{A}_c$ is therefore directly dependent on the geometry, sampling density, and relative positioning of these surfaces with respect to the equivalent surface Σ. This means that the conditioning of the problem is inherently tied to the joint configuration of the NF and FF domains, rather than being determined by each surface independently. The distribution of the singular values $\mathbf{S}$ for matrices $\mathbf{A}$ (associated to the half-box S) and $\mathbf{A}'$ is shown in Fig. III.21 and Fig. III.22, respectively.

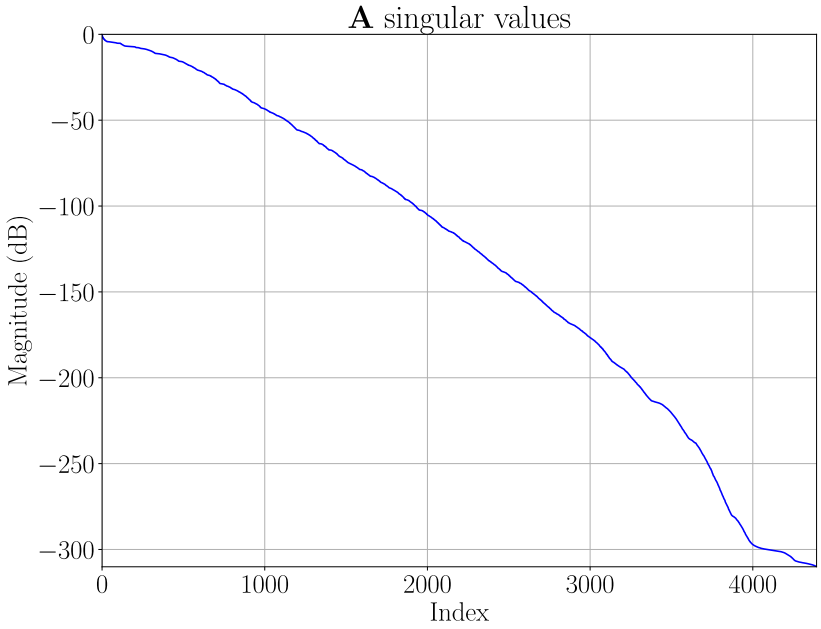

Figure III.21 – The singular value distribution of the matrix $\mathbf{A}$.

In Fig. III.23, the singular values of the concatenated matrix $\mathbf{A}_c$ constructed from $\mathbf{A}$ and $\mathbf{A}'$ are shown. As a reminder, all the singular values presented in this document are normalized relative to their maximum.

The specific behavior of NF measurement surface S is well described by the singular values of the concatenated matrix while the FF observation surface S' is not impacting the distribution. This is due to the difference of scale between the singular values associated with the NF and FF parts inside the matrix $\mathbf{A}_c$. Indeed, the distance gap between the two geometric spaces is clearly mirrored in the singular value distribution of $\mathbf{A}_c$. Thus, for this linked problem, this is mainly the NF measurement surface S that determines how

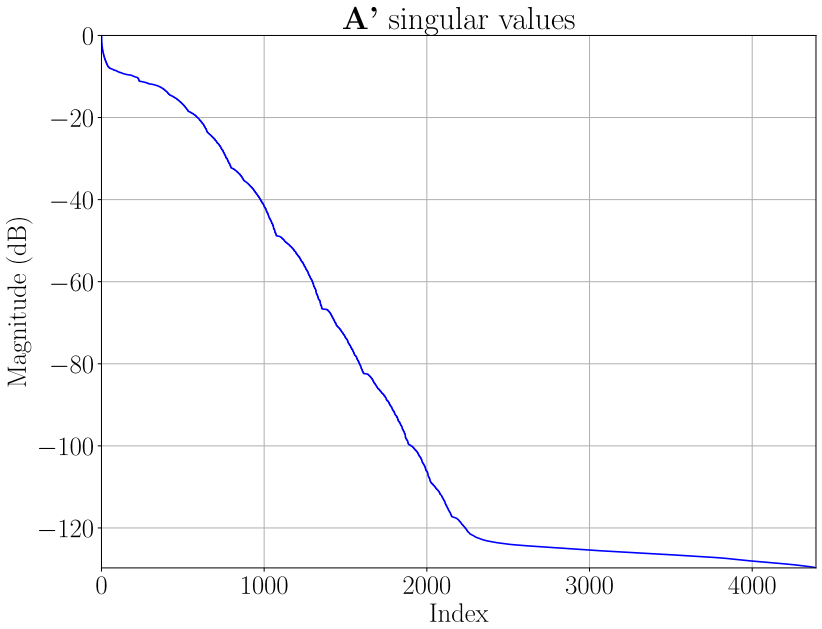

Figure III.22 – The singular value distribution of the matrix $\mathbf{A}'$.

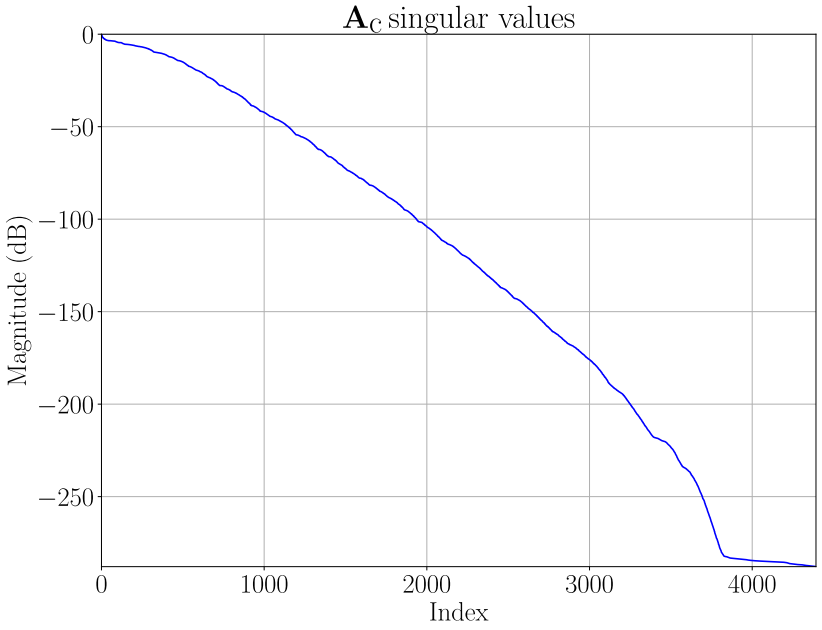

Figure III.23 – The singular value distribution of $\mathbf{A}_c$ in the case of a linked problem with information on both NF and FF surfaces.

the SVD operates, although the information of the FF observation surface S' is effectively present inside the radiation matrix.

The comparison of the computed co-polarization on the E-plane using the ROM-NFFFT and IP methods is shown in Fig. III.24 for a significant sampling reduction to 20% of the points on a half-box-shaped NF measurement surface S relative to classical planar sampling.

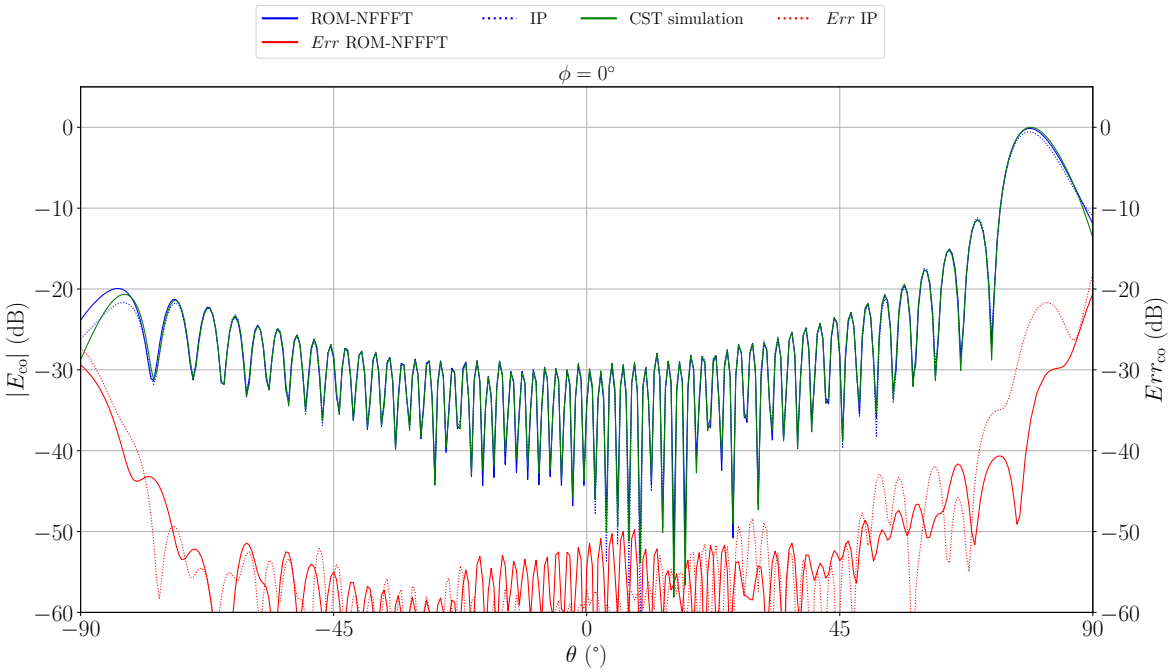

Figure III.24 – Beam at $\theta_{\text{beam}} = 80°$: comparison of computed co-polarization between ROM-NFFFT and IP methods using Fibonacci subsampling for a half-box NF measurement surface S.

The associated ENL values for the different computed FF zones related to the planar surface S are detailed below in Table III.2.

Method	ENL (dB)	ENL_{WZ} (dB)	ENL_{GZ} (dB)	ENL_{BZ} (dB)
IP	-48.9	-57.6	-51.6	-38.3
ROM-NFFFT	-53.7	-57.6	-55.7	-45.8

Table III.2 – Beam at $\theta_{\text{beam}} = 80°$: comparison of the computed FF accuracy between the IP and ROM-NFFFT methods while conserving 20% of the NF samples on a half-box-shaped NF measurement surface S.

The same trends observed for the IP and ROM-IP methods regarding sampling reduction and truncation effects are confirmed for the ROM-NFFFT. Moreover, the co-polarization cut-plane and the detailed errors computed in each zone show a clear improvement in the FF computation with this direct NFFFT. In the BZ, which is the most

challenging zone for characterizing the radiation pattern, the ENL_{BZ} decreases by $-7.5\,\mathrm{dB}$ relative to the FF computation achieved using the IP technique. More generally, an improvement in accuracy is observed compared to methods that rely on a least-squares solution, confirming the benefit of using ROM-NFFFT for precise and straightforward characterization. However, it should be noted that these results have been obtained in the absence of measurement noise, and the relative advantage may be less pronounced under realistic noisy conditions.

In this section, a new characterization method named ROM-NFFFT has been introduced to avoid the need for regularization parameters associated with least-squares solving in the IP, ROM-IP, and ROM-PWE methods while fully exploiting the benefits of the ROM construction. An application to a simulation case has confirmed the advantage of this direct NFFFT compared to the other approaches presented in this work. In the final chapter, all the developed characterization methods will be applied to experimental cases to definitively validate their applicability to real-life antennas.

III.5 Conclusion

The development steps leading to a new direct NFFFT based on our approach have been detailed.

First, the construction of a ROM for the characterization problem is explained, with particular emphasis on the crucial SVD step. The importance of properly regularizing the radiation matrices when dealing with an ill-posed problem, and the choice of an appropriate truncation level for this purpose, have been demonstrated. Furthermore, the properties of the ROM in pre-determining the number of samples required to achieve accurate characterization, while providing a decomposition basis in the radiation field space, highlight the potential of this technique to both reduce the measurement effort and improve computed FF accuracy.

Non-conventional sampling strategies, inspired by the work of Mézières in the context of spherical measurements, have been adapted to estimate the number of samples needed for FF computation using a ROM. This led to a significant reduction in sampling size. Moreover, the over-sampling criterion empirically determined by Mézières's analysis has been confirmed to provide a safe margin that ensures reliable FF computation in the case of planar NF measurements. Additionally, the use of irregular sampling distributions on non-planar NF measurement surfaces S, as introduced in the previous chapter, further

demonstrated the benefits of applying the ROM to radiation matrices derived from an equivalent model, both in reducing the number of samples and mitigating truncation effects.

The determination of a decomposition basis for the radiated field space also enabled the development of new characterization methods based on NF interpolation. The resulting methods, ROM-IP and ROM-PWE, illustrated the multiple possibilities offered by the ROM and its advantages in regularization and sample reduction.

Finally, this work proposes a new interpretation of the characterization problem, which, when combined with the use of a ROM, leads to an easy-to-use method lead to an easy-to-use method based on constructing a transition matrix for a direct NFFFT. This approach overcomes the drawbacks of previous methods, enabling the ROM-NFFFT technique to be reused in generic characterization scenarios. The effectiveness of this method is demonstrated in the next chapter on experimental cases, with probe compensation integrated into the model, leading to a complete and practically applicable approach.

Chapter IV

Application of characterization methods on experimental cases

IV.1 Introduction

IV.1.a Motivations

The characterization methods developed in this manuscript have been first validated on numerical cases. However, our goal is to demonstrate that our procedure can be integrated into standard planar NF measurement procedures. This requires proposing a reliable method to account for probe effects, which significantly influence the measurements in NF ranges.

Therefore, the first part of this chapter introduces several probe compensation techniques, which can be grouped into two main categories. The first relies on analytical formulas to model the probe radiation pattern, enabling proper retrieval of the AUT FF. The second applies our equivalent modeling approach directly to the measurement probe. Based on this model, new compensation methods are proposed using either the NF or FF data radiated by the probe, obtained through numerical simulations or measurements.

Furthermore, these compensation techniques are designed for seamless integration into the radiation matrix associated with the NF measurement surface S, i. e., forming the central element of the model proposed in this work. This integration ensures a practical and efficient implementation of the developed characterization methods. In particular, incorporating probe effects enables the formulation of a complete ROM-NFFFT method that can be applied to realistic measurement scenarios, while exploiting the sampling reduction and truncation limitation strategies presented in previous chapters. The final section of this chapter demonstrates this through two experimental validations: one on a W-band horn antenna and another on an X-band Luneburg lens with high beam-steering capability.

IV.1.b State of the art

In physics, regardless of the application domain, the fundamental principle of measurement remains the same: a physical quantity must be determined using a device capable of capturing it accurately. In the context of antenna characterization, and more specifically when assessing radiation properties, one of the primary quantities of interest is the radiation pattern of the AUT. The measurement device to achieve this assessment is typically another antenna acting as a probe to capture the radiated field. All standard antenna measurement systems rely on such probes to acquire field data at each sampling position on the NF measurement surface S. A crucial aspect of the post-processing step is the need to account for the influence of the measurement probe on the acquired field data. Two different mechanisms must be distinguished.

First, the probe's own radiation pattern acts as a spatial filter on the measured field. These probe-induced effects are systematic and depends only on the probe characteristics. It is precisely this contribution that is modeled and compensated in the present work. Second, there is the possibility of genuine electromagnetic coupling between the AUT and the probe, which alters the radiation of both systems. Such interactions are more complex to address and are not included in the present compensation framework. Thus, accurate FF computation of the AUT true radiation pattern requires a dedicated post-processing step known as probe compensation to remove these perturbations.

The first step in probe compensation is to characterize the radiation pattern of the probe itself. This is a critical but non-trivial task, often achieved by preliminary probe characterization and either performing measurements with a well-calibrated reference probe or using high-fidelity full-wave electromagnetic simulations to determine its FF pattern [104].

During the NF acquisition process, the probe scans the measurement surface S following a predefined sampling grid. At each sampling point, the probe influence on the measured field must be compensated by applying probe correction coefficients, which represent the probe radiated field integrated to the chosen field representation in the NFFFT, as determined by the measurement geometry [24]. These coefficients form the probe correction matrix, which is incorporated into the transformation process to de-embed the probe effects and compute the AUT true radiation pattern.

Thus, the implementation of probe compensation depends on the geometry of the measurement setup. In spherical NF measurements, probe correction is based on the probe SWE, as formulated by Hansen [14]. However, since this correction is not inherently in-

tegrated into the spherical NFFFT, additional steps are required to apply it properly. These steps can be complex, and practical implementations often rely on first-order approximations of the probe spectral coefficients. While this simplifies computation, it can introduce notable errors in the final FF computation. To mitigate this, recent works have focused on refining SWE-based corrections [105, 106] and incorporating equivalent source modeling approaches [107, 57]. Nevertheless, the reliance on simplified approximations often restricts the use of probes to standard configurations such as OEWG, limiting measurement bandwidth and flexibility. To overcome these limitations, Saccardi *et al.* [108] proposed an enhanced approach to improve probe compensation accuracy within the SWE framework.

In the planar case, probe compensation is more straightforward because it is inherently integrated into the PWE method [11]. The probe correction coefficients are generally obtained analytically or numerically, interpolating the probe FF radiation pattern at the required spectral points to achieve accurate de-embedding during the NFFFT.

However, a recent study from Paulus *et al.* [109] proposes a fully probe-corrected NFFFT to handle cases where the probe characteristics are not completely known. These methods estimate or compensate for the unknown probe effects, enabling accurate computation of the antenna FF pattern from NF measurements without requiring complete knowledge of the probe. This interesting work is based on the use of an equivalent model of the AUT which is directly related to the compensation methods discussed in this chapter.

Proper probe compensation is essential for ensuring high-accuracy characterization, particularly for electrically large antennas or complex measurement configurations, such as those addressed in this work.

IV.1.c Contributions

To compensate for probe effects in the present study, both analytical and numerical strategies are proposed. First, common techniques such as analytical formulas and spline interpolation are implemented to compute the probe radiation characteristics. Then, a more advanced numerical method is introduced, which consists of constructing an equivalent model of the measurement probe, using the same approach developed in this thesis for the AUT. In this case, from either NF or FF data, the equivalent currents of the probe are estimated, and the radiated field generated by these currents is computed. All of these techniques are validated on simulation test cases to accurately reproduce the radiation pattern of the measurement probe.

These compensation techniques are subsequently integrated into the developed characterization framework to propose new probe correction procedures. In particular, the radiation matrix associated with the NF measurement surface S is corrected and successfully tested through simulated NF measurement scenarios of an X-band horn antenna. This step demonstrates the feasibility and robustness of including probe modeling directly into the equivalent model-based characterization process.

Finally, the complete set of characterization methods, including probe compensation, is experimentally applied to two different antennas: a W-band horn antenna and an X-band Luneburg lens. These two AUTs have been selected because they present radiation properties that define challenging characterization cases to test our approach. In particular, the applicability of the ROM-NFFFT is assessed in terms of reusability, computational efficiency, and ease of integration into measurement workflows. Discussions are also provided on the role of measurement errors and their influence on the probe compensation step.

Moreover, detailed analyses are conducted on the impact of sampling distribution and truncation mitigation strategies on the characterization accuracy. In line with the objectives of this thesis, a significant reduction in the number of required samples and an effective limitation of truncation effects are achieved, thereby validating the trends previously observed in simulation and confirming the robustness of the proposed approach in experimental scenarios.

IV.2 Probe compensation

To achieve the main objective of this work which is developing characterization methods that overcome the limitations of classical transforms for planar NF measurements, accurate probe compensation is essential. While the PWE method inherently integrates probe de-embedding within its NFFFT procedure, our goal is to design an equally direct and reliable approach for retrieving the true radiation pattern of the AUT. This enables the development of complete equivalent model-based characterization methods that can be readily applied to practical measurement scenarios.

IV.2.a Probe compensation in near-field measurements

The transmission between the probe and the AUT is fundamentally governed by the Lorentz reciprocity theorem, which states that in a linear, passive, time-invariant, and reciprocal medium such as free space, if an antenna A transmits an electromagnetic field and an antenna B receives it, the signal received at B is identical to that at A if their roles are reversed [5]. This principle underlies the use of probes in antenna measurements: whether the probe operates in transmit or receive mode, the mutual interaction with the AUT remains consistent.

In classical measurement systems, the probe can operate either in transmission or reception, depending on whether the AUT is tested in emission or in reception. When the AUT is in emission, the probe typically operates in reception mode to sample the radiated field. Conversely, when the AUT is in reception, the probe acts as the transmitter, illuminating the AUT. By reciprocity, these two configurations are fully equivalent. In both cases, the probe radiation pattern acts as a spatial filter, weighting the contributions of the AUT field components differently across its aperture and angular spectrum [11]. In the spectral domain, this filtering effect manifests as a convolution between the AUT radiation pattern and the probe reception pattern.

At FF distances, the probe behaves as an ideal receiving antenna. The measured field corresponds to the product of the AUT radiation and the probe pattern, and compensation is achieved by dividing the measured data by the known FF pattern of the probe at the observation angles of interest.

In the NF region, however, particularly in the reactive zone, the measured field contains not only propagating components but also evanescent components that decay rapidly with distance and are sensitive to the exact geometry and position of the probe. Moreover, the probe scanning path across the NF measurement surface S introduces additional phase and amplitude variations that must be compensated to ensure accurate FF computation. In practice, the probe is positioned in the radiating NF region to minimize perturbations caused by reactive effects and rapidly decaying evanescent modes, which do not influence the computed FF pattern [32]. Consequently, sophisticated probe correction techniques are required to mitigate these effects and accurately recover the corresponding FF pattern.

For planar NF measurement surfaces S, the impact of probe-AUT transmission is highly sensitive to the probe radiation characteristics. Ideally, the probe should approximate an isotropic infinitesimal dipole, minimizing spatial filtering effects across the AUT aperture. Since such a probe is physically unrealizable, electrically small, low-gain, and

linearly polarized antennas such as OEWGs or standard gain horns are commonly used. These probes offer relatively simple and well-understood radiation patterns that can be modeled accurately for correction [24, 11, 110]. An example of a OEWG used for X-band NF measurements is presented in Fig. IV.1.

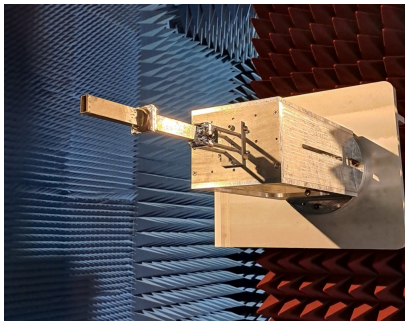

Figure IV.1 – Representation of an X-band OEWG used for NF measurement at IETR laboratory.

Nevertheless, deviations from the idealized probe model such as limited directivity, cross-polarization effects, or positioning uncertainties can introduce significant measurement errors if not properly accounted for during probe correction [42, 111, 112]. Some studies have addressed these limitations through advanced correction methods [113, 114], but their implementation can be complex and probe-specific.

Therefore, accurate probe modeling, rigorous calibration, and well-designed compensation methods are crucial to ensure that the final NFFFT produces a faithful FF computation of the AUT radiation characteristics. This is particularly important when dealing with large or complex antennas, or when applying advanced measurement strategies such as sparse or irregular sampling.

IV.2.b Determination of probe radiation characteristics

Accurate probe compensation requires precise knowledge of the probe radiation behavior. Traditionally, this is achieved by determining the probe FF pattern, but in this work, we also propose a method based on its NF characteristics using an equivalent model. This section reviews classical analytical and numerical methods and introduces the newly developed equivalent model-based approach for probe characterization.

Analytical formulas

Analytical expressions are commonly used to describe the FF radiation pattern of standard probes, such as OEWG or pyramidal horns, whose simple radiation behavior allows closed-form approximations with small interpolation errors.

In this study, only OEWG probes are considered. The widely used Yaghjian approximation [115] describes in the upper half-space the E- and H-plane electric fields ($\mathbf{E}_\mathrm{E}$ and $\mathbf{E}_\mathrm{H}$) radiated by an OEWG of aperture dimensions $a \times b$ and polarized along the y direction:

$$\begin{aligned}
\frac{\beta}{k_0} &= \sqrt{1 - \left(\frac{\pi}{k_0 a}\right)^2} \\
\mathbf{E}_\mathrm{E}(\theta) &= A_\mathrm{E} \frac{\left[1 + \frac{\beta}{k_0}\cos(\theta) + \Gamma\left(1 - \frac{\beta}{k_0}\cos(\theta)\right)\right]}{\left[1 + \frac{\beta}{k_0} + \Gamma\left(1 - \frac{\beta}{k_0}\right)\right]} \frac{\sin\left(\frac{k_0 b}{2}\sin(\theta)\right)}{\frac{k_0 b}{2}\sin(\theta)} \\
\mathbf{E}_\mathrm{H}(\theta) &= A_\mathrm{E}\left(\frac{\pi}{2}\right)^2 \cos(\theta) \frac{\cos\left(\frac{k_0 a}{2}\sin(\theta)\right)}{\left[\left(\frac{\pi}{2}\right)^2 - \left(\frac{k_0 a}{2}\sin(\theta)\right)^2\right]}
\end{aligned} \tag{IV.1}$$

where β/k_0 is the normalized propagation constant, A_E is the incident-mode amplitude (typically 1), and Γ is the reflection coefficient. The fields are interpolated over the whole upper half-space as follows:

$$\begin{aligned}
\mathbf{E}_\theta(\theta, \phi) &= \mathbf{E}_\mathrm{E}(\theta)\sin(\phi) \\
\mathbf{E}_\phi(\theta, \phi) &= \mathbf{E}_\mathrm{H}(\theta)\cos(\phi)
\end{aligned} \tag{IV.2}$$

These formulas only approximate the co-polarized component of the probe FF. Then, it is important to notice that the resulting FF is independent of the observation distance and normalized to represent the ideal probe behavior as a filter.

Spline interpolation

An alternative to the analytical approach is to rely on numerical methods, which allow the probe radiation pattern to be characterized without being restricted to simple or canonical behaviors such as those of an OEWG or a horn antenna. One such method is spline interpolation, which provides a flexible way of reconstructing the probe response from discrete data.

The general idea is to use either full-wave electromagnetic simulations or dedicated

FF measurement campaigns to obtain reference radiation data of the probe. From these samples, a multidimensional spline interpolation is constructed to approximate the probe radiation pattern over the entire angular directions of interest. This interpolation is performed by constructing piecewise polynomials between adjacent sampled points, ensuring continuity of the function and its derivatives up to the desired order. As a result, the interpolated radiation pattern provides a smooth and accurate representation of the probe response, even in regions where no direct samples are available.

Nevertheless, spline interpolation also introduces practical challenges. The quality of the reconstructed probe pattern strongly depends on the density and coverage of the initial sampling grid. Sparse or non-uniform data may lead to interpolation errors, especially in regions where the probe exhibits sharp radiation features or nulls. Moreover, for broadband probes, separate interpolations must be constructed at multiple frequency points, which increases the amount of required input data.

Equivalent model

Then, the last proposed technique is to employ the equivalent model developed in this work. This approach is particularly valuable because it allows us to construct a compensation technique based on the probe NF, which is central to the proposed compensation method described in the following parts.

The equivalent model represents the probe as a distribution of infinitesimal dipoles. This model can be reused in different measurement configurations and adapted to any type of probe, as demonstrated in the previous sections. The equivalent currents of the probe, denoted $\mathbf{X}_{\mathrm{P}}$, can be determined in two ways:

- by solving an IP using NF data $\mathbf{E}_{\mathrm{P}}$;
- by performing a RA using FF data $\mathbf{E}'_{\mathrm{P}}$.

Illustrations of both approaches are shown in Fig. IV.2 and Fig. IV.3.

Both methods share the same goal: to accurately estimate the equivalent currents of the measurement probe. Once determined, these currents can be used to compute the probe radiated field at either NF or FF ranges. This capability is essential for compensating the probe effects directly in the NFFFT-based characterization process.

It is important to emphasize the difference between the IP and RA approaches.

- The IP method uses NF data to retrieve the equivalent currents. Since NF measurements contain some information about the radial component of the electric field,

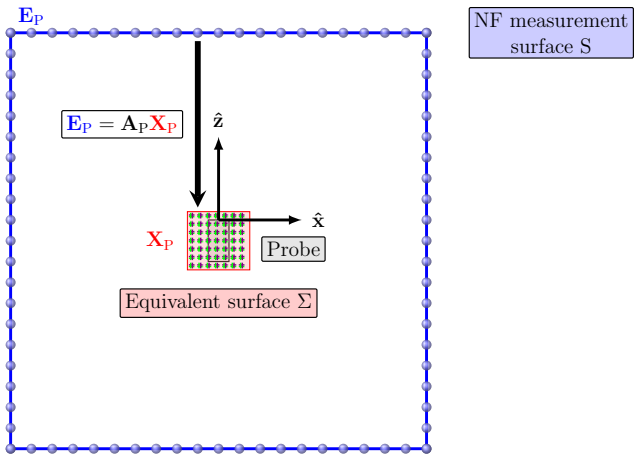

Figure IV.2 – Illustration of the equivalent currents determination using the IP method.

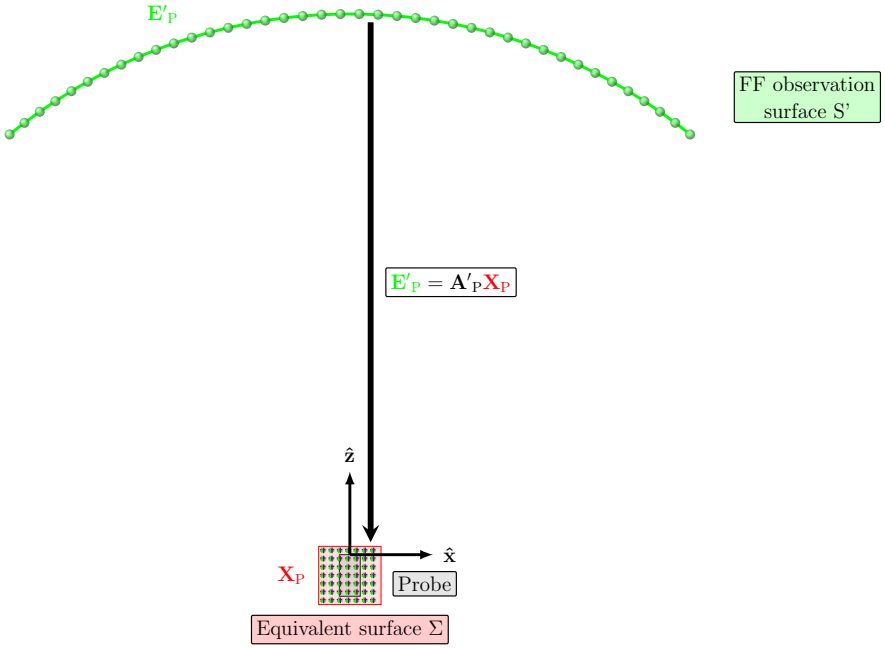

Figure IV.3 – Illustration of the equivalent currents determination using the RA method.

this method allows a highly accurate reconstruction of the probe NF. Consequently, it is particularly suited for the proposed compensation technique, which operates in the NF domain.

- The RA method uses FF data to determine the equivalent currents. While this method yields slightly better accuracy in the FF, it is less precise for the NF reconstruction because the FF does not capture the radial field components explicitly. However, this method is more practical for real measurements since FF data can be obtained experimentally without prior knowledge of the probe radiation pattern.

Hence, although both approaches allow the computation of NF and FF fields, the model constructed from a specific type of data (NF or FF) naturally performs best in the corresponding range. This distinction is crucial for the compensation methodology proposed in the next section: the NF reconstruction used for compensation rely on the IP-based model, while the FF characterization of the probe use the RA-based model.

Validations

The analytical and numerical methods are validated through CST simulations of an X-band OEWG operating at 10 GHz. The goal is to verify that the proposed techniques to compute the probe radiation characteristics yields to a correct accuracy and can be used to compensate the probe effects in the characterization process. In particular, ensuring that both NF (equivalent model-based method) and FF can be correctly computed, ensuring that the compensation procedures are sustainable.

The different methods developed to determine the probe characteristics are summarized in the diagram shown in Fig. IV.4.

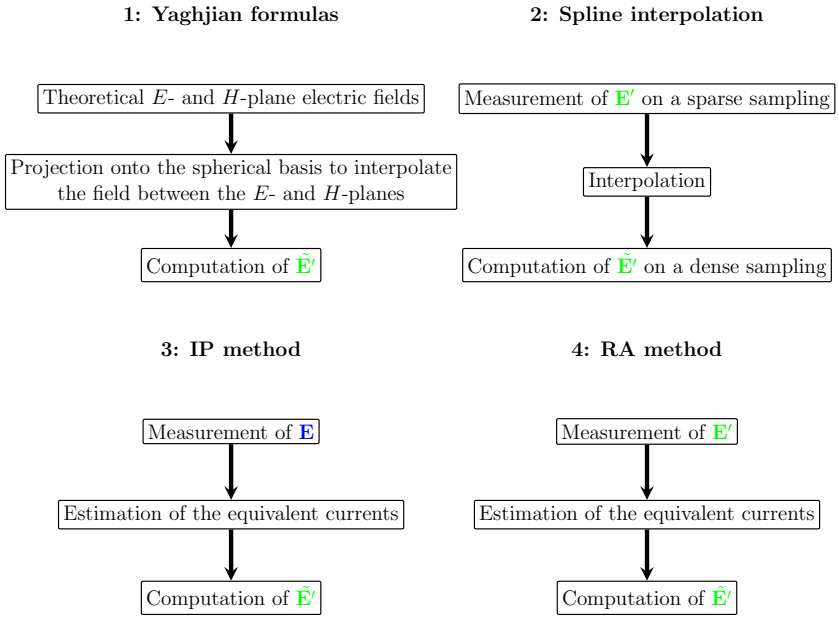

Figure IV.4 – Illustration of the different proposed methods to compute the radiation pattern of the measurement probe.

The waveguide has dimensions $(0.76\lambda \times 0.34\lambda \times 2.00\lambda)$ and is enclosed by a box-shaped equivalent surface Σ of dimensions $(1.0\lambda \times 0.5\lambda \times 2.5\lambda)$, sampled with a mesh size of $\frac{\lambda}{6}$. Indeed, since the antenna dimensions are too small to satisfy the safety criteria defined

in Section II.4, the spacing between dipoles must be refined to $\frac{\lambda}{6}$. The equivalent model of the probe is shown in Fig. IV.5.

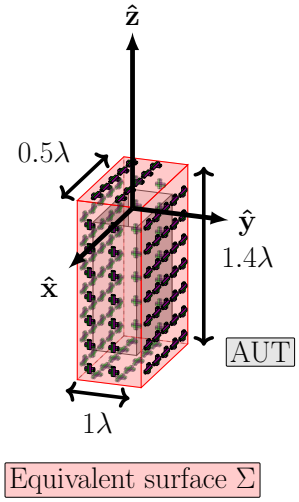

Figure IV.5 – Equivalent model of the simulated measurement probe.

The NF measurement surface S is defined as a $10\lambda \times 10\lambda \times 10\lambda$ box centered on the probe to fully capture its radiated field in all directions. The FF observation surface S' is a sphere with equiangular sampling $\Delta_\theta = \Delta_\phi = 1°$. For both analytical and equivalent model-based methods, the computed fields are compared to a CST reference FF, and error metrics are computed using reference-based normalization.

The analytical Yaghjian approach is applied using $a = 0.76\lambda$, $b = 0.34\lambda$. The reflection coefficient is set to $\Gamma = 0.1$, consistent with the value obtained from CST simulation. Its radiation pattern is shown for the cut-planes $\phi = 0°$ and $\phi = 90°$ in Fig. IV.6.

While the general behavior is well captured, limitations appear near grazing angles and in reproducing ripples along the $\phi = 0°$ cut-plane, with $ENL = -11.3\,\text{dB}$. These elevated errors can be explained by the definition of Yaghjian's formulas, which are strictly valid in the upper-half radiation space and are therefore poorly suited to model probe back-propagation directions.

Then, from the FF data simulated in CST with an angular sampling step of $\Delta_\theta = \Delta_\phi = 1°$, a spline interpolation is applied in order to reconstruct the field on a finer grid of $\Delta_\theta = \Delta_\phi = 0.3°$. The main idea is that the spline provides a smooth, higher-order interpolation of the sampled data, thereby enabling an accurate computation of the probe radiation pattern over arbitrary angular directions. The computed radiation pattern is then compared with the FF reference simulated directly on the dense angular grid of $\Delta_\theta = \Delta_\phi = 0.3°$ in Fig. IV.7.

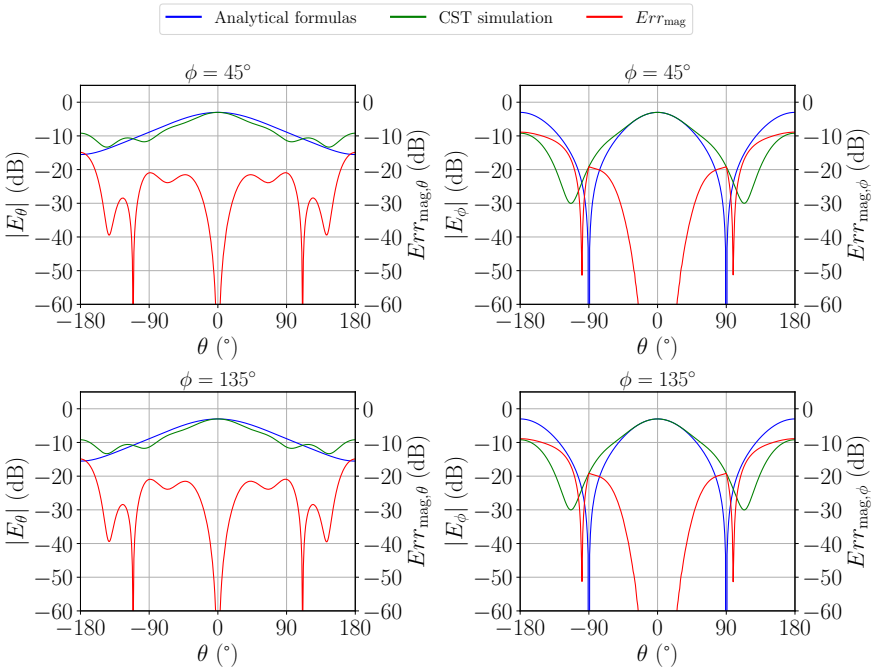

Figure IV.6 – FF computation of the measurement probe using Yaghjian's closed-form formulas compared to the CST reference.

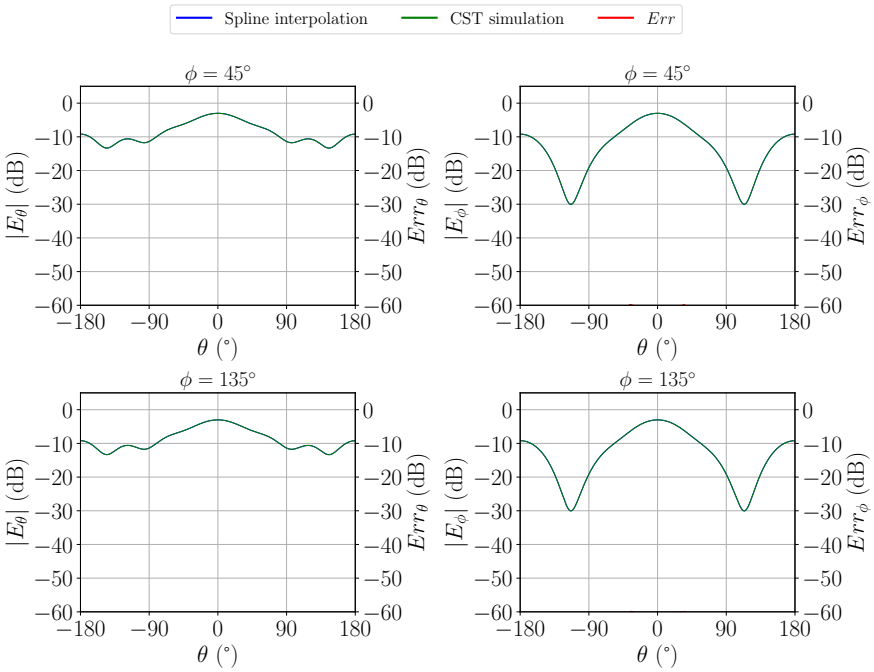

Figure IV.7 – FF computation of the measurement probe using spline interpolation compared to the CST reference.

The obtained ENL value of $-61.7\,\mathrm{dB}$ demonstrates a significant improvement in determining the probe characteristics using the spline interpolation method compared to analytical formulas. This technique is flexible and can be applied to both simulated and measured FF data whenever such information is available.

For the equivalent models, *rcond* is set to 10^{-2}. Using the IP method, the FF computation achieves $ENL = -45.2\,\mathrm{dB}$ (Fig. IV.8), while the NF reconstruction reaches $ENL = -66.1\,\mathrm{dB}$. This confirms that the IP model, derived from NF data, provides highly accurate NF characterization, which is essential for the proposed compensation method.

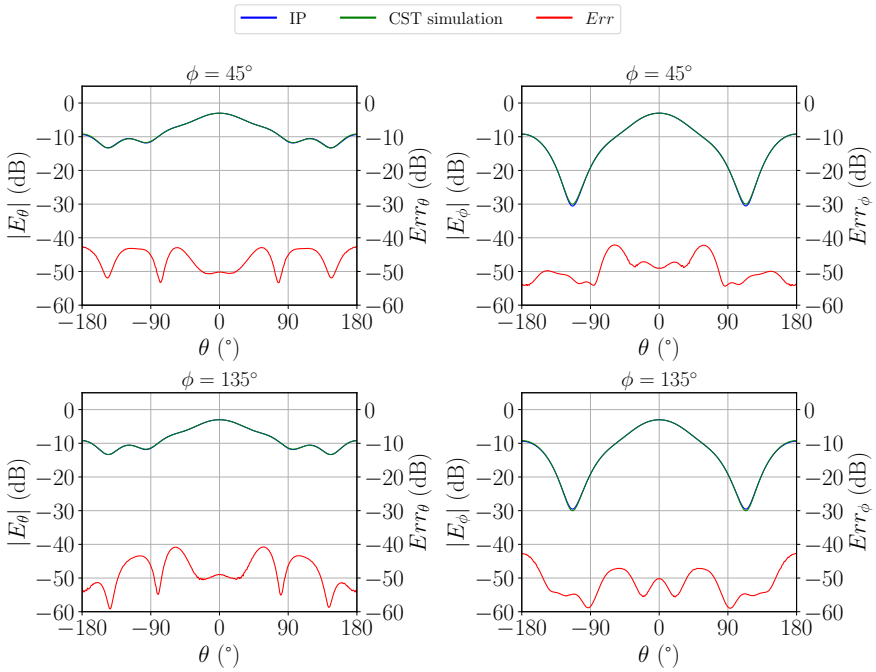

Figure IV.8 – FF computation of the measurement probe using the IP method compared to the CST reference.

The RA-based model (FF data) achieves $ENL = -63.8\,\mathrm{dB}$ in FF but only $ENL = -50.5\,\mathrm{dB}$ in NF (Fig. IV.9), illustrating that models are most accurate in the range corresponding to the data used for construction.

Overall, the equivalent model-based methods confirm the expected trends and clearly outperform analytical formulas, providing a more accurate characterization of the probe radiation pattern, including cross-polarization components and full angular coverage. As anticipated, the IP-based model, constructed from NF data, is ideal for NF computation, while the RA-based model, built from FF data, is best suited for FF characterization.

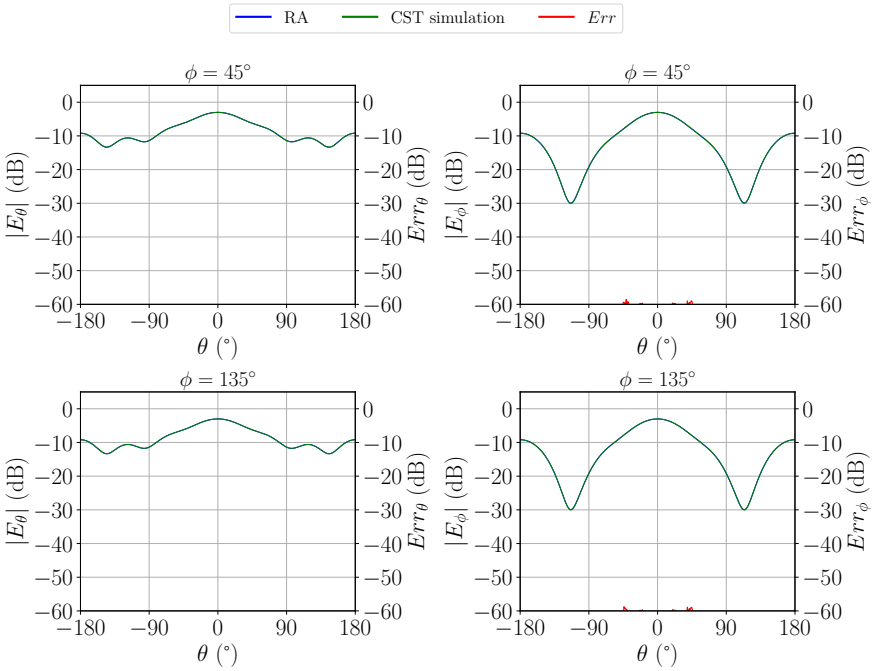

Figure IV.9 – FF computation of the measurement probe using the RA method compared to the CST reference.

Both models can be employed in the compensation techniques proposed later, targeting NF- or FF-based procedures.

Although these methods yield better results than analytical formulas, they require the additional step of constructing an equivalent model, which is more complex than using analytical expressions that are limited to co-polarization and valid only in the upper half-space. Furthermore, NF data are only accessible in simulation, making IP-based models impractical for experimental use. In contrast, FF data can be acquired in real measurements, making RA-based equivalent models more flexible and broadly applicable. This highlights the practical advantage of the RA approach for both simulation and measurement scenarios.

Summary

This section has presented several approaches for modeling the radiation characteristics of the measurement probe, including analytical formulas, the spline interpolation method, and, in particular, the equivalent model-based FF computations derived from either NF or FF data. With these characterization results established, the next step is to incorporate them into a probe compensation procedure. Such compensation is essential to accurately

extract the intrinsic field of the AUT from the NF measurements, thereby ensuring a reliable computation of its FF radiation pattern.

IV.2.c Model integration of probe compensation

In our planar NF measurement configuration, based on the parametric study in Section II.5, measuring only the x- and y-components is sufficient for accurate FF computation. This allows avoiding the use of a robotic arm [74] to acquire the NF data along other axes. Thus, the probe is oriented to acquire both E_x and E_y, corresponding to two orthogonal orientations $\hat{\boldsymbol{\alpha}}$ and $\hat{\boldsymbol{\beta}}$ collinear to $\hat{\boldsymbol{x}}$ and $\hat{\boldsymbol{y}}$, respectively, as shown in Fig. IV.10.

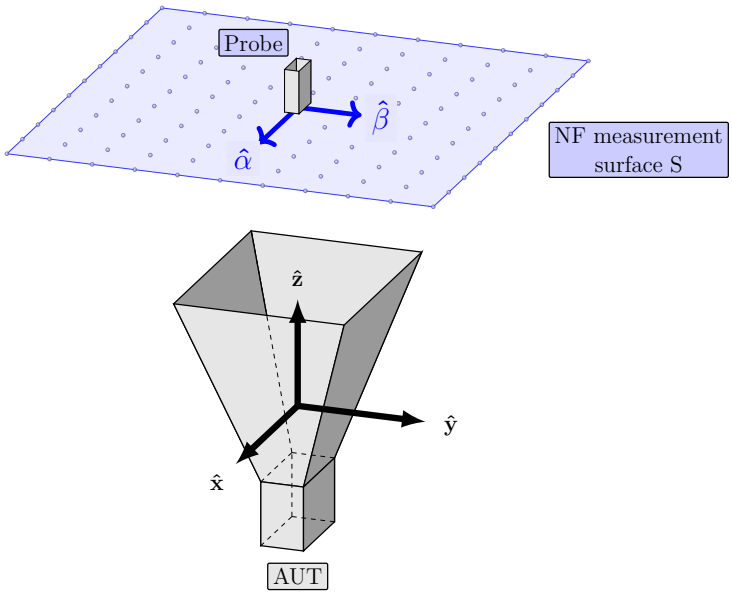

Figure IV.10 – Representation of the measurement probe system on the NF measurement surface S.

To implement probe compensation in our framework, the probe effects must be incorporated into the radiation model. This involves two main steps:

1. constructing the probe coefficient matrices $\mathbf{P}_\alpha$ and $\mathbf{P}_\beta$ for the probe orientations $\hat{\boldsymbol{\alpha}}$ and $\hat{\boldsymbol{\beta}}$, respectively, using the selected method (Yaghjian, spline, IP, or RA). These matrices represent the spatial filtering effect of the probe, i. e., how its radiation pattern weights the measured field components;
2. modifying the radiation matrix $\mathbf{A}$ associated with the NF measurement surface S to account for the probe influence.

Probe coefficients

In this part, details are given on how is constructed the probe coefficient matrix $\mathbf{P}_\alpha$ associated to the probe orientation $\hat{\boldsymbol{\alpha}}$. The same procedure is applied to compute the probe coefficient matrix $\mathbf{P}_\beta$ for the other orientation $\hat{\boldsymbol{\beta}}$.

The probe coefficient matrix $\mathbf{P}_\alpha$ is defined as the radiation matrix that maps the measurement points of the probe to the equivalent dipoles of the AUT for an orientation $\hat{\boldsymbol{\alpha}}$ of the probe. In other words, $\mathbf{P}_\alpha$ encodes how the fields recorded by the probe at each position on the NF measurement surface S contribute to the excitation of the AUT equivalent sources, as it is represented in Fig. IV.11

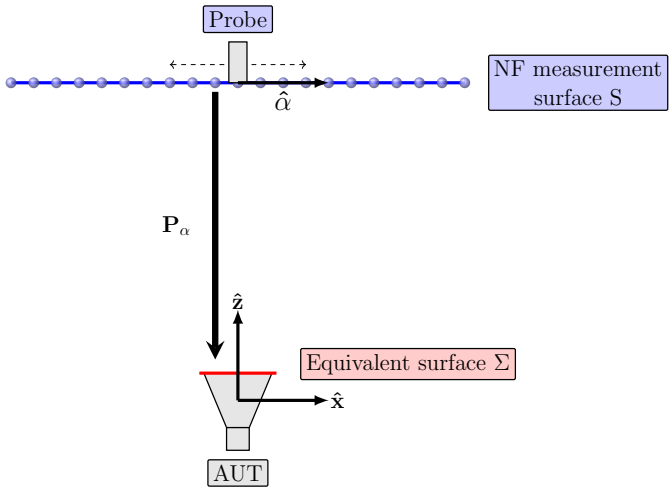

Figure IV.11 – Illustration of the construction of the coefficient matrix $\mathbf{P}_\alpha$ for a probe oriented to the α-axis.

First, Yaghjian analytical formulas allow directly computing $\mathbf{P}_\alpha$ at the angular directions defined between the dipole positions of the AUT and the probe positions, without any additional computation step. Contrary to spline interpolation where once the field is interpolated and the matrix $\mathbf{P}_\alpha$ constructed, a normalization must be applied to ensure the probe to behave like a spatial filter with no distance relation.

Finally, to achieve probe coefficient determination, equivalent model-based methods employs the probe radiation matrix $\mathbf{A}_P$, which directly relates the dipoles of the probe model to the dipoles of the AUT. The matrix $\mathbf{P}_\alpha$ is constructed column by column using $\mathbf{A}_P$ and the probe equivalent currents computed using the equivalent model-based methods previously introduced (IP or RA) for each measurement position. Thereby translating the probe dipole-based description into a global probe measurement position-based description (see Fig. IV.12).

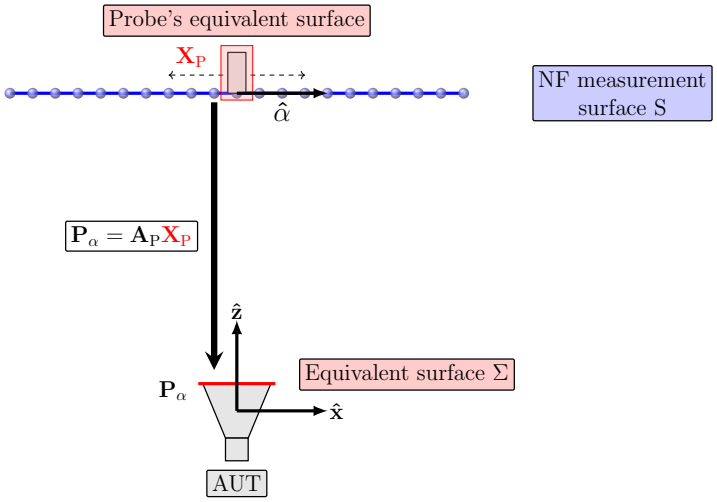

Figure IV.12 – Link between the probe radiation matrix $\mathbf{A}_P$ and the probe coefficient matrix $\mathbf{P}_\alpha$, which maps measurement points to AUT dipoles.

Depending on how the probe model is obtained, two approaches are used:

- NF-based (RA) model: when the probe model is derived from NF data, the geometrical distance between probe and AUT is preserved in the computation of $\mathbf{A}_P$. Therefore, to not take into account twice the phase information and attenuation relative to the distance between the NF measurement surface S and the equivalent surface Σ, this implies to normalize the radiation matrix $\mathbf{P}_\alpha$.
- FF-based (RA) model: when the probe model is constructed from FF data, the distance dependence is not explicitly encoded, and the probe acts as a directional filter. To achieve this required form, the coefficient matrix $\mathbf{P}_\alpha$ has to be computed only regarding the angular distribution between the NF measurement surface S and the equivalent surface Σ. This is done by fixing the distance between both surfaces (Σ and S) at FF range when computing the $\mathbf{A}_P$. In this case, $\mathbf{P}_\alpha$ is obtained from $\mathbf{A}_P$ and then normalized to ensure a consistent gain reference.

The resulting $\mathbf{P}_\alpha$ is thus a measurement-to-source mapping that fully incorporates the probe radiation behavior while preserving the appropriate amplitude reference for either NF or FF probe compensation technique.

The exact same process is applied to construct $\mathbf{P}_\beta$, by rotating the dipole positions of the AUT by $\frac{\pi}{2}$ around the z-axis, relative to either the positions of the measurement probe or, in the case of equivalent model-based methods, relative to its own dipoles. This rotation emulates a probe orientation aligned with the $\hat{\boldsymbol{\beta}}$ direction.

Correction of the equivalent model

Once the probe coefficient matrices $\mathbf{P}_\alpha$ and $\mathbf{P}_\beta$ are constructed for the two orthogonal probe orientations $\hat{\boldsymbol{\alpha}}$ and $\hat{\boldsymbol{\beta}}$, they are integrated into the equivalent model to account for the probe effect on the measurement.

The probe coefficient matrices must be expressed in the same coordinate system as the radiation matrix $\mathbf{A}$ of the AUT. For example, in a Cartesian system, $\mathbf{A}$ is decomposed into its components $\mathbf{A}_x$, $\mathbf{A}_y$, and $\mathbf{A}_z$. Similarly, $\mathbf{P}_\alpha$ is decomposed into $\mathbf{P}_{\alpha,x}$, $\mathbf{P}_{\alpha,y}$, and $\mathbf{P}_{\alpha,z}$, and the same applies to $\mathbf{P}_\beta$.

The corrected radiation matrices are then obtained by weighting each Cartesian component of $\mathbf{A}$ with the corresponding probe coefficient, yielding:

$$\begin{aligned} \mathbf{A}_\alpha &= \mathbf{A}_x \odot \mathbf{P}_{\alpha,x} + \mathbf{A}_y \odot \mathbf{P}_{\alpha,y} + \mathbf{A}_z \odot \mathbf{P}_{\alpha,z} \\ \mathbf{A}_\beta &= \mathbf{A}_x \odot \mathbf{P}_{\beta,x} + \mathbf{A}_y \odot \mathbf{P}_{\beta,y} + \mathbf{A}_z \odot \mathbf{P}_{\beta,z} \end{aligned} \tag{IV.3}$$

where $\odot$ denotes element-wise (Hadamard) multiplication.

These formulas reflect the principle that at FF distances, the measurement probe behaves like a spatial filter: the measured field is approximately the product of the AUT radiation pattern and the measurement probe pattern. Thus, the response of each infinitesimal dipole of the AUT equivalent model must be scaled according to the probe characteristics in both $\hat{\boldsymbol{\alpha}}$ and $\hat{\boldsymbol{\beta}}$ orientations.

Through this correction, each infinitesimal dipole contribution is adjusted to embed the probe effect within the model, enabling accurate probe compensation.

IV.2.d Validations

To validate the proposed probe compensation methods, a representative application case is performed using CST. The AUT is an X-band pyramidal horn operating at 10 GHz. In the simulation, the X-band OEWG probe described in Section IV.2.b is used, and its measurement path is configured to acquire simulated NF data for both x- and y-components.

The AUT is an X-band pyramidal horn operating at 10 GHz. In the simulation, the X-band OEWG probe described in Section IV.2.b is also explicitly modeled in CST and included in the measurement configuration in order to deliberately perturb the radiated field of the AUT. This allows simulated NF data to be acquired for both x- and y-

components while enabling a controlled assessment of the probe compensation process. Therefore the objective is to compensate for these effects.

The determination of the probe radiation characteristics is performed as described in Section IV.2.b, using either Yaghjian formulas, spline interpolation, IP, or RA methods. The regularization parameter *rcond* is set to 10^{-2} for equivalent model-based methods.

The equivalent model of the AUT is represented by a planar equivalent surface Σ of size $5\lambda \times 5\lambda$ with a regular spacing of $\frac{\lambda}{4}$, placed at the antenna aperture, located at 3.1λ from the coordinate system origin.

NF data are simulated for two different measurement geometries of S: a planar surface and a half-box. FF data are extracted from CST computations using an equiangular distribution over a half-sphere with $\Delta_\theta = \Delta_\phi = 1°$.

To focus the validation on probe compensation, the ROM-NFFFT method is applied to characterize the AUT. R parameter for the truncation level of the singular values $\mathbf{S}$ of the matrix $\mathbf{A}$ is fixed to $-40\,\text{dB}$. The main goal is to verify the correct integration of probe compensation in the AUT model to accurately compute its radiated FF. Then, the impact of probe compensation on the model is also analyzed, particularly during the SVD step, which can be critical when the NF measurement surface S is a half-box. The following scenarios are investigated:

1. no compensation;
2. compensation using Yaghjian formulas;
3. compensation using spline interpolation;
4. compensation using an equivalent model constructed from NF data (IP method);
5. compensation using an equivalent model constructed from FF data (RA method).

A separate simulation is performed without the probe, and the computed FF results from this case serve as an additional reference, alongside the CST-simulated reference FF data, to isolate the probe influence from the FF computation method itself. Therefore, the characterization results presented in this application are compared to the computed FF issued from the ROM-NFFFT method in the case of no probe presence in the simulation.

Except for verifying that the computed FF obtained from simulations without the probe matches the CST-simulated reference FF data, where a reference-based normalization is applied, all error values are consistently computed using independent normalizations. This choice is necessary because the probe scattering parameter S_{21} extracted from

CST already includes its own normalization factor, which introduces amplitude offsets in the computed FF.

Planar measurement surface S

This section examines the influence of probe compensation on the characterization accuracy obtained with the proposed approach for a planar NF measurement surface S. To validate the methodology under different measurement configurations, two planar measurement surfaces S at different distances are considered. The objective is to verify that probe compensation and its integration into the model, particularly its impact on the SVD step of ROM-based methods, does not degrade the accuracy of the computed FF. The dimensions and distances of these planes are selected so that the same WZ is maintained in both cases, enabling a fair comparison.

The first planar NF measurement surface S has dimensions $10\lambda \times 10\lambda$ with a regular sampling step of $\frac{\lambda}{2}$ and is placed at a distance of 7λ from the system origin. The second surface has dimensions $16\lambda \times 16\lambda$, the same sampling step of $\frac{\lambda}{2}$, and is located at a distance of 11.2λ from the origin. The corresponding total WZ in both the E- and H-planes is equal to 78°. An illustration of the two planar NF measurement surfaces S is given in Fig. IV.13.

The ROM-NFFFT method is first applied to the $10\lambda \times 10\lambda$ plane at 7λ from the origin without including any measurement probe (used as reference for the study). The computed FF polarizations are compared to the reference CST-simulated FF data in Fig. IV.14.

The computed ENL is $-45.5\,\mathrm{dB}$, demonstrating that the method achieves high accuracy in this configuration and validating its use as a reference for the subsequent analysis.

The resulting FF computation accuracy and probe compensation durations obtained with the different characterization approaches are presented in Table IV.1, with a specific focus on the WZ.

The results confirm that including probe compensation improves the accuracy of the FF computation. Compensation techniques based on numerical methods yield better results than Yaghjian's analytical compensation approach, in agreement with the trends observed in Section IV.2.b. All the numerical techniques achieve a comparable level of accuracy. However, a significant difference arises in terms of computation time for probe compensation. Specifically, the spline interpolation method is considerably faster than the equivalent model-based approaches, which require multiple probe radiation matrix

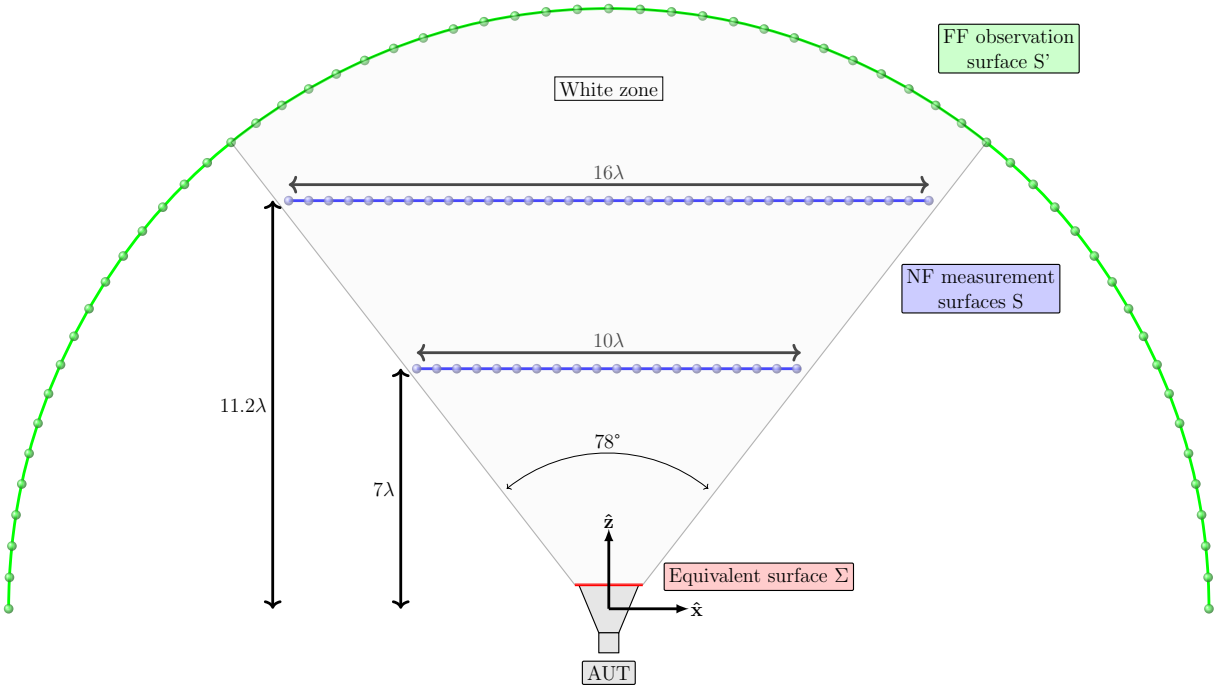

Figure IV.13 – Illustration of the two planar NF measurement surfaces S considered in the characterization procedure with the associated WZ.

Characterization case	ENL_{mag} (dB)	$ENL_{\text{mag, WZ}}$ (dB)	Compensation duration
No compensation	-39.4	-38.4	0 sec
Yaghjian formulas	-41.4	-43.9	3 sec
Spline interpolation	-42.3	-47.5	5 sec
Equivalent model from IP	-42.7	-47.4	25 min 20 sec
Equivalent model from RA	-44.4	-49.5	36 min 31 sec

Table IV.1 – Plane $10\lambda \times 10\lambda$: accuracy of FF computation for different characterization approaches, with and without probe compensation, compared to CST data without probe.

constructions for each measurement position. Even if the algorithm implementation of equivalent model-based compensation techniques is not optimized, a major drawback is highlighted, namely their computational cost, which increases with the number of measurement points and with the number of dipoles used in both the probe and the AUT equivalent models. Consequently, spline interpolation appears to offer the best compromise between accuracy and computational efficiency.

The same procedure is repeated for the second planar surface S ($16\lambda \times 16\lambda$ at 11.2λ). The ROM-NFFFT method without probe compensation produces the reference FF results shown in Fig. IV.15, with an associated $ENL = -43.5$ dB, confirming the suitability of

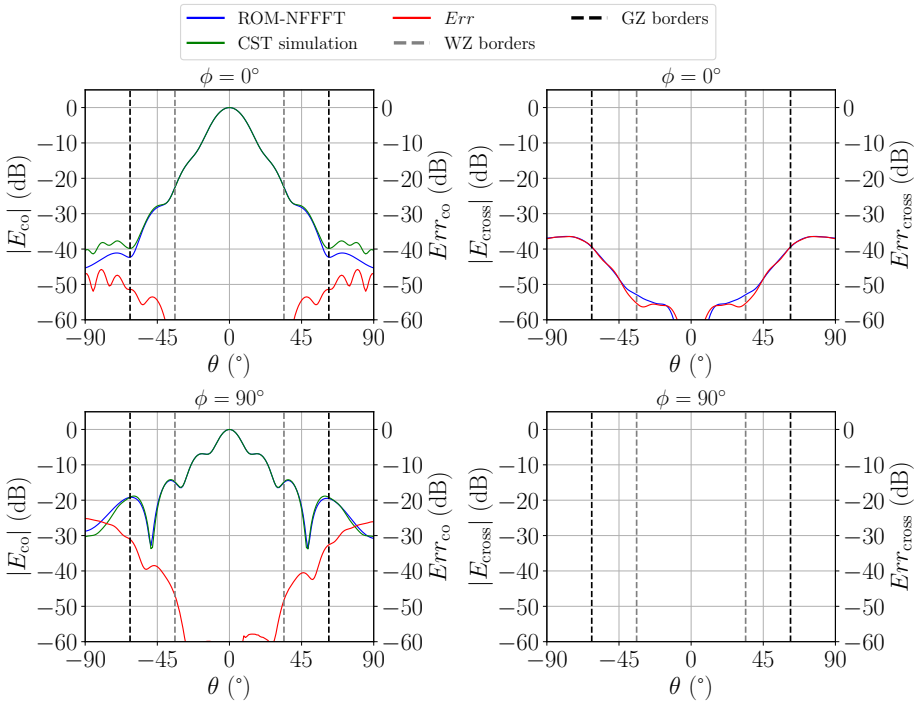

Figure IV.14 – Plane $10\lambda \times 10\lambda$: comparison of the computed FF using the ROM-NFFFT method without probe compensation to the reference CST FF data.

this reference case.

The accuracy results and compensation durations are summarized in Table IV.2.

Characterization case	ENL_{mag} (dB)	$ENL_{\text{mag, WZ}}$ (dB)	Compensation duration
No compensation	-40.5	-37.9	0 sec
Yaghjian formulas	-43.6	-43.2	4 sec
Spline interpolation	-44.8	-49.4	9 sec
Equivalent model from IP	-42.9	-48.6	40 min 23 sec
Equivalent model from RA	-47.1	-51.1	1 h 0 min 45 sec

Table IV.2 – Plane $16\lambda \times 16\lambda$: accuracy of FF computation for different characterization approaches, with and without probe compensation, compared to CST data without probe.

The results show a consistent improvement in accuracy when probe compensation is applied. The best performance is obtained with numerical techniques, confirming the conclusions previously drawn for the first planar NF measurement surface S: the spline interpolation technique appears to be the best compromise between accuracy and computation time. Nevertheless, despite its significantly longer computation duration, constructing an equivalent model of the probe using the RA method provides the highest accuracy in the compensation results.

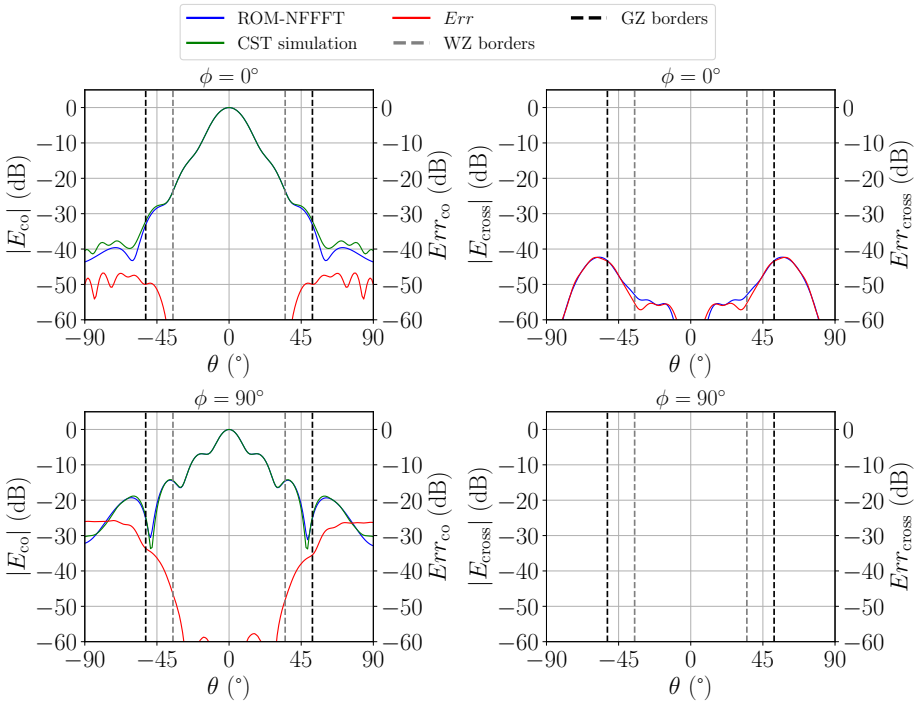

Figure IV.15 – Plane $16\lambda \times 16\lambda$: comparison of the computed FF using the ROM-NFFFT method without probe compensation to the reference CST FF data.

Furthermore, once probe compensation is applied, the measurement distance has little effect on the accuracy, as the results for the two planes are very similar (Table IV.1).

Half-box-shaped measurement surface S

The same analysis is now carried out on a half-box-shaped NF measurement surface S. The half-box S has dimensions $10\lambda \times 10\lambda \times 4\lambda$ with a regular sampling step of $\frac{\lambda}{2}$, centered at $(0\lambda, 0\lambda, 2\lambda)$ from the system origin.

Applying the ROM-NFFFT method without using a measurement probe in the CST simulation yields computed FF that is compared to the reference simulated CST FF data in Fig. IV.16.

The computed ENL is equal to $-55.0\,\text{dB}$, indicating that the method achieves satisfactory accuracy. This validates the choice of reference for the remainder of the study.

The accuracy of the computed FF using the ROM-NFFFT method for the half-box case and the compensation durations is summarized in Table IV.3, for each compensation technique.

Exact same trends are observed as for the planar NF measurement surface S. The

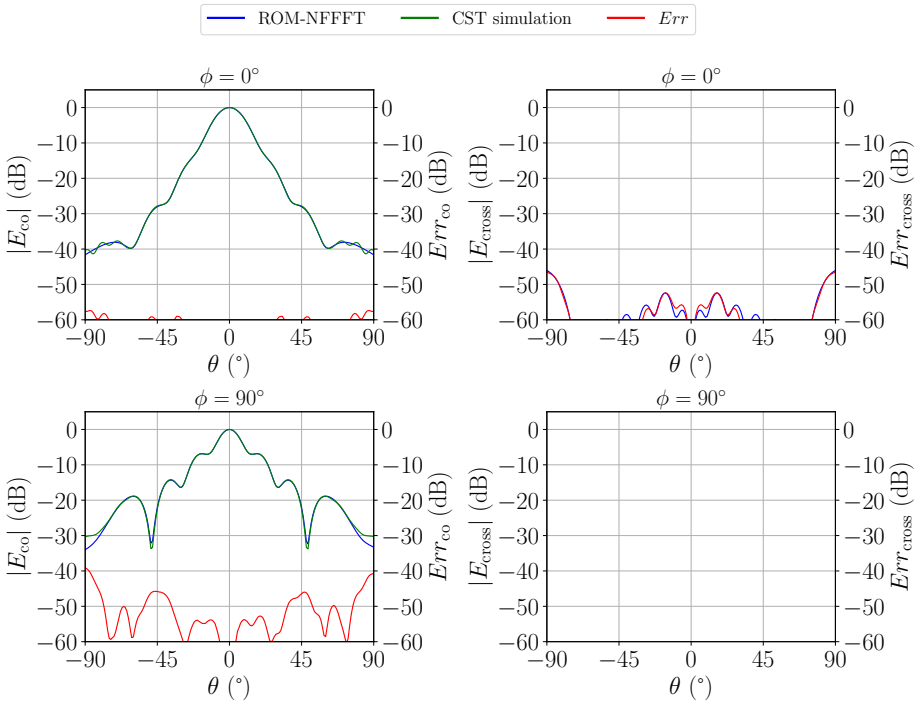

Figure IV.16 – Half-box $10\lambda \times 10\lambda \times 4\lambda$: comparison of the computed FF using the ROM-NFFFT method without probe compensation to the reference simulated CST FF data.

Characterization case	ENL_{mag} (dB)	Compensation duration
No compensation	-37.6	0 sec
Yaghjian formulas	-42.7	4 sec
Spline interpolation	-44.4	9 sec
Equivalent model from IP	-44.2	40 min 36 sec
Equivalent model from RA	-45.8	1 h 2 min 34 sec

Table IV.3 – Half-box $10\lambda \times 10\lambda \times 4\lambda$: accuracy of FF computation for different characterization scenarios with/without probe compensation, compared to a reference FF computed from simulated NF data without probe in CST.

influence of probe compensation on the accuracy of the FF computation is clearly demonstrated: including probe effects in the model significantly improves accuracy compared to the case without compensation. Furthermore, compensation techniques based on numerical methods provide better results than Yaghjian's analytical formulas. However, when equivalent model-based techniques are employed, the computation time required to apply the compensation procedure leads to considerably longer durations. Indeed, for example the spline interpolation method requires only about 9 s while reaching nearly the same level of FF computation accuracy.

This is an interesting result for this half-box geometry of S. In some measurement positions along the probe path, the probe radiates fields toward the back-half radiation space, in the direction of the equivalent surface Σ of the AUT. However, the magnitude of the radiated field in these directions is low, and it directly influences the correction of $\mathbf{A}$. Despite this, these effects do not significantly perturb the accuracy of the computed FF, as the error levels remain comparable to those obtained for a planar S (see Tables IV.1 and IV.2). This validates the proposed probe compensation techniques for different geometries of the NF measurement surface S, which is a crucial step toward developing a complete NFFFT that fully exploits the advantageous properties presented thus far, particularly the mitigation of truncation effects.

Summary

The study sequentially validated the effectiveness of probe compensation techniques on a concrete numerical case involving multiple NF measurement surfaces S with both planar and half-box geometries of varying dimensions. The correct integration of these techniques directly into the developed model has been verified, and their impact on the SVD step of ROM-based characterization methods has been analyzed, showing no major consequences on the overall accuracy. Both analytical and numerical approaches demonstrated clear improvements in FF computation accuracy. In particular, the use of equivalent-probe models, especially those based on the RA method, consistently outperformed analytical formulas in characterizing the probe and compensating its effects. However, these techniques are penalized by the significant computation time required for their implementation. By contrast, the spline interpolation technique provides satisfactory accuracy while maintaining very short compensation durations.

In summary, spline interpolation represents a versatile numerical method for determining the probe radiation pattern, offering the flexibility to capture complex probe behaviors and adapt to realistic measurement scenarios, provided that sufficiently accurate and well-sampled reference data are available.

The systematic validations performed in this part provide a solid foundation to anticipate reliable and accurate FF characterization in practical experimental scenarios.

IV.3 Characterization of a W-band horn

The application of the developed characterization methods to the experimental cases presented here and in the following section primarily aims to validate the proposed approach. These experimental campaigns have been carried out on the M^{2}ARS platform [1], which provides advanced antenna measurement facilities at IETR-UNIVREN (Appendix B). The objective is not to re-demonstrate all trends and behaviors of the model already analyzed in previous sections, but rather to confirm their applicability on real-world data.

The first experimental case considered is a W-band horn antenna. This design has been chosen as it represents a well-established benchmark for comparing characterization methods commonly used in antenna measurements. Operating in the W-band, however, makes the application particularly challenging, since high frequencies exacerbate issues such as positioning errors and rapid spatial field variations, which complicate the accurate characterization of antennas at these frequencies.

As measurement data are available for this AUT, the methods developed in this work are applied to its characterization. In particular, the techniques introduced throughout the manuscript are combined to address one of the main objectives: reducing the number of required samples. The mitigation of truncation effects will be discussed later in the manuscript.

IV.3.a Characterization setup

The AUT is a W-band pyramidal horn operating at 100 GHz, with an aperture of $8.1\lambda \times 6.6\lambda$ and a height of 20.2λ. An illustration of the AUT is presented in Fig. IV.17.



Figure IV.17 – The W-band horn antenna to characterize.

The equivalent surface Σ is defined as a plane of $10\lambda \times 8\lambda$ with a spacing of $\frac{\lambda}{4}$, centered at the system origin. The corresponding number of dipoles is equal to 5120. A visualization of the horn and its equivalent model is given in Fig. IV.18.

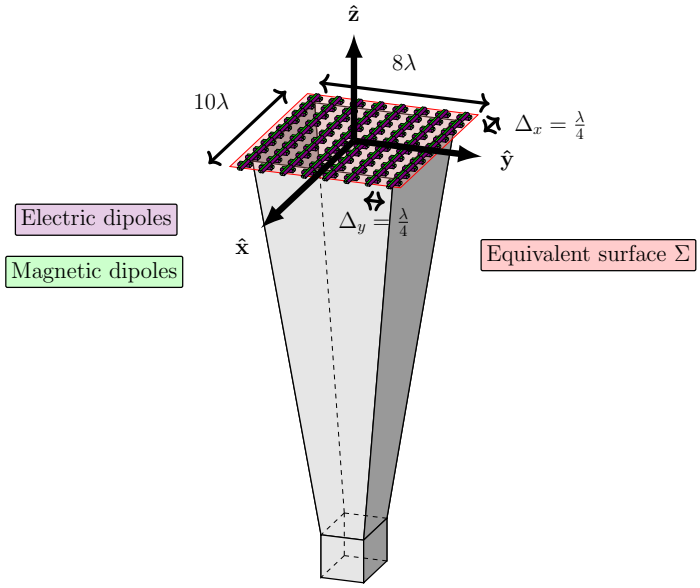

Figure IV.18 – W-band horn antenna and its equivalent surface Σ.

The NF data have been acquired using the in-house XS scanner facility (Appendix B). An acquisition campaign has been performed, measuring the E_x and E_y components on a half-box-shaped NF surface S of $50.85\lambda \times 50.85\lambda \times 6.30\lambda$, sampled with a step of 0.45λ and centered at $(0, 0, 3.2\lambda)$. The total number of measurement points on S is 19041. The measurement configuration is shown in Fig. IV.19.

The probe used to acquire these NF data is a standard W-band OEWG with aperture dimensions $0.85\lambda \times 0.42\lambda$ and a height of 2λ.

Based on the conclusions drawn in Section IV.2, spline interpolation is the most efficient method for probe compensation in terms of both accuracy and computation time. Therefore, only spline interpolation is employed in this experimental case. The accuracy of this approach for computing the probe FF radiation pattern is verified by comparison with CST-simulated reference data on a spherical observation surface S' sampled with $\Delta_\theta = \Delta_\phi = 1°$. To further validate, the spline method is also tested against denser simulated reference data sampled with $\Delta_\theta = \Delta_\phi = 0.3°$.

A comparison between the probe FF computed using spline interpolation and the CST reference is shown in Fig. IV.20.

The associated ENL value is $-63.3\,\mathrm{dB}$. As already observed for the X-band OEWG in Section IV.2.b, this confirms that spline interpolation provides an accurate determination of the probe radiated FF and can reliably be used to compensate probe effects in the proposed characterization procedure.

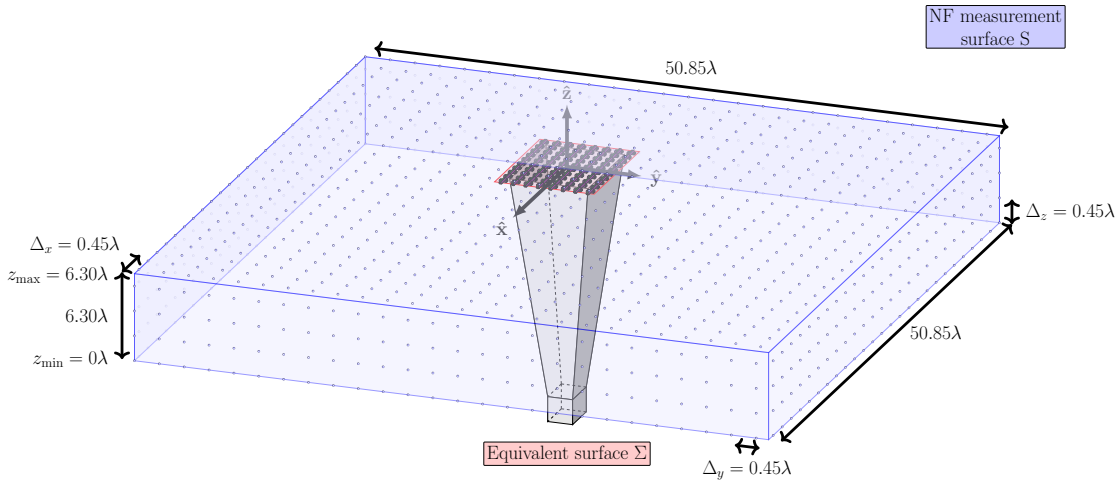

(a) 3D representation

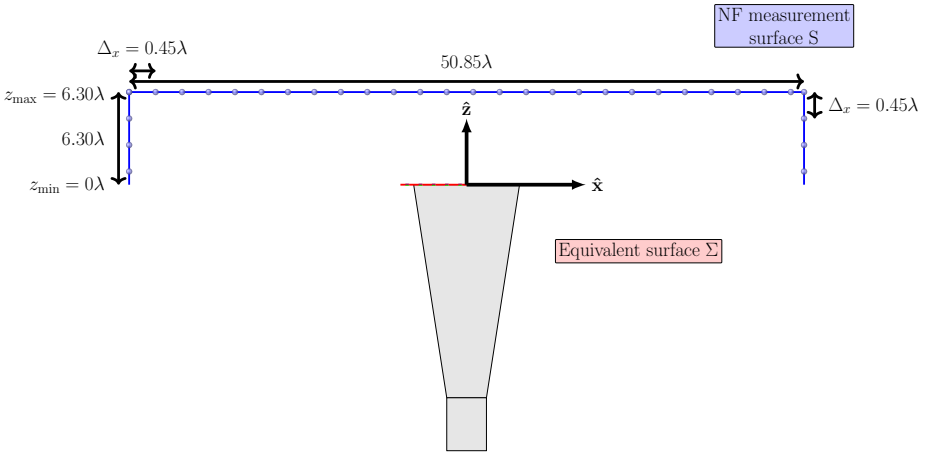

(b) 2D representation (XOZ plane)

Figure IV.19 – W-band pyramidal horn: half-box NF measurement surface S.

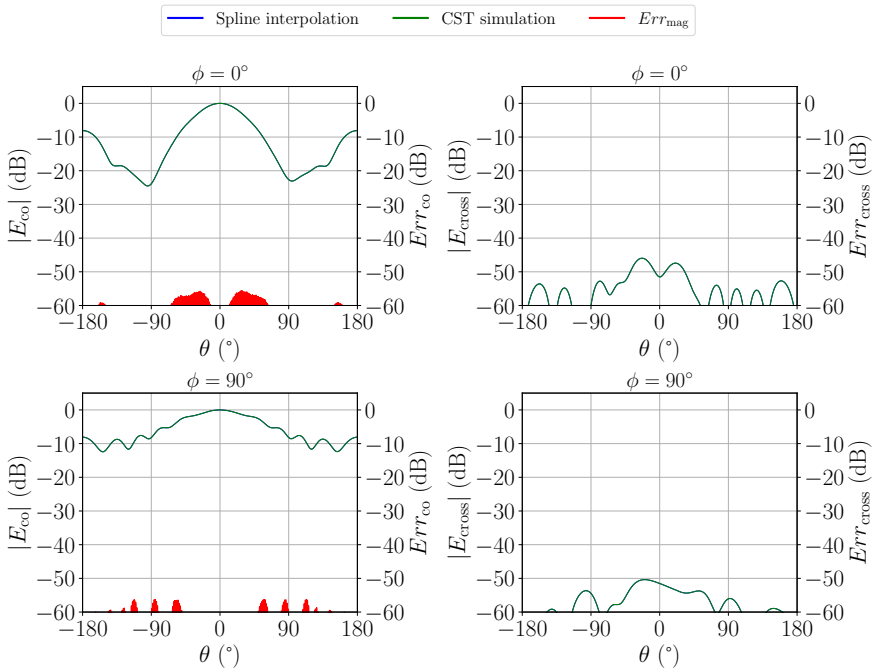

Figure IV.20 – FF computation of the measurement probe using spline interpolation compared to CST-simulated reference FF data.

To apply the ROM-based methods to the measured NF data, the R parameter is set to -40 dB, while the regularization parameter *rcond* for least-squares solving is fixed at 10^{-2}. These values are consistently used for all analyses presented in this section.

Finally, reference FF data have been also acquired using the *Caractérisation d'Antennes en bande MILL et subMILLimétrique* (CAMILL) facility (Appendix B). The observation surface S' is a half-sphere with equiangular sampling $\Delta_\theta = \Delta_\phi = 1°$. The measured magnitudes of the E_{co} and E_{cross} polarizations are shown in Fig. IV.21. Since the exact FF measurement distance is unknown, error metrics are computed using self-normalization when comparing the computed FF to these measurements.

IV.3.b Classical errors for planar near-field measurements

Before applying the proposed characterization methods to the measured NF data, it is useful to review the main sources of error that may affect planar NF measurements. Among these, misalignment errors are the most common and typically have the largest impact. To support the following explanations, Fig. IV.22 illustrates a generic planar NF measurement setup, showing both the AUT coordinate system and the measurement system associated with the scanner.

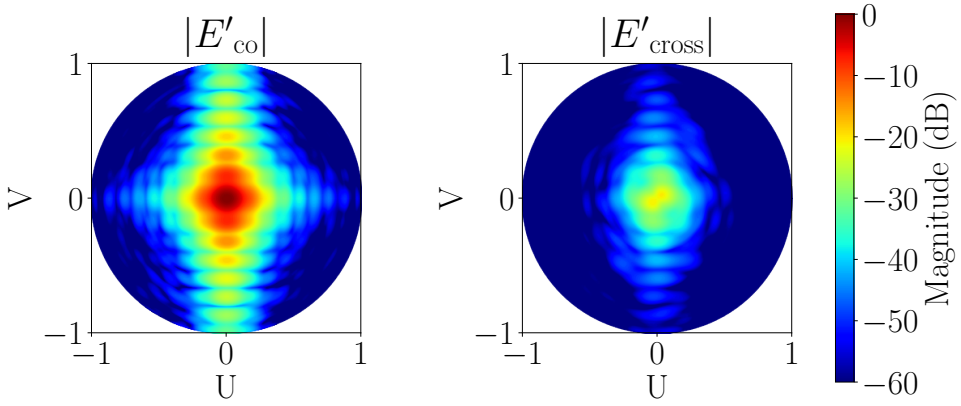

Figure IV.21 – W-band pyramidal horn: measured magnitudes on the FF measurement surface S'.

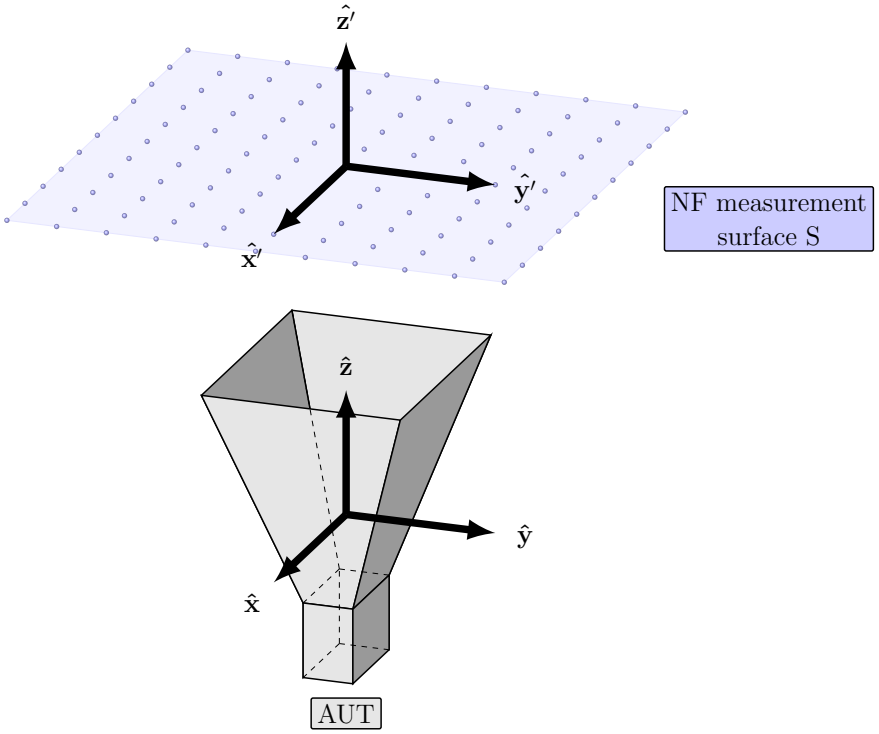

Figure IV.22 – Illustration of the AUT coordinate system and the measurement system associated with the scanning area for planar NF acquisitions.

First, NF measurements are performed using a scanner that moves the probe along predefined paths to sample the radiated field at specific points. If the mechanical system supporting the AUT is not perfectly aligned with the scanner coordinate system, positioning errors occur. In practice, this happens when the XOY, XOZ, and YOZ planes of the AUT coordinate system are not parallel to the corresponding planes of the scanner ($X'O'Y'$, $X'O'Z'$, and $Y'O'Z'$). Angular misalignments around the $\hat{\boldsymbol{x}}$, $\hat{\boldsymbol{y}}$, and $\hat{\boldsymbol{z}}$ axes must

be considered. Such deviations result in measurement positions that differ from those assumed in the numerical model used during the characterization process.

Second, the measurement probe itself may introduce systematic errors. A typical case is when the probe aperture is slightly shifted along the $\hat{\boldsymbol{x}}$ or $\hat{\boldsymbol{y}}$ directions, introducing a constant offset across all measurement positions. This systematic displacement leads to inconsistencies between the physical measurement points and those defined in the computational model.

Finally, polarization misalignment can occur between the AUT and the probe. The polarization basis defined by the probe may not coincide with the physical polarization axes of the AUT. As a consequence, the computed FF obtained after applying the NFFFT may exhibit artificially high cross-polarization levels, particularly in directions where the co-polarization component is dominant.

IV.3.c Characterization results and error analysis

To validate the proposed approach through an experimental application, and in light of the previously identified common errors associated with planar NF measurement systems, a non-exhaustive analysis of measurement errors that can significantly affect the characterization results is carried out. This study is performed independently of the characterization method, as such an evaluation is a crucial step in antenna measurement to critically assess the obtained results.

Then, the developed characterization methods are applied to verify one of the main objectives of this work: the reduction of the sampling size.

Planar near-field measurement surface S

To investigate the measurement errors affecting the computed FF accuracy with the proposed approach, two different characterization methods (IP and ROM-NFFFT) are applied on the upper plane of the NF measurement surface S. Using two distinct methods makes it possible to separate the errors originating from the proposed approach from those due to the measurement setup itself. The error metrics are defined through a normalization with respect to the measured FF data on the observation surface S'.

As a first step, the IP method is applied with probe compensation (spline interpolation). The computed FF is compared with the reference measured FF data along the main cut planes in Fig. IV.23.

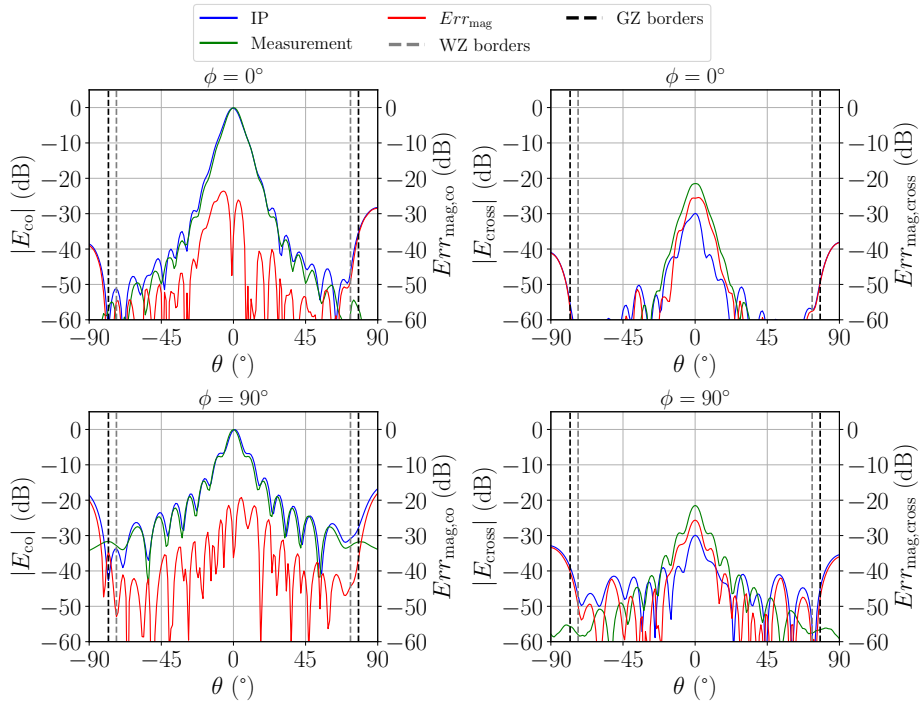

Figure IV.23 – W-band pyramidal horn, upper plane of the NF measurement surface S: comparison between computed FF using the IP method and the reference measured FF data along the principal cut planes.

The UV-plane representation of the computed FF is shown in Fig. IV.24, with the corresponding magnitude error displayed in Fig. IV.25. The resulting ENL_{mag} equals -37.0 dB.

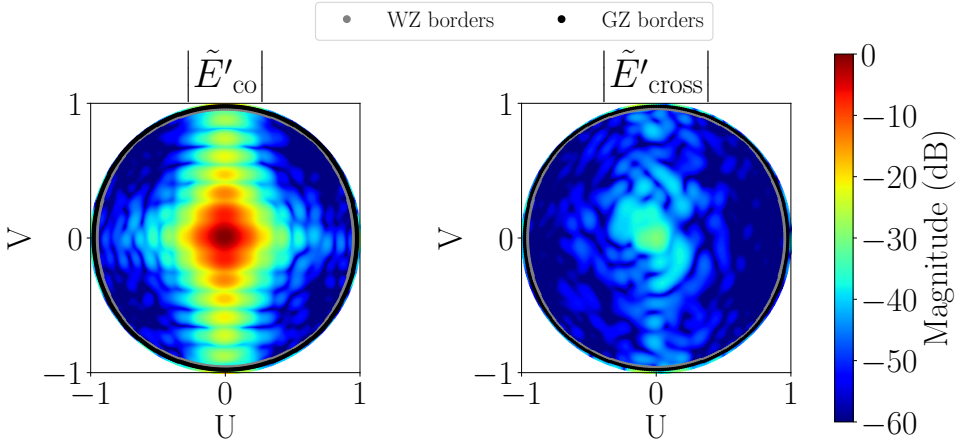

Figure IV.24 – W-band pyramidal horn, upper plane of the NF measurement surface S: UV-plane representation of the computed FF obtained with the IP method.

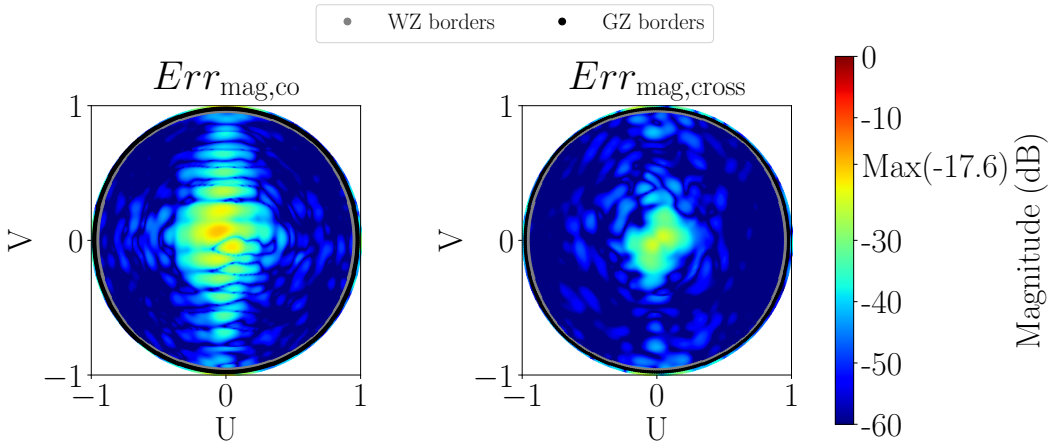

Figure IV.25 – W-band pyramidal horn, upper plane of the NF measurement surface S: UV-plane distribution of the magnitude error between the computed FF (IP method) and the reference measured data.

From these results, two main issues can be identified. First, significant cross-polarization levels are observed both in the reference measured FF data and in the computed FF. Moreover, the distribution of the cross-polarization appears to replicate the co-polarization pattern, scaled by a weighting factor. This behavior is characteristic of a misalignment between the probe polarization and that of the AUT. Second, a slight beam tilt is visible in the $\phi = 90°$ cut plane between both radiation patterns. This effect is particularly clear in Fig. IV.25 for the cut $U = 0$, where the computation error is most pronounced.

To verify whether these effects also occur when using a different characterization method, the ROM-NFFFT is applied to the same upper plane of the NF measurement surface S. The computed FF is compared with the reference measured FF data along the main cut planes in Fig. IV.26. The corresponding ENL_{mag} is also $-37.0\,\text{dB}$.

The UV-plane representation of the computed FF and the associated magnitude error are presented in Fig. IV.27 and Fig. IV.28, respectively.

The same conclusions can be drawn for the ROM-NFFFT as for the IP method:

1. a significant cross-polarization level is observed, with a pattern resembling the co-polarization scaled by a weighting coefficient,
2. a beam tilt is present in the $\phi = 90°$ cut plane.

These results confirm the presence of a misalignment between the probe polarization and the physical polarization of the AUT, leading to an undesired cross-polarization contribution in the computed FF. This issue affects both NF and direct FF measurements.

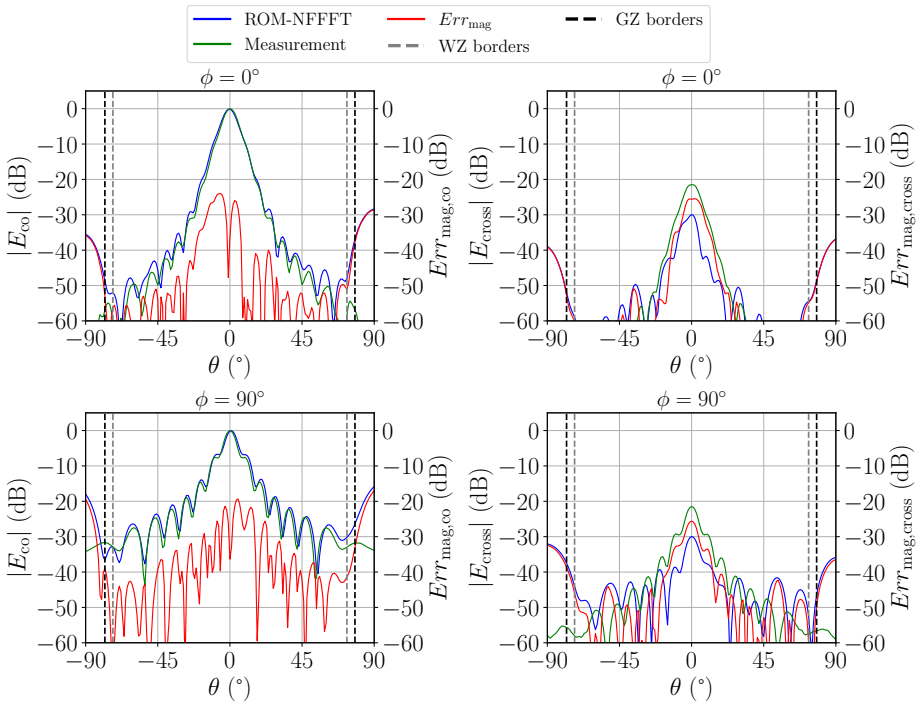

Figure IV.26 – W-band pyramidal horn, upper plane of the NF measurement surface S: comparison between computed FF using the ROM-NFFFT method and the reference measured FF data along the principal cut planes.

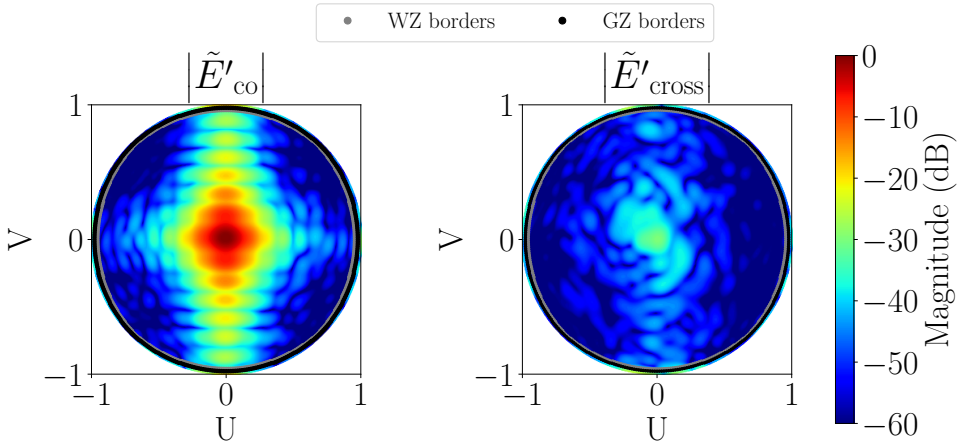

Figure IV.27 – W-band pyramidal horn, upper plane of the NF measurement surface S: UV-plane representation of the computed FF obtained with the ROM-NFFFT method.

To quantify this effect, the rejection ratio for a FF $\mathbf{E}'$ is computed at the main beam location as:

$$RR = 20 \log_{10} \frac{|E'_{\text{co}}|}{|E'_{\text{cross}}|} \tag{IV.4}$$

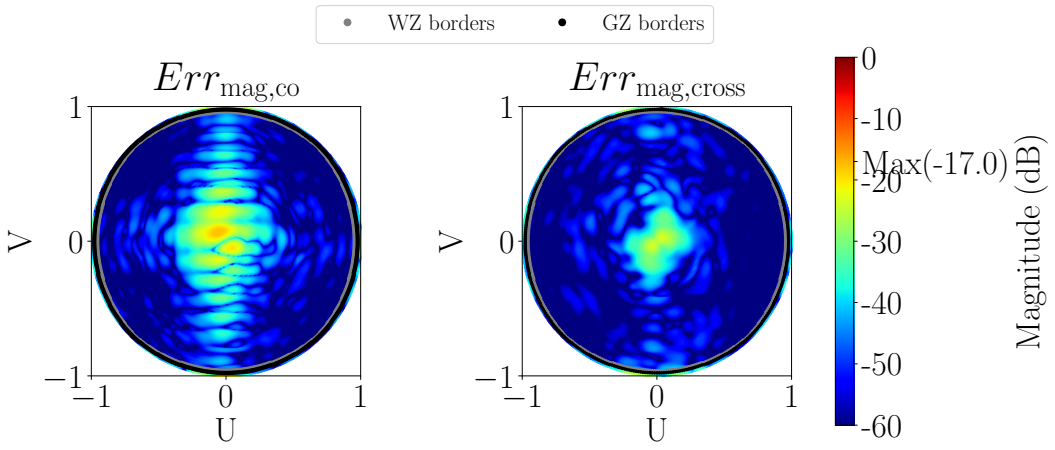

Figure IV.28 – W-band pyramidal horn, upper plane of the NF measurement surface S: UV-plane distribution of the magnitude error between the computed FF (ROM-NFFFT method) and the reference measured data.

The rejection ratio of the reference measured FF data equals 21.5 dB, confirming the misalignment. The RR values obtained are 30.1 dB and 30.2 dB for the IP and ROM-NFFFT methods, respectively, showing that the same conclusion holds for the NF measurements.

Then, the observed beam tilt can be explained by:

- a tilt angle in the YOZ-plane between the probe flanges used for the NF acquisitions in the XS scanner facility,
- mechanical bending of the NF measurement probe under gravity, which is more likely in the YOZ-plane due to the probe mechanical design.

This misalignment is highlighted by locating the main beam at -3 dB in the YOZ-plane (as used to compute the HPBW). Although the discretization of S' is not very fine, it is sufficient to detect the tilt.

For the reference measured FF data, the results give $\theta_{\text{min}} = -3°$ and $\theta_{\text{max}} = 3°$. For both the IP and ROM-NFFFT methods, the corresponding values are $\theta_{\text{min}} = -2°$ and $\theta_{\text{max}} = 4°$. Thus, an offset of approximately 1° exists between the coordinate systems of the AUT and NF measurement system.

All these issues correspond to measurement errors inherent to antenna characterization and must be carefully considered to avoid misinterpretation of the obtained results.

Correction of the identified measurement errors

Once measurement errors have been detected, appropriate corrections must be applied.

To address the issue of cross-polarization misalignment, all coordinate systems are realigned with respect to the true physical polarization of the AUT. This is achieved by minimizing the cross-polarization level for both the computed and the reference measured FF data. Practically, this is done by searching for the minimum value of RR for different rotation angles around the z-axis applied to the field vectors.

Next, to correct the θ-offset observed along the YOZ-plane, the FF observation surface S' used in the characterization methods is rotated by 1° around the x-axis. After computation, the surface is rotated back to its initial position before comparison with the reference measured FF data. The FF is then recomputed considering these corrections.

First, for the IP method, the computed FF is compared to the reference measured FF data along the main cut planes in Fig. IV.29.

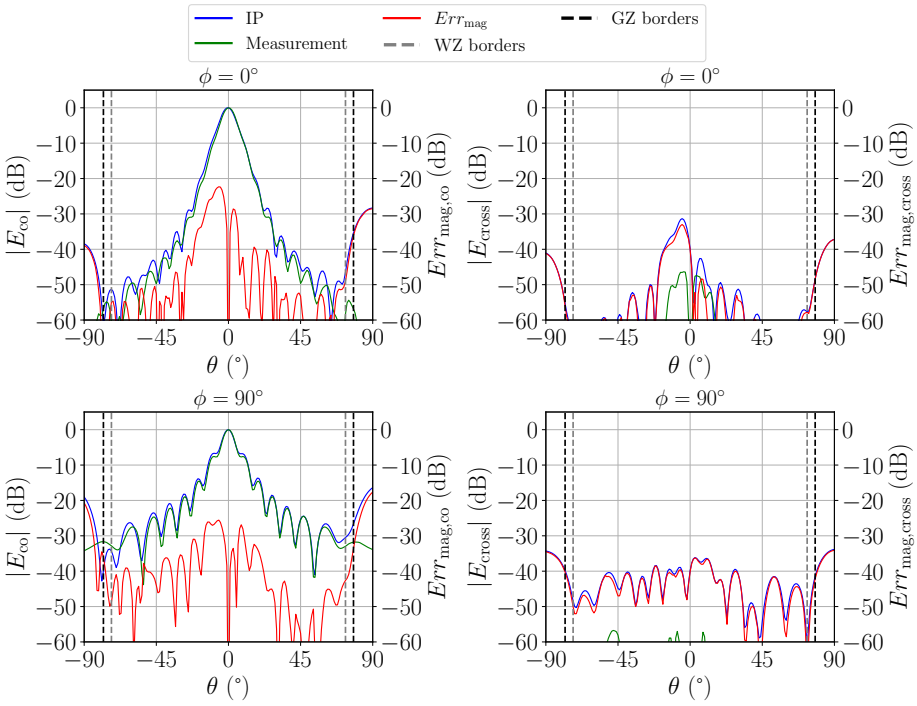

Figure IV.29 – W-band pyramidal horn, upper plane of the NF measurement surface S: comparison of computed FF using the IP method with the reference measured FF data.

The corresponding error distribution is shown in Fig. IV.30.

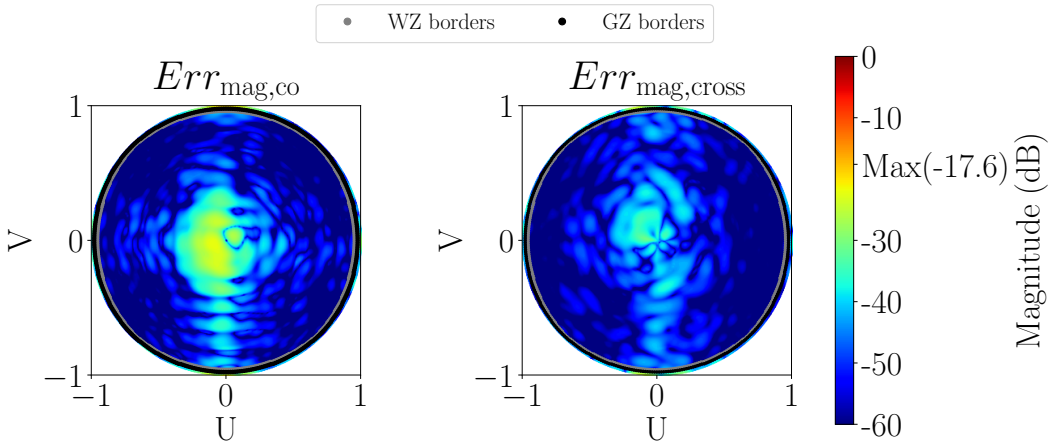

Figure IV.30 – W-band pyramidal horn, upper plane of the NF measurement surface S: UV representation of the error on the magnitude of the computed FF using the IP method relative to the reference measured FF data.

Similarly, the results obtained with the ROM-NFFFT method are shown in Figs. IV.31 and IV.32.

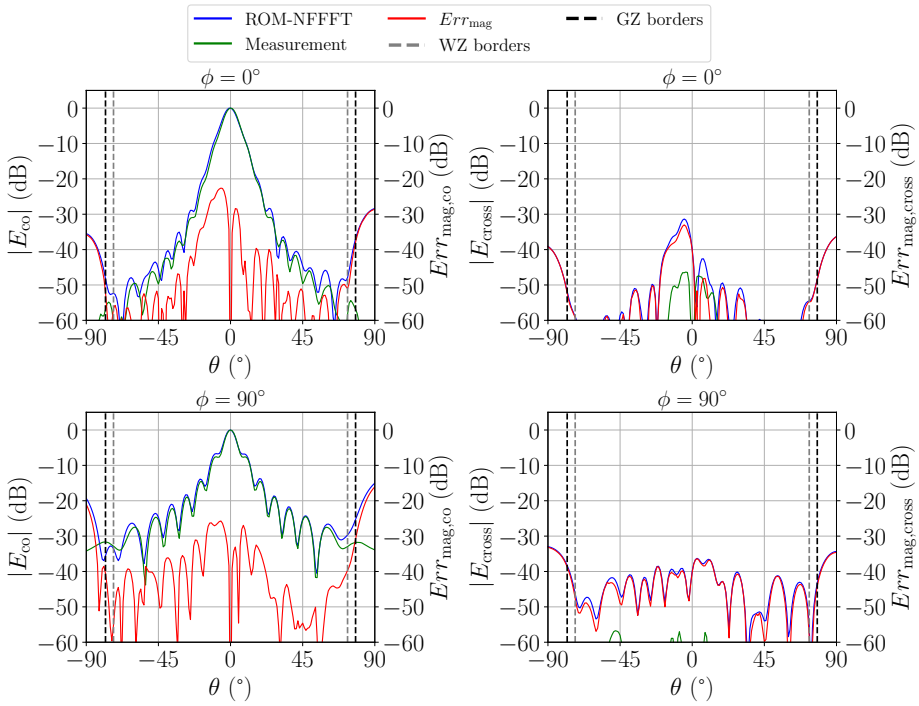

Figure IV.31 – W-band pyramidal horn, upper plane of the NF measurement surface S: comparison of computed FF using the ROM-NFFFT method with the reference measured FF data.

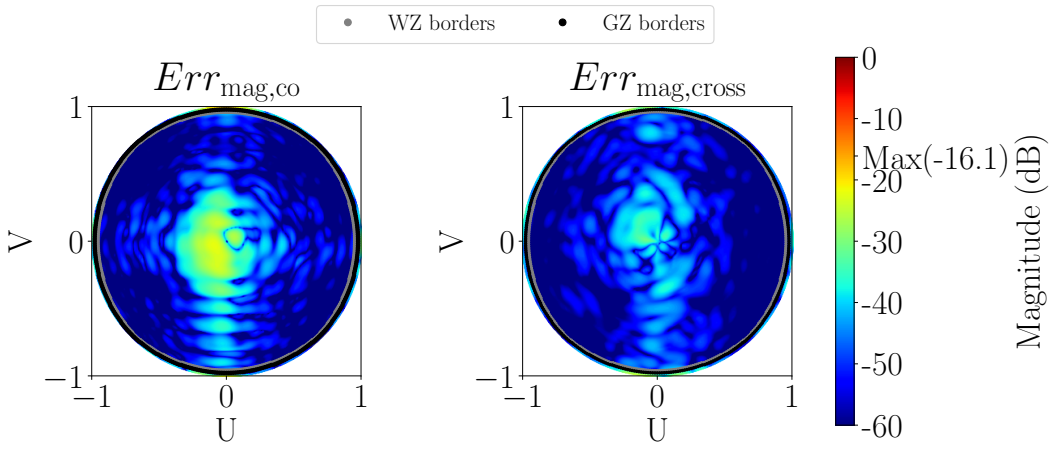

Figure IV.32 – W-band pyramidal horn, upper plane of the NF measurement surface S: UV representation of the error on the magnitude of the computed FF using the ROM-NFFFT method relative to the reference measured FF data.

The associated ENL_{mag} values are computed as $-39.8\,\text{dB}$ for the IP method and $-39.9\,\text{dB}$ for the ROM-NFFFT method. These results confirm the benefit of the applied corrections, as the error levels are consistently reduced. Such corrections are systematically applied in all subsequent FF computations compared to the measured FF data.

Nonetheless, these results also illustrate how measurement errors due to misalignments can strongly impact the interpretation of accuracy and even lead to misleading conclusions. Therefore, the observations must be interpreted with caution, acknowledging the residual uncertainties introduced by measurement errors in both NF and FF data. This is particularly critical when reference data are used to compare different developed methods, as in our case. A more exhaustive list of possible measurement errors, depending on the type of measurement facility employed, is provided in the IEEE standards [9]. Moreover, all measurement errors are quantified by dedicated verification measurements on the facility. In this regard, geometrical measurements are currently being carried out in the in-house XS scanner measurement system to accurately assess the induced systematic errors (Appendix B).

Measurement probe

Before selecting an appropriate reference to study sampling reduction with our approach, measurement errors related to the probe itself must be analyzed. The objective is to evaluate the impact of probe compensation on the computed FF accuracy.

For this purpose, Fig. IV.33 compares the computed FF using the IP method without

probe compensation and with the spline interpolation technique, relative to the measured FF data.

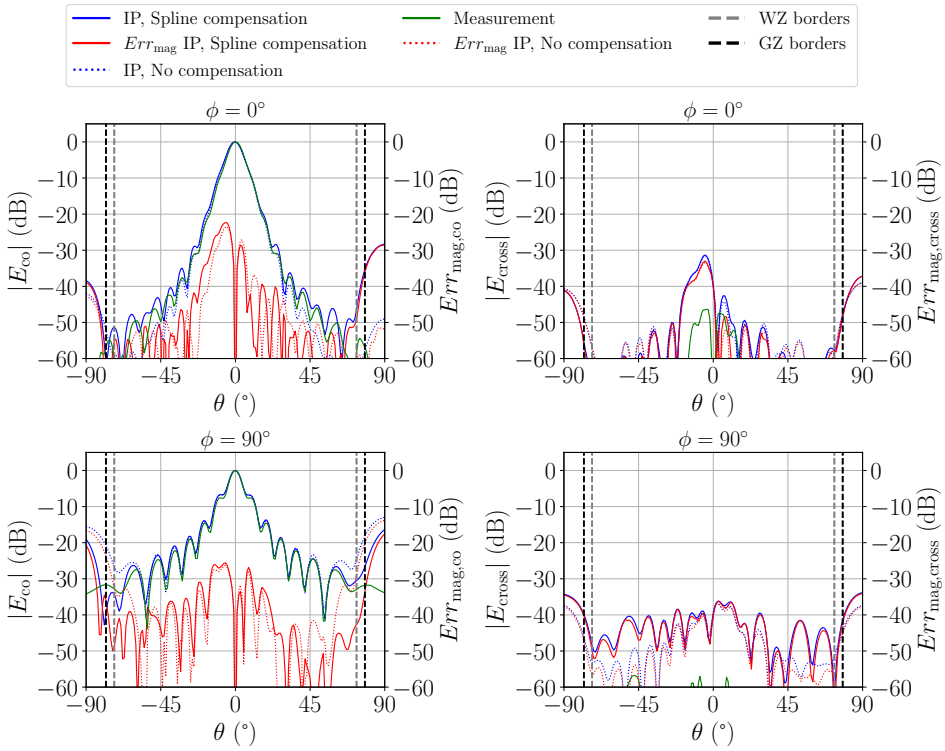

Figure IV.33 – W-band pyramidal horn, half-box-shaped NF measurement surface S: comparison of computed FF using the IP method without probe compensation and with spline interpolation, relative to the reference measured FF data.

The influence of probe compensation is most visible at grazing angles and for low-level side lobes. Further details are provided in Table IV.4.

Characterization case	ENL_{mag} (dB)	$ENL_{\text{mag, WZ}}$ (dB)	$ENL_{\text{mag, GZ}}$ (dB)	$ENL_{\text{mag, BZ}}$ (dB)
No compensation	-40.7	-41.5	-44.4	-35.8
Spline interpolation	-39.8	-40.3	-45.6	-35.8

Table IV.4 – W-band pyramidal horn: accuracy of FF computation using the IP method, with and without probe compensation, relative to the reference measured FF data.

The overall error difference between the computed FF with and without probe compensation remains small across all FF zones. Hence, the impact of probe compensation on the characterization accuracy is low. The observed FF errors are therefore not induced by this step but may originate from other measurement errors. This limited influence of probe compensation may be explained by an imperfect representation of the actual probe

radiation pattern combined with additional measurement errors.

Indeed, probe compensation techniques rely on accurate knowledge of the probe radiation characteristics. If the simulated probe does not exactly reproduce the one used during acquisition, discrepancies arise. For instance, absorbing materials surrounding the measurement probe in the IDEM facility have not been included in the CST model of the W-band OEWG. These absorbers can introduce ripples in the probe radiation pattern, as discussed by Salazar *et al.* [116]. Neglecting this effect may lead to significant differences between the simulated and actual probe radiation patterns.

In addition, several measurement-related error sources may contribute, such as:

- probe reflectivity affecting the AUT,
- channel imbalance due to cable rotation between the probe and the VNA when acquiring both polarizations.

Since no quantitative data are available to estimate these contributions, their precise impact cannot be assessed here.

Half-box-shaped measurement surface S

After identifying the measurement errors affecting the characterization of the W-band pyramidal horn, the study of sampling reduction using our approach is carried out.

Here, the NF data measured on the entire half-box-shaped surface S are exploited. One of the objectives is to verify the robustness of the proposed characterization process with probe compensation for a non-conventional NF measurement surface while reducing the number of measurement points. This configuration introduces stronger probe filtering effects on the lateral faces, which may perturb both characterization accuracy and sampling reduction. This impact is now analyzed when facing measurement noises on an experimental case.

The construction of a ROM for the half-box-shaped NF measurement surface S with a truncation level set to $R = -40\,\mathrm{dB}$ yields a truncation index of $T = 831$. From this value, the number of required NF measurement points is computed. The SVD analysis indicates that $N_{\mathrm{SVD}} = 1032$ points must be selected among the 19041 points of S. The selection of the subsampling is performed following the procedure described in Section III.3. For comparison, the classical measurement setup using the upper plane of S requires 12769 points, which means that the available sampling reduction corresponds to $N_{\mathrm{SVD}}/N_{\mathrm{PWE}} = 8.1\%$.

Subsequently, IP, ROM-IP, and ROM-NFFFT are applied on a subsampled half-box-shaped NF measurement surface S to establish comparisons between the methods on an experimental case and verify the trends observed in simulation. The subsampling is performed using a Fibonacci projection that retains 1202 points (6.3% of the 19041 total), corresponding to $N/N_{\mathrm{PWE}} = 9.4\%$ compared to the classical setup. An illustration of the selected points is shown in Fig. IV.34.

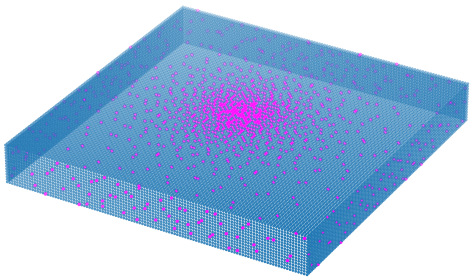

Figure IV.34 – Perspective projection of a Fibonacci subsampling (magenta, 1202 points) into the regular sampling over the half-box-shaped NF measurement surface S (blue, 19041 points).

The results on the accuracy of the computed FF compared to the reference measured FF data are reported in Table IV.5.

Characterization method	ENL_{mag} (dB)
IP	-40.0
ROM-IP	-40.0
ROM-NFFFT	-39.8

Table IV.5 – W-band pyramidal horn: accuracy of FF computation using IP, ROM-IP, and ROM-NFFFT methods on a subsampled half-box-shaped NF measurement surface S (9.4% of points compared to the classical setup). Spline interpolation is applied in all cases for probe compensation.

A representative case is shown in Fig. IV.35, where the computed FF polarizations using ROM-NFFFT on the subsampled S and non-subsampled case are compared to the reference measured FF data.

The error levels confirm that a drastic sampling reduction of about 90% compared to a classical measurement setup is possible without degrading the AUT characterization. Moreover, probe compensation does not affect this reduction for any of the tested

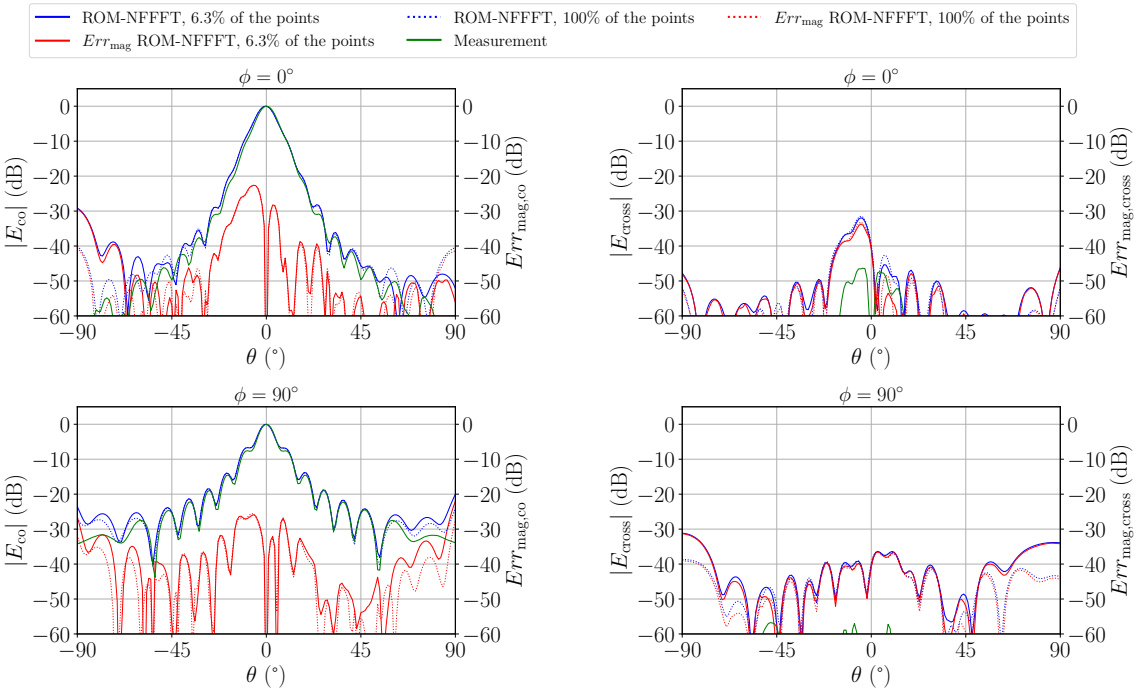

Figure IV.35 – W-band pyramidal horn, half-box-shaped NF measurement surface S: comparison of the computed FF using the ROM-NFFFT method with and without Fibonacci subsampling. Spline interpolation is applied in both cases for probe compensation.

characterization methods while using a non-conventional sampling strategy on S. This result validates the proposed global approach on a challenging experimental case, given the frequencies involved, and certifies the robustness and flexibility of the developed characterization methods. In addition, the fact that the ROM-NFFFT achieves the same accuracy as the other methods highlights its advantage: once the reduced basis in the field space $\mathbf{U}_T$ is precomputed, the method is straightforward to use and does not require solving a linear system.

Conclusion on the observations

Then, this experimental study confirms that a drastic reduction of the sampling size down to about 10% of the classical measurement setup can be achieved without compromising the accuracy of the FF characterization. Among the tested techniques, the ROM-NFFFT method proves particularly advantageous, since it combines high accuracy with a straightforward implementation once the transition matrix has been computed. This property is crucial to propose a simplified industrial implementation of this characterization method. Indeed, the only two steps (matrix pseudo-inverse computation and

matrix multiplication) to compute the transition matrix from the reduced basis $\mathbf{U}_T$ obtained by the ROM construction can be embedded in a Field-Programmable Gate Array (FPGA) to enable fast characterization.

Furthermore, the error analyses presented in this section demonstrate the robustness of the developed model with respect to typical measurement uncertainties, such as probe misalignments, polarization mismatches, and AUT positioning offsets, particularly at high frequencies. After applying systematic corrections, the computed characterization errors remain acceptable and consistent across methods, confirming that the proposed approach maintains high accuracy even under realistic non-ideal conditions.

Nonetheless, a limitation is observed with respect to probe compensation, which does not provide additional accuracy in the computed FF. Possible explanations for the observed trends have been proposed, but they require further investigation, particularly through the second experimental case presented in the following section.

However, the results validate the applicability of our global approach to experimental scenarios and naturally lead to the next investigation, which focuses beyond sampling reduction on the limitations induced by truncation effects in practical measurement conditions.

IV.4 Characterization of an X-band Luneburg lens

The second experimental case concerns an X-band Luneburg lens. The objective is to characterize an AUT that exhibits properties similar to the AESA antennas targeted in this study. Indeed, the combination of the Luneburg lens with an illuminating source enables the formation of highly directive beams under various tilt scenarios. This radiating system is designed to be flexible and easily reconfigurable, ensuring repeatability across different operating modes in both NF and FF measurement setups.

Additionally, the antenna dimensions are comparable to those of the Thales DMS AUT of interest. The frequency band also matches the operational scenario relevant to the company, making the Luneburg lens a suitable and challenging test case provided by the IETR laboratory. Its electrical size and complexity provide a rigorous validation for the developed characterization methods while highlighting computational considerations.

The proposed methods are applied with the two main goals of reducing the number of measurement samples and mitigating truncation effects.

IV.4.a Characterization setup

The AUT is an X-band Luneburg lens with a radius of 200 mm, operating at 10 GHz (Appendix C). An illustration of the AUT is presented in Fig. IV.36.

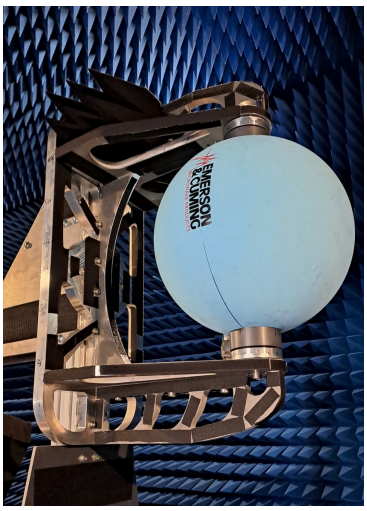

Figure IV.36 – The X-band Luneburg lens to characterize.

The radiating system, consisting of the illuminating OEWG and the lens, produces three main beam directions: $(\theta_{\text{beam}} = 0°, \phi_{\text{beam}} = 0°)$, $(\theta_{\text{beam}} = 44°, \phi_{\text{beam}} = 356°)$, and $(\theta_{\text{beam}} = 53°, \phi_{\text{beam}} = 65°)$.

Given the large electrical size of the lens (13.3λ), an equivalent surface Σ is modeled as a half-box of dimensions $15\lambda \times 15\lambda \times 7\lambda$ covering the upper radiation space of the AUT. To reduce problem size and computational cost while ensuring feasible characterization, the dipole spacing is relaxed to $\frac{\lambda}{2}$. This reduces the number of dipoles to 10320, compared to 23220 for a $\frac{\lambda}{3}$ spacing. Σ is centered at $(0\lambda, 0\lambda, 3.25\lambda)$. A visualization of the lens and its equivalent model is shown in Fig. IV.37.

The NF data have been acquired at the *Imagerie et Diagnostic ElectroMagnétique* (IDEM) facility (Appendix B). Both E_x and E_y components have been measured on a half-box-shaped NF surface S of size $36.8\lambda \times 33.6\lambda \times 13.6\lambda$, with a sampling step of 0.4λ, centered at $(0, 0, 6.8\lambda)$. The number of measurement points on S is equal to 19873. The measurement configuration is illustrated in Fig. IV.38.

The measurement setup is constrained by the scanner dimensions of the planar NF system available at Thales DMS, reflecting realistic industrial limitations.

The probe used for NF acquisition is a standard X-band OEWG, identical to that described in Section IV.2.b. Spline interpolation is applied for probe compensation, leveraging previously validated probe FF patterns.

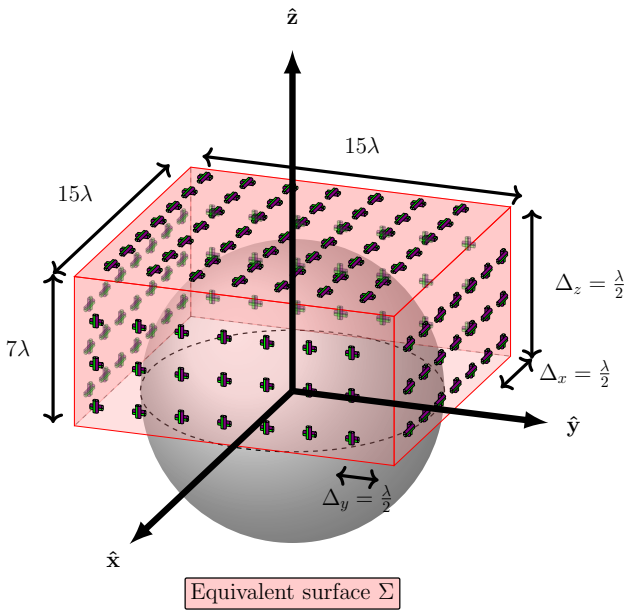

Figure IV.37 – X-band Luneburg lens antenna and its equivalent surface Σ.

For all ROM-based analyses, the truncation parameter is set to $R = -40\,\text{dB}$ and the regularization parameter *rcond* in the least-squares solver is fixed at 10^{-2}.

FF data have been acquired in the *CAractérisation en bande CENtimétrique de Dispositifs RAyonnants* (CACENDRA) facility for the three main beam directions. This facility uses spherical measurement techniques and serves as a reliable reference. The observation surface S' is a half-sphere sampled with an equiangular distribution with $\Delta_\theta = \Delta_\phi = 1°$. Since the exact FF distance is unknown, error metrics are computed using self-normalization.

FF measured magnitudes of the co- and cross-polarizations are presented in Figs. IV.39-IV.41 for the three beam directions.

IV.4.b Discussion on the measurement errors

As in the experimental case of the W-band pyramidal horn, the Luneburg lens acquisition campaign is subject to measurement errors, as detailed in Section IV.3.b.

To evaluate whether these errors may affect the characterization results, a focused study is performed on the main beam direction ($\theta_{\text{beam}} = 0°, \phi_{\text{beam}} = 0°$). Only the ROM-NFFFT method is applied for this analysis of the measurement errors as previous study achieved for the W-band horn confirmed the similarities between three equivalent model-based methods (IP, ROM-IP and ROM-NFFFT). Error metrics are defined using self-

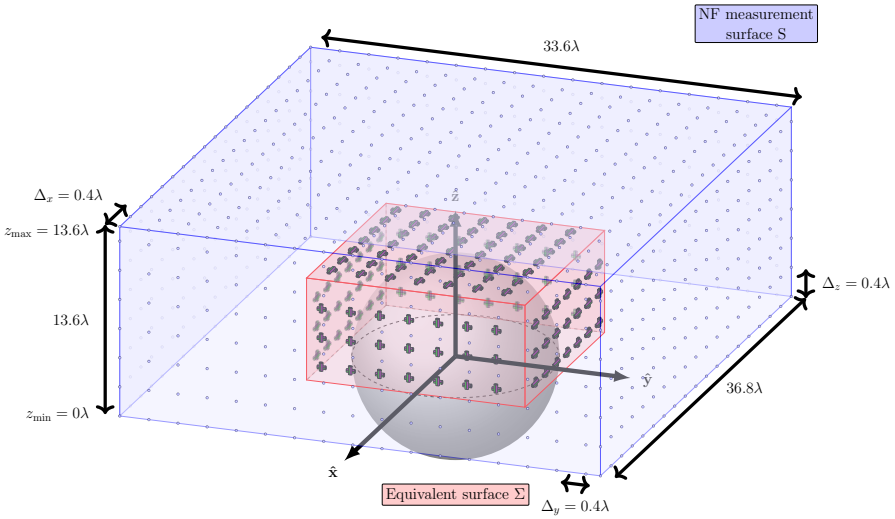

(a) 3D representation

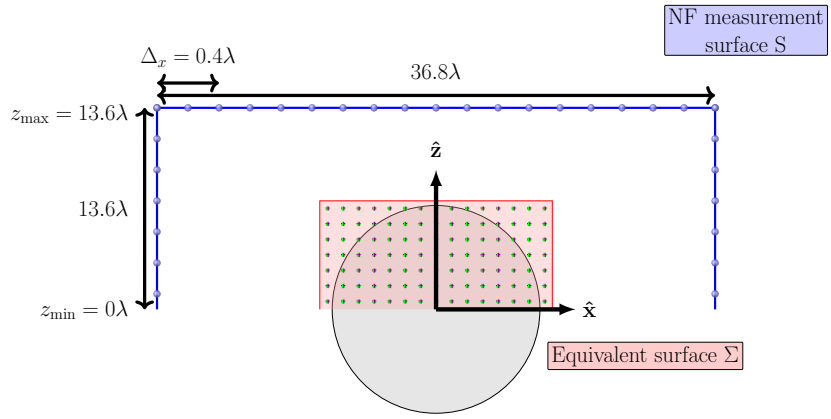

(b) XOZ plane

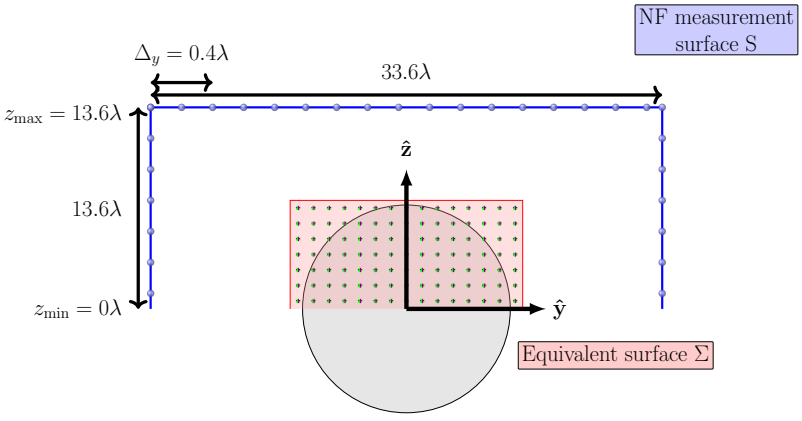

(c) YOZ plane

Figure IV.38 – X-band Luneburg lens: half-box NF measurement surface S.

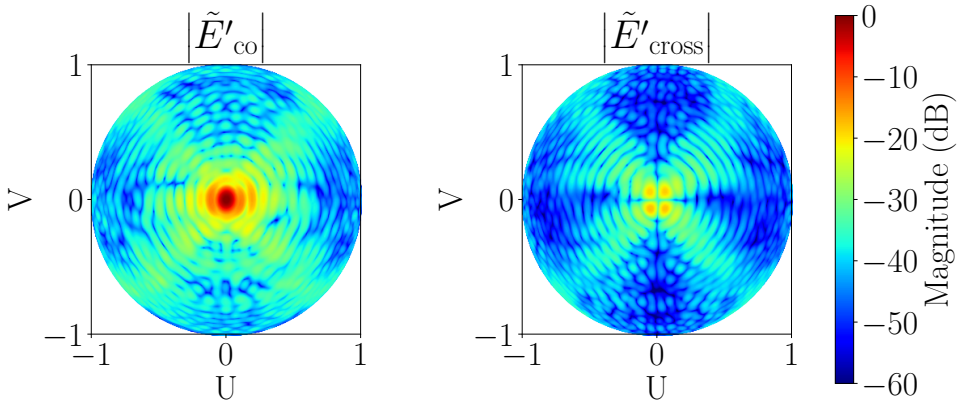

Figure IV.39 – X-band Luneburg lens, ($\theta_{\text{beam}} = 0°, \phi_{\text{beam}} = 0°$): measured FF magnitude on S'.

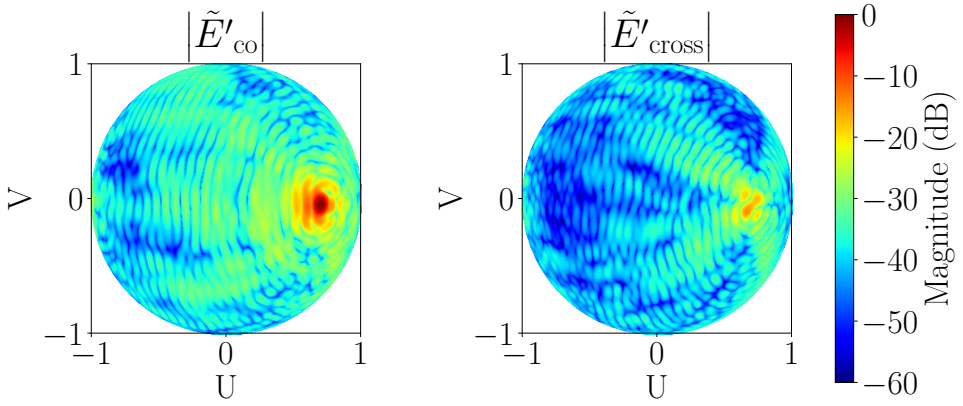

Figure IV.40 – X-band Luneburg lens, ($\theta_{\text{beam}} = 44°, \phi_{\text{beam}} = 356°$): measured FF magnitude on S'.

normalization relative to the measured FF data on the observation surface S'.

Fig. IV.42 shows the comparison between the computed FF and the reference data along the principal cut planes, also yielding $ENL_{\text{mag}} = -38.1\,\text{dB}$.

The UV representations of the ROM-NFFFT computed FF and the corresponding magnitude error are given in Figs. IV.43 and IV.44, respectively.

To investigate potential misalignments in direct FF measurements, the rejection ratio RR is computed. The reference measured FF data show $RR = 36.3\,\text{dB}$, confirming significant misalignment. The computed NF-based FF estimates yield $RR = 32.2\,\text{dB}$, indicating a consistent presence of misalignments and elevated cross-polarization.

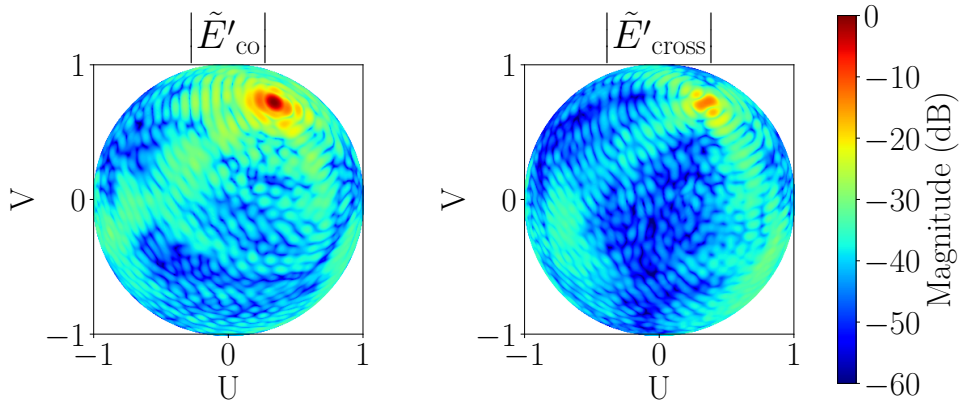

Figure IV.41 – X-band Luneburg lens, ($\theta_{\mathrm{beam}} = 53°, \phi_{\mathrm{beam}} = 65°$): measured FF magnitude on S'.

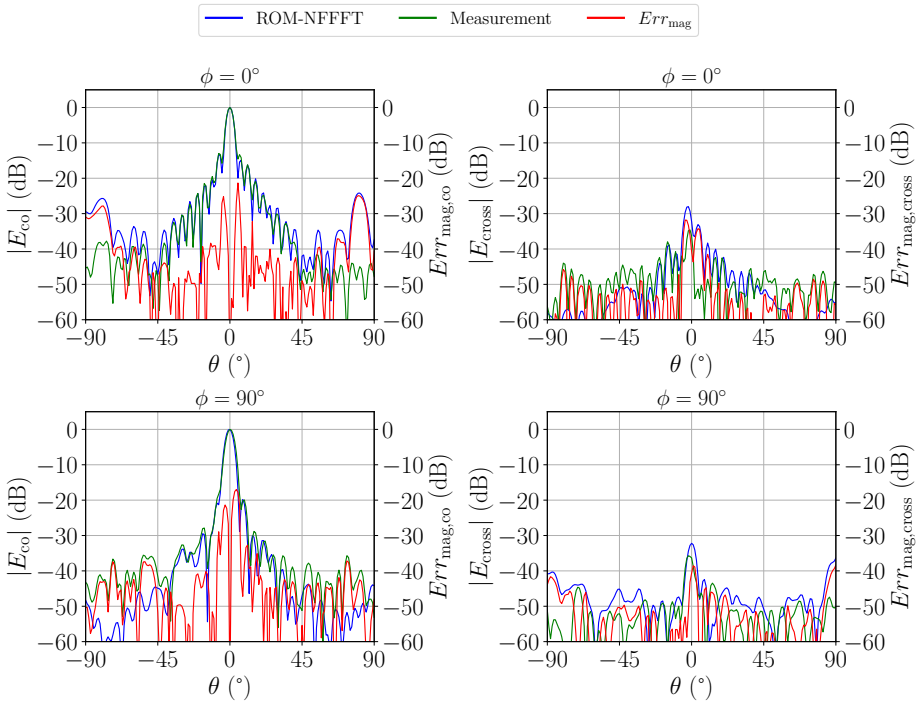

Figure IV.42 – X-band Luneburg lens, ($\theta_{\mathrm{beam}} = 0°, \phi_{\mathrm{beam}} = 0°$): comparison of computed FF using the ROM-NFFFT method with the reference measured FF data.

To mitigate these effects, all coordinate systems are realigned with respect to the true physical polarization of the AUT by minimizing the cross-polarization level simultaneously in the computed and reference FF data.

Then, a slight beam tilt is mainly observed in the $\phi = 90°$ plane. Angular mismatches between the AUT and the scanner coordinate systems are identified using a laser tracker

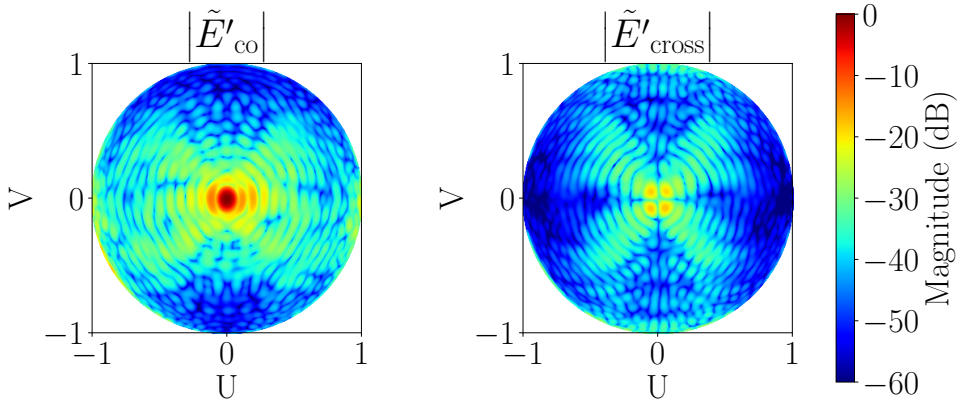

Figure IV.43 – X-band Luneburg lens, ($\theta_{\text{beam}} = 0°, \phi_{\text{beam}} = 0°$): UV representation of the computed FF using the ROM-NFFFT method.

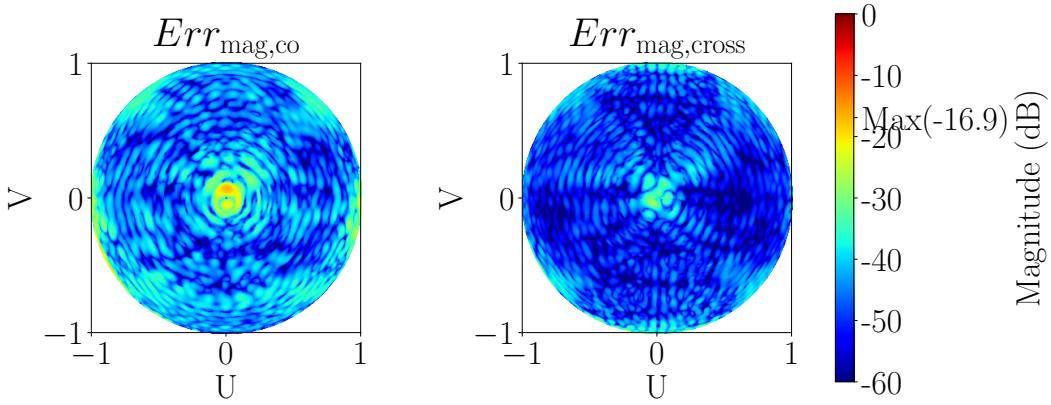

Figure IV.44 – X-band Luneburg lens, ($\theta_{\text{beam}} = 0°, \phi_{\text{beam}} = 0°$): UV representation of the magnitude error of the computed FF using the ROM-NFFFT method with respect to the reference measured FF data.

(Appendix B). Unlike the W-band horn experiment, these offsets cannot be fully corrected by a simple rotation.

Therefore, to correct these offsets the FF observation surface S' can be rotated around all three axes ($\hat{\boldsymbol{x}}, \hat{\boldsymbol{y}}, \hat{\boldsymbol{z}}$) for alignment during computation. The theoretical positions can then be used for analysis and comparison with reference measurements. This procedure has not yet been applied to the remaining presented results.

Measurement probe

Before selecting a suitable reference for the study of sampling reduction and truncation effect mitigation with our approach, measurement errors related to the probe must first be analyzed.

To this end, the ROM-NFFFT method is applied on the half-box-shaped NF measurement surface S, including probe compensation based on spline interpolation. The objective is to quantify the impact of probe compensation on the accuracy of the computed FF.

Fig. IV.45 compares the computed FF obtained with and without probe compensation against the measured FF data for the main beam direction ($\theta_{\text{beam}} = 0°, \phi_{\text{beam}} = 0°$).

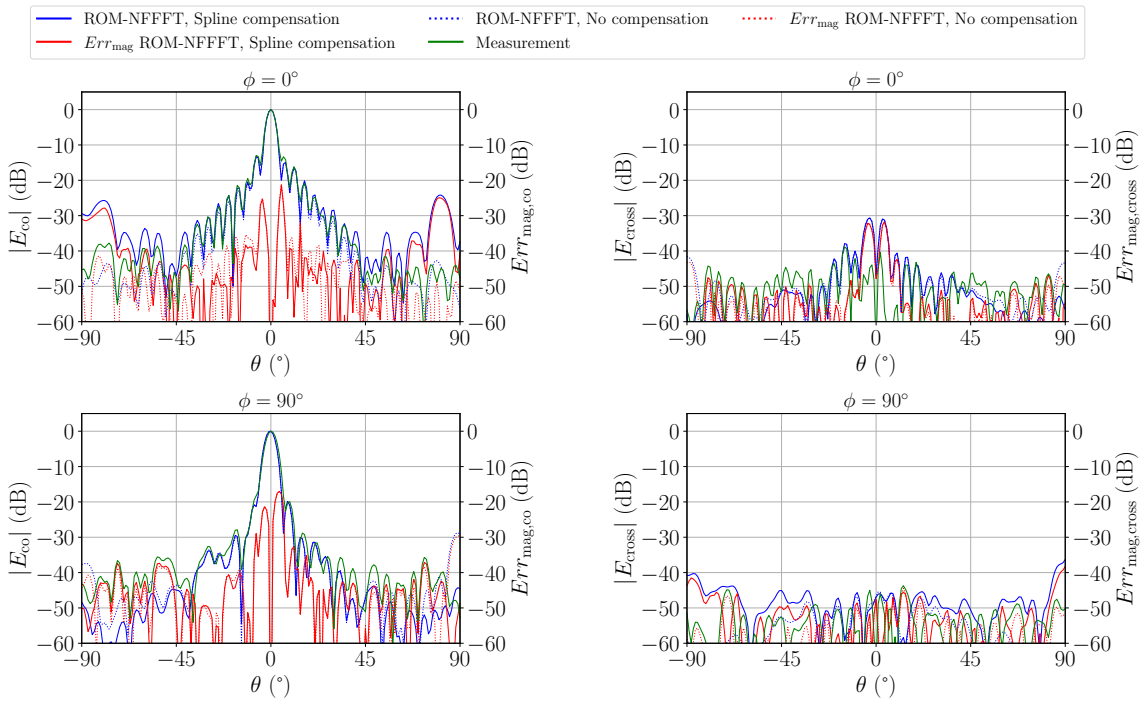

Figure IV.45 – X-band Luneburg lens, ($\theta_{\text{beam}} = 0°, \phi_{\text{beam}} = 0°$): comparison of computed FF using the ROM-NFFFT method without probe compensation and with spline interpolation, compared to the reference measured FF data.

The results show that, contrary to expectations, probe compensation slightly degrades the characterization accuracy. This is confirmed by the ENL_{mag} values: −38.7 dB without compensation versus −38.2 dB with compensation.

As also observed in the previous section, the influence of probe compensation is most noticeable at grazing angles and in low-level sidelobe regions. In these critical FF areas, error levels increase significantly, most likely due to an imperfect representation of the actual probe radiation pattern, compounded by additional measurement uncertainties. Another possible explanation is linked to our equivalent model-based approach. Specifically, for a half-box NF surface, certain measurement points may lie below some of the dipoles constituting Σ (i. e. the signed displacement in the z-coordinate between a dipole and a measurement point is negative). In such cases, if the reconstructed probe radiation

pattern from CST simulations does not accurately match the real one in these back-propagation directions, the probe compensation process can itself introduce errors in the treatment.

Further investigations would be required to confirm that the integration of probe effects into the proposed model remains valid, as already demonstrated in simulation studies, and that the discrepancies observed here are not intrinsic to the approach itself.

Despite these limitations, and because probe effects cannot be neglected in practical scenarios, the spline interpolation technique is retained for the subsequent characterization results.

IV.4.c Characterization results and analysis

After identifying the measurement errors affecting the characterization of the X-band Luneburg lens, the analysis now turns to sampling reduction and mitigation of truncation effects using the proposed approach. To this end, two tilted beam directions are considered: $(\theta_{\text{beam}} = 44°, \phi_{\text{beam}} = 356°)$ and $(\theta_{\text{beam}} = 53°, \phi_{\text{beam}} = 65°)$. For these operating modes, the characterization becomes even more challenging than in the no-tilt case, which further underlines the practical relevance of our developed methodology.

Methodology

To ensure that probe compensation errors and uncorrected misalignments do not bias the interpretation of the characterization results, a two-step methodology is adopted depending on the choice of FF reference.

First, to investigate sampling reduction independently of measurement errors, a computed FF reference is used instead of the measured FF data. Specifically, the FF obtained with the ROM-NFFFT method, including spline interpolation for probe compensation, is selected as the reference. In this case, error metrics are evaluated using reference-based normalization.

Second, a global analysis is performed to assess both the sampling reduction and the mitigation of truncation effects relative to the measured FF data. Here, the associated errors are computed using self-normalization.

For the reduction of NF measurement points, a ROM is constructed for the half-box-shaped surface S with truncation level $R = -40\,\text{dB}$, yielding a truncation index $T = 4180$. From this, the number of required NF measurement points is determined. The

SVD analysis indicates that $N_{\mathrm{SVD}} = 5225$ points are needed, compared with the 19873 points of S. Here again, the positions of the subsamples on S are determined according the process exposed in the Section III.3. For reference, the classical setup using only the upper plane of S and a PWE requires 7905 points, meaning that the proposed approach achieves a sampling reduction ratio of $N_{\mathrm{SVD}}/N_{\mathrm{PWE}} = 66.1\%$. Since this characterization setup applies to all beam directions considered, the analysis is carried out only once.

Furthermore, to study the mitigation of truncation effects when adopting non-conventional sampling geometries, FF computation zones are defined relative to the upper plane of S. These zones are superimposed on the amplitude of the reference measured FF data in Fig. IV.46 for both tilted main beam directions.

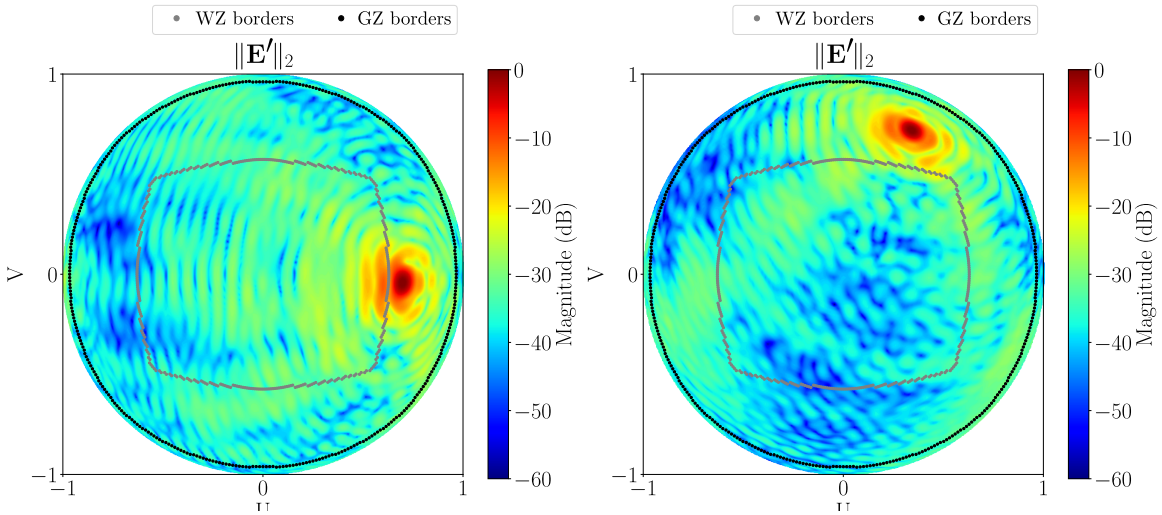

(a) $(\theta_{\mathrm{beam}} = 44°, \phi_{\mathrm{beam}} = 356°)$ (b) $(\theta_{\mathrm{beam}} = 53°, \phi_{\mathrm{beam}} = 65°)$

Figure IV.46 – UV representations of the amplitude of the reference measured FF data for both tilted main beam directions. The FF zones corresponding to the upper plane of the NF measurement surface S are shown.

In both operating conditions, $(\theta_{\mathrm{beam}} = 44°, \phi_{\mathrm{beam}} = 356°)$ and $(\theta_{\mathrm{beam}} = 53°, \phi_{\mathrm{beam}} = 65°)$, the main radiated power lies within the GZ. This implies that, for a classical setup limited to the upper plane of S, these characterization scenarios are critical since truncation effects are expected to be significant. The defined zones therefore provide a consistent framework for comparing the FF computed with the ROM-NFFFT method when applied to both the half-box-shaped surface S and its upper plane.

Reduction of the sampling size and truncation effects

First, the ROM-NFFFT method is applied on a subsampled half-box-shaped NF measurement surface S. The subsampling is performed using a Fibonacci projection that retains 5554 points (27.9% of the total 19873), corresponding to $N/N_{\mathrm{PWE}} = 70.2\%$ compared to the classical setup. An illustration of the selected points is shown in Fig. IV.47.

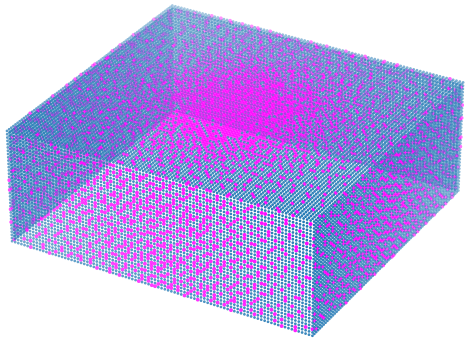

Figure IV.47 – Perspective projection of a Fibonacci subsampling (magenta) of 5554 points onto the regular sampling over the half-box-shaped NF measurement surface S (blue, 19873 points).

The computed polarizations using the ROM-NFFFT method, with and without Fibonacci subsampling and including probe effect compensation, are compared in Fig. IV.48 for $(\theta_{\mathrm{beam}} = 44°, \phi_{\mathrm{beam}} = 356°)$.

The corresponding ENL value, equal to $-54.9\,\mathrm{dB}$, confirms that a sampling reduction of about 30% relative to a classical setup can be achieved without degrading the computed FF accuracy. This result is important, as it shows that a reduced number of NF samples still allows for an accurate characterization of the AUT, without visible impact from measurement noise or the tilted beam configuration.

Next, to verify the mitigation of truncation effects while reducing the number of measurement points, comparisons are made between the computed FF using the ROM-NFFFT method on both the half-box-shaped S and its upper plane, relative to the reference measured FF data for tilted beam directions.

First, the characterization is performed without applying probe compensation. This isolates the effects of using a non-conventional NF measurement surface S and subsampling on the accuracy of the FF computation for tilted main beams. Figs. IV.49 and IV.50

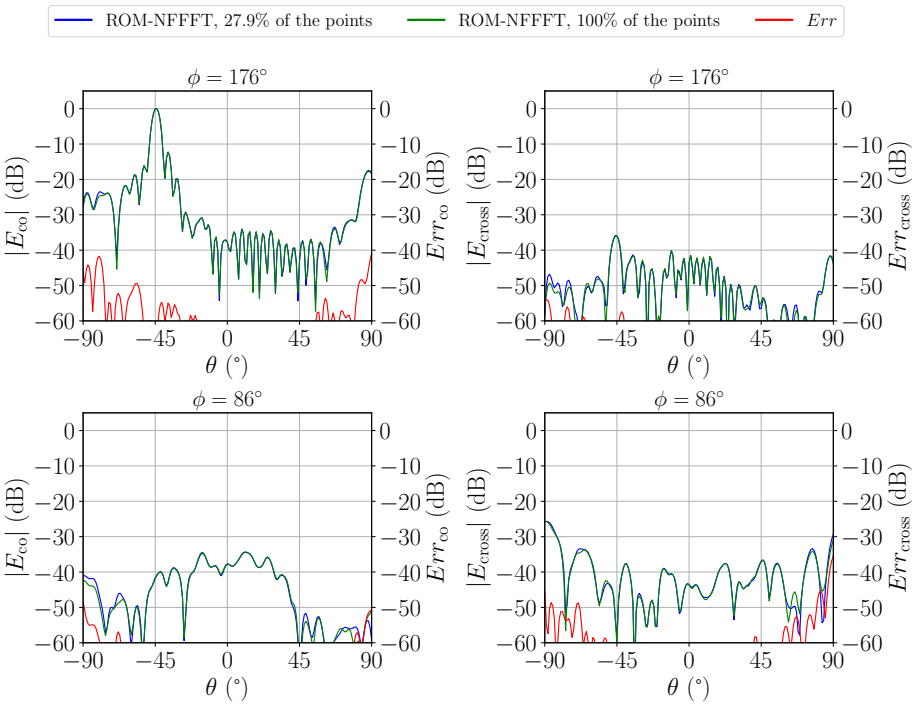

Figure IV.48 – X-band Luneburg lens, ($\theta_{beam} = 44°, \phi_{beam} = 356°$): comparison of the computed FF using the ROM-NFFFT method with and without Fibonacci subsampling of the half-box-shaped S. Probe compensation via spline interpolation is applied in both cases.

show the co- and cross-polarizations in the main cut planes, while the corresponding error metrics for each computation zone are summarized in Tables IV.6 and IV.7.

Geometry of S	ENL_{mag} (dB)	$ENL_{mag,\ WZ}$ (dB)	$ENL_{mag,\ GZ}$ (dB)	$ENL_{mag,\ BZ}$ (dB)
Plane	-40.1	-41.4	-38.9	-39.9
Half-box	-40.1	-41.4	-40.9	-36.0

Table IV.6 – Beam at ($\theta_{beam} = 44°, \phi_{beam} = 356°$): comparison of FF precision obtained with the ROM-NFFFT method between a subsampled half-box-shaped NF measurement surface S ($N/N_{PWE} = 70.2\%$) and the classical measurement setup represented by the upper plane of S (without subsampling). No probe compensation is applied.

The FF computed from the half-box S demonstrates localized improvements in Err_{mag}, particularly around the main lobe and within the GZ, compared to the classical plane setup. This trend is observed for both tilted beam configurations and highlights that the half-box geometry can enhance accuracy even when approximately 30% of the measurement points are removed.

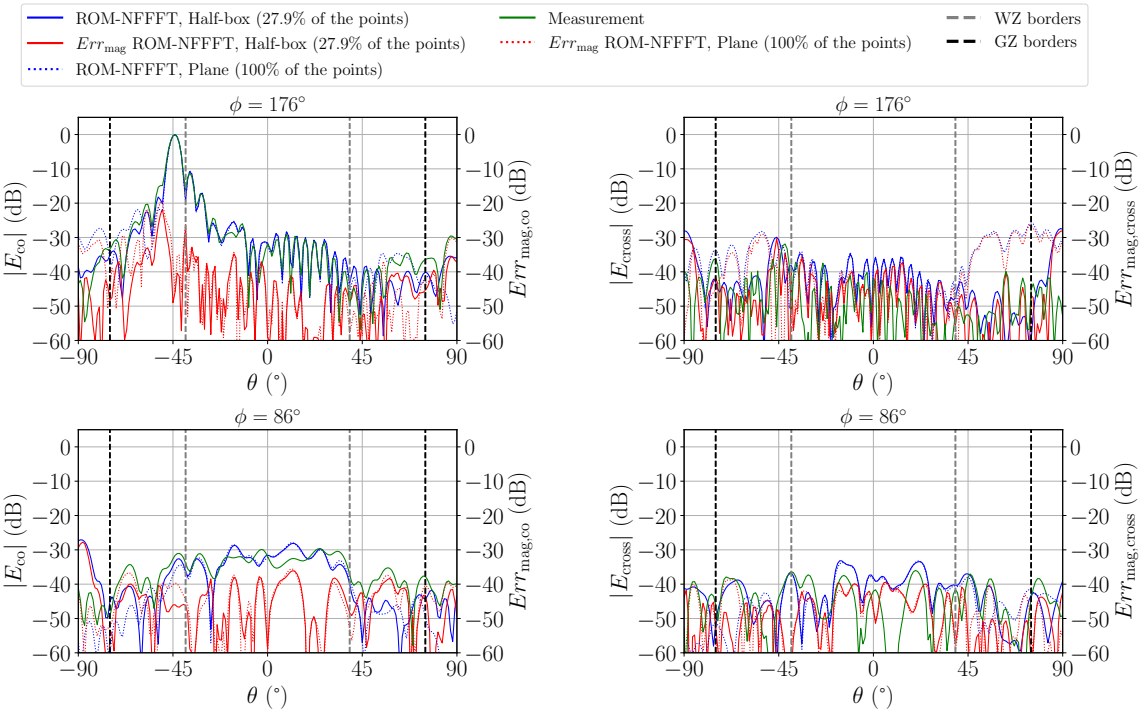

Figure IV.49 – X-band Luneburg lens, ($\theta_{\text{beam}} = 44°, \phi_{\text{beam}} = 356°$): comparison of the computed FF using the ROM-NFFFT method on the half-box-shaped S (with Fibonacci subsampling) and its upper plane (classical setup). No probe compensation is applied.

Geometry of S	ENL_{mag} (dB)	$ENL_{\text{mag, WZ}}$ (dB)	$ENL_{\text{mag, GZ}}$ (dB)	$ENL_{\text{mag, BZ}}$ (dB)
Plane	-37.0	-39.0	-35.1	-37.4
Half-box	-38.6	-41.6	-39.8	-31.7

Table IV.7 – Beam at ($\theta_{\text{beam}} = 53°, \phi_{\text{beam}} = 65°$): comparison of FF precision obtained with the ROM-NFFFT method between a subsampled half-box-shaped NF measurement surface S ($N/N_{\text{PWE}} = 70.2\%$) and the classical measurement setup represented by the upper plane of S (without subsampling). No probe compensation is applied.

Conversely, within the BZ, higher errors are observed at grazing angles. These degradations may be attributed to a combination of factors:

- the loss of orthonormality in the modal basis caused by the sampling reduction, and
- the absence of probe compensation, which is particularly significant on the lateral faces where filtering effects are more pronounced.

It should be noted that, in the GZ and BZ, the accuracy of the computed FF is inherently limited in the classical setup. In particular, no accurate characterization results can be expected in the BZ. Therefore, the improvements observed in the GZ highlight a

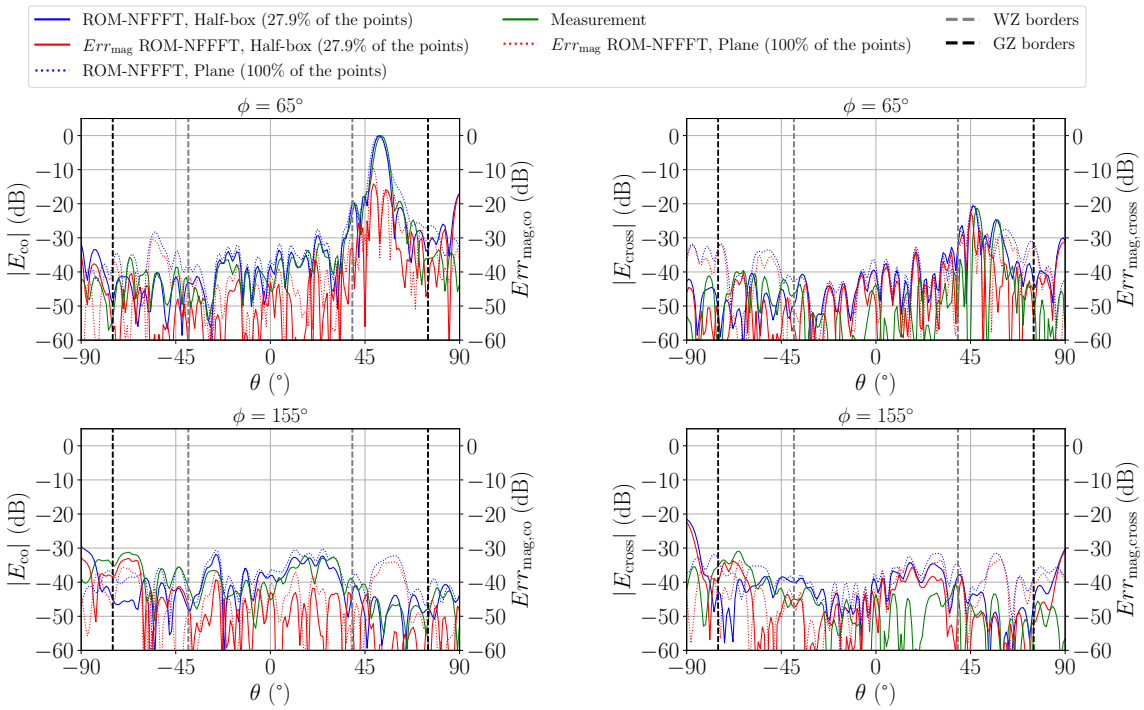

Figure IV.50 – X-band Luneburg lens, ($\theta_{\text{beam}} = 53°, \phi_{\text{beam}} = 65°$): comparison of the computed FF using the ROM-NFFFT method on the half-box-shaped S (with Fibonacci subsampling) and its upper plane (classical setup). No probe compensation is applied.

meaningful advantage of employing a half-box-shaped NF measurement surface S.

Subsequently, probe compensation using spline interpolation is applied. The resulting co- and cross-polarizations are presented in Figs. IV.51 and IV.52, and the corresponding FF accuracy for each computation zone is given in Tables IV.8 and IV.9.

Geometry of S	ENL_{mag} (dB)	$ENL_{\text{mag, WZ}}$ (dB)	$ENL_{\text{mag, GZ}}$ (dB)	$ENL_{\text{mag, BZ}}$ (dB)
Plane	-39.0	-39.2	-38.4	-39.9
Half-box	-38.3	-39.2	-38.7	-35.2

Table IV.8 – Beam at ($\theta_{\text{beam}} = 44°, \phi_{\text{beam}} = 356°$): comparison of FF accuracy obtained with the ROM-NFFFT method between a subsampled half-box-shaped NF measurement surface S ($N/N_{\text{PWE}} = 70.2\%$) and the classical measurement setup represented by the upper plane of S (without subsampling). Probe compensation via spline interpolation is applied in both cases.

As expected, the combination of measurement uncertainties and the effects introduced by probe compensation can lead to localized degradations in FF accuracy. While global trends are difficult to extract and the benefits of non-conventional sampling strategies such as Fibonacci subsampling applied on a half-box S are not uniformly evident, improvements

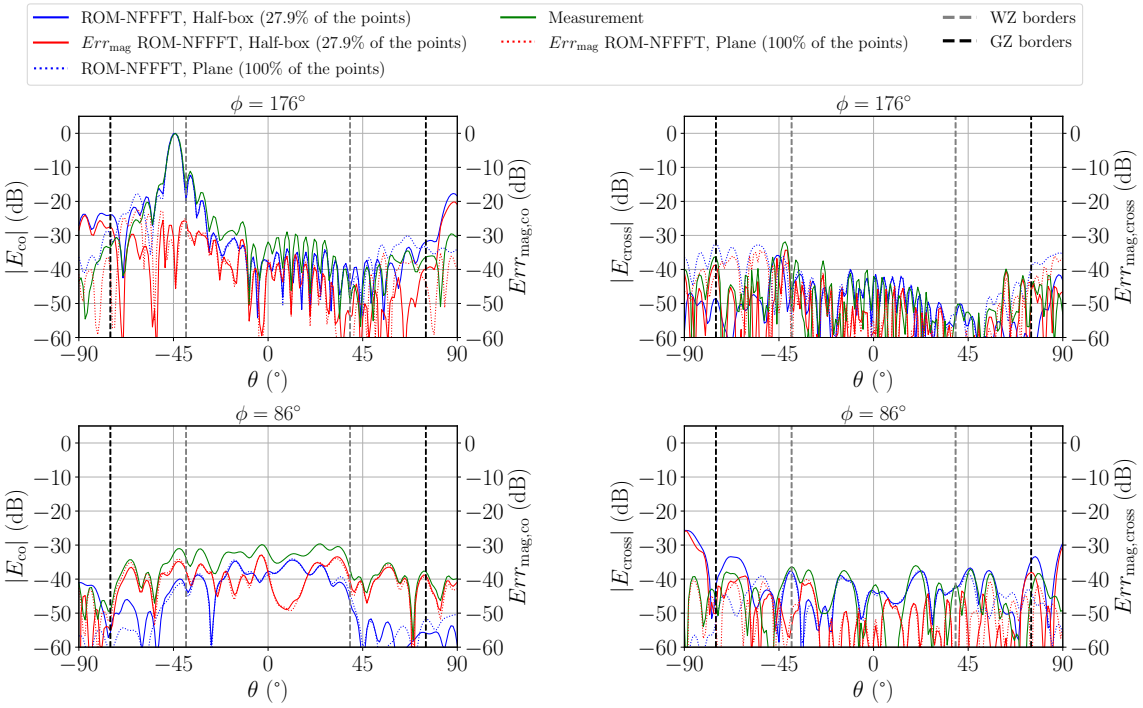

Figure IV.51 – X-band Luneburg lens, ($\theta_{beam} = 44°, \phi_{beam} = 356°$): comparison of the computed FF using the ROM-NFFFT method on the half-box-shaped S (with Fibonacci subsampling) and its upper plane (classical setup). Probe compensation via spline interpolation is applied in both cases.

Geometry of S	ENL_{mag} (dB)	$ENL_{mag,\,WZ}$ (dB)	$ENL_{mag,\,GZ}$ (dB)	$ENL_{mag,\,BZ}$ (dB)
Plane	-32.6	-35.4	-30.2	-32.9
Half-box	-33.6	-37.1	-34.0	-27.3

Table IV.9 – Beam at ($\theta_{beam} = 53°, \phi_{beam} = 65°$): comparison of FF accuracy obtained with the ROM-NFFFT method between a subsampled half-box-shaped NF measurement surface S ($N/N_{PWE} = 70.2\%$) and the classical measurement setup represented by the upper plane of S (without subsampling). Probe compensation via spline interpolation is applied in both cases.

in Err_{mag} are still observed around the main lobe and within the GZ. This confirms that the half-box geometry can enhance accuracy compared to the classical plane setup, even with a reduction of approximately 30% in measurement points.

In contrast, higher errors persist within the BZ, particularly at grazing angles. These errors are likely due to limitations in the probe radiation pattern characterization, as discussed in Section IV.4.b. This observation complements the previously noted hypothesis of orthonormality loss induced by strong sampling reductions.

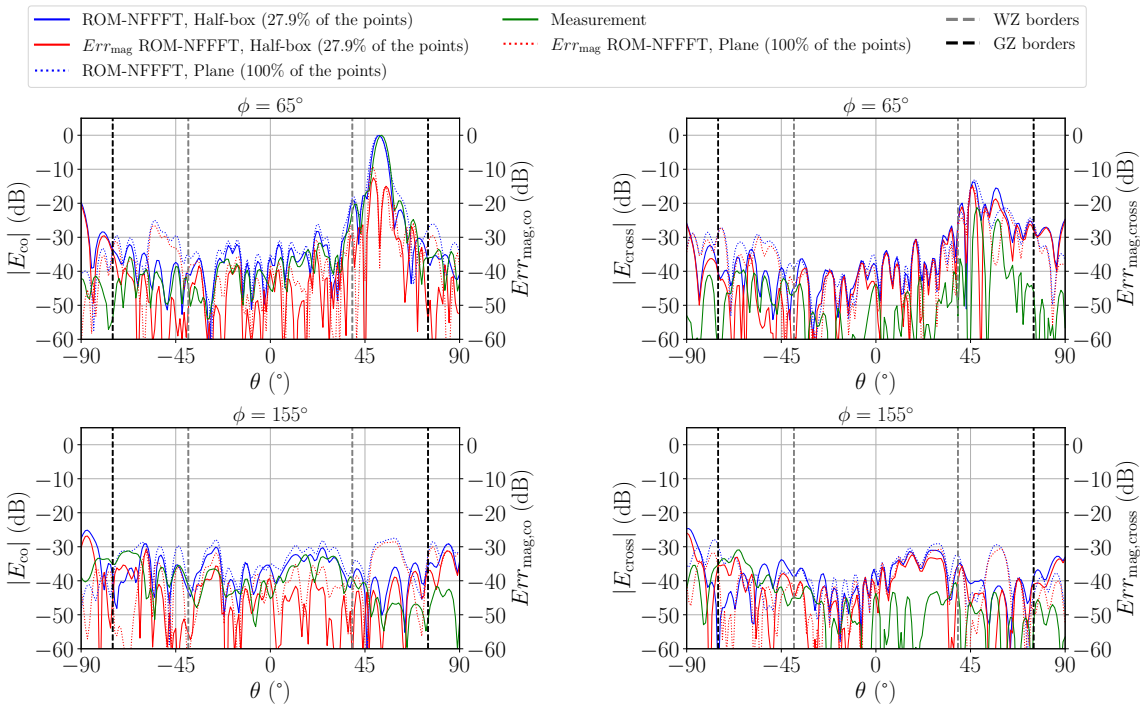

Figure IV.52 – X-band Luneburg lens, ($\theta_{\text{beam}} = 53°, \phi_{\text{beam}} = 65°$): comparison of the computed FF using the ROM-NFFFT method on the half-box-shaped S (with Fibonacci subsampling) and its upper plane (classical setup). Probe compensation via spline interpolation is applied in both cases.

Despite these mixed results, the study highlights several promising aspects of the proposed approach. The improvements observed around the main beam and the robustness against subsampling confirm that the method has potential for reducing the required number of NF measurements without significant accuracy loss. Nevertheless, some challenges remain. In particular, corrections for possible misalignments of the NF measurement setup should be carefully considered, as they can further degrade the stability of the inversion process when combined with probe compensation.

Furthermore, additional investigations are required to better quantify the role of probe compensation under more demanding conditions, such as steered beams. In these cases, the contribution of the lateral faces of the half-box-shaped surface S becomes more significant, and the accuracy of the compensation strongly influences the overall characterization. A dedicated analysis focusing on these aspects would provide valuable insights into the limits and robustness of the proposed methodology.

Overall, while this experimental case illustrates both the benefits and challenges of applying the ROM-NFFFT method with subsampling and probe compensation, the results

remain encouraging and point toward clear directions for future work.

Conclusion on the observations

The study highlights the complexity of characterizing a challenging experimental case such as the X-band Luneburg lens, where tilted main beams, large dimensions, and measurement uncertainties make accurate FF reconstruction particularly demanding. Despite these difficulties, the proposed approach demonstrates its effectiveness by enabling a reduction of the sampling size by approximately 30% relative to a classical plane setup, without degrading the overall FF accuracy. The use of Fibonacci subsampling on the half-box-shaped NF measurement surface S preserves the quality of the results and confirms the robustness of the method with respect to subsampling.

In addition, the employment of non-conventional sampling geometries contributes to mitigating truncation effects. Improvements are observed in critical regions, notably around the main beam and within the GZ, where the half-box geometry outperforms the classical plane setup. These results are encouraging, as they validate the potential of the method to limit truncation-induced errors while reducing the number of NF measurement points.

Nevertheless, some interrogations remain concerning the probe compensation. Residual inaccuracies, especially at grazing angles or in low-level side lobes, point to limitations in the probe modeling and the influence of measurement errors. These aspects highlight the need for further dedicated analyses, particularly concerning the impact of probe compensation on the lateral faces of the half-box geometry for the NF measurement surface S under steered and directive beam conditions.

Overall, these observations validate the proposed approach on a demanding experimental case, given the AUT properties (large dimensions, high directivity, and tilted beams). Although the construction of the reduced basis $\mathbf{U}_T$ from the ROM requires significant computational resources due to the antenna size and frequency, once this step is completed, the characterization process becomes straightforward. The resulting method is not only easy to apply but also naturally adaptable to different subsampling strategies. This combination of robustness, reduced sampling requirements, and flexibility underscores the strong potential of the approach for efficient and accurate antenna characterization, even in challenging measurement scenarios. Future work will refine probe compensation strategies and address misalignment corrections to further consolidate its applicability.

IV.5 Conclusion

In this work, the proposed characterization framework has been experimentally validated on two demanding cases: a W-band horn antenna and an X-band Luneburg lens. These scenarios differ significantly in terms of frequency, aperture size, directivity, and beam tilt, thus providing complementary validation of the methodology under realistic conditions.

The results confirm that a substantial reduction of the NF sampling size is achievable without compromising FF accuracy. For the W-band horn, a drastic reduction down to about 10% of the classical setup has been obtained, while for the Luneburg lens, the sampling has been reduced by approximately 30% using Fibonacci subsampling on a half-box-shaped measurement surface. In both cases, the method maintained reliable characterization performance, thereby demonstrating its robustness and flexibility across very different experimental contexts.

Another key outcome lies in the mitigation of truncation effects. Non-conventional sampling geometries, particularly the half-box configuration, proved effective in improving accuracy in critical regions such as the main beam and the grazing zone, compared to traditional planar setups. This highlights the ability of the approach to not only reduce measurement effort but also enhance characterization quality in practical conditions.

At the same time, both studies revealed persistent limitations related to probe compensation. In particular, residual inaccuracies at grazing angles or in low-level side lobes underline the sensitivity of the approach to probe modeling and measurement errors. These findings indicate that further dedicated analyses are required to refine probe compensation, especially for lateral surfaces, high-power levels, and beam-steering configurations.

Overall, the ROM-NFFFT method emerges as a robust, accurate, and adaptable solution for antenna characterization. Although the construction of the reduced basis $\mathbf{U}_T$ requires significant computational resources, once completed, the process becomes straightforward and easily adaptable to different subsampling strategies. The simplicity of the characterization step and the possibility of embedding the computation in FPGA hardware further strengthen its potential for industrial use.

In summary, the combined results of the two experimental cases validate the method efficiency in reducing sampling requirements, mitigating truncation effects, and maintaining accuracy under realistic measurement uncertainties. Future work will address probe

compensation refinements and misalignment corrections to consolidate the applicability of this approach in demanding experimental campaigns involving large-aperture, high-directivity, and beam-steering antennas.

Conclusion

Summary and outcomes

This work has presented innovative characterization methods for complex antennas, particularly those with AESA-like architectures, focusing on improving accuracy and reducing measurement time compared to classical FT-based techniques. The central idea lies in using an equivalent model of the AUT, composed of infinitesimal dipoles placed on an arbitrary equivalent surface, enabling the definition of a radiation matrix that links the equivalent currents to the radiated field on any surface of interest.

The first methodological step demonstrated that such an equivalent model can solve the IP of computing the FF radiation pattern from planar NF measurements. Analytical and numerical validations has confirmed the feasibility and accuracy of the approach. Parametric studies have also been conducted to analyze the behavior of the model with respect to variations in both the equivalent model parameters and those of the NF measurement surface, leading to a set of trends and guidelines that must be followed to ensure accurate characterization. Furthermore, the model has been extended to include the effects of the measurement probe. Probe coefficient matrices, derived for orthogonal probe orientations, have been integrated into the radiation model to account for spatial filtering effects, ensuring realistic performance in experimental contexts.

A significant contribution of this work is the mitigation of truncation effects, which often degrade FF computation from finite planar NF measurements. By decoupling the model from strict geometric constraints, non-conventional measurement surfaces and sampling distributions have been proposed and validated, illustrating their ability to reduce truncation artifacts while maintaining computational efficiency.

The development of a ROM for the treated characterization problem, which is based on SVD of the radiation matrix associated to the NF measurement surface, has provided an additional breakthrough. This step enables the estimate of the minimum number of NF samples necessary for accurate computation. First, the criterion used to predetermine the required number of samples has been validated in our context of planar NF measurements. Subsequently, the ROM-based approach confirmed that this number of samples can be

significantly reduced thus shortening measurement time without compromising accuracy.

Finally, all these advancements have been merged into a unified and practical ROM-NFFFT method. This approach relies on the pre-computation of a reduced-basis in the field space, issued from a ROM construction while incorporating probe compensation and optimized sampling strategies. The resulting method reduces the characterization process to two key steps: first, computing a pseudo-inverse, and second, performing a matrix multiplication. Together, these steps ensure numerical stability while keeping the post-processing workflow simple and efficient. Experimental validations on a W-band horn antenna and an X-band Luneburg lens confirmed the robustness, accuracy, and practical applicability of this new generation of characterization methods. These real characterization cases have been carried out in the measurement facilities of the IETR laboratory.

Perspectives

Building on the results obtained in this work, several promising directions can be envisioned:

Broadband and ultra-wideband extensions

While the proposed equivalent model and characterization approaches have been applied to narrowband antennas at specific operating frequencies, an important perspective is to generalize these methods to wideband antennas. This would require handling multiple frequencies simultaneously, ensuring that the equivalent model accurately captures the frequency-dependent behavior of the AUT across its entire operational bandwidth.

Non-conventional sampling strategies

The present work focused on a limited set of non-conventional sampling strategies for the NF measurement surface. Exploring additional sampling distributions could further improve characterization efficiency and accuracy. For instance, approaches inspired by Capozzoli *et al.* [40] have shown potential in optimizing measurement locations to minimize the number of samples required for planar NF acquisitions. Systematic studies in this direction could reveal novel sampling strategies particularly suitable for complex or electrically large antennas. Moreover, the use of a randomized SVD in the context of planar NF measurements, as presented by Fuchs *et al.* [63], offers a promising means to define

an objective criterion for selecting the necessary samples. This approach is particularly interesting to test with the developed model in this thesis, as it enables efficient antenna characterization while maintaining high accuracy, potentially reducing measurement time and computational cost for large or high-directivity systems.

Uncertainty quantification and error control

The precise quantification of uncertainties and measurement errors remains a key challenge. The characterization methods presented involve numerous parameters, both from the equivalent model and the measurement system. In particular, the influence of probe compensation errors, especially for non-conventional measurement geometries where significant filtering effects occur, requires deeper investigation. Providing confidence intervals, sensitivity analyses, or probabilistic bounds on the computed FF patterns would enhance the reliability of the characterization, allowing more informed decisions in practical antenna design and validation. Developing efficient methods to manage and propagate these uncertainties through the equivalent model and the NFFFT procedure represents an important direction for future research.

Integration into industrial measurement frameworks

Finally, transferring these methods to industrial antenna measurement facilities requires further research on robustness, calibration procedures, and automation. This includes developing user-friendly software tools for pre-processing, matrix construction, and visualization of computed patterns. In particular, the implementation and validation of these methods in Thales' industrial environment will be one of the missions pursued following this PhD.

Overall, the approaches developed in this work provide a strong foundation for next-generation antenna characterization methods, combining physical rigor, numerical efficiency, and experimental applicability. They open the way for hybrid methods where physics-based modeling, adaptive sampling, and data-driven approaches work together to achieve unprecedented levels of accuracy and efficiency in antenna measurements.

APPENDICES

A Simulated CST X-band patch

Various validation cases presented in this thesis are numerical applications based on patch arrays simulated using CST Studio Suite. In this section the elementary X-band (between 8 GHz and 12 GHz) patch element used to build the 8×8 planar array and the 60×1 linear array referenced in this manuscript is described in detail. Emphasis is given both to the practical choices made for the simulations and to the theoretical background that motivates these choices.

Architecture of the patch antenna

The chosen radiating element is a probe-fed rectangular microstrip patch antenna. The design frequency is chosen as $f_0 = 10\,\text{GHz}$ (X-band). The patch can be approximately modeled as a resonant cavity with electric walls along the radiating edges and magnetic walls along the non-radiating edges. Classically, this cavity is represented by a patch and a ground plane which are separated by a dielectric substrate. The radiating element has a length L_e, a width W_e and a height H_e, while the patch has a length L and a width W. The substrate height is denoted h. All these parameters are represented in Fig. A.1.

In this configuration, the electric field has a dominant component perpendicular to the patch plane (z-axis), and no transverse electric field exists along the thickness of the patch. Therefore, the dominant resonant mode is the TM_{10} mode. The resonant frequency for which the maximum power is radiated by the element depends primarily on the patch length L, while the width W influences input impedance and bandwidth.

The classical closed-form design expressions are [117, 5]:

1. effective dielectric constant:

$$\varepsilon_{\text{eff}} = \frac{\varepsilon_r + 1}{2} + \frac{\varepsilon_r - 1}{2}\left[1 + 12\frac{h}{W}\right]^{-1/2}$$

where h is the substrate thickness and ε_r its relative permittivity;

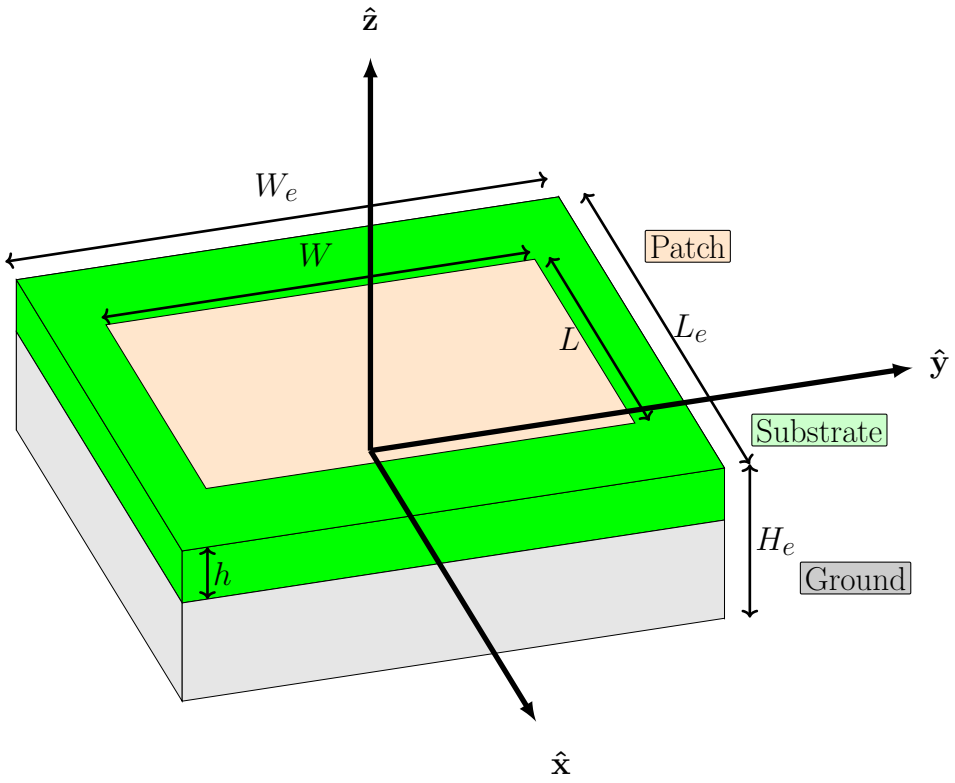

Figure A.1 – Representation of a rectangular microstrip patch antenna.

2. patch width:

$$W = \frac{c}{2f_0}\sqrt{\frac{2}{\varepsilon_r + 1}};$$

3. patch length:

$$L = \frac{c}{2f_0\sqrt{\varepsilon_{\text{eff}}}} - 2\Delta L$$

where the fringing extension ΔL is

$$\Delta L = 0.412h\frac{(\varepsilon_{\text{eff}} + 0.3)(\frac{W}{h} + 0.264)}{(\varepsilon_{\text{eff}} - 0.258)(\frac{W}{h} + 0.8)}.$$

The resonant frequency depends primarily on the patch length L.

The coaxial probe excites the patch at an offset x_p from the patch center to match the input impedance Z_{in} to a reference $Z_0 = 50\,\Omega$. From [5]:

$$
\begin{aligned}
Z_0 &= \frac{138}{\sqrt{\varepsilon_r}} \log_{10}\left(\frac{D_o}{D_p}\right), \\
Z_{\text{in}} &\approx 90 \frac{\varepsilon_r^2}{\varepsilon_r - 1} \left(\frac{L}{W}\right)^2, \\
x_p &= \frac{L}{\pi} \arccos\left(\sqrt{\frac{Z_0}{Z_{\text{in}}}}\right),
\end{aligned}
$$

where D_o and D_i are the outer and inner diameters of the coaxial feed.

Design parameters and radiation

The free-space wavelength at the frequency f_0 is

$$\lambda_0 = 30\,\text{mm}.$$

On CST, the following material properties are selected to construct the radiating element:

- Substrate: Rogers RO4350, $\varepsilon_r = 2.2$, $\tan\delta \approx 0.0009$.
- Patch: PEC.
- Ground plane: PEC.
- Coaxial: PEC.

Then, the width of the patch corresponding to this design frequency is taken from [118]. The resulting mechanical parameters can be found:

$$
\begin{aligned}
L_e &= 15\,\text{mm}, \\
W_e &= 15\,\text{mm}, \\
h &= 1.588\,\text{mm}, \\
H_e &= 4.588\,\text{mm}, \\
L &= 9.06\,\text{mm}, \\
W &= 11.86\,\text{mm},
\end{aligned}
$$

The element dimensions L_e and W_e are fixed large enough to avoid edge effects in particular when our objective is to create patch array with multi-elements. In the same way, the ground is set as being thick (3 mm) to avoid back-propagation.

Then, the coaxial feed parameters are determined:

$$\begin{aligned} D_p &= 1.161\,\text{mm}, \\ Z_{\text{in}} &= 223.7\,\Omega, \\ x_p &= 3.067\,\text{mm}, \end{aligned}$$

A representation of the radiating element is given in Fig. A.2.

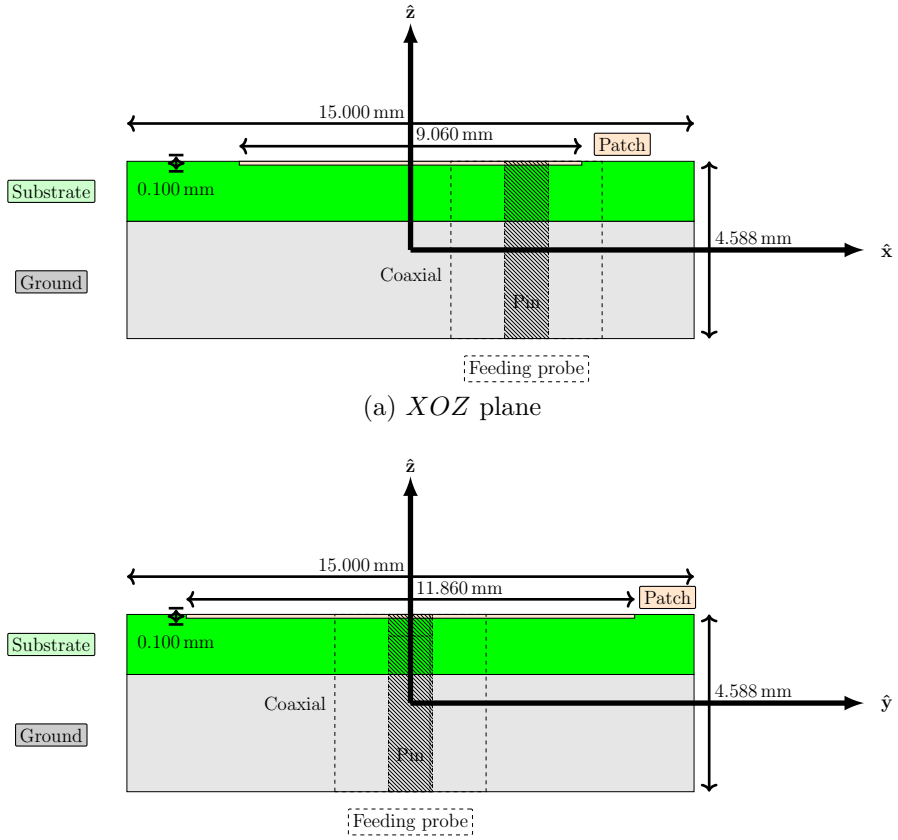

(a) XOZ plane

(b) YOZ plane

Figure A.2 – 2D representation of the radiating element microstrip patch antenna.

Once the parameters are fixed, a time-domain simulation solver is used to verify the radiation characteristics of the patch antenna. Figure A.3 presents the S_{11} parameter also known as the return-loss level of this patch antenna which determines how the resonance

is varying for a frequency sweep performed in the X-band.

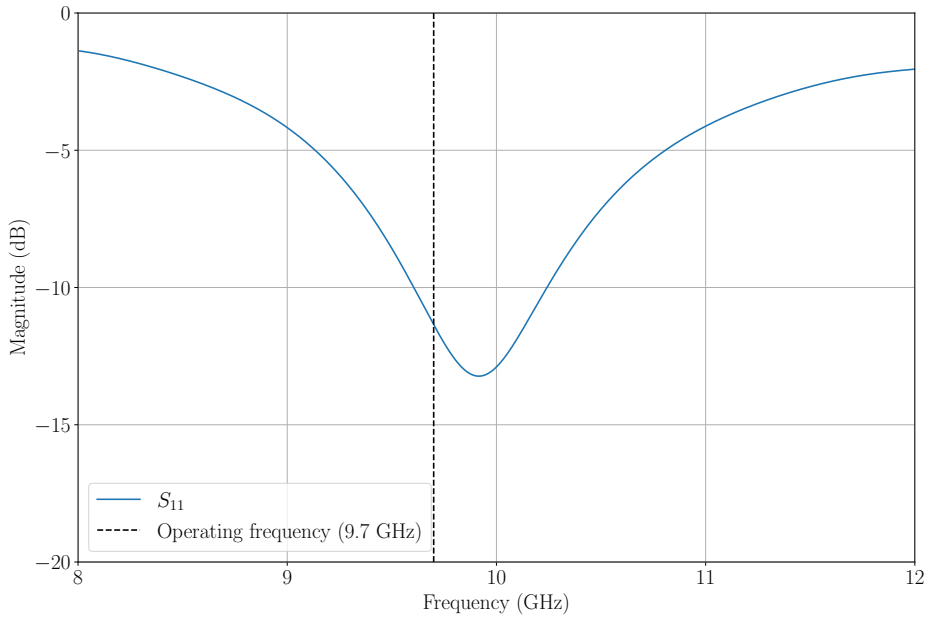

Figure A.3 – Patch antenna S_{11} parameter according to the X-band frequencies.

Although, in general the objective in antenna design domain is to locate the minimum of the S_{11} parameter which indicates the best possible frequency for a maximized power radiation, our approach is not this one. Indeed, our goal is to construct numerical array antennas with high beam steering which radiates correctly (target $S_{11} < -10\,\mathrm{dB}$) but not in the optimal way to test our developed model. Therefore, imprefections in the antenna design step are not that important in our context and furthermore it can brings some non-ideal behavior that are interesting to study through our approach validations. In that sense, the operating frequency is selected at $f = 9.7\,\mathrm{GHz}$ to avoid rounded numbers compared to the design frequency (10 GHz) in the simulated data positions that are considered in our model allowing a global complexification of the treated cases.

The corresponding FF radiation pattern of the antenna is given in Fig. A.4.

Construction of the arrays

The two array configurations studied in the thesis are constructed from the elementary patch described above:

Inter-element spacing is set to $d = \lambda_0/2 = 15\,\mathrm{mm}$ in both principal directions for the planar array. For the linear 60×1 case the same spacing is used along the x- axis. This choice prevents grating lobes for broadside scan angles while limiting mutual coupling

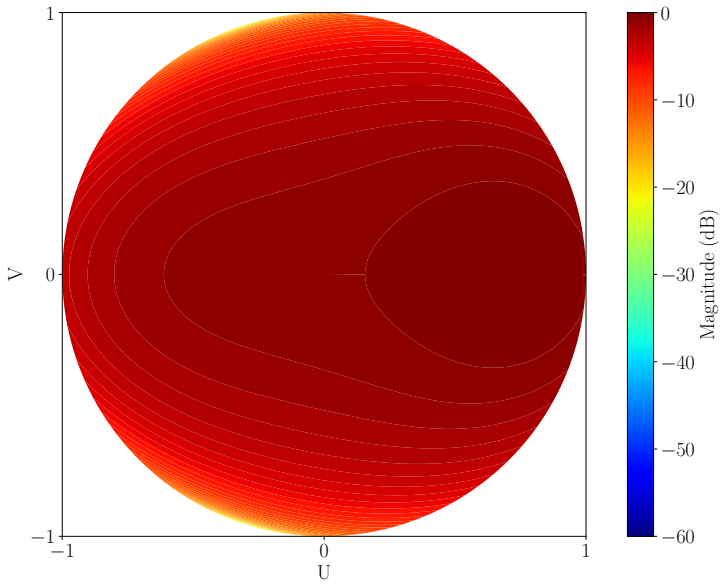

Figure A.4 – UV representation of the patch antenna radiation pattern.

to acceptable levels. Larger spacings would reduce the physical array size but introduce grating lobes when steering beyond high angles.

An illustration of both 8×8 and 60×1 arrays from a XOY planar view is given in Fig. A.5.

The total radiated field of an array is the product (or convolution in angular domain depending on approach) of the element pattern and the array factor. For progressive phase steering to angle θ_{beam} in the E-plane (steering XOZ plane) the required inter-element progressive phase shift is:

$$\Delta\psi = -k_0 d \sin\theta_{\text{beam}},$$

In practice, phase shifters are applied on CST to each element to implement this progressive phase, producing a main beam steered to θ_{beam}.

Summary

The rectangular probe-fed patch provides a compact, easily modelled element for the X-band arrays used in this thesis. The theoretical sizing formulas supply first-order dimensions, which are then refined in full-wave simulation to obtain the desired resonance and match. Arraying with half-wavelength spacing enables robust beam steering while mitigating grating lobes; nonetheless, mutual coupling and truncation effects remain important. This complex behavior constitutes interesting and challenging simulated validation cases presented throughout this work.

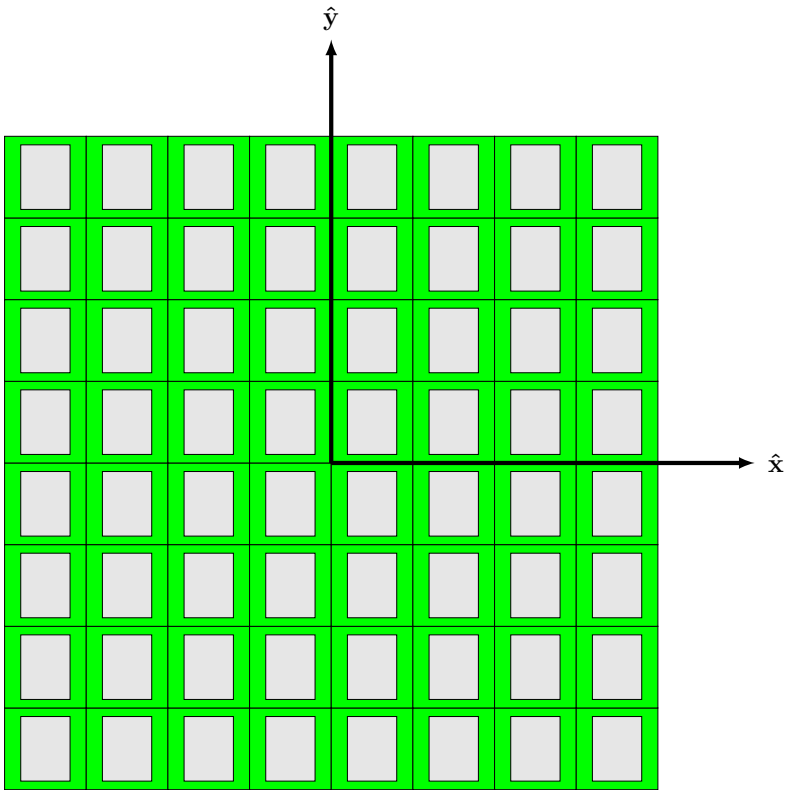

(a) 8×8 array

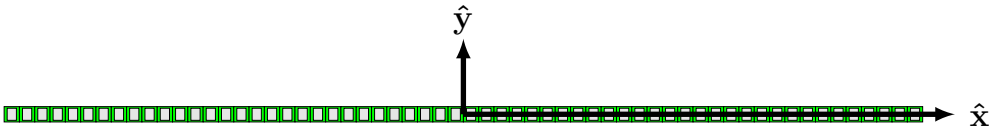

(b) 60×1 array

Figure A.5 – Illustration in the XOY plane of the 8×8 (a) and 60×1 (b) patch arrays.

B IETR measurement facilities for experimental validations

All developments presented in this manuscript rely on comparisons between computed FF data obtained using various characterization methods from measured NF data. To perform these analyses on real-world cases, both NF and FF measurements are necessary. Experimental campaigns have been therefore conducted on the M^{2}ARS platform [1], which provides advanced antenna measurement facilities at IETR-UNIVREN.

This section describes the measurement facilities employed for the W-band pyramidal horn and X-band Luneburg lens campaigns. A particular focus is placed on the planar NF measurement systems, given their influence on measurement errors. Finally, the acquired NF data for both antennas are presented.

Measurement facilities

The *Imagerie et Diagnostic ElectroMagnétique* (IDEM) facility supports measurements from 10 GHz to 500 GHz, including planar NF acquisitions using two XYZ scanners. While IDEM can also perform FF measurements, only NF data have been acquired for the Luneburg lens campaign. A representation of the scanner is shown in Fig. B.1.

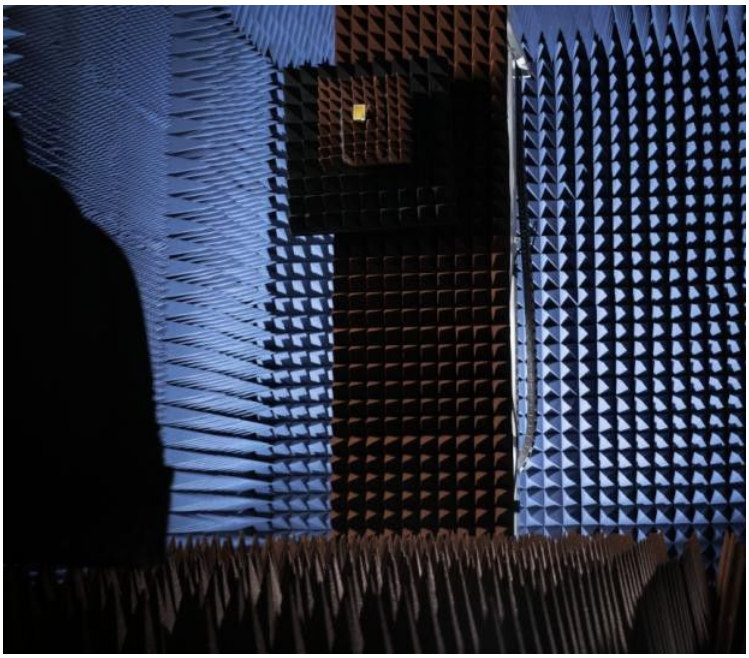

Figure B.1 – The XYZ planar scanner of IDEM, with a measurement volume of 600 mm × 600 mm × 600 mm.

The *Caractérisation d'Antennes en bande MILL et subMILLimétrique* (CAMILL) facility operates from 18 GHz to 330 GHz, and supports either direct FF measurements or CATR-assisted FF acquisitions, as shown in Fig. B.2. The integrated CATR system has been used to obtain reference FF data for the W-band horn antenna.

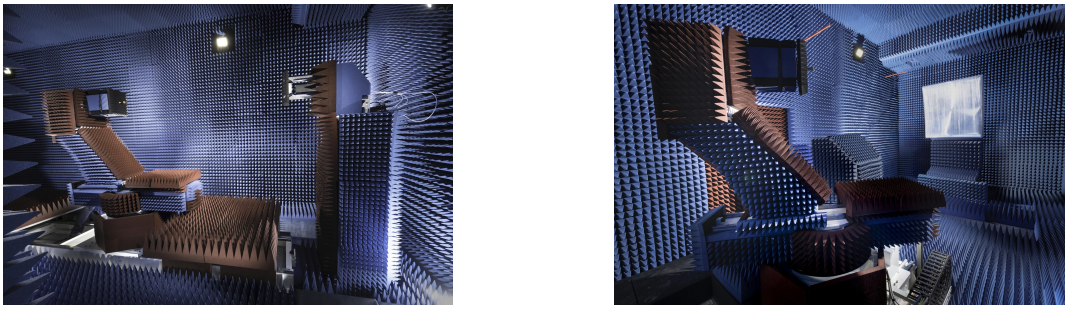

(a) Direct illumination (b) CATR

Figure B.2 – The CAMILL measurement facility in two configurations: direct illumination (a) or CATR (b).

The XS scanner is an in-house roll/XYZ positioning system developed by the M^{2}ARS unit, based on three 300 mm slide axes and one roll axis, all supplied by Newport Spectra-Physics. The roll axis is carried by the vertical XY scanner, enabling rotation of the probe or the AUT, while the z-axis adjusts the antenna or probe position. The XS scanner is dedicated to millimeter- and submillimeter-wave measurements, using a VNA with Virginia Diodes Inc. frequency extenders. Fig. B.3 shows the XS scanner.

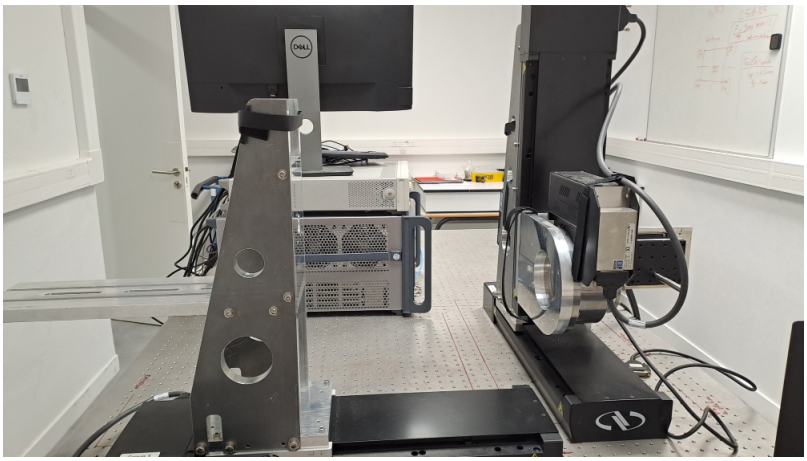

Figure B.3 – In-house XS scanner used for W-band NF measurements at the M^{2}ARS platform.

For the X-band Luneburg lens, FF data have been acquired in the *CAractérisation en bande CENtimétrique de Dispositifs RAyonnants* (CACENDRA) anechoic chamber. This

facility supports planar, cylindrical, and spherical NF measurements, as well as direct FF measurements for electrically large systems from 0.8 GHz to 26.5 GHz. Fig. B.4 illustrates the Luneburg lens positioned in the chamber.

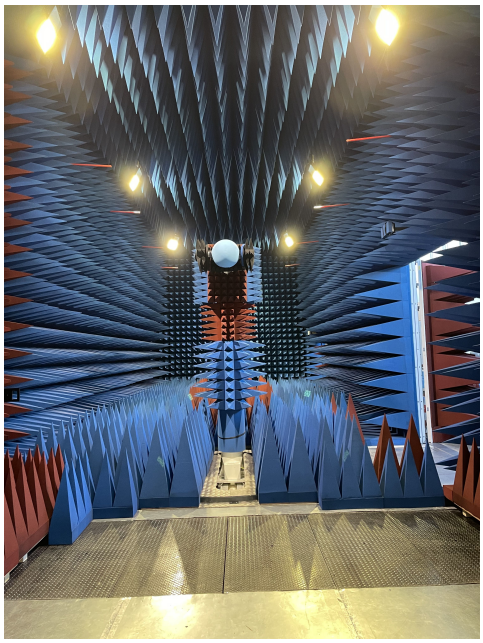

Figure B.4 – Luneburg lens prototype mounted on the positioner in the CACENDRA chamber for FF measurements.

Analysis of measurement errors in the near-field systems

As previously discussed, measurement errors induced by the facilities are a critical consideration in planar NF measurements and warrant dedicated quantification procedures. In this study, the focus is placed on misalignments between the AUT coordinate system and the scanner plane, analyzed for both the XS scanner and IDEM facilities.

For the XS scanner, interferometric laser measurements have been planned to quantify geometric misalignments. However, the results are not yet available for integration into the characterization process.

In contrast, the IDEM facility allowed partial error quantification using a tracking laser. The setup and measured angular deviations are illustrated in Fig. B.5. The measured misalignment angles between the scanner and AUT coordinate systems are:

- Rotation between XOZ and $X'O'Z'$ planes: $-0.60°$
- Rotation between YOZ and $Y'O'Z'$ planes: $0.11°$

- Rotation between XOY and $X'O'Y'$ planes: 0.11°

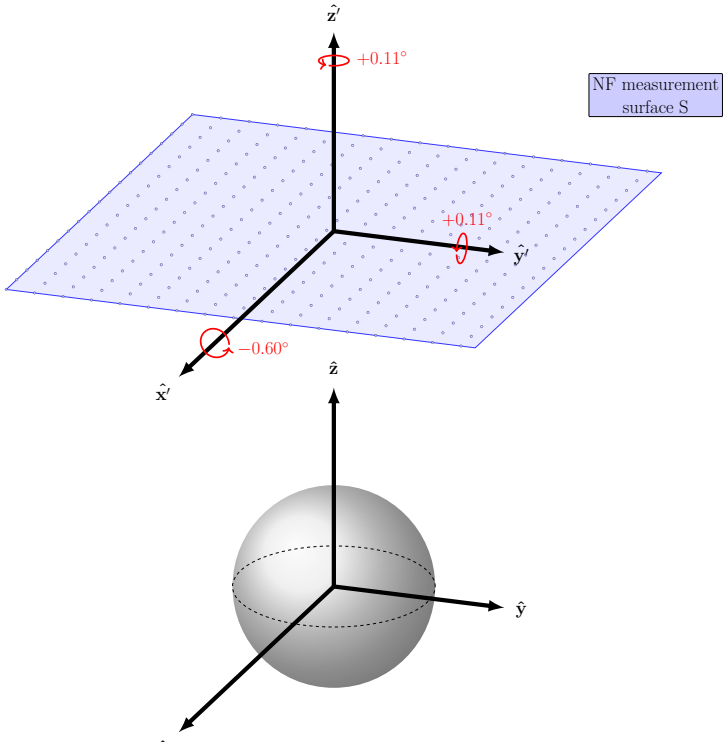

Figure B.5 – Illustration of misalignment quantification using a tracking laser between the AUT and scanner coordinate systems inside the IDEM anechoic chamber. The measured rotation angles along each axis are shown relative to the AUT system.

To mitigate these systematic errors in future campaigns, correction procedures will be incorporated into the measurement process, ensuring improved alignment between the AUT and scanner coordinate systems for more accurate NF and FF characterization.

Near-field measurements of a W-band pyramidal horn

In the case of the W-band pyramidal horn, an acquisition campaign has been performed to acquire the E_x and E_y components. A half-box-shaped NF surface S of $50.85\lambda \times 50.85\lambda \times 6.30\lambda$, with a sampling step of 0.45λ, centered at $(0, 0, 3.2\lambda)$ is defined. The measured NF amplitudes on the faces of the half-box S orthogonal to $\hat{\boldsymbol{x}}$, $\hat{\boldsymbol{y}}$, and $\hat{\boldsymbol{z}}$ are shown in Figs. B.6, B.7, and B.8, respectively.

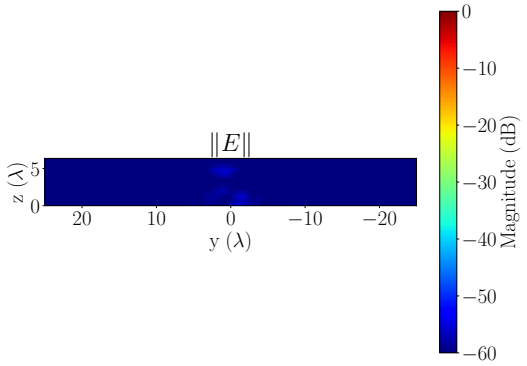

(a) Face for a minimum x

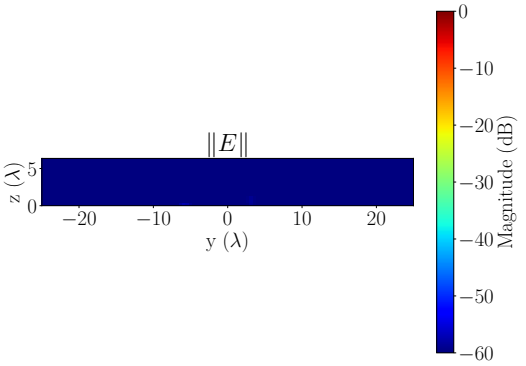

(b) Face for a maximum x

Figure B.6 – W-band pyramidal horn: measured amplitude of the NF on the faces orthogonal to the $\hat{\boldsymbol{x}}$ direction: the face at a minimal x (a) and the opposite (b).

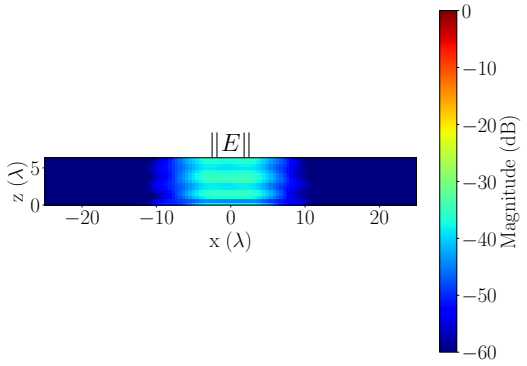

(a) Face for a minimum y

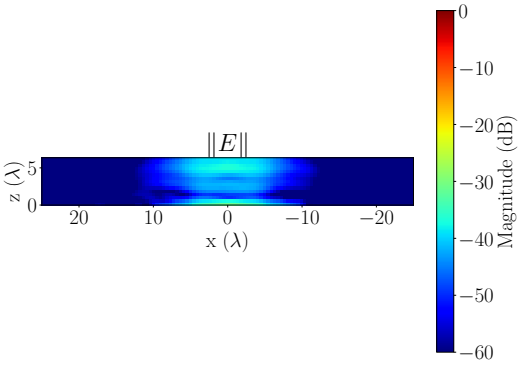

(b) Face for a maximum y

Figure B.7 – W-band pyramidal horn: measured amplitude of the NF on the faces orthogonal to the $\hat{\boldsymbol{y}}$ direction: the face at a minimal y (a) and the opposite (b).

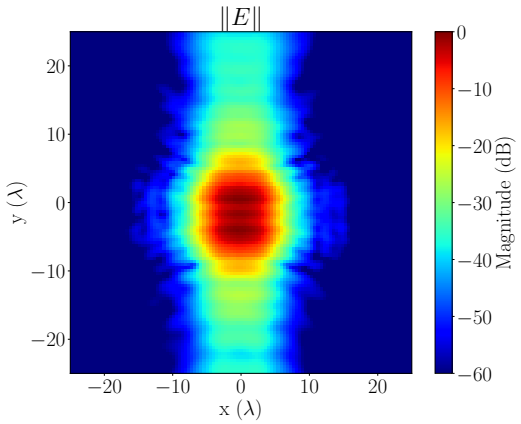

Figure B.8 – W-band pyramidal horn: measured amplitude of the NF on the upper plane of the NF measurement surface S.

Near-field measurements of an X-band Luneburg lens

The E_x and E_y components have been measured on a half-box-shaped NF surface S of size $36.8\lambda \times 33.6\lambda \times 13.6\lambda$, with a sampling step of 0.4λ. The surface is centered at $(0, 0, 6.8\lambda)$.

Examples of the measured NF amplitudes on the faces of the half-box S orthogonal to $\hat{\boldsymbol{x}}$, $\hat{\boldsymbol{y}}$, and $\hat{\boldsymbol{z}}$, are shown in Figs. B.9-B.11, B.12-B.14 and B.15-B.17 for the main beam directions $(\theta_{\text{beam}} = 0°, \phi_{\text{beam}} = 0°)$, $(\theta_{\text{beam}} = 44°, \phi_{\text{beam}} = 356°)$ and $(\theta_{\text{beam}} = 53°, \phi_{\text{beam}} = 65°)$, respectively.

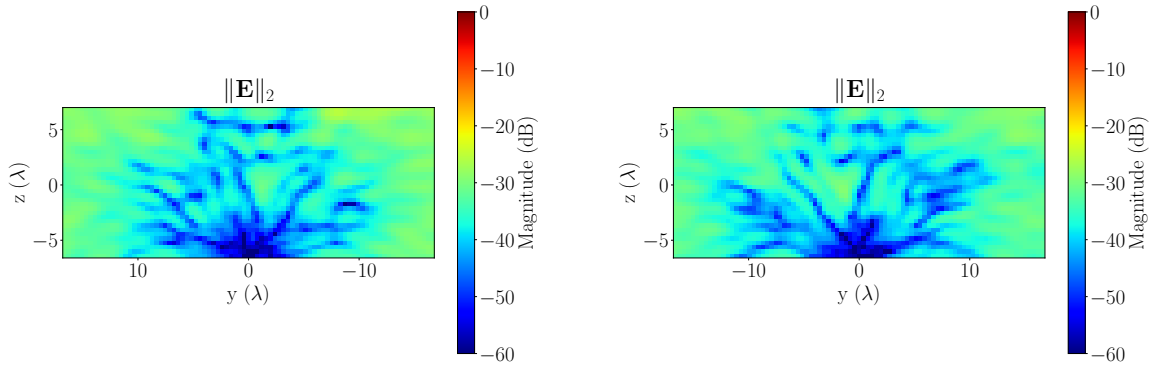

(a) Face at minimal x (b) Face at maximal x

Figure B.9 – Luneburg lens, $(\theta_{\text{beam}} = 0°, \phi_{\text{beam}} = 0°)$: measured NF amplitude on faces orthogonal to $\hat{\boldsymbol{x}}$.

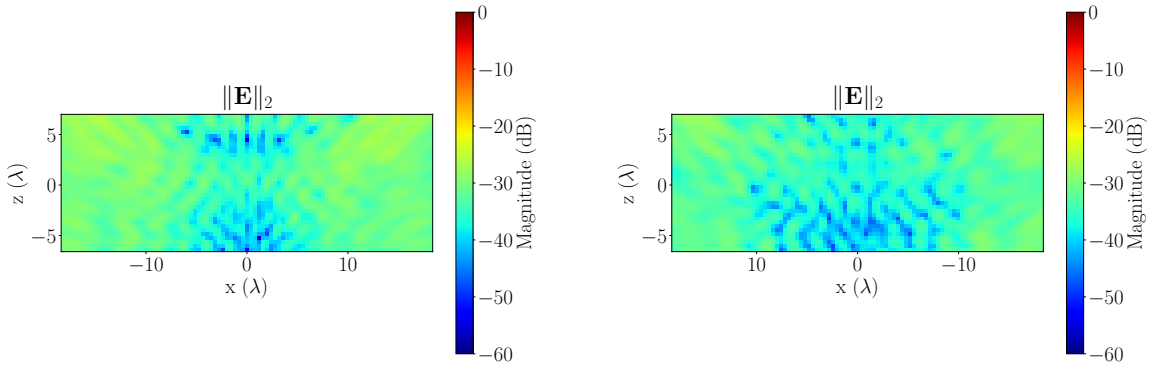

(a) Face at minimal y

(b) Face at maximal y

Figure B.10 – Luneburg lens, ($\theta_{\text{beam}} = 0°, \phi_{\text{beam}} = 0°$): measured NF amplitude on faces orthogonal to $\hat{\boldsymbol{y}}$.

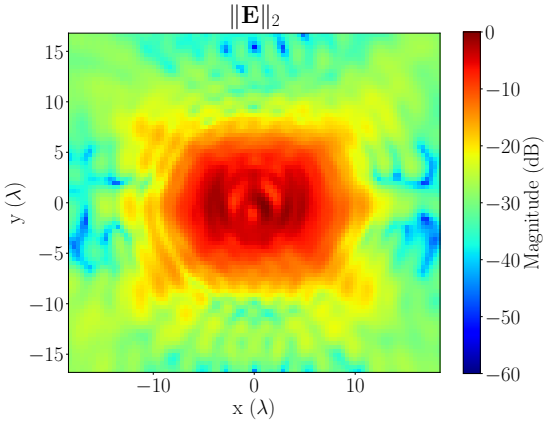

Figure B.11 – Luneburg lens, ($\theta_{\text{beam}} = 0°, \phi_{\text{beam}} = 0°$): measured NF amplitude on the upper face of the measurement surface S.

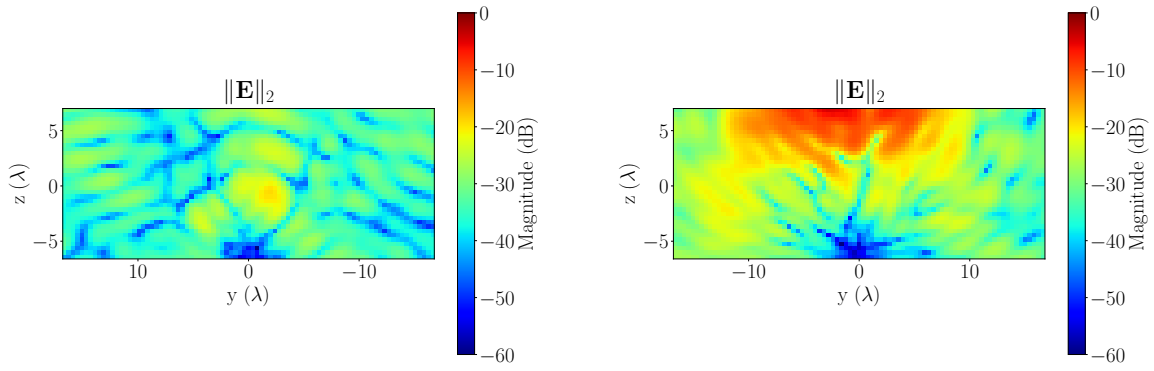

(a) Face at minimal x

(b) Face at maximal x

Figure B.12 – Luneburg lens, ($\theta_{\text{beam}} = 44°, \phi_{\text{beam}} = 356°$): measured NF amplitude on faces orthogonal to $\hat{\boldsymbol{x}}$.

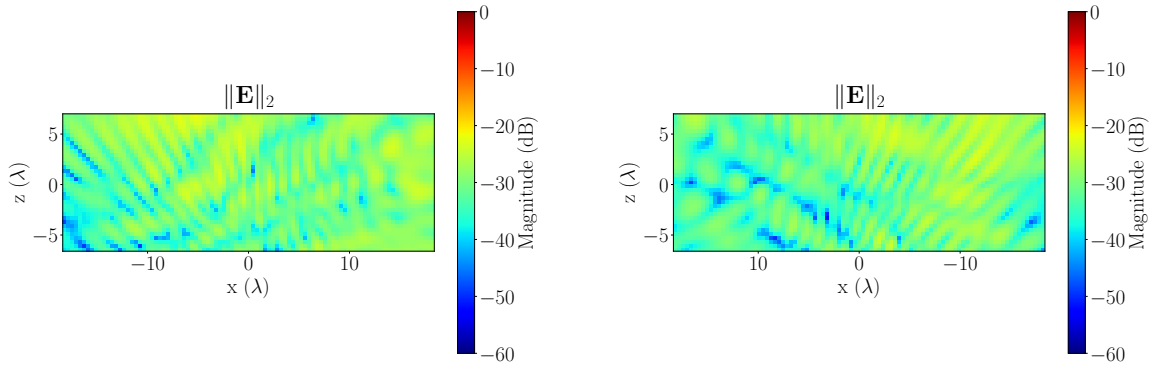

(a) Face at minimal y

(b) Face at maximal y

Figure B.13 – Luneburg lens, ($\theta_{\text{beam}} = 44°, \phi_{\text{beam}} = 356°$): measured NF amplitude on faces orthogonal to $\hat{\boldsymbol{y}}$.

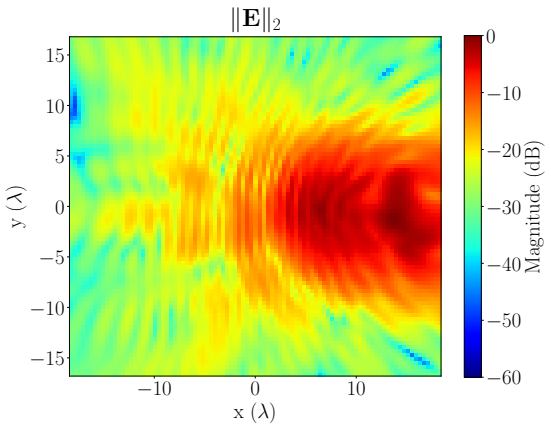

Figure B.14 – Luneburg lens, ($\theta_{\text{beam}} = 44°, \phi_{\text{beam}} = 356°$): measured NF amplitude on the upper face of the measurement surface S.

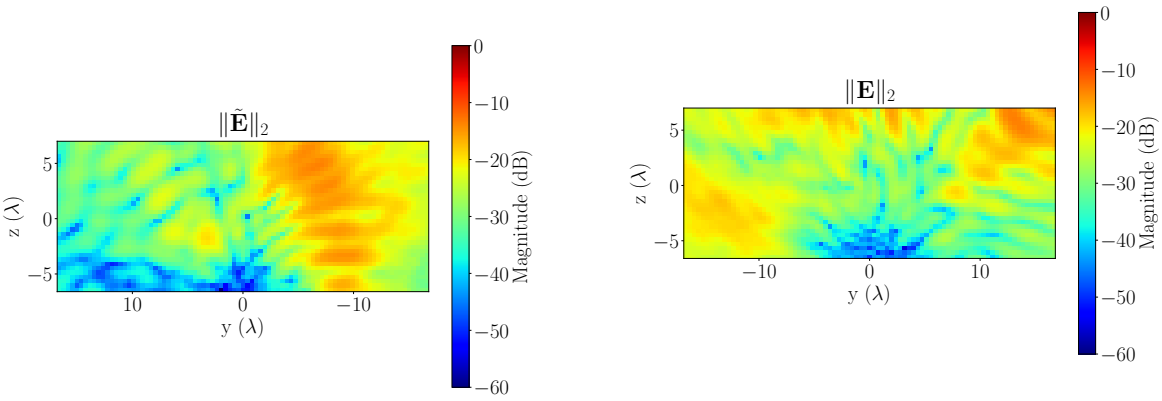

(a) Face at minimal x

(b) Face at maximal x

Figure B.15 – Luneburg lens, ($\theta_{\text{beam}} = 53°, \phi_{\text{beam}} = 65°$): measured NF amplitude on faces orthogonal to $\hat{\boldsymbol{x}}$.

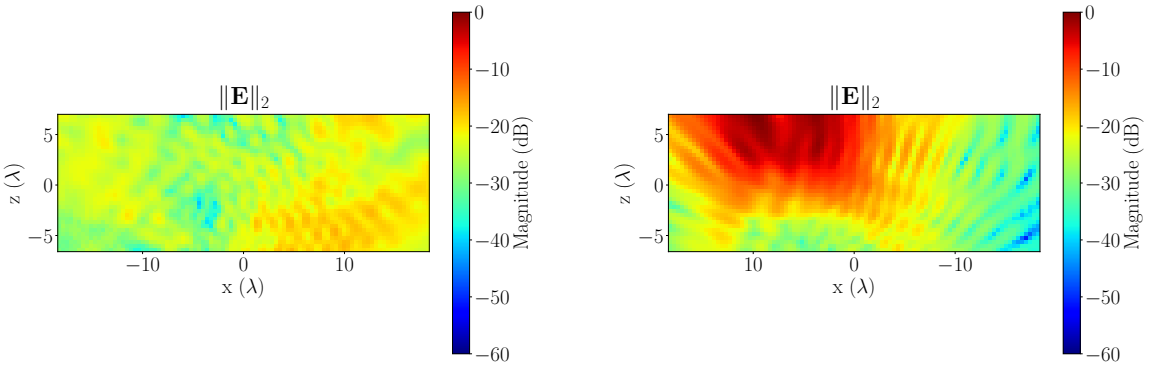

(a) Face at minimal y

(b) Face at maximal y

Figure B.16 – Luneburg lens, ($\theta_{\text{beam}} = 53°, \phi_{\text{beam}} = 65°$): measured NF amplitude on faces orthogonal to $\hat{\boldsymbol{y}}$.

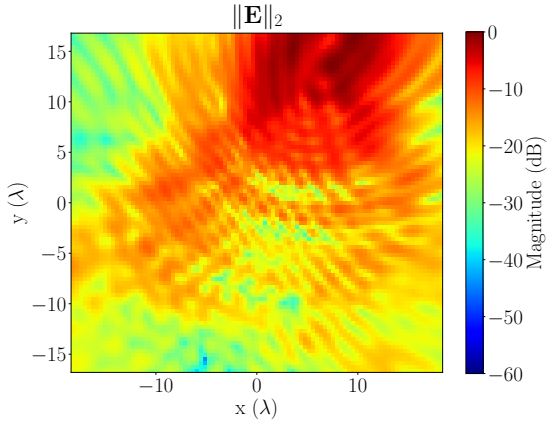

Figure B.17 – Luneburg lens, ($\theta_{\text{beam}} = 53°, \phi_{\text{beam}} = 65°$): measured NF amplitude on the upper face of the measurement surface S.

C Measured X-band Luneburg lens

Along all the developments presented in this manuscript, the most crucial aspect to validate the proposed approach is to apply it to an experimental case that is both challenging to characterize and exhibits multiple properties similar to those of an AESA. For this reason, the idea of using an X-band Luneburg lens has been proposed as the best compromise between the time required to manufacture a prototype and the radiating properties offered in our context.

Properties of the Luneburg lens

A Luneburg lens is a gradient-index dielectric device whose permittivity distribution allows it to focus or collimate electromagnetic waves radiated by an illumination source. The lens available at the IETR laboratory is described by Fuchs *et al.* [119], where the optimization of the dielectric multishells is detailed. This lens is a sphere with a radius of 200 mm and a weight of 10 kg. In this implementation, the lens is fed by an OEWG, which enables the creation of various radiation patterns. These patterns are focused by the lens into directive beams that depend on the position of the OEWG relative to the lens.

This system, composed of the OEWG and the lens, exhibits the following interesting properties:

- highly directive beams can be formed;
- different beam tilts can be achieved by moving the feeding OEWG;
- multiple operating frequencies are supported since it depends on the OEWG bandwidth.

These characteristics are consistent with those of an AESA, making the lens an excellent candidate to test our methods. Although the shape of the lens is spherical, while our interest lies in planar arrays, its geometry nonetheless provides a very challenging validation case for our model. This is because the model relies on constructing an equivalent representation that, in theory, must enclose the considered AUT.

Construction of a prototype

To employ the Luneburg lens for generating datasets in both the NF and FF ranges, a prototype of the lens with its feeding source has been designed. The feeding source has

been chosen as an OEWG.

To enable multiple beam tilts, the OEWG must be rotated around the center of the lens. This requirement led to the construction of an arch to hold the source and allow its rotation. Furthermore, the rotation must be possible around two different axes in order to achieve beam steering in directions corresponding to different combinations of θ and ϕ values. An illustration of this rotation system, used to move the illuminating source around the lens, is presented in Fig. C.1.

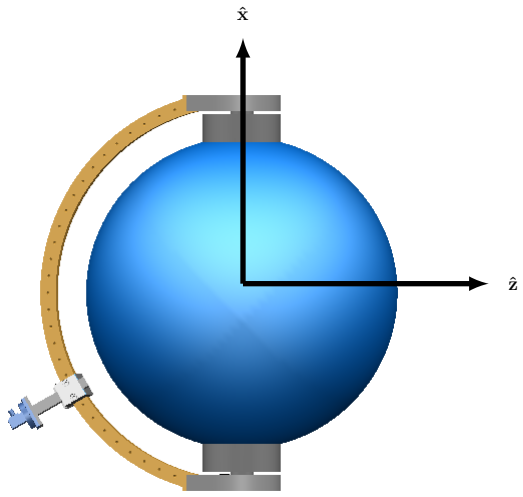

(a) XOZ plane

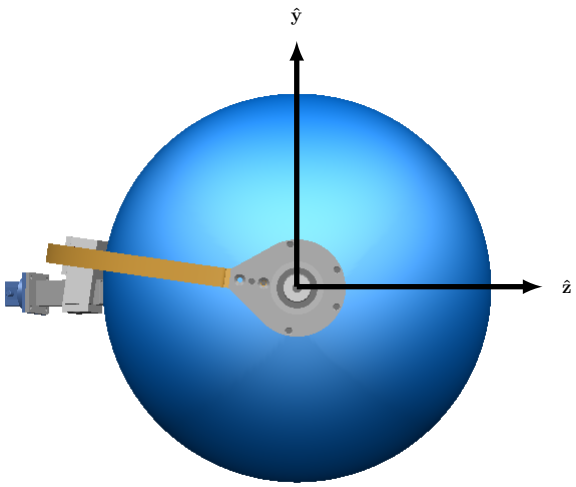

(b) YOZ plane

Figure C.1 – 2D representation of the Luneburg lens antenna and its measurement coordinate system.

The positions of the OEWG along the arch are discretized using holes in the supporting structure and can be adjusted manually with a pin and blocking support.

Implementation in the measurement facilities

The system, composed of the Luneburg lens and the feeding OEWG, had to be adapted for integration into the measurement facilities.

First, the FF data measurements have been performed inside the CACENDRA anechoic chamber. CACENDRA is a measurement facility equipped with the necessary instrumentation to characterize antennas in the NF (planar, cylindrical, or spherical) or FF range (direct illumination) for electrically large systems operating between 0.8 GHz and 26.5 GHz.

To properly acquire the FF radiation patterns of the Luneburg lens, the antenna structure had to be fixed to the positioner. A mounting support has been therefore designed and manufactured by the technical team at the IETR. The design and simulations have been first carried out using Autodesk PowerShape [120] and Fusion 360 [121] software before fabrication. Illustrations of the simulated prototype are shown in Fig. C.2.

One of the main challenges of this prototype has been ensuring reliable 3D direct FF measurements, which required rotating the AUT on the positioner. To verify that the structural constraints applied to the antenna support have been not significant, structural analyses of the displacements induced by gravity along the x- and y-axes have been performed. The results are shown in Fig. C.3.

Before starting the measurements, absorbing materials have been placed around the support structure of the lens to avoid unwanted diffraction effects. The layout of the absorbing materials is represented in Fig. C.4, and the final setup mounted in the CACENDRA chamber for FF acquisitions is illustrated in Fig. C.5.

Finally, an additional support has been designed to perform the NF data measurements inside the IDEM chamber. To acquire the data, the antenna structure had to be fixed to the positioner and correctly aligned with the XYZ scanner. Illustrations of the simulated prototype are shown in Fig. C.6.

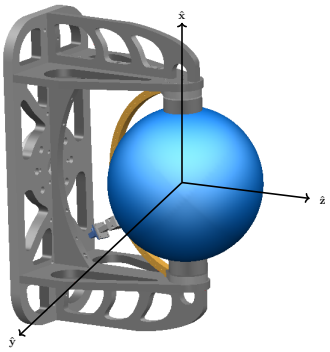

(a) 3D representation

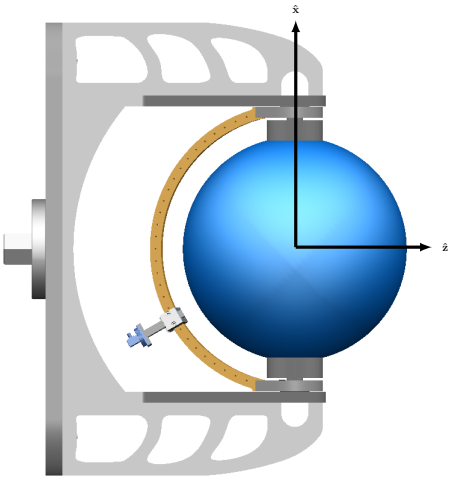

(b) 2D representation: XOZ plane

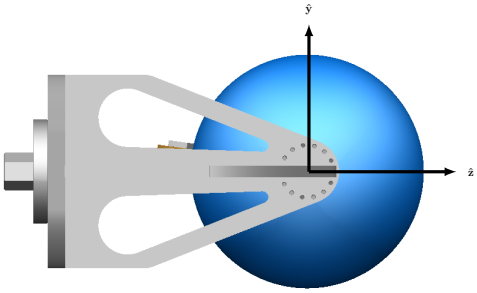

(c) 2D representation: YOZ plane

Figure C.2 – Representations of the Luneburg lens prototype mounted on the positioner in the CACENDRA chamber for FF data measurements.

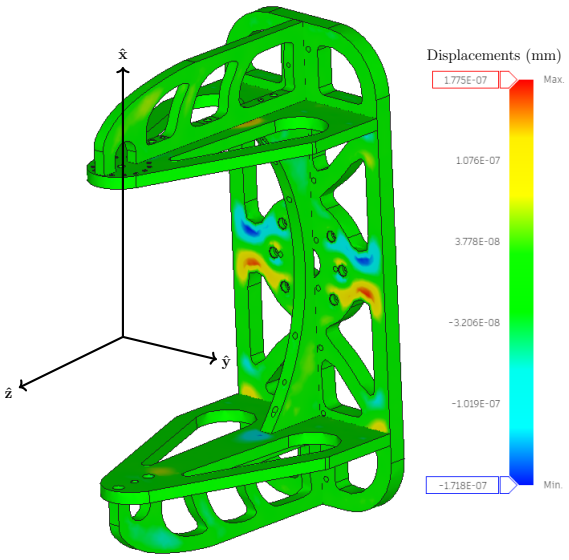

(a) x-axis

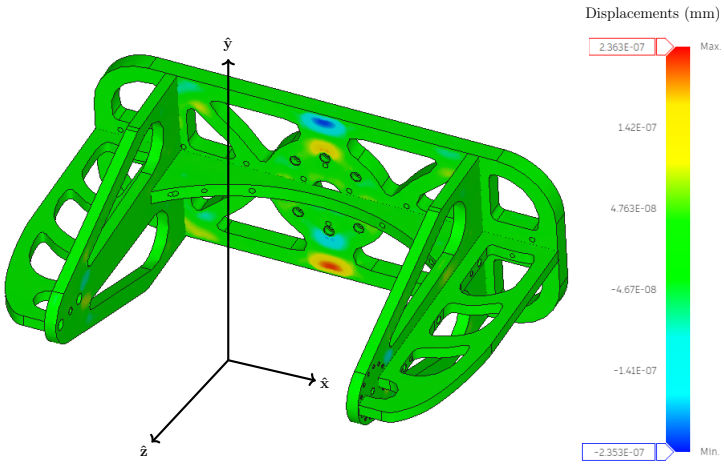

(b) y-axis

Figure C.3 – Structural analysis of the Luneburg lens prototype: displacements induced by gravity along the x-axis (a) and y-axis (b).

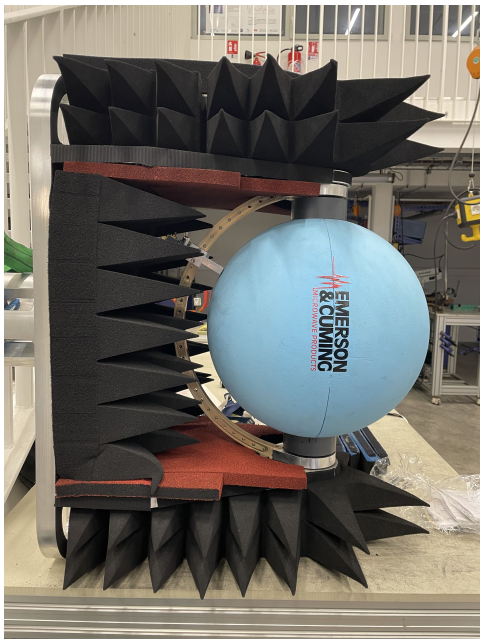

Figure C.4 – Absorbing material layout placed around the Luneburg lens structure.

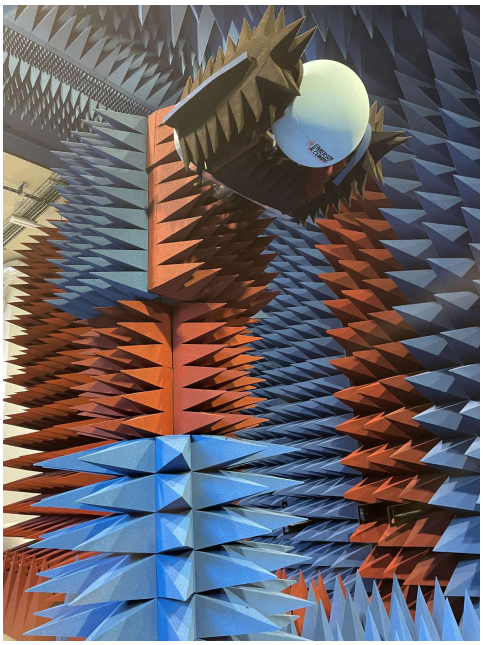

Figure C.5 – Luneburg lens mounted on the positioner in the CACENDRA chamber for FF measurements.

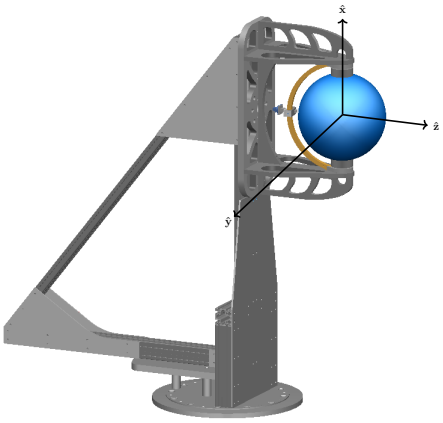

(a) 3D representation

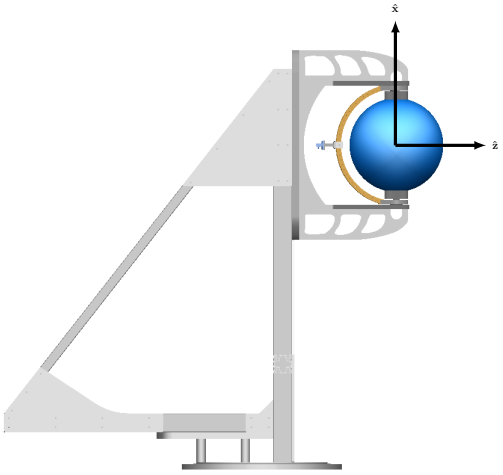

(b) 2D representation: XOZ plane

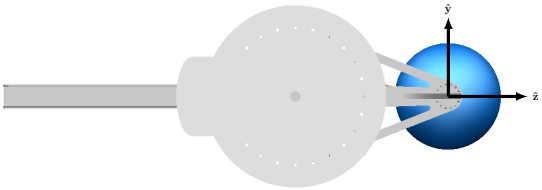

(c) 2D representation: YOZ plane

Figure C.6 – Representations of the Luneburg lens prototype mounted on the positioner in the IDEM chamber for NF data measurements.

PUBLICATION LIST

Conference papers

1. V. Morin, S. Corre, R. Loison, L. Le Coq, and E. Estebe, **Application du Modèle d'Ordre Réduit à la Caractérisation d'Antennes à partir de Mesures en Champ Proche Planaire**. *XXIIIèmes Journées Nationales Microondes* pp. 1–4, 2024.
2. V. Morin, S. Corre, R. Loison, L. Le Coq, and E. Estebe, **Application of the Reduced-Order Model to Planar Near-Field Antenna Measurements**. *19th European Conference on Antennas and Propagation* pp. 1–5, 2025.
3. V. Morin, S. Corre, R. Loison, L. Le Coq, and E. Estebe, **Improving Near-Field Measurements Using a Reduced-Order Model**. *20th European Conference on Antennas and Propagation* pp. 1–5, 2026 (not published yet).

Journal papers

1. V. Morin, S. Corre, R. Loison, L. Le Coq, and E. Estebe, **Efficient Sampling Strategies Based on a Reduced-Order Model for Antenna Planar Measurements**. *International Journal of Microwave and Wireless Technologies* pp. 1–7, 2025.

BIBLIOGRAPHY

[1] UR IETR, *M2ARS platform*, URL: https://www.ietr.fr/plateforme-m2ars-manufacturing-measurement-analysis-radiating-systems, 2024.

[2] O. M. Bucci, C. Gennarelli, and C. Savarese, **Representation of Electromagnetic Fields over Arbitrary Surfaces by a Finite and Nonredundant Number of Samples**. *IEEE Transactions on Antennas and Propagation*, 46.3 pp. 351–359, 1998.

[3] A. D. Brown, **Active Electronically Scanned Arrays: Fundamentals and Applications**, Wiley, 2022.

[4] A. C. Newell and G. Hindman, **Antenna Spherical Coordinate Systems and their Application in Combining Results from Different Antenna Orientations**. *ESTEC*, 1999.

[5] C. Balanis, **Antenna Theory: Analysis and Design, 4th Edition**, Wiley, 2016.

[6] **IEEE Standard for Definitions of Terms for Antenna**. *IEEE Std. 145-2013 (Revision of Std. 145-1993)* pp. 1–50, 2014.

[7] BIPM, **Le Système international d'unités / The International System of Units ('The SI Brochure')**, Bureau international des poids et mesures, 2019.

[8] A. C. Ludwig, **The Definition of Cross Polarization**. *IEEE Transactions on Antennas and Propagation*, 21.1 pp. 116–119, 1973.

[9] **IEEE Recommended Practice for Antenna Measurements**. *IEEE Std. 149-2021* pp. 1–207, 2021.

[10] K. Kaslis, **Advanced Near-Field Antenna Measurement Techniques**, Technical University of Denmark, 2025.

[11] S. F. Gregson, J. McCormick, and C. Parini, **Principles of Planar Near-Field Antenna Measurements**, 2007.

[12] B. Fuchs, L. Le Coq, S. Rondineau, and M. D. Migliore, **Fast Antenna Far-Field Characterization via Sparse Spherical Harmonic Expansion**. *IEEE Transactions on Antennas and Propagation*, 65.10 pp. 5503–5510, 2017.

[13] N. Mézières et al., **On the Application of Sparse Spherical Harmonic Expansion for Fast Antenna Far-Field Measurements**. *IEEE Antennas and Wireless Propagation Letters*, 19.5 pp. 746–750, 2020.

[14] J. E. Hansen, **Spherical Near-field Antenna Measurements**, 1988.

[15] O. Breinbjerg, **High-Accuracy Spherical Near-Field Measurements for Satellite Antenna Testing**. *11th European Conference on Antennas and Propagation* pp. 2931–2934, 2017.

[16] F. R. Varela et al., **Fast Radome Antenna Testing using Single-Cut and Slide Measurements**. *17th European Conference on Antennas and Propagation* pp. 1–4, 2023.

[17] J. J. H. Wang, **An Examination of the Theory and Practices of Planar Near-Field Measurement**. *IEEE Transactions on Antennas and Propagation*, 36.6 pp. 746–753, 1988.

[18] G. Strang, **Linear Algebra and Learning from Data**, Wellesley- Cambridge Press, 2019.

[19] S. Axler, **Linear Algebra Done Right**, Springer, 2024.

[20] A. C. Newell and M. L. Crawford, **Planar Near-Field Measurements on High Performance Array Antennas**, National Bureau of Standards, 1974.

[21] D. M. Kerns, **Plane-Wave Scattering-Matrix Theory of Antennas Antenna-Antenna Interactions: Formulation and Applications**, National Bureau of Standards, 1975.

[22] A. C. Newell, **Upper Bound Errors in Far-Field Antenna Parameters Determined from Planar Near-Field Measurements Part 2: Analysis and Computer Simulation**, National Bureau of Standards, 1975.

[23] G. K. Huddleston, **Optimum Probes for Near-Field Antenna Measurements on a Plane**, Georgia Institute of Technology, 1978.

[24] A. D. Yaghjian, **An Overview of Near-Field Antenna Measurements**. *IEEE Transactions on Antennas and Propagation*, 34.1 pp. 30–45, 1986.

[25] J. A. Stratton, **Electromagnetic Theory**, Wiley-IEEE Press, 2007.

[26] J. D. Jackson, **Classical Electrodynamics, 3rd Edition**, Wiley, 1999.

[27] R. P. Feynman, R. B. Leighton, and M. Sands, **Lectures on Physics, Volume II**, Basic Books, 2010.

[28] K. R. Grimm, **Ultralow Sidelobe Planar Near Field Measurement Study**, 1982.

[29] C. H. Schmidt, M. M. Leibfritz, and T. F. Eibert, **Fully Probe-Corrected Near-Field Far-Field Transformation Employing Plane Wave Expansion and Diagonal Translation Operators**. *IEEE Transactions on Antennas and Propagation*, 56.3 pp. 737–746, 2008.

[30] C. H. Schmidt and T. F. Eibert, **Multilevel Plane Wave Based Near-Field Far-Field Transformation for Electrically Large Antennas in Free-Space or Above Material Halfspace**. *IEEE Transactions on Antennas and Propagation*, 57.5 pp. 1382–1390, 2009.

[31] C. E. Shannon, **Communication in the Presence of Noise**. *Proceedings of the IRE*, 37.1 pp. 10–21, 1949.

[32] **IEEE Recommended Practice for Near-Field Antenna Measurement**. *IEEE Std 1720-2012* pp. 1–102, 2012.

[33] O. M. Bucci, C. Gennarelli, G. Riccio, and C. Savarese, **Fast and Accurate Far-Field Evaluation from a Non-Redundant Finite Number of Plane-Polar Measurements**. *Proceedings of IEEE Antennas and Propagation Society International Symposium and URSI National Radio Science Meeting* pp. 540–543, 1994.

[34] S. F. Gregson, B.. Pyne, H. Saito, K. Tanaka, and C. G. Parini, **Highly Efficient Near-Field to Far-Field Transform for Polar Near-Field Scanned Data**. *2022 Antenna Measurement Techniques Association Symposium*, 2022.

[35] O. M. Bucci, C. Gennarelli, and C. Savarese, **Interpolation of Electromagnetic Radiated Fields Over a Plane by Nonuniform Samples**. *IEEE Transactions on Antennas and Propagation*, 41.11 pp. 1501–1508, 1993.

[36] V. Dehghanian, M. Okhovvat, and M. Hakkak, **A New Interpolation Technique for the Reconstruction of Uniformly Spaced Samples from Non-Uniformly Spaced Ones in Plane-Rectangular Near-Field Antenna Measurements**. *Progress In Electromagnetics Research*, 72 pp. 47–59, 2007.

[37] M. A. Qureshi, C. H. Schmidt, and T. F. Eibert, **Adaptative Sampling in Multilevel Plane Wave Based Near-Field Far-Field Transformed Planar Near-Field Measurements**. *Progress In Electromagnetics Research*, 126 pp. 481–497, 2012.

[38] G. Parsons, D. A. McNamara, and D. J. Janse van Rensburg, **An Investigation of Adaptive Acquisition Techniques for Planar Near-Field Antenna Measurements**. *2007 IEEE Antennas and Propagation Society International Symposium* pp. 1621–1624, 2007.

[39] O. M. Bucci, C. Gennarelli, G. Riccio, and C. Savarese, **Near-Field Far-Field Transformation from Nonredundant Plane-Polar Data: Effective Modellings of the Source**. *IEE Proceedings - Microwaves, Antennas and Propagation*, 145.1 pp. 33–38, 1988.

[40] A. Capozzoli, C. Curcio, and A. Liseno, **An Efficient Approach to the Near-Field Sampling of Electromagnetic Fields**. *Proceedings of the 5th European Conference on Antennas and Propagation* pp. 2023–2027, 2011.

[41] G. Giordanengo, M. Righero, F. Vipiana, G. Vecchi, and M. Sabbadini, **Fast Antenna Testing With Reduced Near Field Sampling**. *IEEE Transactions on Antennas and Propagation*, 62.5 pp. 2501–2513, 2014.

[42] A. C. Newell, **Error Analysis Techniques for Planar Near-Field Measurements**. *IEEE Transactions on Antennas and Propagation*, 36.6 pp. 754–768, 1988.

[43] R. T. Cutshall, J. Dobbins, J. Freking, and B. Hertneky, **A New Valid Angle Equation for PNF Measurements**. *2022 Antenna Measurement Techniques Association Symposium*, 2022.

[44] O. M. Bucci, G. D'Elia, and M. D. Migliore, **A New Strategy to Reduce the Truncation Error in Near-Field/Far-Field Transformations**. *Radio Science*, 35.1 pp. 3–17, 2000.

[45] E. Martini, O. Breinbjerg, and S. Maci, **Reduction of Truncation Errors in Planar Near-Field Aperture Antenna Measurements Using the Gerchberg-Papoulis Algorithm**. *IEEE Transactions on Antennas and Propagation*, 56.11 pp. 3485–3493, 2008.

[46] F. J. Cano-Fácila, S. Pivnenko, and M. Sierra-Castañer, **Reduction of Truncation Errors in Planar, Cylindrical, and Partial Spherical Near-Field Antenna Measurements**. *International Journal of Antennas and Propagation*, 2012 pp. 1687–5869, 2012.

[47] W. C. Gibson, **The Method of Moments in Electromagnetics**, Chapman & Hall/CRC, 2007.

[48] Dassault Systèmes, *CST Studio Suite*, 2023.

[49] K. J. Bathe, **Finite Element Method**, Wiley encyclopedia of computer science and engineering, 2007.

[50] Altair Engineering, *FEKO Electromagnetic Simulation Software*.

[51] Ansys, *Ansys HFSS Software*.

[52] P. Petre and T. K. Sarkar, **Planar Near-Field to Far-Field Transformation Using an Equivalent Magnetic Current Approach**. *IEEE Transactions on Antennas and Propagation*, 40.11 pp. 1348–1356, 1992.

[53] P. Petre and T. K. Sarkar, **Differences Between Modal Expansion and Integral Equation Methods for Planar Near-Field to Far-Field Transformation**. *Progress In Electromagnetics Research*, 12 pp. 37–56, 1996.

[54] T. K. Sarkar and A. Taaghol, **Near-Field to Near/Far-Field Transformation for Arbitrary Near-Field Geometry Utilizing an Equivalent Electric Current and MoM**. *IEEE Transactions on Antennas and Propagation*, 47.3 pp. 566–573, 1999.

[55] M. Salucci, M. D. Migliore, G. Oliveri, and A. Massa, **Antenna Measurements-by-Design for Antenna Qualification**. *IEEE Transactions on Antennas and Propagation*, 66.11 pp. 6300–6312, 2018.

[56] S. Rao, D. Wilton, and A. Glisson, **Electromagnetic Scattering by Surfaces of Arbitrary Shape**. *IEEE Transactions on Antennas and Propagation*, 30.3 pp. 409–418, 1982.

[57] O. Breinbjerg, **Dipole and Quadrupole Modes in Spherical Wave Expansions for Derivative Probes**. *19th European Conference on Antennas and Propagation* pp. 1–5, 2025.

[58] M. Serhir, J. M. Geffrin, A. Litman, and P. Besnier, **Aperture Antenna Modeling by a Finite Number of Elemental Dipoles From Spherical Field Measurements**. *IEEE Transactions on Antennas and Propagation*, 58.4 pp. 1260–1268, 2010.

[59] J. Rubio J.F. Izquierdo and J. Zapata, **Antenna-Generalized Scattering Matrix in Terms of Equivalent Infinitesimal Dipoles: Application to Finite Array Problems**. *IEEE Transactions on Antennas and Propagation*, 70.10 pp. 4601–4609, 2012.

[60] S. Lambot and F. André, **Full-Wave Modeling of Near-Field Radar Data for Planar Layered Media Reconstruction**. *IEEE Transactions on Geoscience and Remote Sensing*, 52.5 pp. 2295–2303, 2014.

[61] A. Litman S. Nounouh C. Eyraud and H. Tortel, **Quantitative Imaging With Incident Field Modeling From Multistatic Measurements on Line Segments**. *IEEE Antennas and Wireless Propagation Letters*, 14 pp. 253–256, 2015.

[62] M. Sierra-Castañer, **Revision of Diagnosis Techniques: Holographic and Equivalent Currents Reconstructions**. *19th European Conference on Antennas and Propagation* pp. 1–5, 2025.

[63] B. Fuchs and A. G. Polimeridis, **Reduced Order Models for Fast Antenna Characterization**. *IEEE Transactions on Antennas and Propagation*, 67.8 pp. 5673–5677, 2019.

[64] E. Martini, G. Carli, S. Maci, and A. Massa, **An Equivalence Theorem Based on the Use of Electric Currents Radiating in Free Space**. *IEEE Antennas and Wireless Propagation Letters*, 7 pp. 421–424, 2008.

[65] M. A. Saporetti et al., **Reduced Sampling in NF Antenna Measurement Using Numerical Defined Expansion Functions**. *EuCAP*, 13, 2019.

[66] O. Rodrigues, **Des Lois Géométriques qui Régissent les Déplacements d'un Système Solide dans l'Espace, et de la Variation des Coordonnées Provenant de ces Déplacements Considérés Indépendants des Causes**

qui Peuvent les Produire. *Journal de Mathématiques Pures et Appliquées*, 5 pp. 380–440, 1840.

[67] J. Hadamard, **Sur les Problèmes aux Dérivées Partielles et leur Signification Physique**. *Princeton University Bulletin*, 13.4 pp. 49–52, 1902.

[68] The MathWorks Inc., *MATLAB (R2022b)*.

[69] Guido Van Rossum and Fred L. Drake, **Python 3 Reference Manual**, 2009.

[70] N. Mézières, M. Mattes, and B. Fuchs, **Antenna Characterization From a Small Number of Far-Field Measurements via Reduced-Order Models**. *IEEE Transactions on Antennas and Propagation*, 70.4 pp. 2422–2430, 2022.

[71] F. Soldovieri and R. Persico, **Reconstruction of Dielectric Profiles of Buried Objects Under the Born Approximation**. *IEEE Transactions on Geoscience and Remote Sensing*, 42.11 pp. 2349–2358, 2004.

[72] F. Soldovieri, I. Catapano, and R. Persico, **A Linear Inverse Scattering Algorithm for GPR Imaging**. *IEEE Transactions on Antennas and Propagation*, 54.1 pp. 282–288, 2006.

[73] I. Catapano, F. Soldovieri, and R. Persico, **On the Resolution of GPR Imaging Systems in Aspect-Limited Configurations**. *Journal of Applied Geophysics*, 67.3 pp. 195–202, 2009.

[74] B. L. Moiser, J. A. Gordon, and A. J. Petruska, **Increased Efficiency in Planar Near-Field Scanning Using Combined Multi-Robot Motion**. *19th European Conference on Antennas and Propagation* pp. 1–5, 2025.

[75] B. Stupfel and Y. Morel, **Singular Value Decomposition of the Radiation Operator—Application to Model-Order and Far-Field Reduction**. *IEEE Transactions on Antennas and Propagation*, 56.6 pp. 1605–1615, 2008.

[76] A. Hochman et al., **Reduced-Order Models for Electromagnetic Scattering Problems**. *IEEE Transactions on Antennas and Propagation*, 62.6 pp. 3150–3162, 2014.

[77] X. F. He, L. Li, S. Lanteri, and K. Li, **Model Order Reduction for Parameterized Electromagnetic Problems Using Matrix Decomposition and Deep Neural Networks**, 2022.

[78] R. Cornelius, D. Heberling, N. Koep, A. Behboodi, and R. Mathar, **A Compressed Sensing Applied to Spherical Near-field to Far-field Transformation**. *10th European Conference on Antennas and Propagation* pp. 1–4, 2016.

[79] C. G. Parini and S. F. Gregson, **Planar Near-Field Array Antenna Diagnostics for Production Testing Using Compressive Sensing and a Fixed Sparce Sensing Array**. *19th European Conference on Antennas and Propagation* pp. 1–5, 2025.

[80] N. Mézières, B. Fuchs, and M. Mattes, **Reduced-Order Model for Antenna Pattern Characterization from a Small Number of Samples**. *2021 Antenna Measurement Techniques Association Symposium*, 2021.

[81] F. R. Varela, A. Arboleya, C. Fontá, E. Martinez-de-Rioja, and J. C. Maeso, **Fast Planar Near-Field Measurements of Reduced Angular Pattern Domains**. *IEEE Transactions on Antennas and Propagation*, 2024.

[82] S. Corre, L. Le Coq, N. Mézières, M. Mattes, and B. Fuchs, **Numerical Considerations to Improve the Reduced-Order Model Approach for Antenna Measurements**. *2022 Antenna Measurement Techniques Association Symposium*, 2022.

[83] A. Capozzoli et al., **A Learned-SVD Approach to the Electromagnetic Inverse Source Problem**. *Sensors*, 24.14, 2024.

[84] H. Kim and J. Rossignac, **Parabola-Based Discrete Curvature Estimation**. *15th Int. Conf. on Computer Graphics, Visualization and Computer Vision*, 2005.

[85] R. Pierri and F. Soldovieri, **On the Information Content of the Radiated Fields in the Near Zzone Over Bounded Domains**. *Inverse Problems*, 14.21 pp. 321–337, 1998.

[86] M. Fuhry and L. Reichel, **A New Tikhonov Regularization Method**. *Numerical Algorithms*, 59.3 pp. 433–445, 2012.

[87] L. I. Rudin, S. Osher, and E. Fatemi, **Nonlinear Total Variation Based Noise Removal Algorithms**. *Physica D*, 60 pp. 259–268, 1992.

[88] F. Soldovieri, R. Solimene, L. Lo Monte, M. Bavusi, and A. Loperte, **Sparse Reconstruction From GPR Data With Applications to Rebar Detection**. *IEEE Transactions on Instrumentation and Measurement*, 60.3 pp. 1070–1079, 2011.

[89] C. Clason, **Regularization of Inverse Problems**, 2021.

[90] C. R. Harris et al., **Array Programming With NumPy**. *Nature*, 585.7825 pp. 357–362, 2020.

[91] P. Virtanen et al., **SciPy 1.0: Fundamental Algorithms for Scientific Computing in Python**. *Nature Methods*, 17 pp. 261–272, 2020.

[92] F. Pedregosa et al., **Scikit-learn: Machine Learning in Python**. *Journal of Machine Learning Research*, 12 pp. 2825–2830, 2011.

[93] N. Mézières, **Contributions to Fast and Accurate Antenna Characterization**, 2021.

[94] P. C. Hansen, **Truncated Singular Value Decomposition Solutions to Discrete Ill-Posed Problems with Ill-Determined Numerical Rank**. *SIAM Journal on Scientific and Statistical Computing*, 11.3 pp. 503–518, 1990.

[95] A. Azzarelli, C. Brezinski, C. Fenu, M. Redivo-Zaglia, and G. Rodriguez, **Parameter Choice Rules for Discrete Ill-Posed Problems Based on Extrapolation Methods**. *Journal of Scientific Computing*, 103.9 pp. 1–22, 2025.

[96] B. Hofmann, O. Neitz, and T. Eibert, **On the Minimum Number of Samples for Sparse Recovery in Spherical Antenna Near-Field Measurements**. *IEEE Transactions on Antennas and Propagation*, 67.12 pp. 7597–7610, 2019.

[97] R. Marques, C. Bouville, M. Ribardière, L. P. Santos, and K. Bouatouch, **Spherical Fibonacci Point Sets for Illumination Integrals**. *Computer Graphics Forum*, 32.8, 2013.

[98] R. Moretta, F. Pascariello, G. Petraglia, M. Feo, and M. A. Maisto, **Planar Near-Field Antenna Measurements With a Uniform Step Larger Than Half-Wavelength**. *arXiv preprint arXiv:2402.07333*, 2024.

[99] M. A. Maisto, C. Bhat, and R. Solimene, **An Insight into the Warping Spatial Sampling Method in Subsurface Radar Imaging and Its Experimental Validation**. *Remote Sensing*, 15.12 p. 3012, 2023.

[100] M. A. Maisto, R. Pierri, and R. Solimene, **Near-Field Warping Sampling Scheme for Broad-Side Antenna Characterization**. *Electronics*, 9.6 p. 1047, 2020.

[101] V. Morin, S. Corre, R. Loison, L. Le Coq, and E. Estebe, **Application du Modèle d'Ordre Réduit à la Caractérisation d'Antennes à partir de Mesures en Champ Proche Planaire**. *XXIIIèmes Journées Nationales Microondes* pp. 1–4, 2024.

[102] V. Morin, S. Corre, R. Loison, L. Le Coq, and E. Estebe, **Efficient Sampling Strategies Based on a Reduced-Order Model for Antenna Planar Measurements**. *International Journal of Microwave and Wireless Technologies* pp. 1–7, 2025.

[103] V. Morin, S. Corre, R. Loison, L. Le Coq, and E. Estebe, **Application of the Reduced-Order Model to Planar Near-Field Antenna Measurements**. *19th European Conference on Antennas and Propagation* pp. 1–5, 2025.

[104] F. Saccardi, A. Giacomini, and L. J. Foged, **Comparative Investigation of Spherical NF Measurements with Full and First Order Probe Correction Using Calibrated or Simulated Probe**. *11th European Conference on Antennas and Propagation* pp. 1–5, 2017.

[105] T. A. Laitinen, S. Pivnenko, and O. Breinbjerg, **Iterative Probe Correction Technique for Spherical Near-Field Antenna Measurements**. *IEEE Antennas and Wireless Propagation Letters*, 4 pp. 221–223, 2005.

[106] M. M. Leibfritz and F. M. Landstorfer, **Full Probe-Correction for Near-Field Antenna Measurements**. *2006 IEEE Antennas and Propagation Society International Symposium* pp. 1–4, 2006.

[107] F. R. Varela, B. G. Iragüen, and M. S. Castañer, **Probe-Corrected Near-Field to Far-Field Transformation Using Multiple Spherical Wave Expansions**. *13th European Conference on Antennas and Propagation* pp. 1–5, 2021.

[108] F. Saccardi, A. Giacomini, L. M. Tancioni, and L. J. Foged, **Full Probe Corrected Spherical Near Field Measurement Technique using Standard Wideband Antennas as Probes**. *12th European Conference on Antennas and Propagation* pp. 1–5, 2018.

[109] A. Paulus and T. F. Eibert, **Fully Probe-Corrected Near-Field Far-Field Transformations With Unknown Probe Antennas**. *IEEE Transactions on Antennas and Propagation*, 71.7 pp. 5967–5980, 2023.

[110] G. F. Masters, **Probe-Correction Coefficients From Near-Field Measurements**. *1991 Antenna Measurements Techniques Association Conference* pp. 1–10, 1991.

[111] L. A. Muth and R. L. Lewis, **An Iterative Technique to Correct Probe Position Errors in Planar Near-Field to Far-Field Transformations**, 1988.

[112] M. A. Qureshi, **Near-Field Error Analysis and Efficient Sampling Techniques for the Fast Irregular Antenna Field Transformation Algorithm**, 2013.

[113] L. A. Muth and R. L. Lewis, **A General Technique to Correct Probe Position Errors in Planar Near-Field Measurements to Arbitrary Accuracy**. *IEEE Transactions on Antennas and Propagation*, 38.12 pp. 1925–1932, 2002.

[114] D. R. Reddy, **Correction for Probe-Position Error in Planar, Near-Field Scanning**, 1986.

[115] A. D. Yaghjian, **Approximate Formulas for the Far Field and Gain of Open-Ended Rectangular Waveguide**. *IEEE Transactions on Antennas and Propagation*, 32.4 pp. 378–384, 1984.

[116] J. L. Salazar-Cerreno, L. F. Moncada, E. A. Oblitas, and C. Nelson, **An Overview of Induced Ripples on Near-Field and Far-Field Patterns Produced by the Collar Absorber of an Open Waveguide Probe on a Planar Near-Field System**. *2024 Antenna Measurement Techniques Association Symposium*, 2024.

[117] D. M. Pozar, **Microwave Engineering, 4th Edition**, Wiley, 2012.

[118] H. Errifi, A. Baghdad, and A. Badri, **Effect of Change in Feedpoint on the Antenna Performance in Edge, Probe and Inset-Feed Microstrip Patch Antenna for 10 GHZ**. *International Journal of Emerging Trends in Engineering and Development*, 1.4 pp. 81–93, 2014.

[119] B. Fuchs, L. Le Coq, O. Lafond, S. Rondineau, and M. Himdi, **Design Optimization of Multishell Luneburg Lenses**. *IEEE Transactions on Antennas and Propagation*, 55.2 pp. 283–289, 2007.

[120] Inc. Autodesk, *Autodesk PowerShape*, 2023.

[121] Inc. Autodesk, *Autodesk Fusion 360*, 2023.

COLLEGE MATHS, TELECOMS
DOCTORAL INFORMATIQUE, SIGNAL
BRETAGNE SYSTEMES, ELECTRONIQUE

INSA INSTITUT NATIONAL DES SCIENCES APPLIQUÉES RENNES

Titre : Contributions à la Caractérisation d'Antennes à partir de Mesures Champ Proche Cartésiennes Non Conventionnelles : Application de Nouvelles Méthodes de Transformée Champ Proche Champ Lointain sur des Grilles Non Planes et Non Régulières pour la Mesure d'Antennes Directives à Fort Angle de Dépointage de Faisceau

Mot clés : Électromagnétisme, métrologie, antennes, champ proche, échantillonnage

Résumé : Cette thèse présente de nouvelles méthodes de caractérisation et d'optimisation d'antennes réseaux électriquement grandes, à forte directivité, multi-fréquences et à forts angles d'inclinaison de faisceau, à partir de mesures en champ proche planaire. Les transformations classiques champ proche-champ lointain étant limitées par les effets d'échantillonnage et de troncature, des approches alternatives sont développées.

La méthodologie proposée repose sur la construction d'un modèle équivalent de l'antenne basé sur une distribution de dipôles infinitésimaux, conduisant à une matrice de rayonnement permettant des schémas d'échantillonnage non conventionnels et une réduction de la sensibilité à la troncature. Un modèle réduit est ensuite utilisé afin de minimiser le nombre de points de mesure requis, sans perte de précision.

Enfin, une méthode fondée sur le modèle équivalent est présentée, traitant conjointement l'optimisation de l'échantillonnage, la robustesse à la troncature et l'intégration de la correction de sonde dans la transformation directe. Ce cadre a été validé sur des scénarios expérimentaux complexes, démontrant précision et robustesse.

Title: Contributions to Antenna Characterization from Non-Conventional Cartesian Near-Field Measurements: Application of Novel Near-Field to Far-Field Transform Methods on Non-Planar and Irregular Sampling Grids for Directive Antennas with Wide-Angle Beam Scanning

Keywords: Electromagnetism, metrology, antennas, near field, sampling

Abstract: This thesis presents new methods for characterizing and optimizing electrically large, high-directivity, multi-frequency antenna arrays with significant beam tilts, based on planar near-field measurements. Since conventional near-to-far-field transformations are limited by sampling and truncation effects, alternative approaches are investigated.

The proposed methodology relies on an equivalent antenna model based on a distribution of infinitesimal dipoles, leading to a radiation matrix that enables non-conventional sampling schemes and reduced sensitivity to truncation. A reduced-order model is then employed to minimize the number of required measurement points while preserving accuracy.

Finally, an equivalent model-based method is introduced that jointly addresses sampling optimization, truncation robustness, and probe correction directly embedded in the transformation. The complete framework is validated through complex experimental scenarios, demonstrating both accuracy and robustness.